Dissertation zur Erlangung des Doktorgrades der Fakultät für Chemie und Pharmazie der Ludwig-Maximilians-Universität München

Structural studies of stringent response mechanisms in bacteria using cryo-EM

Maha William Eissa Abdelshahid

Aus Kairo, Ägypten

2019

Erklärung

Diese Dissertation wurde im Sinne von § 7 der Promotionsordnung vom 28. November 2011 von Herrn Prof. Dr. Daniel N. Wilson betreut.

Eidesstattliche Versicherung

Diese Dissertation wurde eigenständig und ohne unerlaubte Hilfe erarbeitet.

München, am 23.05.2019

_____

(Maha Abdelshahid)

Dissertation eingereicht am 23.05.2019

1. Gutachter: Herr Prof. Dr. Daniel N. Wilson

2. Gutachter: Herr Prof. Dr. Roland Beckmann

Mündliche Prüfung am 12.07.2019

Table of Contents

Acknowledgements

I would like to thank Prof. Dr. Daniel Wilson, who has made all this work possible and gave me the great opportunity to work under his supervision in Munich. I highly appreciate the patience he has shown me during my thesis. I would also like to thank Prof. Dr. Roland Beckmann for kindly sharing almost all laboratory facilities with us as well as the electron microscope. Not only on the scientific level but also during conferences and celebrations, it was so much fun for me to be in the Beckmann-Wilson parties. I would also like to thank the AG Beckmann, for their support and sharing the experience. In addition, I want to thank the Cryo-EM team including Dr. Otto Berninghausen, Charlotte Ungewickell, Susanne Rieder, with the latter two, for nicely preparing the EM-grids. In addition, I would like to give special thanks to Heidemarie Sieber, Joanna Musial, and Andrea Gilmozzi for their cooperation.

I cannot forget to thank Dr. Daniel Sohmen for his surprising patience in teaching and for knowing how to simplify the material according to everyone's background. He has given me great support and hope when I was completely broken and never judged my lack of knowledge in the field. He always answered my questions without complaining or being annoyed of how basic they were. I owe him for how far I have reached in the academic field. I also would like to thank my colleagues for the nice laboratory environment including Dr. Paul Huter, Dr. Michael Graf, Claudia, Aga, Maxi, Caillan, Timm, Dr. Fabian Nguyen, Dr. Bertrand Beckert, and Dr. Stefan Arenz.

Last but not least, I want to thank my family for believing in me and their continuous support. I would also like to thank my friends for bearing with me during stress and depressing moments especially Aninjya "the wise man", I thank him a lot for his continuous support and sense of humor. As well as "the freezing guy", for proofreading my thesis.

Abbreviations

30S	small ribosomal subunit
50S	large ribosomal subunit
30SIC	30S initiation complex
70SIC	70S initiation complex
30SPIC	30S pre-initiation complex
A	adenine
ABC	ATP- binding cassette
ACT	aspartate kinase, chorismate mutase and tyrA
AH	alpha helical
AMP	adenosine monophosphate
ARE ABC	antibiotic resistance ATP- binding cassette
aSD	anti-Shine Dalgarno
ASL	anticodon stem loop
ATP	adenosine triphosphate
A-site	Aminoacyl-site on ribosome
A-tRNA	A-site tRNA
C	cytosine
CC	conserved cysteine
CCW	counter clockwise
CTD	C-terminal domain
CW	clockwise
DC	decoding
DNA	deoxyribonucleic acid
EF-G	elongation factor GTPase
EF-Tu	elongation factor thermo-unstable
E-site	Exit site on ribosome
E-tRNA	E-site tRNA
FA	fusidic acid
fMet	formyl-methionine

G	guanine
GAC	GTPase associated center
GDP	guanosine-5’-diphosphate
GTP	guanosine-5’-triphosphate
HPF	hibernation promoting factor
IF	initiation factor
kDa	kilodalton
LSU	large subunit
MDR	multidrug resistant strains
mRNA	messenger RNA
MRSA	multidrug resistant *Staphylococcus aureus*
ms	millisecond
NTD	N-terminal domain
PDR	pan-drug resistant strains
Pi	inorganic phosphate
(P)ppGpp	guanosine-3’-diphosphate-5’-triphosphate
PTC	peptidyl transferase center
P-site	Peptidyl-site on ribosome
P-tRNA	P-site tRNA
RSH	RelA/ SpoT homologue
RaiA	ribosome associated inhibitor A
RC	ribosome complex
RF	release factor
RIS	ribosome intersubunit
RMF	ribosome modulation factor
RNA	ribonucleic acid
RRF	ribosome release factor
RRM	RNA recognition motif
rRNA	ribosomal ribonucleic acid
SAH	short alarmone hydrolase
SAS	short alarmone synthetase

SD	Shine-Dalgarno
SRL	sarcin ricin loop
SSU	small subunit
T	thymine
TGS	threonyl-tRNA synthetase, GTPase, and SpoT
tRNA	transfer RNA
TS	transition state
U	uracil
XDR	extensively drug resistant
ZFD	zinc finger domain

Publications List

Publication 1

The stringent factor RelA adopts an open conformation on the ribosome to stimulate ppGpp synthesis.

Stefan Arenz*, **Maha Abdelshahid***, Daniel Sohmen*, Roshani Payoe, Agata L. Starosta, Otto Berninghausen, Vasili Hauryliuk, Roland Beckmann, and Daniel N. Wilson. 2016.
Nucleic Acids Res, 44: 6471-81.

Publication 2

Stringent response control by bifunctional RelA enzyme in the presence and absence of the ribosome

Patrick Pausch, **Maha Abdelshahid**, Wieland Steinchen, Heinrich Schäfer, Fabio Lino Gratani, Sven-Andreas Freibert, Christiane Wolz, Kürşad Turgay, Daniel N. Wilson and Gert Bange.
Manuscript ready for submission

Publication 3

Structure of the *Bacillus subtilis* hibernating 100S ribosome reveals the basis for 70S dimerization.

Bertrand Beckert*, **Maha Abdelshahid***, Heinrich Schafer, WIeland Steinchen, Stefan Arenz, Otto Berninghausen, Roland Beckmann, Gert Bange, Kürşad Turgay, and Daniel N. Wilson. 2017.
EMBO J, 36: 2061-72.

Publication 4

Structural basis for antibiotic resistance mediated by the *Bacillus subtilis* ABCF ATPase VmlR

Caillan Crowe-McAuliffe, Michael Graf, Paul Huter, Hiraku Takada, **Maha Abdelshahid**, Jiří Novacek, Victoriia Murina, Gemma C. Atkinson, Vasili Hauryliuk, and Daniel N. Wilson. 2018.
Proc Natl Acad Sci U S A, 115: 8978-83.

* These authors contributed equally to this work

Contribution Report

This dissertation includes work that was conducted during the period of May 2015 to April 2019 at the Gene Center of the Ludwig-Maximilians University in Munich and the University of Hamburg. This research has been done in collaboration with other groups; Roland Beckmann (Munich, Germany), Gert Bange (Marburg, Germany), Vasili Hauryliuk (Umeå, Sweden), Kürşad Turgay (Hannover, Germany), and Gemma C. Atkinson (Umeå, Sweden).

Publication 1 (Arenz et al., 2016)

This publication presents the cryo-EM structure of *Escherichia coli* 70S ribosome in complex with *E. coli* RelA at an average resolution of 3.7 Å. This structural study reveals that RelA binds to the ribosome in an elongated conformation as well as the interactions of RelA with the ribosomal components. I purified the *E. coli* RelA and used the disome approach to assemble the complex of RelA on the ribosome for further investigations using cryo-EM. I also contributed in writing of the manuscript.

Publication 2 (Pausch et al., unpublished)

This paper comprises the first cryo-EM structure of bifunctional Rel on the ribosome in addition to the crystal structure of Rel ΔRIS-ACT off of the ribosome. This research illustrates the mechanism associated with the switch of activity of Rel between hydrolysis and synthesis. I purified the ribosomes for assembling the complex and formed the complex using the disome system, which needed to be established for *B. subtilis*. I processed the cryo-EM data and built a molecular model. I participated in the interpretation of the cryo-EM structure as well as figure preparation (main figure 1b, c, d and supplementary figures 1-5) and writing of the manuscript.

Publication 3 (Beckert et al., 2017)

This publication presents the cryo-EM structure of the 100S hibernating ribosome from *Bacillus subtilis* at an average resolution of 3.8 Å. The structure reveals the long HPF mediated hibernating ribosome as well as the binding site of long HPF including the CTD on the

ribosome. I purified the 100S from *B. subtilis* extract and helped with cryo-EM data processing. I also contributed to interpretation of the structure, writing the manuscript, figure preparation (main figures 1-4 except 2D, 3D-G, 4 zoomed plots) and assisted with supplementary figures. Moreover, I performed sucrose density centrifugation assays monitoring the 100S in HPF mutants.

Publication 4 (Crowe-McAuliffe et al., 2018)

This paper provides the cryo-EM structure of an ABCF member, VmlR, to *B. subtilis* stalled ribosomal complex at a resolution of 3.5 Å. The structure sheds the light on the binding of VmlR in the E-site with the antibiotic resistance domain extending toward the PTC. It also clarifies the mechanism by which ABCF proteins confer resistance toward various antibiotics. I contributed by providing the stalled ribosomal complexes used for binding the VmlR to be structurally determined using cryo-EM as well as assisted with writing of the manuscript.

Summary

The ribosome is the machinery concerned with the translation of the genetic information, present in the form of mRNA, into proteins. Translation is a multistep process; starting with initiation, followed by elongation and termination, and ending with ribosome recycling to prepare for a new round of translation. In each step, a group of factors are involved to ensure catalysis, speed, and high fidelity of the translated protein. Therefore, translation is not just a major target for the antibiotics and antimicrobials, but also a target for various environmental stimuli. One such environmental stimulus is nutrient limitation, which causes the bacterium to induce a stringent response to help the cells cope with such harsh conditions. It is well-known that the stringent response is mediated by the action of RSH (RelA/ SpoT homologue) proteins. Using cryo-EM, we show the binding of RelA in an elongated conformation on the ribosome, while being wrapped under the deacylated-tRNA. This in turn stabilizes the tRNA in a distorted conformation known as A/R-tRNA. The structure also illustrates the detailed interactions between RelA and the ribosome including the interaction between the deacylated-tRNA and the TGS (Threonyl tRNA synthetase, GTPase, and SpoT) domain of RelA which is crucial for sensing starvation conditions. The second cryo-EM structure represents the first structure of a bifunctional Rel protein bound to the ribosome showing the high similarity between both the bifunctional Rel and the monofunctional RelA in their binding site to the ribosome. The third study focuses on the mechanism of ribosome hibernation in Gram-positive bacteria via long HPF (hibernation promoting factor) during the transition into the stationary phase. A cryo-EM structure reveals the mechanism by which LHPF binds to the ribosome and induces ribosome dimerization to form 100S. LHPF-NTD (N-terminal domain) is connected to the LHPF-CTD (C-terminal domain) via a flexible linker which allows the NTD binding between the head and the body on the 30S, whereas the CTD binds on the solvent side of the 30S. The CTD of one LHPF molecule interacts with that of the second LHPF molecule on the neighboring ribosome. Thus the CTD plays an important role in stabilizing the 100S formation, while the NTD binding site overlaps with the tRNAs binding site resulting in an inactively translating ribosomes. Inactive ribosomes during stationary phase represent an energy saving mode of bacterial cells during stress conditions.

1. Introduction

1.1. Protein synthesis in prokaryotes

Genetic information is stored in the form of deoxyribonucleic acid (DNA), this is then transferred into ribonucleic acid (RNA) via transcription. RNA is used as a template for the production of protein via the process of protein translation. This whole process is known as the central dogma of molecular biology that has been characterized in all living organisms by Crick (Crick 1970). The process of protein synthesis (translation) is catalyzed by the action of ribosomes. The ribosome (also known as the protein factory) is a large ribonucleoprotein molecule found in all kingdoms of life. It is composed of two subunits that are made up of both rRNA (ribosomal RNA) and proteins (Figure 1A). The prokaryotic ribosome as a whole is called the 70S ribosome; this consists of two subunits, the small 30S subunit and the large 50S subunit. These numbers refer to the sedimentation coefficient in Svedberg units. The small subunit contains the entry site for the messenger RNA (mRNA) and is responsible for decoding, while peptide bond formation occurs on the large subunit. Decoding and peptide bond formation require the action of transfer RNAs (tRNAs). Three tRNA binding sites are shared between both ribosomal subunits (Figure 1B), the A- (aminoacyl), P- (peptidyl), and E- (exit) sites. The aminoacylated tRNA binds to the A-site and the tRNA carrying the peptidyl chain binds to the P-site, while the deacylated tRNA exits the ribosome through the E-site. Three rRNAs are distributed among the 70S; the 16S rRNA is located in the 30S while the 23S and the 5S rRNAs are found in the 50S. In *E. coli*, the small subunit is composed of 21 ribosomal proteins (S1-S21) while the large subunit contains 33. Unlike the catalytic function exerted by the rRNA, the ribosomal proteins are rather crucial for the folding of the rRNA in the catalytically active conformation, in addition to their role in maintaining translation fidelity (Ban et al. 2000; Schluenzen et al. 2000; Wimberly et al. 2000) reviewed in (Melnikov et al. 2012; Ramakrishnan 2002; Williamson 2009).

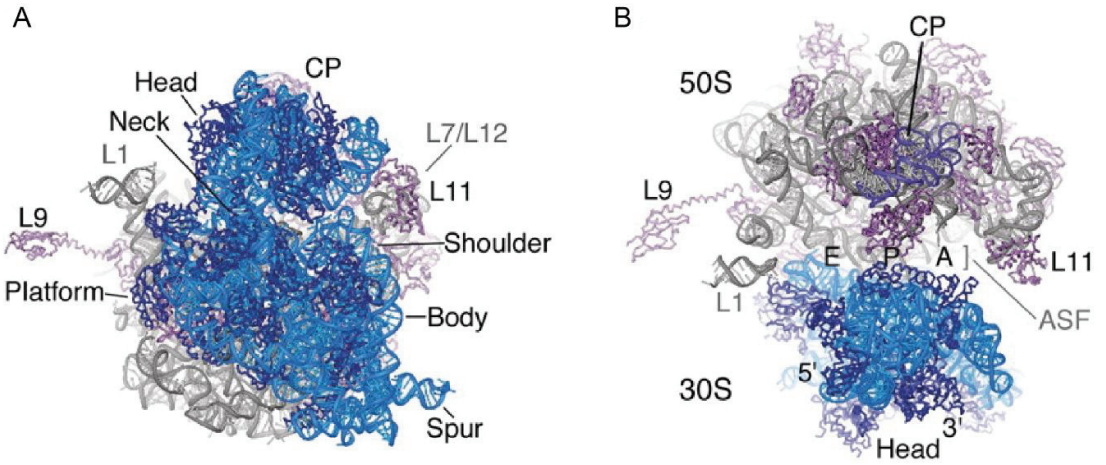

Figure 1. Structure of *E. coli* 70S ribosome. (A) Solvent side view of the 70S ribosome showing its main features including head, neck, shoulder, body, platform, and spur. Light blue and dark blue colors resemble 16S rRNA and proteins, respectively. While grey and magenta are used for 23S rRNA and proteins, respectively and the 5S rRNA is shown in purple. **(B)** Top view of the intact 70S presenting the shared binding sites for the A-, P-, and E-tRNAs on both ribosomal subunits. CP (Central Protuberance) and ASF (A-site Finger) are also presented on the 50S. This figure is adapted from (Schuwirth et al. 2005) with permission.

1.2. Translation

Translation, the last step in gene expression following transcription, involves the conversion of the nucleotide information in the mRNA into an amino acid sequence that folds into a protein. This process involves four distinct steps: initiation, elongation, termination, and recycling. Although significant differences are observed in the detailed mechanism of each event between eukaryotes and prokaryotes, many aspects are highly conserved.

1.2.1. Initiation

Translation initiation is an essential and rate limiting step (Ray and Pearson 1975) and reviewed in (Jacques and Dreyfus 1990). In bacterial cells, the initiation step could occur at the same time as the transcription (co-transcriptionally), via the interaction of the RNA polymerase (RNAP) and the ribosome (Kohler et al. 2017; Landick, Carey, and Yanofsky 1985; Proshkin et al. 2010). In order for the initiation process to occur, a pre-initiation complex is required as an intermediate. This involves the 30S, the initiator fMet (formylmethionine)-$tRNA^{fMet}$, and three initiation factors (IF1, IF2 and IF3), which are found in comparable amounts to the ribosome. Although prokaryotes contain different types of mRNA, those

containing the Shine Dalgarno (SD) are usually the most highly expressed and also most extensively studied. The matching of Shine-Dalgarno (SD) sequence (an 8-10 nucleotide (nt) sequence upstream of the start codon) on the 5' end of the mRNA the variable element to the anti-Shine Dalgarno (aSD) sequence on the 3' end of the 16S rRNA, leads to 30SPIC (pre-initiation complex) conversion into 30SIC (initiation complex). Once the 30SIC is formed, the 50S ribosomal subunit is recruited and attaches to the small subunit forming the 70S initiation complex (70SIC) (Shine and Dalgarno 1974; Hui and De 1987; Simonetti et al. 2008; Jacob, Santer, and Dahlberg 1987).

The formation of the 70SIC requires several pre-initiation steps; one of which is the binding of the initiation factor 3 (IF3) to the 30S of the bacterial ribosome to prevent premature re-association with the 50S. IF3 has been shown to bind to the 30S platform with the NTD, while the CTD approaches the P- site (Hussain et al. 2016). Next the initiation factor IF2, a guanosine 5' triphosphatase (GTPase), binds to the 30S of the ribosome recruiting the fMet-$tRNA^{fMet}$. Unlike the elongator aminoacyl-tRNAs, the fMet-$tRNA^{fMet}$ enters the P-site directly, disregarding the A-site. Structural studies show the role of the IF2 in distinguishing the initiator fMet-$tRNA^{fMet}$ from the elongator using domain IV (also known as C2 domain). This recognition takes place via the interaction between Domain IV and the CCA-3' of fMet-$tRNA^{fMet}$ in a similar manner to that used between EF-Tu and elongator tRNA. (Hussain et al. 2016; Caban et al. 2017; Sprink et al. 2016).

The last and smallest of the initiation factors, initiation factor 1 (IF1), encoded by the *infA* gene, binds in a cleft between the 530 loop, the nucleotide bases A1492 and A1493 in helix 44 (H44) of the 16S rRNA and ribosomal protein S12 (Cummings et al. 1991; Moazed et al. 1995; Carter et al. 2001; Boelens and Gualerzi 2002). This is located at the A site of the bacterial ribosome, suggesting that the cooperation of IF1 and IF2 may have an "initiation fidelity function", since this is the same site where the aminoacyl-tRNA (aa-tRNA) binds during elongation (Boelens and Gualerzi 2002). By occupying this location, IF1 may prevent the premature binding of aa-tRNAs. Another function of the IF1 is to strengthen the binding of IF2 to the 30S complex (30S-IF2), since the ejection of this factor during the 70SIC assemble is assumed to lower the affinity of the 30S-IF2 complex. A similar relation is observed for the IF2 and the 30S-IF1, which could mean that they are conformationally mediated (Stringer, Sarkar, and Maitra 1977; Celano, Pawlik, and Gualerzi 1988; Zucker and Hershey 1986).

Although, the recruitment of the initiation factors to the 30S does not follow a specific order, a kinetically preferred sequence does exist where IF3 and IF2 bind first, followed by IF1 and lastly the fMet-tRNA^{fMet} (Milon et al. 2012). As observed, the three initiation factors (IF1, IF2 and IF3) play several vital roles in the translation initiation process, in order to fulfil the formation of the 70SIC. Such as the interaction between the fMet-tRNA^{fMet} and mRNA, ensuring correct codon-anticodon interaction and correct placement of the mRNA start codon (AUG) in the P-site on the 30S (Nakagawa et al. 2010; Yusupova et al. 2001). 30S initiation complex formation upon codon-anticodon recognition is then followed by recruitment of the large ribosomal subunit (50S) via the action of IF2 forming the 70SIC (consisting of the 70S with fMet-tRNA^{fMet} in the P-site interacting with the AUG on the mRNA) (Sprink et al. 2016).

1.2.2. Elongation

The elongation step in translation is a rapid and accurate process. The incorporation of amino acid during translation is dependent on both codon and growth condition. This means that under optimal growth conditions, the elongation step in *E. coli* may take as little as 50 milliseconds (ms) to complete (rate of approximately 17-20 amino acids/second) (Pedersen 1984; Kruger et al. 1998). The steps involved in the elongation cycle require the addition of amino acids to the polypeptide chain. This starts off with an empty A-site and the peptidyl-tRNA carrying the fMet-tRNA^{fMet}. Elongation is composed of three steps, decoding, peptide bond formation and translocation.

Decoding

Decoding involves the newly incoming aa-tRNA anticodon being checked for a match with the mRNA codon in the A-site. It involves the delivery of the next amino acid in a ternary complex to the empty A-site; this is a rapid process with a rate of around 20 amino acids/second (Liang et al. 2000). This stable ternary complex consists of a GTPase called the elongation factor Tu (EF-Tu), an aminoacyl-tRNA (aa-tRNA) and a guanosine-5´-triphosphate (GTP) (Schmeing and Ramakrishnan 2009; Fischer et al. 2015).

The initial binding of the ternary complex to the ribosome is not codon specific, but is assisted with the interaction of the EF-Tu to the flexible C-terminal domains of the ribosomal protein L7/L12. On *E. coli* ribosomes, the L12 exists as two dimers (4 copies) bound to L10 via their N-terminal domains (NTD). The importance of the L12 for the EF-Tu ribosome

binding and for GTP hydrolysis has been shown in extraction/complementation experiments. Furthermore, specific mutations in the L12 C-terminal domain (CTD) affect the binding of the EF-Tu-GTP-aa-tRNA, ternary complex, to the ribosome (Kothe et al. 2004; Diaconu et al. 2005; Rodnina et al. 1996; Blanchard, Gonzalez, et al. 2004). This step is reversible and is considered as the first proofreading step, since it ensures the dissociation of the ternary complex upon sensing codon-anticodon mismatch. Scanning of the different ternary complexes by the ribosome occurs with a rate of 1-2 millisecond/aa-tRNA (Diaconu et al. 2005). It is noteworthy, that only cognate and near cognate aa- tRNA complexes are recruited by the ribosome while non-cognate ones do not even bind to the ribosome (Figure 2A) (Pape, Wintermeyer, and Rodnina 1999).

Initial codon-anticodon recognition results in rearrangements of A1492, A1493, and G530 of the rRNA, such that the first two bases flip-out of helix 44. Their rearrangement leads to interactions with the first two positions of the codon-anticodon helix. In addition, the highly conserved G530 interacts with the second base pair as a result of changing to the anti-conformation. The induced interactions between the first base pair and A1492, and the second base pair with both A1493 and G530 permit Watson-Crick base pairing within the first two bases, but might allow wobbling of the third. The stabilized interactions and the derived energy would induce the 30S shoulder movement toward the ternary complex known as domain closure, in the case of cognate aa-tRNA interaction (Figure 2B). While in the case of near cognate tRNA, the destabilized interactions result in dissociation of the tRNA off of the ribosome (Ogle et al. 2001; Ogle et al. 2002; Nissen et al. 2001). A recent study by Loveland has shed light into the discrimination between cognate and near cognate ternary complexes at the decoding center. The recognition of cognate codon- anticodon interaction induces the stabilization of the essential decoding center nucleotides G530, A1492, and A1493. This stabilization in turn favors the 30S domain closure and hence activation of EF-Tu and GTP hydrolysis in case of cognate tRNA, but not in near cognate one (Figure 2B, C) (Loveland et al. 2017).

EF-Tu is composed of three domains (domain I-III) with GTP binding site being in domain I, while domain II localizes next to the 30S shoulder upon binding to the ribosome. A series of conformational changes occur within EF-Tu following cognate tRNA recognition. This accurately positions EF-Tu for GTP hydrolysis activation via the action of sarcin-ricin loop (SRL), also known as the GTPase activating center (Wool, Gluck, and Endo 1992; Schmeing and Ramakrishnan 2009). SRL is responsible for rearranging His84 (*E. coli*

numbering) into the GTPase center and positions the water molecule to attack the GTP ɣ-phosphate leading to GTP hydrolysis (Wallin, Kamerlin, and Aqvist 2013; Adamczyk and Warshel 2011; Aqvist and Kamerlin 2015). Mutational analysis has shown the role of His84 by converting it to alanine; which resulted to a dramatic decrease in the GTP hydrolysis rate (Daviter, Wieden, and Rodnina 2003; Voorhees and Ramakrishnan 2013; Voorhees et al. 2010; Maracci et al. 2014). Following inorganic phosphate release, EF-Tu-GDP dissociates of the ribosome as a result of the weakened interactions with the SRL and the tRNA (Rodnina et al. 2017).

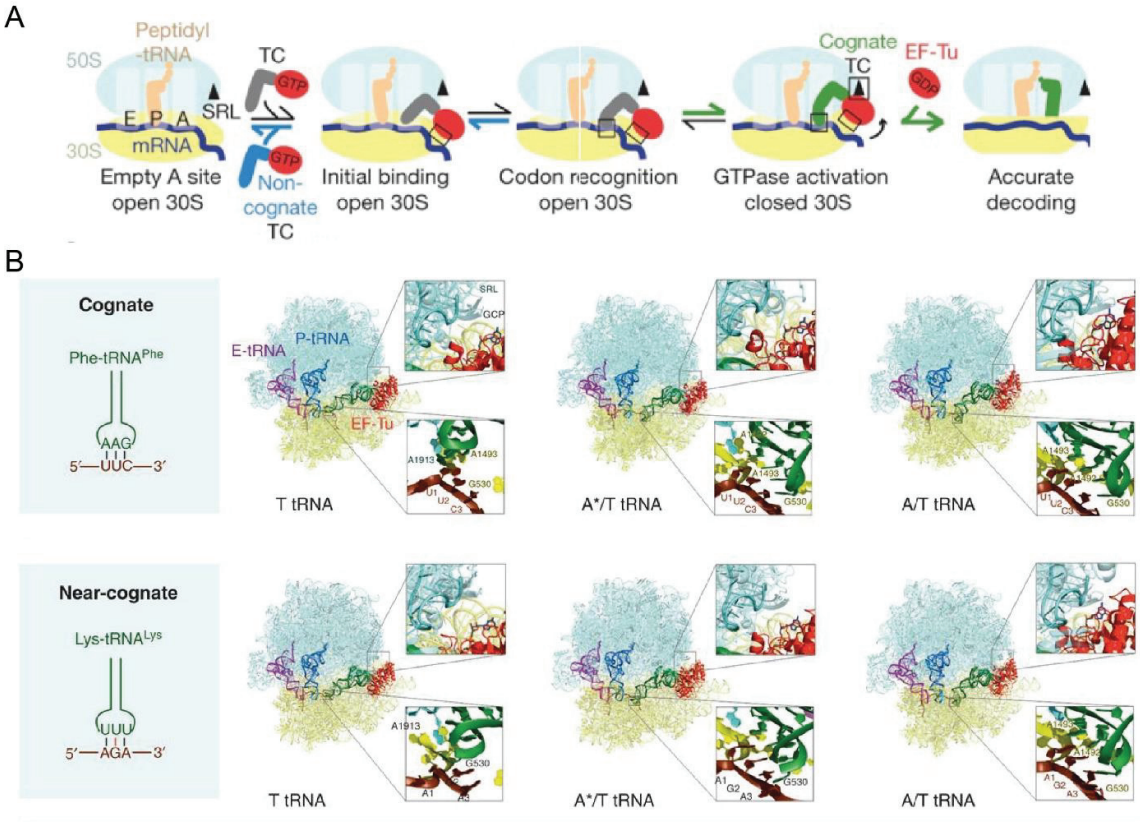

Figure 2. Mechanism of initial aminoacyl-tRNA selection and conformational changes during decoding. **(A)** Schematic representation of the structural mechanism during the initial aminoacyl-tRNA recruitment (TC stands for ternary complex). Equilibrium shifts for cognate and non-cognate TC are represented in green and blue arrows, respectively. **(B)** Cryo-EM representation of the decoding process during cognate and near-cognate TC. The first column in panel **(B)** shows the schematic diagrams of the codon-anticodon interaction. Column 2- 4 represent the different codon recognition steps and the changes within the decoding center essential nucleotides A1492, A1493, and G530 till the docking of the EF-Tu onto the SRL. Panel **(B)** is provided by Loveland (Rodnina 2018) based on a previously published structure (Loveland et al. 2017) and modified with permission. While Panel **(A)** is reproduced from the latter with permission.

During decoding, the aa-tRNA is held in the A/T conformation in which the D-stem and the anticodon stem are distorted. This conformation allows for the interaction of the anticodon with the mRNA, on the 30S A-site and with the EF-Tu on the 50S. Mutations at the distorted sites of the aa-tRNA have a negative effect on GTP hydrolysis. Thus the importance of such a conformation has been shown for the interaction with EF-Tu and stabilization of His84 in the required conformation for catalyzing GTP hydrolysis (Schmeing et al. 2009; Loveland et al. 2017; Valle et al. 2002; Stark et al. 1997). The last step in decoding, following GTP hydrolysis, involves the accommodation of the A/T-tRNA into the A/A-tRNA state. This requires the relaxation of both the tRNA body and the acceptor stem, so that the CCA-3' end (3' end tail of the tRNA) moves into the PTC (peptidyl transferase center) (Sanbonmatsu, Joseph, and Tung 2005). Hence, tRNA accommodation is the second proofreading step during decoding to avoid incorporation of wrong amino acids into the peptide chain via sensing and increasing the dissociation rate of the tRNAs with low accommodation rates. This is based on the observation that near cognate tRNA, which escapes the codon-anticodon scanning step has a slower accommodation rates compares to cognate tRNA (Gromadski and Rodnina 2004; Rodnina et al. 2017). The completion of decoding, marked with successful tRNA accommodation, signals the continuation into the peptide bond formation step.

Peptide Bond Formation

Peptide bond formation occurs in the catalytic site located within domain V of the large ribosomal subunit called the peptidyl transferase center (PTC) (Hansen et al. 2002; Nissen et al. 2000; Schlünzen et al. 2001; Ban et al. 2000). This site has been shown via crystal structures to be comprised entirely of closely packed rRNA with L16 (archaea/eukaryotes) and L27 (bacteria) being the closest protein to the PTC, at a distance of 8-16 Å, supporting the idea that the ribosome is a ribozyme (Polikanov, Steitz, and Innis 2014; Maguire et al. 2005). The sequence of the rRNA within the PTC has been shown to have a high degree of conservation. Even though the mechanism of peptide bond formation is highly conserved in all organisms, it is still presumed that the interacting groups within the PTC might be differently arranged among species, (Noller and al. 1981; Gutell et al. 1985; Harms et al. 2001; Ban et al. 2000). The nascent peptide chain is linked via an ester bond, using its peptide carbonyl carbon, to the oxygen of the 3' A76 in the peptidyl-tRNA. Peptide bond formation requires the nucleophilic attack of the aa-tRNA, specifically the α-amino group on the peptide carbonyl carbon of the P-tRNA (Figure 3A). This leads to breakage of the ester bond which is linking the nascent

peptide chain to the P-tRNA and peptide bond formation with the aa-tRNA (Figure 3B). The resulting peptide chain is one amino acid longer following peptide bond formation (Rodnina 2018; Rodnina, Beringer, and Wintermeyer 2007).

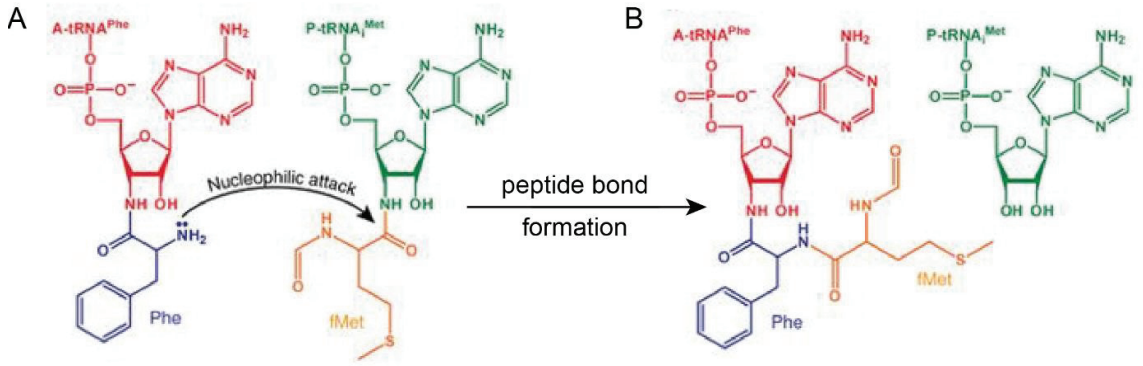

Figure 3. The chemical structure of peptide bond formation. (A) Pre-peptide bond formation between Phe-tRNA^{Phe} and fMet-tRNA$_i^{Met}$. **(B)** Post-peptide bond formation with the fMet-Phe-tRNA^{Phe} in the A- site and tRNA$_i^{Met}$ in the P- site. This figure is modified from (Polikanov, Steitz, and Innis 2014) with permission.

The CCA-3' end of the fully accommodated A- and P-tRNAs base pair with nucleotides of the A- and P-loops on the 50S, respectively. Thus binding of the aa-tRNA in the A-site induces a conformational change in the PTC nucleotides U2506, G2583, U2584, and A2585. Such changes assist in positioning the P-site ester linkage for nucleophilic attack. Whereas, in the absence of the A-tRNA, these nucleotides are oriented to prevent premature nascent chain cleavage via the protection of the ester bond from water access (Voorhees et al. 2009; Schmeing, Huang, Kitchen, et al. 2005; Schmeing, Huang, Strobel, et al. 2005). Mutational studies of the conserved nucleotides U2584 and U2585 (*E. coli* numbering), located within domain V, have decreased cell response to many peptidyl transferase inhibitors. These observations support the role played by the highly conserved nucleotides within domain V in the peptidyl transferase catalytic activity including A2451, U2506, U2585, C2452 and A2602 (Noller 1991; Garrett and Rodriguez-Fonseca 1996).

Kinetic analysis experiments indicate that the isolated 50S subunit has similar catalytic activity and can synthesize peptide bonds as rapidly as the 70S ribosome. However, in order to maintain the active conformation of the peptidyl transferase center, the full-length tRNA in the P-site is important (Wohlgemuth, Beringer, and Rodnina 2006). The ribosome, as compared to model substrates in solution, enhances the rate of peptide bond formation by at least 6 orders of magnitude (Sievers et al. 2004). Another characteristic of the ribosome is its ability to utilize most amino acid combinations without additional auxiliary factors to make

peptides. One exception is the synthesis of poly-Pro stretches (Peil et al. 2013; Woolstenhulme et al. 2013).

A variety of mechanisms are employed by enzymes in order to increase their rate of reactions. Examples of these could be the correct positioning of the substrates, transition state stabilization or chemical catalysis (Narlikar and Herschlag 1997; Sharma et al. 2005). However, the catalysis process performed by the ribosome, unlike protein enzymes which provide pKa values at neutral pH, is mainly entropic in nature (i.e. does not involve chemical catalysis). This means that processes facilitated by the ribosome to achieve the peptide bond formation rate enhancement, such as the ordering of the water molecules, rRNA and tRNA positioning and electrostatic shielding, is based on lowering the entropy of activation via conformational changes at the active site (Sievers et al. 2004; Youngman et al. 2004).

The acid-base concept was the first mechanism proposed to account for the peptide bond formation. The hypothesis evolves around the N3 of the residue A2486 (A2451 in *E. coli*) and its proximity to the attacking amino group where a proton is extracted. Thus, facilitating the formation of the tetrahedral intermediate, suggesting its function as a general acid base during peptide bond formation (Nissen et al. 2000). However, the mechanism has been shown to be incorrect by subsequent experiments, which showed peptidyl transferase activity was not significantly changed with mutations at position 2486 and other proximal sites (Polacek et al. 2001; Thompson et al. 2001). Furthermore, higher resolution of the structure has shown that the oxyanion may not be near this base (Hansen et al. 2002). Lastly, by using a range of pH to measure the reaction rate no change was observed, arguing against the general acid-base catalysis due to its independence of pH. It rather seems that A2451 plays a role in stabilization of the structure than chemical catalysis (Beringer et al. 2005; Bieling et al. 2006).

There are currently two models, although disagreeing on the exact pathway; they describe the movement of the three protons in the active site during peptide bond formation in the rate limiting transition state. The first model involves a nucleophilic attack on the P-site ester bond by the A-site amino group via the 2'-OH of the P-site tRNA residue A76. This process is referred to as an intra-reactant proton shuttling and shows significant catalytic effect and favorable energetics. This was discovered by crystal structures of both A- and P- site substrates bound separately to the 50S subunit (Hansen et al. 2002). The positioning of the A76 2'-OH group (the peptidyl-tRNA) allows for hydrogen bond formation with the α-amino nucleophile, this facilitates peptide bond formation. Furthermore, the hydroxyl group acts as a proton shuttle between the α-amino group and the 3'-OH group of A76. This model suggests

that an eight membered transition state is formed by the transfer of a proton from the α-amino group present on the ester carbonyl carbon to the 2'-OH group of the A76 (Figure 4B left panel). This in turn, donates the proton by an adjacent water molecule to the carbonyl oxygen of the P-tRNA (3'-OH) (Kuhlenkoetter, Wintermeyer, and Rodnina 2011; Wallin and Aqvist 2010). Thus, the term 'proton shuttle' since the amino proton is transferred from the hydroxyl group and then donated elsewhere, as dictated by the hydroxyl pKa. The water molecule was observed previously by crystallographic data, which showed a moiety via electron density that is interacting with the 2'-OH group. Further evidence has shown that this moiety is a water molecule and not a metal ion (Schmeing, Huang, Kitchen, et al. 2005).

The importance of the 2'-OH in the peptidyl transferase was considered for decades (Hecht, Kozarich, and Schmidt 1974; Quiggle et al. 1981), where they found that the peptidyl transferase in the P-site was inactive when Phe-tRNA^{Phe} was with a 2'-deoxy A76 residue (Hecht, Kozarich, and Schmidt 1974). Further biochemical experiments confirmed that the 2'-deoxy (Dorner et al. 2003) or 2'-fluoro A76 were inactive or showed a decreased catalytic rate by at least six orders of magnitude, when full-length tRNAs are used in both sites (Weinger et al. 2004). This could be due to the repositioning of either the nucleophile amine group or the carbonyl carbon. Although the proton shuttle has less optimal stereochemistry than the other model, it is the only mechanism that is in line with the observed pH-rate profile and KSIE (kinetic solvent isotope effect) analysis (Kazemi et al. 2018).

Recently, an alternative model known as proton wire model (Figure 4B, right panel), which differs considerably from the previous, was suggested based on the pre-attack and post-catalysis complexes of a 2.6 Å resolution crystal structure of a *Thermus thermophilus* (Tth) 70S ribosome binding to a full-length tRNA. In this model, three ordered water molecules (W1-3) are trapped within the PTC (Figure 4A). A cavity formed by the 23S rRNA residues (A2602 and A2451), the N terminus of protein L27 and the 3' end of the A-site tRNA, holds the W1. According to the structure of the pre-attack complexes, the W1 is not likely to be exchanged during catalysis, due to its tight coordination caused by strong hydrogen bonds with the 5'-phosphate oxygen of residue A78 of the A-site tRNA as well as the N6 amino group of A2602 and the N terminus of the L27 (Polikanov, Steitz, and Innis 2014). W2 and W3 were previously observed in the *Haloarcula marismortui* (*Hma*) 50S subunits buried deep within the PTC (Schmeing, Huang, Kitchen, et al. 2005; Schmeing et al. 2002). The 2'-OH, 3'-N and N3 atoms of the A76 P-site tRNA residue and the 2'-OH of C2063, form hydrogen bonds with the W3. Unlike the *Hma* 50S-subunit complexes, which shows two water molecules present at

the PTC and active site accessibility to the bulk solvent, the *Tth* 70S complex shows how all three water molecules interact with the ribosome and its tRNA substrates. Furthermore, the PTC does not allow any further accessibility to solvent molecules.

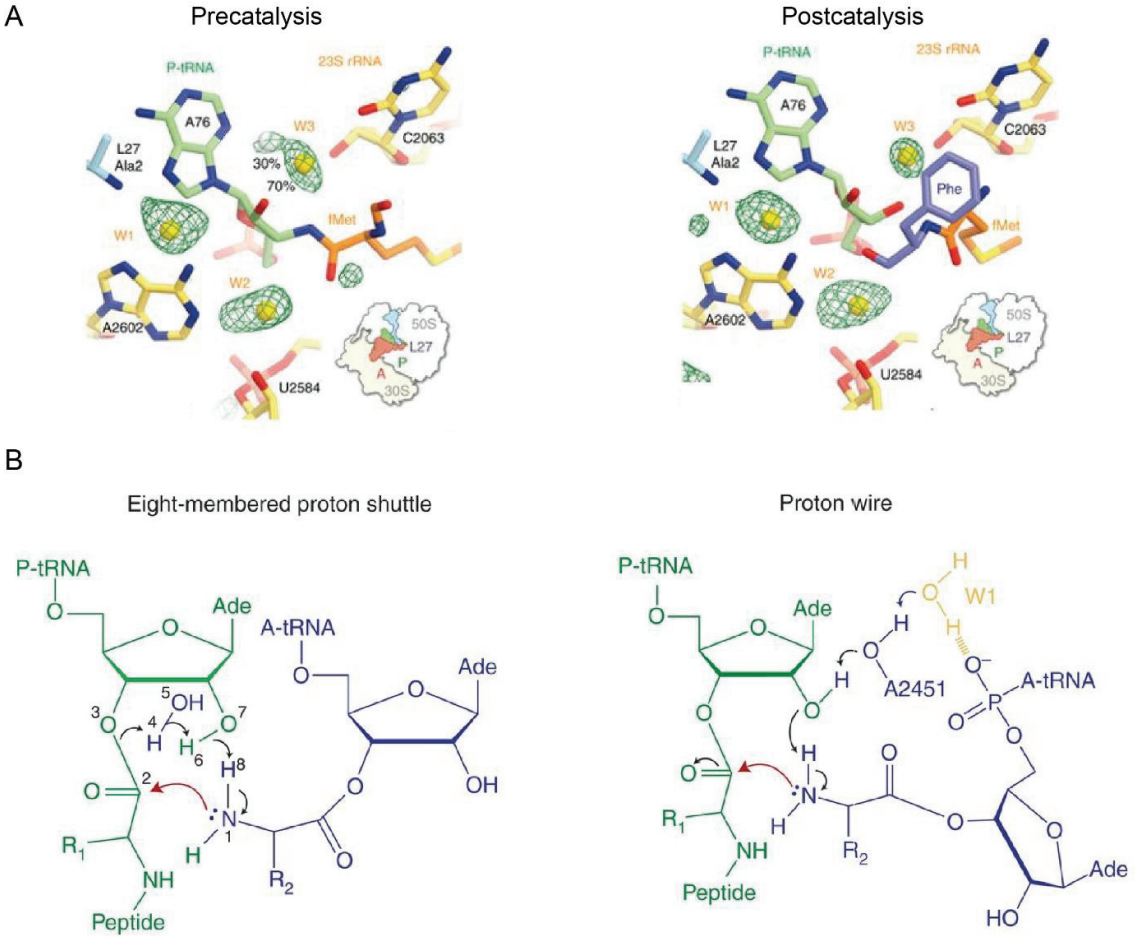

Figure 4. The proposed mechanisms of peptide bond formation. (A) Electron density maps of the decoding center showing the positions of the three water molecules W1-W3 pre and post peptide bond formation according to the proton wire model using cryo-EM. This is reproduced from (Polikanov, Steitz, and Innis 2014) with permission. **(B)** Chemical structure representing the proton transfer pattern during peptide bond formation according to the proton shuttle model on the left and the proton wire on the right. The figure is provided by Loveland (Rodnina 2018) based on previously published structures from (Polikanov, Steitz, and Innis 2014; Kuhlenkoetter, Wintermeyer, and Rodnina 2011) and modified with permission.

One of the benefits of the proton wire is that it is the first model that incorporates the possible role of ribosomal protein L27 in the process of peptide bond formation; this was first described by Voorhees (Voorhees et al. 2009) who showed two *Tth* crystallized structures 3.6 Å and 3.5 Å resolution respectively, with an A-site tRNA whose CCA tail resides within the PTC. The localization of the N-terminal tail of L27 was found to be between the CCA-3' end

of the A- and P-tRNAs. An interesting observation is that the L27 is absent in some organisms, the archaea for example contain no homolog of the L27, instead a protein called L10e (uL16) replaces it. This protein, even though it is disordered by the *Hma* 50S subunit structure (Ban et al. 2000), contains an internal loop that extends toward the 70S ribosome PTC region with bound full-length tRNA substrates. This was confirmed with a cryo-EM model of the eukaryotic L10e homolog (RPL10) using a wheat germ ribosome complex with a P-site tRNA (Armache et al. 2010). However, further studies will need to be performed in order to confirm whether this archaea protein has a comparable role as the L27.

The formation of a negative charge on the W1 is facilitated by the presence of a basic group caused by the deprotonation of the α-amine L27 and the negatively charged 5'-phosphate oxygen of the residue A76 A-site in its immediate vicinity. The 2'-OH of the A76 ribose P-site and the 2'-OH of the A2451 form the proton wire. This proton wire allows the transfer of a concerted proton towards the W1 from the nucleophile, resulting in a negatively charged tetrahedral intermediate (T-). Furthermore, the adjoining W2 might provide a proton yielding a neutral intermediate (T0). This in turn would trap or retain the structure within the closed pocket containing the W1 and W2, due to the lack of groups suitable to propagate proton transfer. One attractive possibility is that the involvement of the proton wire, via the positive charge contained within the W1 pocket, to break down the negatively charged intermediate (T-). This can be achieved by the formation of the hydronium ion formed from the proton transfer between W1 to W3 resulting in the hydrolysis breakdown of the intermediate to yield a deacylated tRNA in the P-site and the peptidyl-tRNA in the A-site (Polikanov, Steitz, and Innis 2014).

The L27 comes into play where its N-terminal delays the proton loss from the W1 to the bulk solvent, thus allowing the W3 to undergo protonation first. The deletion of the N terminus hinders the rates of intermediate structure formation and in turn, its conversion to its products. Another role of the L27 is the formation of a shielded system for the W2 water molecule and the proton wire allowing for the exchange of a proton to occur only with the 2-OH of the A76 ribose P-site and the bulk solvent. This shield is formed by the conserved length of the N-terminal extension. An indication of a closed PTC would be the lack of pH sensitivity for peptide bond formation (Polikanov, Steitz, and Innis 2014). According to the role of L27, one can easily see how shortening the conserved region by a couple (three or more) of residues affects protein synthesis. However, arguments against this model have stated that no effect on peptide bond formation has been observed after the deletion of the L27. Also, the absence of

the L27 was shown not to alter the pH dependence on the peptidyl transfer (Maracci, Wohlgemuth, and Rodnina 2015). Further investigations are required to reveal the role played by L27 during the peptidyl transferase reaction.

Regarding the proton wire and the proton shuttle models, it is noteworthy to mention that in many of structural studies used to study the mechanism of peptide bond formation, tRNA analogs lacking the full tRNA body have been used. Thus the exact substrate positioning and the detailed proton transfer explained here might or might not reflect the exact detailed mechanism of peptide bond formation inside the cell under native conditions. The idea of peptide bond catalysis inside the PTC via two alternative mechanisms cannot be excluded.

Translocation

Translocation is the end of the elongation cycle of protein synthesis. A deacylated-tRNA is left in the P-site after the transfer of the nascent peptide chain from the P- to A-site tRNA, thus a change in acylation states during peptide bond formation. During translocation, this deacylated-tRNA, coupled to the mRNA movement by one codon is then transferred to the E-site of the ribosome, while the peptidyl-tRNA is transferred to the P-site from the A-site. These general changes in positions with respect to the ribosome places the next mRNA codon in the A site (Rodnina et al. 1997). The ribosome plays an integral part in the process of translocation, by providing the environment and actively participating in the process. This involves the rearrangement of the macromolecules of the ribosomal subunits to allow for tRNA movement (Spirin 1969). Ribosomes were thought to originally have only two tRNAs binding sites, the A- (aminoacyl) and P- (peptidyl) site. However, this changed after Nierhaus discovered the E- (exit) site, giving way to the three-site model (Rheinberger, Sternbach, and Nierhaus 1981). These three sites are shared by both the small and large ribosomal subunits. The small subunit is bound by the mRNA and the tRNA anticodon stem-loop (ASL), while, the large subunit is bound by the tRNA acceptor ends; where base pairs are formed between C74 and C75 in the 3’ CCA end of the P-site tRNA and G2252 and G2251, respectively, in the P-loop of the 23S rRNA. The G2553 in the A-loop pairs with the C75 of the A-site tRNA (Selmer et al. 2006; Samaha, Green, and Noller 1995; Kim and Green 1999).

The 30S subunit P- and A-sites are occupied by the anticodons of the two tRNAs in the pre-translocation classical state. The SSU, relative to the LSU, starts to rotate “counterclockwise” (CCW). By this, we refer to the movement of the 30S subunit (foreground), while maintaining the 50S subunit (background) fixed. Since the CCW rotation corresponds with the direction of translocation, we refer to it as forward movement (Frank and

Agrawal 2000; Gao et al. 2003; Valle et al. 2003). Hybrid states are formed when the CCW rotation causes the A- and P-tRNAs CCA-3' end movement from their classical states on the 50S, with the P/E tRNA state formed first. This is then followed by the A/P state. The anticodon ends of the peptidyl- and deacylated- tRNAs remain bound to the A- and P-sites of the SSU, respectively (Fischer et al. 2010). SmFRET (single molecule fluorescence resonance energy transfer) experiments have shown the spontaneity and reversibility of both the hybrid state formation and the CCW rotation, solely driven by thermal energy (Cornish et al. 2008; Blanchard, Kim, et al. 2004; Munro et al. 2007). Ribosome rotation and the movement of the SSU head and body domains have been shown to occur very rapidly (microsecond time scale) via molecular dynamics simulations. Another process that occurs concomitantly with the rotation of the 30S is the movement of the dynamic uL1 stalk from an open to closed formation toward the P-site tRNA (Bock et al. 2013; Munro et al. 2010). This allows for the interaction and stabilization of the newly deacylated P-site tRNA by the L1 stalk throughout translocation, as the P/E hybrid state is formed (Fei et al. 2008). A fluctuation of the ribosome between the hybrid rotated L1 open and the classical non-rotated L1 closed state is the result of the absence of the prokaryotic GTPase elongation factor (EF-G). Even though translocation can take place in the absence of EF-G, GTP hydrolysis is prevented and the translocation process is very slow (reduced by ~40-50 fold) without EF-G (Semenkov et al. 1992; Moazed and Noller 1989). Thus, EF-G plays two distinct roles in different phases of protein synthesis, the other being during the elongation phase.

EF-G is a GTPase consisting of 5 domains, with domain 1 comprising the G domain, which catalysis GTP hydrolysis. EF-G interacts with the intersubunit cleft on the A-site side (Figure 5B, right panel), binding to the 50S ribosome via the G domain (Aevarsson et al. 1994; Czworkowski et al. 1994). The activity of the GTPase by the EF-G is very low intrinsically, however this increases by several magnitudes upon binding of the EF-G·GTP to the ribosome via the isolated L7/12. Furthermore, indication of the importance of the L7/12 is observed when a decrease in GTPase activity occurs upon its depletion (Rodnina et al. 1997; Savelsbergh et al. 2000). Thus, although EF-Tu or EF-G may bind to the ribosome, GTP hydrolysis activity is reduced and Pi release is strongly inhibited upon L7/12 stalk depletion (Mohr, Wintermeyer, and Rodnina 2002). This stalk, present on the large ribosomal subunit, forms part of the binding site of EF-G. EF-G shows structural similarity to the EF-Tu, tRNA and GTP complex, with the anticodon stem-loop of tRNA mimicked by domain IV (Figure 5) (Nissen et al. 1995; Czworkowski et al. 1994). Structural studies, together with smFRET and ensemble kinetics have shown that EF-G, when present at high concentrations, binds reversibly

to both the rotated-hybrid and non-classical state of the ribosome at a rate of >500s^{-1} (Belardinelli et al. 2016; Katunin et al. 2002). EF-G moves from a compact to a more extended conformation, with the extended formation being adopted when bound to the ribosome regardless of the translocation ribosome state (Salsi et al. 2015). Furthermore, the CCW rotation on non-rotated complexes is accelerated with EF-G, as well as blocking the reverse transitions leading to the stabilization of the rotated state. This results in a conversion of the translocating ribosomes to the rotated-hybrid state with a very short lifetime (Lin et al. 2015; Sharma et al. 2016).

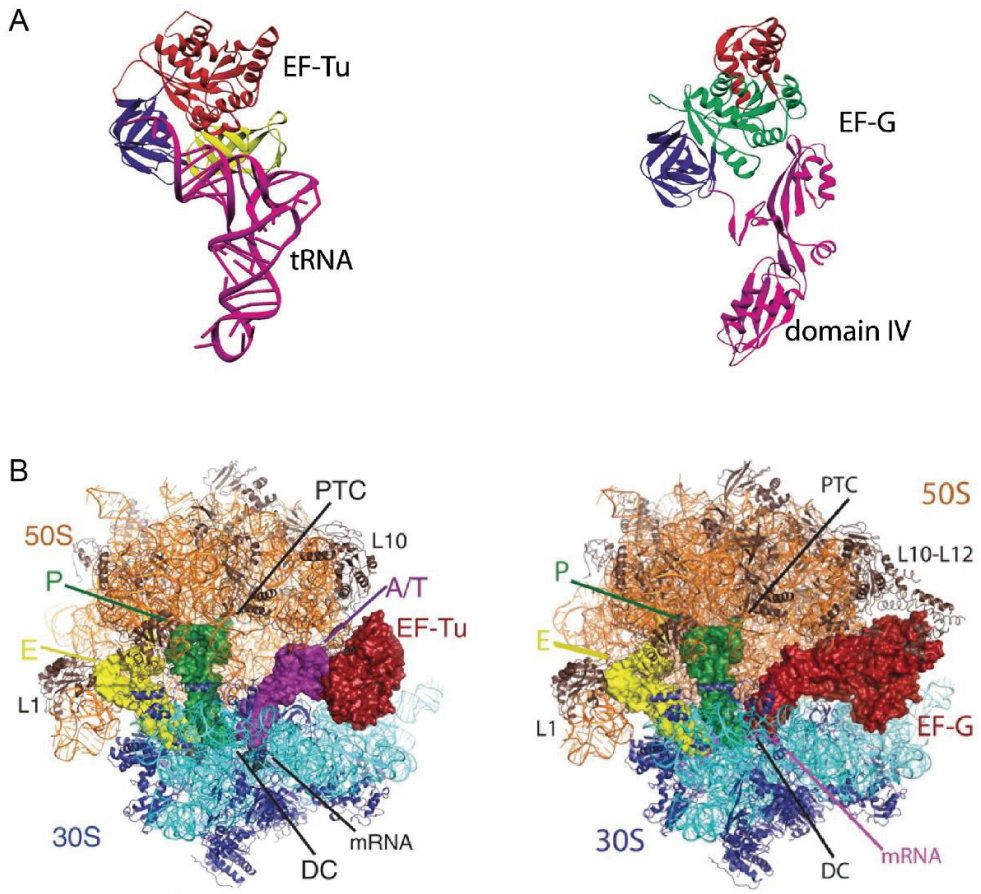

Figure 5. Similarity between EF-Tu and EF-G. (A) Crystal structure of EF-Tu-tRNA-GDPNP and EF-G highlights the high structural similarity between both factors and the mimicry between EF-G domain IV and tRNA. This panel is reformed by (Ramakrishnan 2002) based on studies from (Nissen et al. 1995; Aevarsson et al. 1994; Czworkowski et al. 1994). **(B)** Cryo-EM structures showing the overall binding of EF-Tu (red)-tRNA (purple) on the left and EF-G (red) on the right to the ribosome, expressing the similarity not only structurally but also in their binding modes. This is combined from (Gao et al. 2009; Schmeing et al. 2009) with permission.

Restriction in movement and increase in the physical hurdles for the tRNAs due to the two tRNA interaction with the ribosome, accounts for the unspontaneity of tRNA translocation on the 30S. Beside the previously described CCW rotation of the 30S, following GTP hydrolysis and prior to the inorganic phosphate release (Pi), the 30S head domain encounters a special type of movement known as head swiveling (Bock et al. 2013). The unlocking mechanism is the process in which the uncoupling of the head and body of the SSU occurs, leading to ribosome unlocking. This is caused by the SSU head remaining in the forward-swiveled state, whereas the SSU body rotates backward toward the non-rotated state (CW). The unlocking of the ribosome occurs when the decoding region may open sufficiently allowing the uncoupling of the tRNAs from the interactions with the ribosome that holds the mRNA and tRNA anticodons in the A- and P- site, respectively. Weakened interactions between the 30S and the tRNA occur due to these conformational changes, facilitating the motions of the tRNA during translocation (Guo and Noller 2012; Wasserman et al. 2016). The movement of the SSU body domain in comparison with the position of the SSU head domain leads to displacement of the tRNA ASL position on the body compared to the head domains of the SSU, resulting in the formation of intrasubunit hybrid states (Ramrath et al. 2013; Zhou et al. 2014; Ratje et al. 2010). Following ribosomal unlocking, the SSU head and body return back to their original positions, leading to the tRNAs adopting their canonical post translocation position in the P- and E- sites (classical P/P and E/E states). This leaves the ribosome in a non-rotated classical state with the mRNA and tRNA fully translocated, after a multi-step process. Structural information as well as ensemble and single-molecule kinetic studies distinguish at least eight distinct steps (Ramrath et al. 2013; Zhou et al. 2014).

The inorganic phosphate, Pi, is released by EF-G during the hydrolysis of GTP. Deacylated-tRNA leaves the ribosomal E-site at a rate of $14s^{-1}$. EF-G is dissociated from the ribosome when the SSU head and body continue to move backwards; this is a relatively slow reaction $\sim 4\ s^{-1}$ and completes the re-locking of the ribosome, leading to the classical post state (Belardinelli et al. 2016; Katunin et al. 2002). Neither GTP hydrolysis nor EF-G release is required for reverse movement of the 30S. EF-G plays an important role in the disruption of interaction between the SSU and tRNA by promoting conformational rearrangement in the SSU leading to rapid tRNA translocation. Furthermore, EF-G is required to maintain forward movement of the tRNAs (i.e. from the A to the P- site for the peptidyl-tRNA and from the P- to the E-sites for the deacylated-tRNA). A repositioning process occurs for EF-G, where it moves from its pre-translocation position (~ 20 Å from the A site) to its post-translocation position (domain 4 extending into the A-site). This has been shown through two structures,

one being a cryo-EM structure of ribosome complexes of *E. coli* with EF-G and the other being the tRNA in the hybrid P/E state bound to EF-G with a GTP analog at 2.9 Å, in an X-ray crystallography of *T. thermophilus* (Ratje et al. 2010; Tourigny et al. 2013). The insertion of the extended domain 4 of EF-G into the 30S A-site may function in the prevention of the backward movement of the tRNA by closing the A-site. This could mean that EF-G takes part in a dual motor function, where it maintains the bias of tRNA-mRNA movement (unidirectional movement) and the other in coupling GTP hydrolysis to ribosome unlocking (Wilson and Noller 1998; Ramrath et al. 2013; Rodnina et al. 1997).

One of the most important, yet least understood aspects is the coupling of the tRNA movement with the mRNA movement. If such a process fails, an out-of-frame stop codon due to the shift in the translational reading frame leads to untimely termination (Noller et al. 2002). The release of the tRNA from the E-site of the ribosome in the POST state marks the end of the elongation cycle. In conclusion, the ribosome is now in the POST state, relocked with an empty E- and A-sites, the latter exposing the next mRNA codon, which is decoded by the next ternary complex with the cognate aminoacyl-tRNA in the A site.

1.2.3. Termination

The coding sequence ends when a stop codon enters the A-site, indicating the termination of the elongation cycle. The termination cycle involves three main steps: stop codon recognition, ester bond hydrolysis of the peptidyl-tRNA, and finally the dissociation of the release factors (RFs). The first two steps are performed by the RF1 and RF2. Prokaryotes contain three stop codons that are known as amber (UAG) ochre (UAA) and opal (UGA) (Brenner, Stretton, and Kaplan 1965; Brenner et al. 1967). When one of these codons is encountered by the ribosome, termination occurs; in bacteria, such as *E. coli*, these are recognized by termination or release factors, RF1 (encoded by the gene *prfA*), which reads UAG/UAA, and RF2 (encoded by the gene *prfB*) reads UGA/UAA (Caskey et al. 1984; Weiss, Murphy, and Gallant 1984; Scolnick et al. 1968). These release factors consist of 4 domains, with their locations on the ribosome revealed by structural studies. Domain 1 consists of a three helix bundle close to the GTPase-associated center (GAC) on the 50S and the 30S head. Domain 2 also carries specific tripeptide motifs known as PVT (ProValThr) and SPF (SerProPhe) for RF1 and RF2, respectively, within a loop connecting between β4 to β5. Domain 3, involved in catalyzing peptide hydrolysis, connects the GGQ (GlyGlyGln) loop to

the PTC via its long extending helix 7. Domain 2 and 4 bring the PVT/SPF close to the DC (decoding center) on the small subunit via co-folding into a compact superdomain, allowing for stop-codon recognition. Highly conserved tripeptide motifs, PVT and SPF, have been discovered in RF1 and RF2 respectively, via high resolution crystal structure (Korostelev et al. 2008; Weixlbaumer et al. 2008; Vestergaard et al. 2001; Santos et al. 2013). These motifs recognize the stop codon in the DC of the small ribosomal subunit.

Stop Codon Recognition

The recognition of the stop codon, unlike the sense codons, is independent of tRNAs. Stop codon recognition, during termination, takes place by class 1 RFs. However, the question that arose is whether this recognition is due to direct communication between the RFs and the stop codon or indirectly via stop codon, RF complex, and the nucleotides of the 16S and 23S rRNA. Furthermore, stop codon specificities are changed by swapping of PVT/SPF motifs between RF1 and RF2 (Ito, Uno, and Nakamura 2000). This supported the hypothesis, where the recognition of the stop codon in mRNA is performed by the RF mimicking an anticodon in the tRNA. Indeed, RF1 and RF2 have been shown, via translation termination 70S complex cryo-EM and ~6 ˚A X-ray studies, to bind to the ribosomal A-site with their conserved motifs positioned to interact with the stop codons (Klaholz et al. 2003; Rawat et al. 2003; Rawat et al. 2006). Exciting insights into stop codon recognition were discovered from higher resolution crystal structures of the *Thermus thermophilus* 70S termination complexes. A 3.0-3.6 Å resolution of the three stop codons, with the 4 possible functional ribosome complexes with RF1/RF2 was obtained (Korostelev et al. 2008; Weixlbaumer et al. 2008; Laurberg et al. 2008; Korostelev et al. 2010). It was observed that the threonine in the conserved motif PVT for RF1 and serine in the SPF motif for RF2 do participate in codon recognition.

The amino terminus of helix α5 of either the RF1 or RF2 recognizes the first amino acid, uracil, of all three stop codons. This resembles the Watson-Crick A:U base pairing interaction. The reading of a U at the first base (U1) is restricted by the backbone element present at the N-terminal end of helix α5 of the RFs. The reading of an A at the second position (A2) of the codon is restricted by the threonine of the PVT motif in RF1. A H-bond is donated to the oxygen 4 (O4) of U1 by the β-hydroxyl group of Thr186 (Thr190 in E. coli) of RF1 position between U1 and A2 in the stop codon; due to this reason, a H-bond can only be accepted from A2 defining the specificity of RF1 for A2. However, Ser206 (Ser205 in *E. coli*) of RF2 can accept and donate H-bond from either adenine or guanine at position 2 of the stop codon, as it does not interact with U1. RF1 can read both A and G at position 3 due to a rotation of the

conserved side chain amide of a Gln residue. The Hoogsteen edge of the third stop codon nucleotide is examined by a universally conserved C-terminal threonine in both RF1 and RF2. A hydrogen bond is donated to the purine ring of A3 or G3 by the hydroxyl group side chain, while a hydrogen bond is accepted from the amino group of A3. While in RF2 the hydrophobic Val residue restricts the 3rd position of the stop codon to an A (Laurberg et al. 2008; Korostelev et al. 2010; Korostelev et al. 2008).

Due to crystal structures of the RF complexes, it was proposed that other amino acids within other regions of the release factors were involved in stop-codon recognition. One of which is the hydrogen bond formation between the reading head of domain 2 of either release factors and mRNA nucleotides (Ito, Uno, and Nakamura 1998; Petry et al. 2005). Another set of interactions involved the universally conserved 16S rRNA nucleotides (G530, A1492 and A1493 *E. coli* numbering) at the decoding center undergoing conformational changes. Upon stop codon recognition A1493 remains stacked within helix 44, while G530 and A1492 flip out. This stacking of A1493 is important for allowing RF binding via steric clash prevention with domain 2, different from A1493 conformation in case of recognizing cognate tRNA (Ogle et al. 2001; Korostelev et al. 2008; Weixlbaumer et al. 2008; Laurberg et al. 2008; Korostelev et al. 2010). The coordination of the stop codon recognition with the peptidyl-tRNA hydrolysis is performed by the changes observed in the aforementioned nucleotides, as they participate in the stabilization of the catalytically active conformation of the release factor. The GGQ motif, which has been suggested to be located on the surface of protein globule, might play an essential functional role in class 1 RFs, rather than maintenance of the spatial structure. This reason was concluded from sequence alignments of class 1 RFs that has shown that this motif is in a loop conformation and is strictly conserved in the three kingdoms of life (Frolova et al. 1999). Ester bond hydrolysis of the peptidyl-tRNA is triggered by the GGQ motif of the class I RFs following stop codon recognition.

It was assumed that the peptidyl transferase center (PTC) of the ribosomal 50S subunit catalyzed the hydrolytic reaction through contact with the GGQ motif. However, via *E. coli* RF2 crystal structures, the distance of the SPF motif and the GGQ motif was found to be 23 Å, which is different from the distance that separated the 3' CCA end in a tRNA and the anticodon (75 Å) (Vestergaard et al. 2001; Klaholz et al. 2003). Thus, the existing dogma was thought to be false as the SPF interaction with the stop codon and the GGQ with PTC cannot occur at the same time, since they are expected to interact with the ribosome at areas far from each other. However evidence supporting this model was obtained from cryo-EM structures

of the *E. coli* ribosome with RF2 and 70S-RF1 complex (Klaholz et al. 2003; Rawat et al. 2006; Rawat et al. 2003). It was observed that, compared to the crystal structure, the RF2 adopts an open extended conformation on the ribosome (Figure 6B). The PTC interacts with the GGQ containing domain of the RF2, while the SPF loop is situated close to the mRNA (Klaholz et al. 2003). A crystal structure of the *T. thermophilus* 70S-RF1 and 70S-RF2 complexes with a deacetylated tRNA has confirmed the concept of connecting the decoding center and PTC via RF2 mimicking a tRNA molecule in the A-site (Figure 6A) (Petry et al. 2005).

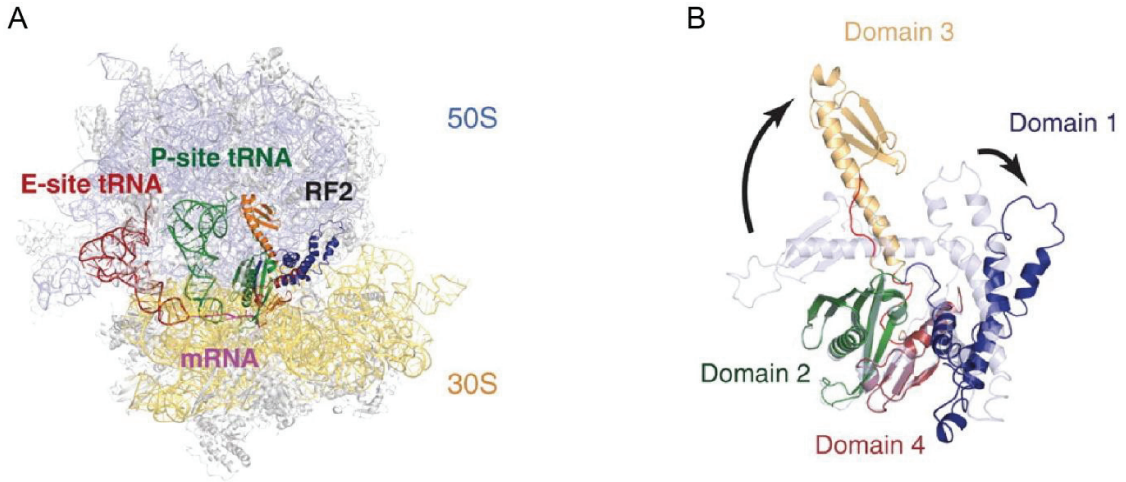

Figure 6. Structure of RF2 on/off the ribosome. (A) Overview of RF2 binding on the ribosome. The different colors within RF2 represent the different domains. **(B)** Alignment of the RF2 off the ribosome obtained from crystal structure (Zoldak et al. 2007) with the RF2 on the ribosome, illustrating the conformational changes that RF2 undergoes upon binding to the ribosome as indicated by arrows. The loop connecting domain 3 with 2 and 4 is shown in red to signify high flexibility. This figure is adapted from (Weixlbaumer et al. 2008) with agreement.

Peptide Hydrolysis

Thermus thermophilus crystal structures have indicated that the NH group of Gln230 backbone in the GGQ motif is held by the G228 and G229 in the GGQ motif within hydrogen bonding distance to the 3-OH of A76 of P-tRNA in the PTC. However, the side chain is oriented away from the ester bond. Thus, the G228 or G229 mutations show a severe decrease in hydrolytic activity (Laurberg et al. 2008; Jin et al. 2010). The H-bonding permits the entry of water into the catalytic site of the PTC, formed by the interaction between A2602 (nucleotide A2602 is buried in a pocket formed by RF2) of the 23 rRNA and the GGQ motif. The reaction is expected to proceed through a tetrahedral intermediate that breaks down to form the free peptide and deacylated-tRNA (Jin et al. 2010). There are two mechanisms explaining the proton transfer for the hydrolysis to take place. The first mechanism indicates that the transition state (TS) of the RF2-dependent hydrolysis reaction involves only one

proton at a time. This mechanism argues against the second mechanism of a concerted proton shuttle in the TS of the hydrolysis reaction, which would require at least two protons being transferred simultaneously (in similar manner to that of peptide bond formation) (Kuhlenkoetter, Wintermeyer, and Rodnina 2011; Indrisiunaite et al. 2015).

Beside the Gln230 NH group role in catalysis of the hydrolysis reaction, it is shown to be important for stabilizing the TS intermediate as well as the deacylated-tRNA product. This stabilization takes place via H-bonding between the formed oxyanion during TS and the 3-OH of the deacylated-tRNA. In order to confirm this, a mutation was performed converting the glutamine 230 to proline, hence eliminating the –NH group. The RF1 catalysis effect was abolished with this mutation, explaining the detrimental effect from such a deletion. Shaw and Green proposed, based on mutational studies on Gln230 to Ser, Ala or Gly that observed a 170-fold increase in the reaction rate using hydroxylamine as nucleophile, that the glutamine side chain excludes nucleophiles bulkier than water (Shaw and Green 2007). Modifying the Gln230 side chain, as observed during post-translation, by the addition of a methyl group is proposed to increase the rate of peptide release due to the methyl group occupying the hydrophobic portion of the glutamine binding site; however this remains to be addressed (Dincbas-Renqvist et al. 2000; Trobro and Aqvist 2009).

Factors Recycling

The RF3 (class II RF) promotes recycling of the RF1 and RF2 from the ribosome. This protein is encoded by the *prfC* gene in *E. coli* (Mikuni et al. 1994) and is the 4th GTPase involved in the translation cycle. Biochemical studies in 1997 by Freistroffer has found that the recycling scheme of Goldstein and Caskey to be favoured as compared to the suggested ternary complex formed by RF3, GTP and RF1/RF2; this is mainly due to similarities of RF3 to EF-Tu (Freistroffer et al. 1997; Goldstein and Caskey 1970; Zhouravleva et al. 1995). To date, the only function of RF3 during termination is the recycling of the class I RFs. The ribosome dependent GTPase activities are believed to be due to the G domains of these GTPase interacting with the ribosome at the conserved site near the sarcin-ricin loop (SRL) (Allen et al. 2005; Stark et al. 1997; La Teana, Gualerzi, and Dahlberg 2001).

The mechanism of the recycling process performed by the RF3 on the class I RFs is controversial. The first model supports GDP-GTP exchange upon entering of the RF3-GDP to the ribosome. Following peptide release, RF3-GDP binds to the ribosome in combination with RF1/2 and deacylated-tRNA in the P-site. Upon binding to the ribosome, RF3 is activated leading to the formation of a more stable complex of RF3 after GDP is released from the

complex. This drives the exchange of the GDP for GTP which promotes RF1/2 recycle followed by GTP hydrolysis and dissociation of RF3. This model is based on affinity studies from Zavialov, suggesting that RF3 favors GDP over GTP binding and the prerequisite of peptide hydrolysis (Zavialov, Buckingham, and Ehrenberg 2001; Zavialov et al. 2002). Further support for this exchange model was provided by the structural study of the complex RF1-apo-RF3 on the *E. coli* ribosome (Pallesen et al. 2013).

Cryo-EM and crystal structures of the *E. coli* and *T. thermophilus* ribosomes bound to the *E. coli* RF3, revealed the conformational changes that take place in the ribosome and RF3 as they move from one state to the other to facilitate RF1/2 recycling (Gao, Zhou, et al. 2007; Jin, Kelley, and Ramakrishnan 2011). However, these studies only represent RF3 bound to the ribosome in the absence of RF1/2. Recently, a cryo-EM structure of the RF1-RF3 on the ribosome, presented by (Graf et al. 2018), elucidated the mechanism of the RF3 mediating the RF1 recycling process. In contrast to the RF1/2, RF3 was found to trigger the rotation of the 30S by approximately 6-10° with respect to the 50S (Figure 7A-C). Beside the changes within the 30S, the GAC on the 50S also undergoes conformational changes, in addition to the inward movement of the L1 stalk (Figure 7D-F) (Gao, Zhou, et al. 2007; Klaholz, Myasnikov, and Van Heel 2004). As a consequence of these reorientations, the interactions between RF1/2 and the ribosome are disturbed (destabilized) leading to their dissociation off the ribosome. Finally the deacylated P-tRNA moves to the hybrid P/E state (Gao, Zhou, et al. 2007). The idea of RF1/2 release due to direct interaction with RF3 on the ribosome, as suggested by (Pallesen et al. 2013), is now questionable due to the distance between both factors, as shown by (Graf et al. 2018). An indirect action of RF3 via induction of the 30S rotation seems to be a more favorable mechanism (Graf et al. 2018; Jin, Kelley, and Ramakrishnan 2011; Gao, Zhou, et al. 2007). It is worth mentioning that the conformational changes occurring during this model is similar to those occurring during translocation upon EF-G binding. Thus, a general mechanism for the action of the RF3 during termination and EF-G during translocation, which involves the ribosomal ratcheting movement, might be considered (Klaholz, Myasnikov, and Van Heel 2004; Gao, Zhou, et al. 2007).

In contrast to the first model, a second model has been suggested based on the affinity measurements of RF3 to GDP and GTP. These measurements disfavor the binding of RF3 to the ribosome in the GDP form, showing only a 10-fold difference in the affinity of RF3 to GDP over GTP. This 10-fold difference is further minimized due to the presence of GTP in excess over GDP. Thus it is presumed that RF3 is mainly found in the GTP bound form in the

cell. RF3-GTP complex binds to the ribosome either in the pre- or the post termination states (i.e. before or after the peptidyl chain hydrolysis); however RF3-GTP binding to the ribosome is more stable with deacylated-tRNA. RF3 then induces ratcheting of the ribosome and the dissociation of RF1/2. Domain I of RF3 then communicates with the SRL on the 50S, promoting GTP hydrolysis followed by RF3-GDP release off the ribosome (Koutmou et al. 2014; Peske et al. 2014). Important steps during the termination, including the dissociation of RF3, have not been captured structurally. Furthermore, coming to an exact, unified model for the termination process requires more investigations. The end product of termination is a ribosome with a P/E deacylated-tRNA and an mRNA in the 30S. Dissociation of the mRNA and the tRNA from the ribosome, as well as the ribosomal subunits is a pre-requisite for the redirection of the translational cycle from post-termination to pre-initiation.

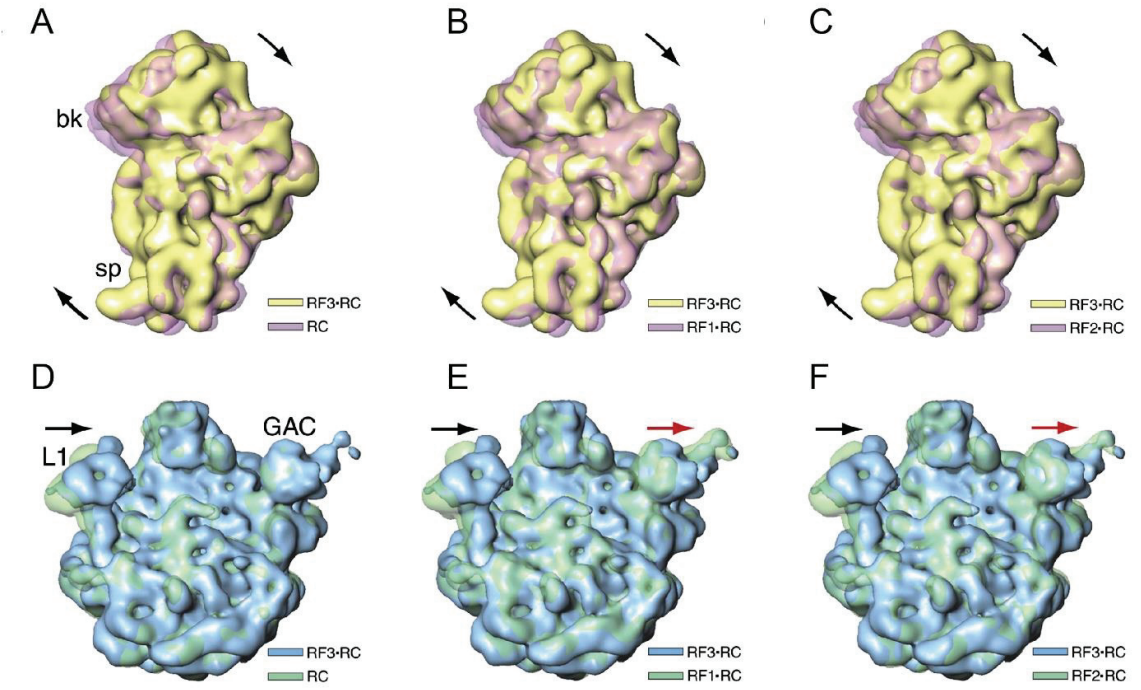

Figure 7. RF3 induced conformational changes within the ribosome. (A)-(C) Conformational rearrangements within the 30S upon binding of RF3 in comparison with 30S of RC **(A)**, RF1-RC **(B)**, RF2-RC **(C)**. Arrows indicate the 30S ratchet motion. **(D)-(F)** Conformational changes of L1 stalk and the GAC (GTPase- associated center) on the 50S compared to the 50S of RC **(D)**, RF1-RC **(E)**, RF2-RC **(F)**. For this comparison, density maps for RF1-RC and RF2-RC published by (Rawat et al. 2006; Rawat et al. 2003) have been used by (Gao, Zhou, et al. 2007) in addition to RF3-RC map from the latter. RC stands for ribosome complex. This figure is reproduced with permission from the concerned journals.

1.2.4. Recycling

For the start of a new round of mRNA translation, following protein synthesis termination, recycling of bacterial ribosomes is a pre-requisite. Recycling, being the final step of protein synthesis, is simply the channel (pipe) which links the termination of protein synthesis to the initiation of a new cycle of polypeptide synthesis. The post-termination complex (PoTC) containing the ribosome, mRNA, and deacylated hybrid P/E-tRNA is the product of termination and is also the substrate for recycling. Three proteins are known to catalyze the disassembly of the PoTC for the purpose of reuse. A universally conserved factor present in bacteria (20 kDa in *E. coli*) able to catalyze the conversion of polysomes to monosomes is called the Ribosome Recycling Factor (RRF) (Hirashima and Kaji 1970; Subramanian and Davis 1973). This factor, bound to ribosomal A-site overlapping class I RFs, was found to be lethal to *E. coli* if not present via the deletion of the gene encoding it (*frr*) (Janosi, Shimizu, and Kaji 1994). The second protein is EF-G, which is required for the activity of the RRF and lastly the initiation factor 3 (IF3) originally called DF (dissociation factor) (Subramanian, Davis, and Beller 1969; Subramanian, Ron, and Davis 1968). In vitro kinetic experiments calculate the ribosome recycling rate of ~5 sec^{-1}; this is compatible with the recycling rate of ribosomes within the rapidly growing *E. coli* (Borg, Pavlov, and Ehrenberg 2016).

Although, RRF and EF-G may bind to the ribosome independently of the other, binding of the RRF to the PTC before the binding of EF-G is important for efficient ribosome recycling. On the other side, the absence of RRF during EF-G GTP binding leads to non-productive GTP hydrolysis while the subunits remain attached (Seo et al. 2004; Savelsbergh, Rodnina, and Wintermeyer 2009; Borg, Pavlov, and Ehrenberg 2016). The RRF crystal structure shows a three stranded α-helix bundle called domain I and a β/α/β- "head" called domain II; these two domains are highly conserved (Kim, Min, and Suh 2000). A similar construction was observed for both the crystal and solution structures of the RRF as compared to other species (Selmer et al. 1999; Yoshida et al. 2001; Saikrishnan et al. 2005). However, the interdomain angle which consists of a flexible hinge that connects both domains was the major difference amongst the structures (Nakano et al. 2003). The flexibility of the RRF is increased due to the presence of these hinges. A range of rotation of domain II was observed for the RRF when NMR (Yoshida et al. 2003), molecular dynamic simulations and solution structures were performed (Yoshida et al. 2001). These hinges were found to be highly important for RRF function in *vivo* after performing mutational experiments of the hinge region (Toyoda et al. 2000).

Furthermore, the RRF domain I has been suggested to be a structural and functional mimic of the tRNA after a crystallographic structure showed prominent similarity to the anticodon stem of the tRNA molecule (Selmer et al. 1999). This suggests subunits dissociation as a result of its translocation through the ribosome by the action of EF-G. This misconception of tRNA mimicry arose from the earliest model for recycling (Kaji's model) (Hirokawa, Kiel, Muto, Selmer, et al. 2002; Hirokawa, Kiel, Muto, Kawai, et al. 2002; Kiel et al. 2003). The proposal was that the RRF binds to the ribosomal A-site in the post-termination state in a similar manner to the A-tRNA, this causes the translocation of the RRF into the P-site via attracting EF-G. Then, the deacylated-tRNA is rapidly detached following its transfer to the E-site. After the RRF and EF-G are also dissociated, the absence of tRNA in the P-site causes destabilization and release of the mRNA. Subsequently, IF3 causes ribosome splitting. Thus, in this model, RRF and EF-G are rather concerned with the removal of the deacylated-tRNA and mRNA while neglecting their role in ribosomal splitting.

Further studies, via hydroxyl radical probing (Lancaster et al. 2002) and cryo-EM reconstructions (Agrawal et al. 2004) of RRF-70S ribosome complexes, have ruled out this translocation like model, since the RRF binds in a position that obliquely transverses the A- and P-tRNAs in the 50S. In other words, the RRF does not bind similar to any tRNA in any way. RRF interacts with two intersubunit bridges, B3 (helix 71) and B2a (helix 69 of 23S rRNA) within the 50S ribosomal subunit. The location of the RRF would be incompatible, causing a clash between domain I of the RRF and the P-site tRNA. A more satisfactory model would involve the RRF binding to the ribosome, stabilizing it in the fully rotated state while containing a deacylated P/E-tRNA. EF-G is then recruited and binds in a similar way during translocation. Cryo-EM and X-ray studies of the 50S bound concomitantly to RRF and EF-G (Gao et al. 2005; Gao, Zavialov, et al. 2007; Wilson et al. 2005) plus mutational analysis (Ito et al. 2002), indicate that both factors are interacting upon binding to the ribosome. Communication between both proteins is thought to be driven by the release of Pi following GTP hydrolysis.

The interaction between EF-G and RRF, involves certain subunits present in domain III of EF-G and the RRF hinge region, as well as residues in domain II of the RRF and domain IV of EF-G. The deletion of H69 of bridge 2a destabilizes subunit interaction considerably, thus preventing the units from being held together (Ali et al. 2006). Movement of domain II RRF destabilizes the interactions between subunits due to the displacement of H69 and other bridges, resulting in the promotion of disassembly of the post-termination complex into

subunits. The movement would be precluded with fusidic acid (FA) bound to EF-G, where FA would strongly inhibit ribosome disassembly (Savelsbergh, Rodnina, and Wintermeyer 2009). This is consistent with an EF-G function involved in ribosome disassembly where GTP hydrolysis causes the release of Pi, which allows EF-G to act as a molecular motor and cause subunit dissociation. Extensive kinetic experiments, smFRET study (Prabhakar et al. 2017) and time resolved cryo-EM (Fu et al. 2016) have supported a model that suggests that EF-G inducing GTP hydrolysis and ribosome splitting into subunits is the result of the subsequent delay of Pi release. Henceforth, the mRNA and tRNA are still attached to the 30S and IF3 promotes the dissociation of tRNA.

Unlike the sequence of events proposed in the previous model, recently, an alternative model has been proposed based on studies that involve long mRNA such that the SD is not in the vicinity of the stop codon, expressing the normal situation after termination (Fu et al. 2016). This model suggests a novel and unexpected function of the EF-G which would be the hydrolysis of GTP, thus promoting mRNA release, followed by tRNA dissociation and lastly subunit splitting. Future experiments are required to clarify the effect of the expected SD-aSD interaction on stabilizing the mRNA binding on the 30S, thus influencing the sequence of tRNA, mRNA release and subunits splitting.

1.3. Stringent Response (SR)

For survival and adaptation, bacteria have evolved a large number of sensory systems to respond to the different environmental and host changes; examples of these environmental changes include nutrient deprivation, oxidative stress, heat shock, or exposure to antimicrobials etc. The aforementioned threats play a significant role on bacterial survival and as such the bacteria have developed several ways to encounter and adapt to such stress. Nutrient starvation is a typical example for a bacterial stress, which occurs during its entry to stationary phase. Henceforth, a stringent response is induced (Cashel et al. 1996) to help the bacteria adapt and survive harsh conditions.

This stress response is mediated by the formation of the secondary messenger guanosine pentaphosphate (pppGpp) or guanosine tetraphosphate (ppGpp), also referred to as alarmones, via the transfer of the pyrophosphate moiety from ATP to the 3´of GTP or GDP, respectively (Figure 8B). The alarmones were first observed in starved *E. coli* cells, using 2D thin layer

chromatography (Cashel and Gallant 1969); back then they were given the name ´magic spots´ as their biological role was still unrevealed. Under normal conditions, basal level of (p)ppGpp regulates the bacterial physiology in terms of growth rate (Potrykus et al. 2011) and general metabolism (Kriel et al. 2012; Gaca et al. 2013). However, upon exposure to stress, there is a rapid increase of (p)ppGpp to the millimolar level (Irving and Corrigan 2018; Starosta et al. 2014). Subsequently, (p)ppGpp exerts its function on diverse cellular processes including transcription, translation as well as replication (Figure 8C).

Rymer and coworkers (Rymer et al. 2012) solved the crystal structure of *S. aureus* DnaG, an RNA polymerase that catalyzes DNA replication via synthesis of RNA primers (Kitani et al. 1985; Rowen and Kornberg 1978), where they revealed how (p)ppGpp restricts primer synthesis by interfering with DnaG's catalytic active site. (p)ppGpp has a diverse impact on transcription, where one of its function includes blocking the ribosome biosynthesis machinery, while on the other hand upregulating amino acid biosynthesis (Dennis and Nomura 1974; Dennis, Ehrenberg, and Bremer 2004; Potrykus and Cashel 2008; Cashel et al. 1996; Magnusson, Farewell, and Nystrom 2005; Nystrom 2004; Zhou and Jin 1998). In Gram negative bacteria, such as *E. coli*, this effect of (p)ppGpp on transcription results from the direct interaction between the nucleotide and RNAP (RNA polymerase) (Barker, Gaal, and Gourse 2001; Barker et al. 2001; Srivatsan and Wang 2008; Haugen, Ross, and Gourse 2008). However, in Gram positive bacteria, like *B. subtilis*, the nucleotide tends to modify transcription via lowering the cellular GTP level required to induce transcription of the ribosomal machinery genes (Krasny and Gourse 2004; Kriel et al. 2012; Kasai et al. 2006; Krasny et al. 2008). Using ITC (Isothermal Titration Calorimetry) and cryo-EM, the alarmone was shown to directly bind to the initiation and elongation factors (IF2 and EF-G, respectively); hence, influencing the translation cycle, in *E. coli*, along with ribosome maturation via interacting with ObgE (ribosome assembly factor) (Feng et al. 2014; Mitkevich et al. 2010). All these cellular processes are modified in a way to direct the vast quantities of energy to general metabolism, rather than ribosome biosynthesis, thus helping the bacteria to adapt to stress conditions (Scott et al. 2010).

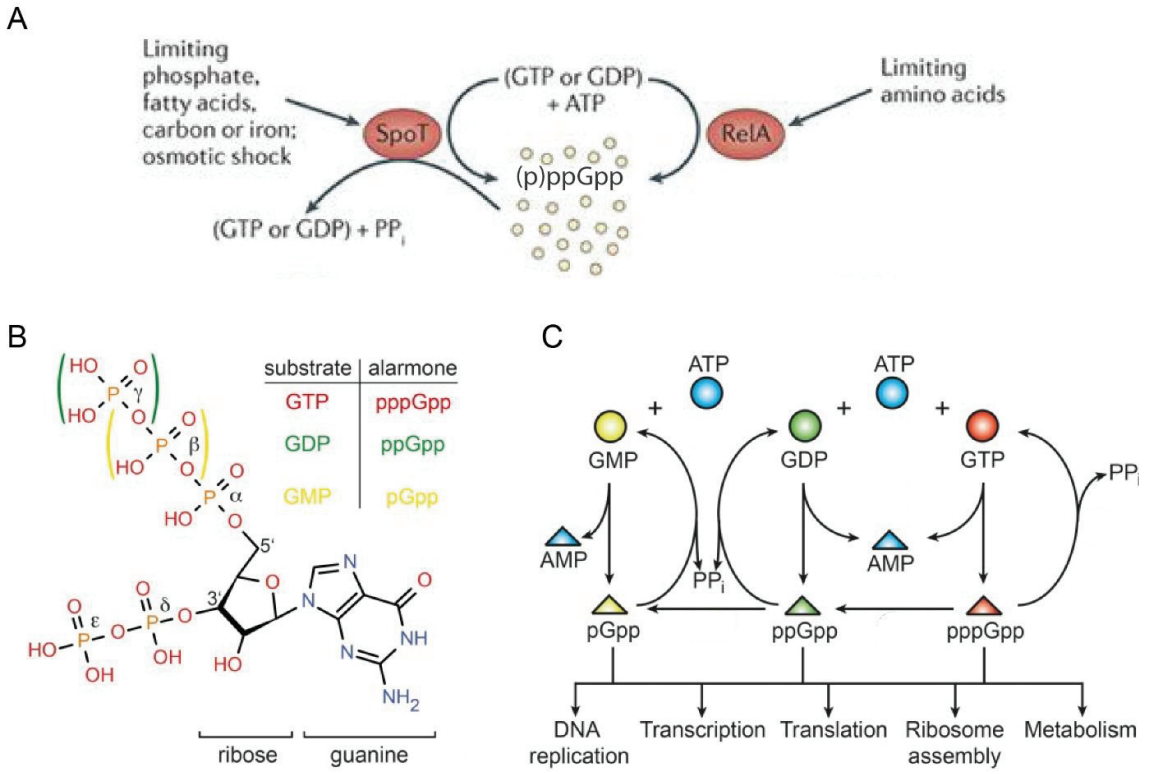

Figure 8. Production and metabolism of (p)ppGpp during stringent response. (A) Schematic diagram representing the induction of (p)ppGpp via SpoT/RelA in response to different stresses. This panel has been extracted from (Dalebroux and Swanson 2012) with permission. **(B)** Chemical structure of (p)ppGpp with the absent phosphates in case of ppGpp and pGpp labelled in green and green/yellow, respectively. **(C)** Schematic diagram showing the different substrates of (p)ppGpp formation including ATP, GTP; GDP, GMP in blue, red, green , and yellow, respectively. In addition, it shows the main cellular processes targeted by the alarmone, (p)ppGpp. PPi stands for the pyrophosphate moiety. Panels **(B)** and **(C)** are adjusted from (Steinchen and Bange 2016) with permission.

The synthesis of (p)ppGpp is catalyzed and regulated by the enzyme family RelA/SpoT homologue (RSH) (Figure 8A) (Potrykus and Cashel 2008; Jishage et al. 2002). Beside their major role in synthesizing the alarmone, they are also capable of hydrolysis and thus, RSH enzymes are distributed into three classes based on their catalytic activity. The first class includes the long RSH, which contain either RelA (monofunctional) along with SpoT (bifunctional) or Rel alone (bifunctional). In spite of the presence of both synthetase and hydrolase domains in the monofunctional RelA, only the synthetase is active whereas the hydrolysis takes place via the SpoT. Bacteria present within the category of Gram negative γ proteobacteria, are examples of bacteria carrying both RelA and SpoT proteins. However, the

majority of bacteria encode for the bifunctional Rel, allowing both synthesis and hydrolysis of the alarmone (Figure 9). In addition to the bifunctional Rel, some bacterial clades respond to stress signals using a second class of RSH enzymes named the small alarmone synthetases (SAS) which contain only the synthetase domain. SAS proteins, such as RelP and RelQ, have been detected in *B. subtilis* (Nanamiya et al. 2008) and *S. aureus* (Geiger et al. 2014), while RelV in *Vibrio cholera* (Das et al. 2009). Eukaryotes on the other hand, except for plant and algae, lack the equivalent of (p)ppGpp synthetase, while metazoan is found to have a third class of RSH family only responsible for the alarmone hydrolysis SAH annotated as small alarmone hydrolase (Sun et al. 2010).

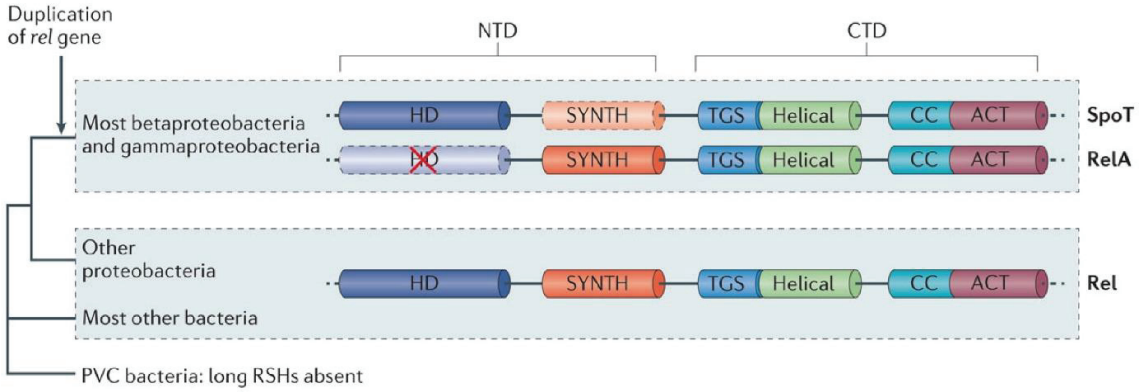

Figure 9. Distribution of SpoT, RelA and Rel proteins in bacteria along with the domain architecture. The domains abbreviations; alarmone hydrolysis (HD), alarmone synthesis (SYNTH), TGS (ThrRS, GTPase, SpoT), conserved cysteine (CC), and ACT (aspartokinase, chorismate, mutase and TyrA). The dashed SYNTH domain in SpoT is to signify weak activity while the crossed HD in RelA represents absence of activity. Arrows signify the duplication of Rel into RelA and SpoT. This figure is adapted from (Hauryliuk et al. 2015) with permission.

In addition to the hydrolysis activity by the RSH, (p)ppGpp is also hydrolyzed to GTP/GDP and pyrophosphate by the action of the highly conserved Nudix hydrolase, consequently preventing the toxic increase in cellular (p)ppGpp levels. These enzymes, Nudix hydrolases, are known as non-RSH enzymes since they are not structurally related to the RSH (McLennan 2013; Ooga et al. 2009). The regulation between hydrolysis and synthesis is important for controlling the alarmone level and avoiding ineffective generation and degradation of (p)ppGpp. The alarm required for Rel/RelA to initiate the synthesis of the alarmone, is the accumulation of deacylated-tRNA that takes place upon amino acid deprivation (Haseltine and Block 1973). Such conditions occur during bacterial transition to the stationary phase and also during the usage of antimicrobials that prevent tRNA acylation by the host. In contrast to RelA/Rel, SpoT synthetase activity is rather essential in cases of

fatty acid, carbon, phosphate, or iron limitations as well as oxidative stress (Figure 8A) (Seyfzadeh, Keener, and Nomura 1993; Vinella et al. 2005; Xiao et al. 1991).

Despite the diversity in response among bacterial species to different stresses, the stringent response orchestrated by RSH proteins resulting in (p)ppGpp formation is highly conserved among bacteria, plant and algae (Atkinson, Tenson, and Hauryliuk 2011). Not to mention, the myriad number of factors regulated by the alarmone resulting in long living cells with a slow growth phenotype. It is this slow growth, caused by the stringent response that allows bacteria to become insusceptible to antimicrobial treatment, since antibiotics are known to target active cellular processes during rapid growth. Therefore, alarmone producing cells have been linked to increasing antibiotic resistance, virulence, persistence and host invasion (Dalebroux et al. 2010). Examples verifying this hypothesis include; *M. tuberculosis* utilizing the stringent response as a defense mechanism against the host immune system. *M. tuberculosis* can survive for many years in harsh conditions inside a granuloma for the right conditions to be available, in order to switch from the latent to the active phase at which the host starts suffering the symptoms (Primm et al. 2000; Dahl et al. 2003). Another example is MRSA (Methicillin resistant *Staphylococcus aureus*), that attacks different body parts and confers resistance to many antibiotics. Experimental studies of these resistant strains have presented a relation between increased levels of (p)ppGpp resulting from point mutations in RelA and the increased resistance toward several antibiotics (Gao et al. 2010). Correspondingly this clarifies the severe phenotype exhibited by bacterial cells that are unable to generate (p)ppGpp. Given the worldwide antibiotic resistance crisis and the high demand for new antibiotic targets, in addition to the absence of (p)ppGpp synthetase counterpart in human, the RSH enzymes along with the alarmone could be possible targets for the design of new antibiotics. Up to now, only one ppGpp analogue, named Relacin has been designed and tested *in vitro*, where it has been shown to have an inhibition effect on RSH synthetic activity (Wexselblatt et al. 2013; Wexselblatt et al. 2012).

The detailed sequence of the RSH mediated SR events, as well as the mechanism by which RSH proteins modulate the alarmone level by switching between hydrolysis and synthesis activities has been controversial. The first debate is about the binding sequence of RelA and uncharged tRNA to the ribosome. Wendrich and coworkers (Wendrich et al. 2002) proposed a model in which the cognate deacylated-tRNA binds first to the ribosomal A-site, upon amino acid deprivation, followed by RelA binding to the stalled ribosomal complexes. This model contradicts an earlier mechanism where, RelA was designated the function of EF-

Tu, where it brought the deacylated-tRNA to the ribosome (Richter 1976). The second debate is concerned with the presence of (p)ppGpp synthesis off or on the ribosome. Where, the first model, called the hopping model, theorizes that RelA is hopping between the stalled ribosomal complexes along with the cognate uncharged tRNA and synthesizes the alarmone while on the ribosome and being inactive off the ribosome (Li et al. 2016). Another model supports that RelA is activated upon recognizing the deacylated-tRNA on the idling ribosome, this is then dissociated from the ribosome and followed by synthesis of (p)ppGpp off the ribosome (English et al. 2011).

Owing to the huge improvements achieved in the field of molecular imaging, the ability to reveal some events of the SR regulated by RelA/Rel has been made possible. Crystal structure of bifunctional truncated Rel, from *Streptococcus equisimilis* Relseq at 2.1 Å, showed two different conformations representing the structural rearrangements underlying the switch of Rel between hydrolysis and synthesis activities (Hogg et al. 2004). A second, more recent, crystal structure of *Mycobacterium tuberculosis* Rel-NTD (N-terminal domain) at 3.7 Å showed, for the first time, the dimer status of Rel-NTD (Singal et al. 2017). However, these crystal structures are lacking insights of the Rel activity on the ribosome as well as the Rel-CTD (C-terminal domain) thought to be responsible for regulating the NTD catalytic activity. Ten years after the crystal structure, the first cryo-EM structure of *E. coli* RelA bound to *T. thermophilus* ribosome at 10.8 Å was reported (Agirrezabala et al. 2013). In spite of the low resolution, it was possible to notice that RelA shares the binding site of ribosomal GTPases on the ribosome in addition, to a distorted deacylated-tRNA, similar to that observed in the case of EF-Tu binding with the CCA end approaching RelA. It has been suggested to be the method followed by RelA in order to sense the acylation/deacylation state of tRNA. Nevertheless, the detailed interaction between RelA, the ribosome and tRNA was missing due to the limited resolution of the map.

This was followed up by three cryo-EM studies at high resolution (Arenz et al. 2016; Brown et al. 2016; Loveland et al. 2016), such that more of the interactions between the RelA and the ribosome, as well as RelA and tRNA became visible. These structures revealed the domain architecture of full length monofunctional RelA with the NTD harboring both synthetase and hydrolase subdomains and the CTD comprising of 4 subdomains; TGS (threonyl tRNA synthetase, GTPase, and SpoT), AH linker (alpha helical linker), RIS/ZFD (ribosomal intersubunit/zinc finger domain), and ACT/RRM (aspartate kinase, chorimate mutase and tyrA/RNA recognition motif). The three structures have proposed that RelA binds

to the ribosome in an extended conformation, wrapped around the previously observed tRNA. The tRNA is attached to both the A-site on the 30S and RelA, thus annotating it as A/R-tRNA. Recently, biochemical investigations by Winther and coworkers (Winther, Roghanian, and Gerdes 2018) have strengthened the previously suggested model where the RelA binds to the deacylated-tRNA off the ribosome and then bind together to the ribosome in a manner similar to that of the EF-Tu. An approach describing (p)ppGpp synthesis by RelA on the ribosome, as a result of an interaction between RelA and SRL on the large ribosomal subunit, has been newly proposed. A combination of cryo-EM and crystallization experiments has been performed to study the bifunctional Rel from *Bacillus subtilis* on the ribosome. The cryo-EM structure has shown that bifunctional Rel binds to the ribosome analogous to that of monofunctional RelA. Whereas the crystal structure of Rel ΔRIS-ACT (ΔRIS-ACT), the longest part of the protein resolved so far off the ribosome, reveals the structural rearrangements responsible for the auto inhibition exerted by CTD on the synthetase domain in absence of the ribosome, keeping the Rel in the hydrolysis mode. Such autoinhibition effect is released upon switching from the closed conformation off the ribosome to the elongated one on the ribosome upon deacylated-tRNA recognition. The crystal structure has also determined the interactions between the NTD of one Rel molecule and the TGS-AH of the other, resulting in the formation of a symmetrical Rel homodimer. The rearrangements accompanied by the homodimer formation play an important role in modulating the protein hydrolysis activity over the synthesis one.

1.4. Hibernating 100S Ribosomes

In addition to the previously introduced stringent response, another bacterial survival tactic during stress is ribosome hibernation. Despite the fact that both strategies follow different pathways, they both share the same aim of adaptation during stress. Ribosome hibernation is characterized by the entrance of a high percentage of the ribosomes into a translationally inactive state (Tissières et al. 1959). This state prevents wasting of unnecessary energy, like the huge amount of energy consumed for ribosome biogenesis and protein translation, during unfavorable environmental conditions. This phenomenon is shown to be considerably different among species.

Ribosome hibernation, in part of gamma-proteobacteria including *E. coli*, is regulated via the action of two proteins, named RMF (ribosome modulation factor) (Wada et al. 1995;

Wada et al. 1990; Yoshida et al. 2002) and HPF (hibernation promoting factor) (Figure 10A) (Maki, Yoshida, and Wada 2000). These two factors play essential roles during ribosome hibernation where the RMF leads to formation of immature 70S dimer (90S), while, HPF is only important for stabilizing the 90S into the mature 100S form (Ueta et al. 2005; Ueta et al. 2008; Maki, Yoshida, and Wada 2000). *In vitro* studies show that cells expressing HPF whilst lacking RMF fail to form the 100S (Ueta et al. 2008). A second mechanism of hibernation, which opposes the 100S formation in gamma-proteobacteria, has been detected to be regulated via a third factor called RaiA (ribosome associated inhibitor A), also referred to as pY and YfiA. Unlike RMF and HPF, which block translational activity and result in the 100S formation, YfiA leads to idling 70S ribosomes (Figure 10B) (Ueta et al. 2005; Agafonov, Kolb, and Spirin 2001; Maki, Yoshida, and Wada 2000). It is noteworthy to mention that few bacteria do not possess the genes for either RMF or HPF, however have the gene for the HPF homologue YfiA only reviewed in (Yoshida and Wada 2014).

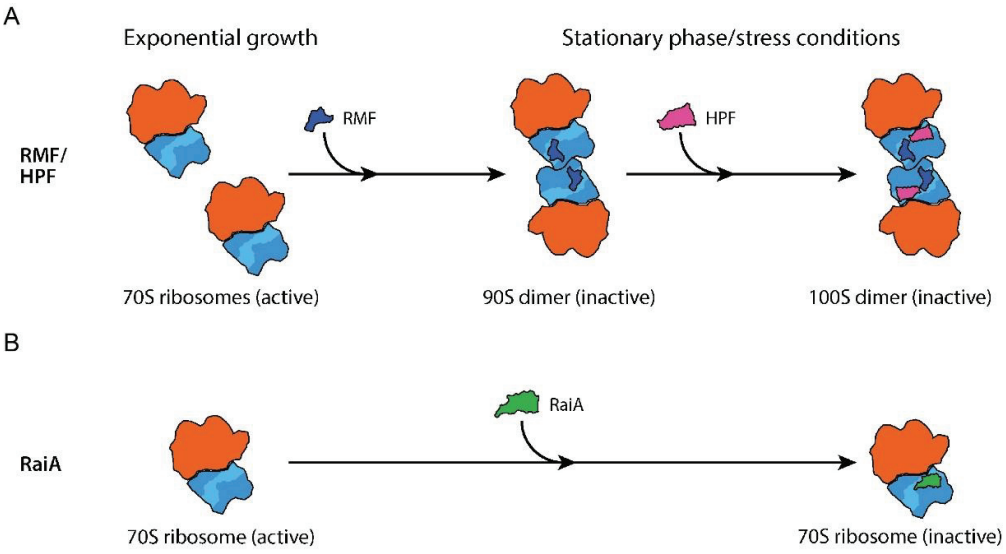

Figure 10. Ribosome hibernation by two different pathways in Gram-negative bacteria. (A) Schematic illustration of ribosome hibernation by RMF and short HPF in a two-step mechanism which leads to ribosome dimerization into the 100S. **(B)** Representation of a second mechanism involved in ribosome hibernation via the stabilizing 70S ribosome using RaiA in a single step. This figure is obtained from (Prossliner et al. 2018) based on permission.

Ribosome hibernation present in the majority of bacteria, other than gamma-proteobacteria, like *Bacillus subtilis* is regulated by a long form of HPF (LHPF); double the size of that expressed by gamma-proteobacteria. Long HPF alone is sufficient to block translation on a large proportion of ribosomes and induces 100S formation. Bacteria belonging

to this category do not have the gene encoding for YfiA and thus lack the second mechanism of hibernation via 70S that is detected in gamma-proteobacteria (Ueta et al. 2013; Ueta, Wada, and Wada 2010; Tagami et al. 2012; Puri et al. 2014; Akanuma et al. 2016; Kline et al. 2015). In addition to prokaryotes, a LHPF homologue is also present in chloroplasts of plants (plastid specific ribosomal protein 1, PSRP1) (Sharma et al. 2010; Sharma et al. 2007). Biochemical investigations assign PSRP1 the function of YfiA due to its inability to form the 100S upon its addition *E. coli* ribosomes; they rather maintained the 70S ribosomes (Sharma et al. 2010). Furthermore, the phenomenon of ribosome dimerization has been noticed in eukaryotes. Starved cancer cells had shown dimerization of the 80S leading to 110S but the factor regulating this process is still to be elucidated (Krokowski et al. 2011).

RMF-mediated 100S formation occurs during the transition from the exponential to the stationary phase with the concomitant appearance of the *rmf* mRNA (Shcherbakova, Nakayama, and Shimamoto 2015; Ueta et al. 2005; Wada et al. 1990). While that mediated by long HPF starts to appear already during the exponential phase (Ueta et al. 2013; Ueta, Wada, and Wada 2010; Kline et al. 2015). Moreover, the hibernation factors are being regulated by several mechanisms, such as the induction of secondary messengers by various stress signals leading to the transcription level changes. Among these stress signals, is amino acid starvation, which stimulates the stringent response catalyzing the formation of (p)ppGpp (second messenger) leading to the upregulation of *rmf* mRNA transcription (Izutsu, Wada, and Wada 2001). (p)ppGpp is also found to be responsible for inducing YfiA and HPF, with the latter being moderately under the control of quorum sensing inducer AI-2 (autoinducer-2) (DeLisa et al. 2001). The secondary messenger cAMP, produced during glucose deprivation, performs two functions one of which includes the induction of *rmf* transcription (Shimada, Yoshida, and Ishihama 2013), although to a lesser extent than (p)ppGpp, while the second one includes the induction of the long HPF in *L. lactis* in response to glucose deprivation (Figure 11) (Breuner et al. 2016). In addition to the secondary messengers, different sigma factors are also among the regulatory mechanisms (Bonocora et al. 2015). The RMF level is quickly reduced accompanied with 100S disappearance within one minute upon transferring the cells to renewed medium (Aiso et al. 2005).

Despite the presence of different factors mediating hibernation among different species, there is a similarity in the factor's sequence. Common conserved moieties have been detected between the short HPF and the NTD of LHPF as well as NTD of YfiA. Negative stain electron microscopy studies performed in 2002 have shown, for the first time, the 100S structure from

E. coli at the stationary phase (Yoshida et al. 2002). The structure showed that the interaction between the two 70S monomers takes place via the 30S subunit leading to the 50S-30S-30S-50S conformation. Eight years later, Kato and coworkers managed to get a cryo-EM structure of 100S, which ratified the previously observed 50S-30S-30S-50S conformation and even detected three ribosomal proteins that are involved in the interface between the 30S (Kato et al. 2010). However the density for the hibernation factors could not be detected in this structure, owing to the low map resolution at 18 Å. The same results have been reached using cryo-electron tomography of 100S from *E. coli*, both *in vitro* as well as within the intact *E. coli* cells (Ortiz et al. 2010). In 2012, Polikanov and colleagues (Polikanov, Blaha, and Steitz 2012) have determined three crystal structures of *T. thermophilus* 70S bound to *E. coli* HPF, RMF, and YfiA at high resolution. This study suggested the binding site for RMF to be near the anti-Shine Dalgarno area, while the HPF and YfiA were shown to overlap with the binding site of the tRNA and mRNA between the head and the body of the 30S. During the years 2017-2018, five different high resolution cryo-EM structures were published, studying the LHPF mediated 100S from different species including *B. subtilis*, *L. lactis*, *S. aureus* and *T. thermophilus* (Beckert et al. 2017; Flygaard et al. 2018; Franken et al. 2017; Khusainov et al. 2017; Matzov et al. 2017). These structures have shed light, for the first time, on the mechanism by which the 100S forms within these bacteria, as well as the role played by the LHPF in bringing both 70S monomers together and inhibiting protein synthesis as a response to stress. In addition to these five structures, a sixth cryo-EM structure with relatively high resolution has presented the 100S formation in *E. coli* and also discussed the mechanistic differences between Gram-positive and Gram-negative bacteria in forming the 100S (Beckert et al. 2018).

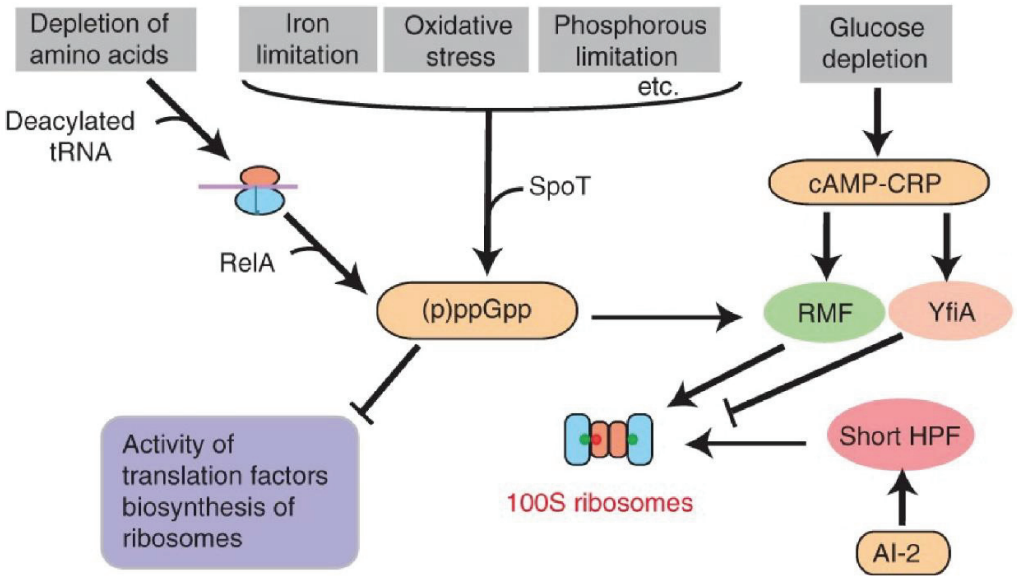

Figure 11. Different signaling pathways activating the ribosome hibernation factors in Gram-negative bacteria. Schematic representation of the different signals which activate various hibernating factors. AI-2 stands for autoinducer-2 and cAMP-CRP stands for cyclic AMP-cAMP receptor protein. Blunt headed arrows represent inhibition. This figure is adapted from (Yoshida and Wada 2014) with permission.

1.5. Antibiotics

The term antibiotic originates from the Greek origin of anti= against while biotic= life. It is commonly used to describe substances that fight against bacteria. The first antibiotic, penicillin, was discovered 90 years ago in London by Alexander Fleming. It was isolated from the growing fungus on *Staphylococcus* agar plates that was surrounded by a bacteria free zone caused by the antibacterial action of penicillin (Fleming 2001). Antibiotics are classified into bacteriostatics that hinder bacterial growth and bacteriocidals which kill bacteria. Both mechanisms take place by targeting various vital processes in the bacteria for instance, inhibition of DNA, RNA, protein synthesis as well as cell wall synthesis. This leads to antibiotic categorization based on the targeted bacterial process reviewed in (Kohanski, Dwyer, and Collins 2010). Following the discovery of penicillin, a myriad of antibiotics have been developed.

Before the release of penicillin into the market, the first resistance against it had already been detected reviewed by (Hede 2014). Despite the wide range of mechanisms of antibiotics, antibiotic resistance is fast growing making it global threat. Methicillin resistant *Staphylococcus aureus* and Vancomycin resistant *S. aureus* are bacterial strains that exhibit resistance against multiple drugs thus considered to be multidrug-resistant strains (MDR). Due to the increase antibiotic resistance, two more classes of strains have been detected. One is known as the pan-drug resistant (PDR) strains, which are resistant to all antibiotics or in other words untreatable. The other class of bacterial strains fall into extensively drug resistant (XDR) group, which show resistance to the first line therapy drugs and at least to one of the three other line of therapeutic agents. Strains of *P. aeruginosa* and *M. tuberculosis* have been found to belong to the PDR and XDR, respectively (Magiorakos et al. 2012; Falagas and Karageorgopoulos 2008; Falagas, Koletsi, and Bliziotis 2006).

Several pathways have been encountered by bacteria in developing resistance against a broad spectrum of antibiotics. Those pathways are comprised of conformational changes in

the antibiotic binding target (Bussiere et al. 1998), decreased uptake of the antibiotic (Delcour 2009), the transport of antibiotic outside of the cell via efflux pumps (Levy 1992), as well as enzymatic digestion of the therapeutic agent (Philippon, Labia, and Jacoby 1989). The high rise of resistant strains, like MDR, PDR and XDR, has led to a vast increase in the health care costs and mortality rate (Klevens et al. 2007). This has led to the urgent demand for studying new pathways applied by bacteria as a defense mechanism against antibiotic treatment in order to identify new drug targets as well as improve the selectivity of the existing ones.

1.5.1. VmlR

The ABC (ATP-binding cassette) protein family is highly conserved among the three kingdoms of life (Davidson et al. 2008). Members of the ABC proteins are distributed into eight subfamilies nominated as ABC A-H. ABC proteins share a common domain architecture consisting of two transmembrane domains (TMD) and two nucleotide binding domains (NBD), also known as ATP binding domains (ABD). Proteins from the subfamilies ABCF and ABCE are an exception to this classical domain architecture, since they contain a fused NBD connected via a linker and lack the TMDs (Dean, Rzhetsky, and Allikmets 2001; Kerr 2004). The development of antibiotic resistance is a biological process mediated by the action of proteins in the ABCF subfamily known as the ARE (Antibiotic REsistance) ABCF class. One of the significances of this process is that bacterial cells protect themselves against antibiotics produced by neighboring bacterial cells (Peschke et al. 1995). ARE ABCF proteins are further classified into subclasses depending on the antibiotics they develop resistance against. For instance, Msr develops resistance to macrolides and streptogramin B whereas Vga and Vml exhibit resistance to streptogramin A and lincosamides. Despite the resistance conferred to a broad range of antibiotics controlled by ARE ABCF proteins, they still do not confer resistance against 30S binding antibiotics (Dunkle et al. 2010; Schwarz et al. 2016).

In addition, the detailed mechanism for ABCF mediated antibiotic resistance was still unknown, until recently. It has been long hypothesized that these proteins enable resistance via transporting the antibiotic out of the cell (antibiotic efflux) (Ross et al. 1990). Later, sequence analyses have shown that ARE ABCF proteins share a high similarity to ABC proteins that function in regulating translation. Cryo-EM study of EttA (energy dependent translational throttle A, previously reported as YjjK), an *E. coli* ABCF protein that functions as translational regulator according to the energy intracellular levels, has shown that EttA-EQ_2

(mutation of the E129 and E432 glutamates into glutamine yielding an ATP non-hydrolyzing protein) is bound to the ribosomal E-site, in close proximity to the PTC (Chen et al. 2014). Crystal structure of EttA at 2.4 Å (Boel et al. 2014) in combination to the cryo-EM study have assigned EttA the function of a translation regulator for the 70S initiation complex to progress into the elongation cycle by sensing the cellular ATP level.

Based on the EttA structural analysis and the high similarity with Vga(A), mutational studies by the Lenart group on Vga(A) have provided more evidence to a previously suggested mechanism of ABCF protein in developing resistance (Lenart et al. 2015). This mechanism emphasizes, for the first time, a ribosomal protection approach of the protein by disturbing the antibiotic inhibition effect on the translational machinery. This has been further supported via *in vitro* studies by Sharkey and colleagues (Sharkey, Edwards, and O'Neill 2016), where they have shown an increased rescue of antibiotic stalled ribosomes by successive addition of ABCF purified proteins from *E. coli* into *S. aureus* system. In the same study, binding assays have shown the prevention of lincomycin binding to *S. aureus* 70S and even replacement of already bound lincomycin with Lsa(A), an ARE ABCF protein which is known to develop resistance against lincomycin. More recently two cryo-EM structures focusing on the mechanism of ARE ABCF protein in conferring resistance toward various antibiotics have been published. The first structure (Su et al. 2018) reported was of MsrE from *Pseudomonas aeruginosa* binding to *T. thermophilus* 70S at 3.6 Å, whereas the second (Crowe-McAuliffe et al. 2018) was of *B. subtilis* 70S bound to VmlR at 3.5 Å. Both studies have shown that ARE ABCF protein bind to the E-site, with the linker extending to the PTC, thus competing with the drug for the same binding site of the drug target by inducing conformational changes. This releases the antibiotic from the ribosome and translation continues.

2. Objectives of these Studies

Structure of *E. coli* RelA and *B. subtilis* Rel (Publication 1/Unpublished manuscript 2).

RelA is a member of the RSH family. The RSH family is an important regulator of the stringent response in bacteria, with the RelA being responsible for stimulating such a response upon starvation, thus allowing the bacteria to cope with stressful conditions. This response is linked to pathogenicity in bacteria including virulence, persistence and antibiotic resistance. The focus of these studies is to determine the binding of RelA/Rel on the ribosome with the

aim of exploring the RelA/Rel mediated stringent response. For the bifunctional Rel protein, the regulatory signal responsible for the switch from the hydrolysis to the synthesis of the alarmone was also investigated. Collectively, these studies might open the way for a new class of antimicrobials targeting RelA/Rel and coping with the increased antibiotic resistance problem.

Structure of *B. subtilis* LHPF (Publication 3).

Upon transition to stationary phase, a large portion of the ribosomes in Gram-positive bacteria enter a state of hibernation where they become translationally inactive. This is accompanied by the dimerization of the 70S ribosomes forming the 100S. The 100S is assumed to protect the ribosomes during stress from degradation, as well as easy return to the translating pool following stress removal. Thus, this mechanism helps the bacteria to resist antimicrobial treatments that are considered a stress signal. There has been no available structure for the LHPF binding to the ribosome and thus this publication aims to provide structural insight into the mechanism of LHPF-mediated 100S formation.

Structure of *B. subtilis* VmlR (Publication 4).

VmlR is one of the members of the antibiotic resistance ABCF subfamily, which confers resistance to a range of peptidyltransferase inhibitors. The detailed mechanism by which VmlR confers resistance is of great interest in the field of drug design, especially with the increased need for the development of new antibiotics. The mechanism by which ABCF proteins confer resistance has been controversial due to the lack of structural studies concerning the ABCF proteins. Therefore, this study aims to investigate the acquired antibiotic resistance due to VmlR.

3. Cumulative Thesis: Publications Summary

3.1. Publication 1: The stringent factor RelA adopts an open conformation on the ribosome to stimulate ppGpp synthesis

Stefan Arenz, Maha Abdelshahid, Daniel Sohmen, Roshani Payoe, Agata L. Starosta, Otto Berninghausen, Vasili Hauryliuk, Roland Beckmann, and Daniel N. Wilson. 2016.
Nucleic Acids Res, 44: 6471-81.

The stringent response has been studied in bacteria since a long time because it is a crucial mechanism that evolved to help bacteria to communicate with the external environment. One of the unfavorable environmental changes to which the bacterium must adjust its cellular metabolism in order to adapt is nutrient deprivation (Cashel and Gallant 1969). This adaptation requires the synthesis of (p)ppGpp mediated by RelA/SpoT homologue proteins on the ribosome. The SR is highly conserved among bacteria concomitant with its linkage to various bacterial characteristics, including persistence, virulence and antibiotic resistance (Atkinson, Tenson, and Hauryliuk 2011). This coincides with the absence of a counterpart system in eukaryotes, which together makes it a good candidate for designing antimicrobials that target the main players in the SR. However, the absence of high-resolution structural information as well as the controversial mechanisms of how exactly the RelA mediates the stringent response via (p)ppGpp, makes it challenging to design antimicrobials targeting it. A crystal structure of the bifunctional Rel from *Streptococcus equislimilis* has been reported by Hogg and coworkers. Nevertheless, the structure lacked the CTD which has an important regulatory function on the protein action (Hogg et al. 2004). The ribosome is an important activator of the Rel/RelA protein; nonetheless the structure has been representing the Rel-NTD in absence of the ribosome. An 11 Å cryo-EM structure of the monofunctional RelA on *T. thermophilus* ribosome could only show a general view of RelA approaching a distorted form of A-tRNA that shares some features with A/T-rRNA (Agirrezabala et al. 2013). The detailed interactions between RelA and the ribosome, along with the domain architecture of the CTD, were not reliably interpreted at such low resolution owing to the protein flexibility. In this publication, we managed to generate a complex of *E. coli* RelA bound to *E. coli* 70S using the ErmCL_S10K (erythromycin resistance leader peptide) disome approach. The complex was then applied to a cryo-EM, followed by single particle reconstruction. Even though the local resolution of RelA was ranging from 4 to over 10 Å compared to average resolution of 3.7 Å, the interactions of RelA subdomains with the ribosomal RNA and protein

was noticeable. The RelA is wrapped around an unusual form of A-tRNA in an elongated conformation on the ribosome through an alpha helical linker in the CTD. This distorted tRNA has been given the name A/R-tRNA since it binds to the A-site on the 30S, while on the 50S it interacts with RelA. The alpha helical linker is preceded by TGS (Threonyl-tRNA synthetase, GTPase, and SpoT), the first subdomain in the CTD, which senses the deacylation status of the tRNA by means of interacting with the CCA-3' end of the A/R-tRNA. The last two subdomains in the CTD are called CC and ACT, named after the conserved cysteine and Aspartokinase, Chorismate mutase and TyrA, respectively. They are located in the intersubunit cavity of the ribosome, with the ACT interacting with the 50S only, while the CC subdomain bridges the 50S with the 30S via interacting with helix 38 and S19. In contrast to the CTD, that shows several interactions with the ribosome, the NTD is rather flexible and protrudes toward the A-site intersubunit solvent toward the 30S spur. The cryo-EM structure has enabled us to provide a model where RelA binding to the ribosome facilitates the release of RelA CTD auto-inhibition on the synthetase activity resulting in increased intracellular (p)ppGpp levels.

3.2. Publication 2: Stringent response control by bifunctional RelA enzyme in the presence and absence of the ribosome

Patrick Pausch, Maha Abdelshahid, Wieland Steinchen, Heinrich Schäfer, Fabio Lino Gratani, Sven-Andreas Freibert, Christiane Wolz, Kürşad Turgay, Daniel N. Wilson and Gert Bange.
Unpublished

In contrast to monofunctional RelA that possess an active synthetase domain and an inactive hydrolase domain (pseudo hydrolase) compensated for by SpoT, Gram-positive bacteria like *B. subtilis* have a bifunctional Rel that is responsible for both hydrolysis and synthesis of (p)ppGpp (Atkinson, Tenson, and Hauryliuk 2011). In current publications the signal that regulates the exchange between hydrolysis and synthesis modes of Rel is missing. This publication presents not only the first cryo-EM structure of bifunctional Rel on the ribosome, but also the first crystal structure that comprises subdomains from the CTD and NTD and not just the NTD like that proposed in Relseq in the absence of the ribosome. The cryo-EM complex of *B. subtilis* Rel bound to the 70S ribosome has been obtained using the disome approach of ErmDL_R8K. It has been observed that the bifunctional Rel shares a similar binding site and interactions with the ribosome as that of the monofunctional RelA. This result excludes any special interaction between the ribosome and Rel as being responsible for activating hydrolysis over synthesis. The crystal structure of the Rel ΔRIS-ACT, off the ribosome, reveals a symmetric homodimer formed via interaction between the NTD of one

molecule and the TGS-AH subdomains of the corresponding molecule. Further proof for the homodimer formation has been detected using size exclusion chromatography. The conformation obtained in the crystal structure, when compared to that of the Relseq, is clear that it best fits the same structural rearrangements as that of the Hydrolase ON/ Synthetase OFF state. Based on these results, it has become possible to assign the conformational changes that result in the stabilization of the hydrolysis active site over the synthetase one and vice versa. The alignment of the Rel bound ribosome to the free Rel has revealed the readjustments that Rel undergoes during these two different states. In addition to the interactions between both molecules that are necessary for the homodimer, an interaction between the NTD and TGS within the same Rel molecule (*in cis*) has been described. The *cis* interaction is exhibiting the inhibition effect of CTD on the synthetic activity. In order to assess the important residues responsible for the auto inhibition effect of CTD, different Rel-CTD truncations as well as point mutations within the *cis* interface between TGS and NTD has been tested using Rel activity studies both *in vivo* and *in vitro*. Both, the structural and biochemical investigations have reinforced the following model; the homodimer Rel prevents the binding of deacylated-tRNA and hence the homodimer is hydrolytically active. Nonetheless upon accumulation of deacylated-tRNA, the homodimer dissociates and deacylated-tRNA binds to Rel bringing it to the idling ribosome and stabilizing the extended conformation of Rel on the ribosome. This in turn removes the CTD auto-inhibition effect and permits the synthetic activity of the alarmone.

3.3. Publication 3: Structure of the *Bacillus subtilis* hibernating 100S ribosome reveals the basis for 70S dimerization

Bertrand Beckert, Maha Abdelshahid, Heinrich Schafer, WIeland Steinchen, Stefan Arenz, Otto Berninghausen, Roland Beckmann, Gert Bange, Kürşad Turgay, and Daniel N. Wilson. 2017. *EMBO J*, 36: 2061-72.

Similar to animal dormancy, characterized by a state of inactivation and lowered metabolic rate, bacterial ribosomes undergo a hibernation state in response to various stresses. An ideal example of stress is nutrient limitation, which controls bacterial growth leading to the transition from exponential to stationary phase. This induces bacterial conserved stringent response which in turn elevates the alarmone secondary messenger (p)ppGpp (Izutsu, Wada, and Wada 2001). On the other hand, other forms of stress include glucose deprivation, which leads to increased cellular cAMP levels (Shimada, Yoshida, and Ishihama 2013). Both (p)ppGpp and cAMP play similar roles in upregulating transcription of different genes

involved in hibernation. Three different states have been identified in Gram-negative bacteria, such as *E. coli* (gamma-proteobacteria), actively translating 70S, inactively translating 70S, mediated by the action of YfiA, and 70S dimers known as 100S, mediated by the action of RMF and short HPF (Maki, Yoshida, and Wada 2000; Ueta et al. 2008; Ueta et al. 2005). However, in Gram-positive bacteria, YfiA is absent leaving only the translating 70S and the inactive 100S, mediated by long HPF homologue (Ueta et al. 2013; Ueta, Wada, and Wada 2010; Tagami et al. 2012). The 100S formation is the bacterial self-defense mechanism activated in cases of environmental changes; it aims to set priorities for energy consumption, helping the bacteria to survive such conditions and to easily get back to the translation pool upon stress removal. Understanding the mechanism of 100S formation is of great importance, since it is strongly related to the increasing public health emergency of antibiotic resistance. Most of the biochemical and structural studies have been performed on *E. coli* cells, while the mechanism of 100S formation in Gram-positive bacteria harboring the LHPF homologue has been lacking. The cryo-EM study of the 100S from *B. subtilis*, natively purified from S12 extract, was performed with an average resolution of 3.8 Å. The structure revealed, for the first time, the LHPF binding site on the 100S, with the LHPF-NTD located on the channel between the head and the body of the 30S. The NTD is connected via a seemingly long linker, reaching the Shine Dalgarno helix, where the CTD is dimerized with that of the second molecule at the back of the 30S. Translational blockade is shown to be due to the interference of the NTD with the binding site of the mRNA and anticodon stem loop tRNA. This is consistent with the absence of both the tRNA and mRNA. The linker is also assumed to be interfering with the formation of a SD-aSD helix resembling the role of RMF in *E. coli*, however due to the highly flexible linker clear structural evidence was lacking. The CTD, on the other side, has been assigned the role of stabilizing the 100S formation through interactions between the CTD and the 70S monomer as well as between the two CTDs. This dimerization is essential for bringing both 70S monomers in close proximity, which results in further interactions between the ribosomal proteins on one ribosome and the rRNA on the facing ribosome; this strengthens the 100S dimer further.

3.4. Publication 4: Structural basis for antibiotic resistance mediated by the *Bacillus subtilis* ABCF ATPase VmlR

Caillan Crowe-McAuliffe, Michael Graf, Paul Huter, Hiraku Takada, Maha Abdelshahid, Jiří Novacek, Victoriia Murina, Gemma C. Atkinson, Vasili Hauryliuk, and Daniel N. Wilson. 2018.
Proc Natl Acad Sci U S A, 115: 8978-83.

The bacterium applies several strategies to confer resistance against current antibiotics. ABC (ATP-binding cassette) superfamily proteins are composed of two ABC domains and two transmembrane domains (TMD). They are known to use ATP for the efflux of antibiotics out of the cell. However, proteins of the ABCF subfamily are lacking the TMDs (Davidson et al. 2008; Dean, Rzhetsky, and Allikmets 2001; Kerr 2004). VmlR is one of the members of the antibiotic resistance ABCF subfamily which confers resistance to a range of antibiotics including Virginamycin M, Lincomycin and Streptogramin A. The detailed mechanism by which VmlR confers resistance is of great interest in the field of drug design, especially with the increased need for the development of new antibiotics. The only structural studies available are from a non-ARE ABCF protein called EttA, which functions as a translation regulator dependent on the cellular ATP level (Chen et al. 2014; Boel et al. 2014). Here we present a cryo-EM structure of *B. subtilis* VmlR-EQ_2 bound to the 70S ribosome at 3.5 Å (Crowe-McAuliffe et al. 2018). The structure reveals the binding mode of VmlR in the ribosomal E-site with the linker extending toward the PTC stabilizing the L1 stalk in an open conformation. The structure also shows the C-terminal extension (CTE) comprised of two alpha helices and its involvement in creating the interaction between VmlR and the small subunit. Such interactions stabilize the P-tRNA in a noncanonical conformation referred to as P/V-tRNA through the induction of small subunit rotation. Both the conformational changes occurring in the PTC, along with the noncanonical conformation of the P-tRNA, work together to facilitate the drug falling off the ribosome. The study reveals the mechanism of action of VmlR as a ribosomal protection protein by overlapping with the drug binding site as well as inducing conformational changes destabilizing the binding of the drug.

4. Discussion

4.1. Publication 1: The stringent factor RelA adopts an open conformation on the ribosome to stimulate ppGpp synthesis
Publication 2: Stringent response control by bifunctional RelA enzyme in the presence and absence of the ribosome

Rel/RelA belong to the RSH proteins and are the main players in the bacterial stringent response. In the case of Rel, they play a role in catalyzing the formation, as well as degradation, of the alarmone (p)ppGpp (Atkinson, Tenson, and Hauryliuk 2011; Cashel and Gallant 1969). The alarmone then targets various cellular compartments in order to switch cellular metabolism toward saving energy and surviving unfavourable conditions like nutrient deprivation. The stringent response is one of the mechanisms by which bacteria becomes more invasive and persistent. Furthermore, the SR is linked to the increasing threat of antibiotic resistance, which gives rise to untreatable bacteria that could eventually lead to serious diseases and even death. This has been the drive to study the approach by which RelA catalyzes the alarmone production on the ribosome, as well as studying the regulation of the contrasting effects of Rel concerning both production and degradation of the alarmone.

Concerning RelA (monofunctional), three high resolution cryo-EM structures of RelA associated to the ribosome have been published (Brown et al. 2016; Arenz et al. 2016; Loveland et al. 2016). The three structures were detected using RelA and 70S ribosomes purified from the most commonly studied organism, *E. coli*. The first structure was reported by Brown and coworkers at 3 Å overall resolution. The complex has been prepared *in vitro* using an excess of deacylated-tRNA^{Phe} to mimic the nutrient starvation condition. RelA substrates have also been provided using GDP, along with the non-hydrolysable ATP form named AMPCPP, in order to block RelA on the ribosome. Paromomycin has been used to stabilize the mRNA-tRNA interaction at the A-site. The main challenge in studying RelA is the protein susceptibility to precipitation, as well as its flexibility. The data was then processed using Relion. 3D classification was applied on ribosomal particles with an A-site tRNA occupancy. This has resulted in two classes of ribosomes having RelA and A-site tRNA, but differ in the 30S conformation.

To enhance RelA resolution and isolate different conformations, focused classification on separate domains has been performed. The structure revealed that RelA exhibits an elongated conformation on the ribosome with an uncharged tRNA binding to the ribosomal A-

site. However, this was not in the classical accommodated state, but in a distorted conformation. The conformation of this A-tRNA is similar to that observed in case of A/T-tRNA (Schmeing et al. 2009), but still distorted. It has been given the name A/R-tRNA, representing tRNA binding to the A-site on the 30S and CCA end approaching the RelA. The NTD, harboring both synthetase and hydrolase domains, has shown the highest flexibility among RelA domains. This is due to its position between the SRL and the 30S spur, which are flexible ribosomal elements, as well as its extension toward the solvent with low ribosomal interactions. This study has shown that the CCA-3' end of the A/R-tRNA interacts with the TGS domain of RelA via stacking interactions and H-bonding. Which then drives the contact between β5 strand of the TGS and the 3'OH of the adenosine in the uncharged tRNA. This has been proposed as a mechanism of activation of RelA upon recognizing the uncharged tRNA, which would not be the case with charged tRNA due to steric clash.

Several studies have shown a link between uL11 and (p)ppGpp synthesis where synthesis is impaired in case of a mutated uL11 (Yang and Ishiguro 2001; Wendrich et al. 2002). This leads to the expectation that RelA might be interacting with uL11. However, this sort of interaction was not detected in the structure. The CTD showed the most extensive interaction with the ribosome, which was detected in detail for the first time in this publication. The TGS is followed by a poorly resolved linker that is wrapped around the A/R-tRNA connecting the TGS to the ZFD (also referred to as RIS). The ZFD is in contact with H38 of the 23S rRNA, known as the A-site finger. The ZFD is followed by RRM motif (also referred to as ACT) which folds back to interact with the ribosomal protein uL16.

The second structure from Arenz and colleagues (Arenz et al. 2016) was prepared in a similar manner to that used by the Brown group, in which the purified RelA was incubated with the purified ribosomes in the presence of non-hydrolysable ATP and GDP, as well as cognate deacylated-tRNA^{Lys}. In this case, no paromomycin has been added, and the ribosomes were purified using the disome construct ErmCL-S10K in the presence of the macrolide erythromycin in order to create the idling ribosomes. The data has been processed using SPIDER software and has led to 13% of ribosomes showing A/R-tRNA, P-tRNA and RelA occupancy at 3.7 ˚A. However the local resolution on A/R-tRNA and RelA was lower, ranging from 4 -10 Å.

The main features of RelA binding to the ribosome are in agreement with that observed in the first structure from Brown et al 2016. RelA binds in the elongated conformation with the TGS – helical domains being wrapped around the distorted A-tRNA (A/R-tRNA). The

NTD is protruding toward the ribosome periphery at the A site intersubunit space, which is unlike any of the translation factors binding sites. The NTD shows the lowest resolved domain among RelA, owing to its high flexibility and low ribosomal contact. On the other hand, the CTD is responsible for the most interactions with the ribosome. In both structures, it is believed that RelA activation takes place independent of the NTD catalytic domain interactions with the risbosome. This is a consequence of the lack of prominent and stable contact between the NTD and the 30S spur in both cryo-EM, except for few classes in Brown study. This has supported a model of RelA activation where synthesis is derived from the removal of the auto-inhibition effect upon binding to the ribosome in the elongated conformation, rather than direct activation of the synthetase domain via interaction between NTD and the ribosome.

The role of the TGS subdomain in detecting the tRNA acylation/deacylation state is agreed upon. In the first structure, it was described to be due to the 3'OH group of the terminal adenosine in the uncharged tRNA. But the resolution in our study (Arenz study) was not high enough to confirm a detailed recognition mechanism of tRNA by TGS. The link between the TGS and the last two subdomains of the CTD has not been well resolved, which probably reflected it's flexibility. This could be the result of binding to the flexibly distorted A/R-tRNA element. Preceding the ACT, another subdomain referred to as CC (cysteine conserved) subdomain was not modelled. This CC subdomains is referred to as ZFD in the previous structure, for which a de novo model was built. The CC subdomain shows interactions with both the small and large ribosomal subunits, while the ACT subdomain contacts only the large ribosomal subunit, in addition to the A/R-tRNA elbow.

The third publication was presented by Loveland (Loveland et al. 2016). Unlike the two previous studies, the complex within this study has been assembled in absence of substrate nucleotides. FREALIGN was applied on the dataset for single particle reconstruction and resulted in three structures (II-IV) with different rearrangements in the RelA, A/R-tRNA and the 30S; Where structure I is lacking any density for A-tRNA. Similar to the structure by Brown, no interaction between L11 and RelA has been detected, but rather an interaction between L11 and A/R-tRNA. Such interaction could result in directing the deacylated-tRNA in order to activate RelA, elucidating why mutated L11 ribosomes have defected (p)ppGpp synthesis.

In the Loveland study, a class of ribosomes (structure I) that does not contain the uncharged A-site tRNA but still has a density for RIS and ACT subdomains was detected. Such a population where RelA is present on the ribosome in absence of the A/R-tRNA was

not identified in the other two studies. This observation could be due to the preparation method of the complex, which was lacking RelA substrates. This state of RelA-CTD binding in absence of A-site tRNA could resemble an intermediate state that was not noticed when the substrates were provided, which would rather derive the alarmone synthesis followed by rapid dissociation of RelA from the ribosome.

The difference in complex assembly has not only resulted in a population of RelA binding in absence of the A/R-tRNA, but also in the continual rearrangements of the uncharged tRNA along with the decoding center on the 30S. This is from structure II to structure III, and further until structure IV where the tRNA resides in the A-site on the 30S accompanied by domain closure on the 30S subunit. Thus, structure IV has been suggested to resemble the conformation that is required for RelA activation. This is in agreement with the results that show the failure of RelA activation using near cognate tRNA, as is the case in structures II-III. These tRNA rearrangements might be happening faster in the presence of RelA substrates, and thus were only notable in the Loveland study in the absence of RelA substrates. Both Arenz and Brown structures adopt the model in which deacylated-tRNA forms a complex with RelA prior to ribosomal binding. But the Loveland study does not exclude RelA binding to the ribosome in absence of deacylated-tRNA owing to the subpopulation that has a binding RelA-CTD with ribosomes lacking deacylated-tRNA.

The structural studies of the monofunctional *E. coli* RelA represents a great step in unrevealing the binding site of RelA on the ribosome and the interaction partners of the ribosomal RNAs and proteins as well as tRNA. This, in turn, increases the understanding of the SR mechanism. However, many questions regarding the sequence of RelA binding on the ribosome still need to be answered. One main question is whether RelA recognizes the deacylated tRNA on or off the ribosome. Only recently, a publication (Winther, Roghanian, and Gerdes 2018) has shown that RelA recognizes the tRNA off the ribosome, while upon binding to the ribosome, it becomes activated. This is in line with the binding nature of RelA, which is wrapped around the A/R-tRNA. Therefore, it is presumed that the binding of RelA-deacylated-tRNA complex to the ribosome would extend RelA in a more relaxed form. Thus, it seems structurally more favored for the RelA to wrap around the tRNA of the ribosome than snaking under the A/R-tRNA which is already bound to the ribosome. The biochemical data has also shown that the CTD is important for ribosomal binding, but not essential for RelA binding to the tRNA.

The three structures have suggested a model for RelA, but they still show some differences. It is clear that upon accumulation of cognate deacylated-tRNA, RelA-uncharged-A-tRNA-stalled-ribosome complex is formed. The uncharged tRNA undergoes rearrangements to reach an accommodation on the 30S A-site, which is accompanied by the extension of RelA. This results in the elimination of the auto-inhibition effect of the CTD, as well as a possible interaction between the NTD with the spur. Then, finally, (p)ppGpp synthesis takes place.

Regarding the bifunctional Rel, so far only one cryo-EM structure of bifunctional Rel from *B. subtilis* on the ribosome is available. This structure has been obtained from a complex assembled in a similar manner to that mentioned before in Arenz study (Arenz et al. 2016) of *E. coli* RelA with the change of the ErmCL-S10K with the ErmDL-R8K. This change of constructs has been due to the failure of disome formation using the ErmCL-S10K with ribosomes from *B. subtilis*. The data has been processed using the RELION software package and has resulted in a 10.3% population that contained A-site tRNA and Rel which is very similar to the 13% that was obtained for the *E. coli* RelA study. The resolution of the ribosome core reached 3.8 Å, but the local resolution of the Rel and the A/R-tRNA was again worse. The poor resolution on the factor again suggest considerable protein flexibility on the ribosome.

The cryo-EM structure of *B. subtilis* Rel on the ribosome shows that bifunctional Rel binds in an analogous manner to the ribosome as the monofunctional RelA. A high conservation of the RSH proteins regulating SR was observed, but it simply excludes the involvement of the ribosome in regulating the bifunctional Rel activity. A crystal structure of *B. subtilis* Rel ΔRIS-ACT off the ribosome has also been detected. The crystal structure has revealed, for the first time a homodimer conformation via the TGS-AH of one monomer and the NTD of the other. The Rel conformation in the homodimer state has been assessed using the crystal structure by Hogg (Hogg et al. 2004) to be in the hydrolysis ON / synthesis OFF condition. In addition a trans-interaction is required for the homodimer stabilization. Whereas the *in cis* interaction between the TGS-AH and the synthetase domain of the same monomer is found to be involved in protein regulation. The CTD auto-inhibition effect has always been postulated, however the important residues, as well as the detailed interactions between the CTD and NTD that lead to such an effect, has not been detected before.

The detailed rearrangements occurring in the catalytic sites of the hydrolase and the synthetase domains that favor one or the other are now revealed. Such rearrangements have

been studied using the superimposition tool of the crystal structure of *B. subtilis* Rel and the available crystal structure of Relseq. Biochemical experiments assessing the hydrolytic and synthetic activity of successively truncated Rel domains show that the TGS and the AH domains are essential for maintaining hydrolysis over synthesis action, both *in vivo* and *in vitro*.

For the first time it was shown, that the alignment of the crystal structure off the ribosome, with that of the cryo-EM on the ribosome has provided insights into the rearrangements acquired upon Rel binding to the ribosome. The main changes are taking place in the helices connecting the CTD and NTD domains (α7 and α16), TGS, and α20 in AH subdomain. In addition to the large shifts going on the TGS, as well as α20 in the AH subdomain, which is bent in case of binding to deacylated-tRNA to stabilize the wrapping conformation seen on the ribosome, compared to a straight conformation off the ribosome. The straight α20 is rather important for the homodimer formation, where it enters the cleft formed by the synthetase and hydrolase subdomains in the NTD.

From the studied structures plus the biochemical investigations, a model of Rel mediated SR was proposed. This model suggests that in absence of stress, Rel forms a homodimer with hydrolysis of the alarmone to prevent cell growth inhibition. Whereas upon amino acid starvation and deacylated-tRNA accumulation, Rel is switched from the homodimer to the monomer, followed by association with the deacylated-tRNA and together bind to the idling ribosome. This binding stabilizes the detected elongated conformation of Rel, which removes the auto-inhibition effect of the CTD (TGS-AH) on the synthetic domain. This leads to RelA activation and alarmone synthesis, in the case of RelA where the hydrolase subdomain is inactive.

Even though the structural studies and the biochemistry have uncovered a lot about Rel/RelA mediated SR, there is still many things unknown. Different snapshots of a high resolution Rel/RelA on the ribosome is still required for enhanced insight into the NTD, which was disordered in all the structures published so far. Such a disorder makes it difficult to assess if there is an interaction between Rel/RelA and the 30S spur as well as SRL or not, since this might play a role in the protein regulation. Another important aspect is whether the synthesis of (p)ppGpp continues after the protein dissociation from the ribosome, or is it just restricted to the ribosome. Since the Rel homodimer has been designated to be hydrolytically active, so whether the monofunctional RelA with the pseudo hydrolase undergoes such homodimerization or not, is still a question to be addressed.

4.2. Publication 3: Structure of the *Bacillus subtilis* hibernating 100S ribosome reveals the basis for 70S dimerization

Among the adaptation mechanisms of bacterial cells in response to environmental changes is ribosome hibernation. Ribosome hibernation is characterized, mainly, by the inhibition of protein synthesis on a large percentage of the ribosomes in the translating pool in order to save energy consumption under stress conditions. In addition, this hibernating state also protects the ribosomes. Thus, upon removal of the stress factor, the ribosomes quickly return to the translating pool and become translationally active. Hibernating ribosomes are induced by RMF and short HPF in a subclass of gamma-proteobacteria including *E. coli* (Maki, Yoshida, and Wada 2000; Wada et al. 1990; Yoshida et al. 2002). Both factors are required for the dimerization of the 70S leading to the formation of 100S. An antagonistic action is exerted by YfiA (also called pY or RaiA), which stabilizes the 70S by inhibiting translation (Maki, Yoshida, and Wada 2000). However, Gram-positive bacteria only have a long HPF homologue, which plays the role of both RMF and short HPF in forming 100S and blocking translation (Ueta et al. 2013; Ueta, Wada, and Wada 2010). Such inter-species variations could play an important part in developing new antimicrobial agents, as well as enhancing the already existing antimicrobials' selectivity, which would be of great benefit in overcoming antibiotic resistance.

Five cryo-EM structures have revealed the mechanism underlying the 100S formation in different Gram-positive bacteria mediated by the LHPF (Beckert et al. 2017; Flygaard et al. 2018; Franken et al. 2017; Khusainov et al. 2017; Matzov et al. 2017). Beckert and coworkers (Beckert et al. 2017) have presented the structure of the 100S isolated from *B. subtilis*, grown until the late exponential phase. The structure shows that the rearrangement of the 100S in Gram-positive bacteria has a side-to-side interaction between the small subunits, differing from the back-to-back interaction observed in *E. coli* (Kato et al. 2010). In addition, the 30S subunits are in a non-rotated conformation, in contrast with the swiveled 30S head proposed in *E. coli*. The binding site of the long HPF-NTD was detected on the 30S at 3.5-5 Å, overlapping the mRNA as well as A- and P-tRNAs anticodons, which elucidates its role in inhibiting translation and explains the absence of tRNAs in the detected 100S structure. The NTD is followed by a 34 amino acid long linker, which connects the NTD to the CTD. Even though the linker was not well resolved due to its high flexibility, the first few amino acids following the NTD suggest that the linker might be going down the same path as the mRNA. The linker extends to reach the back of the small subunit, where the CTD is located, then the

CTD dimerizes with the second CTD molecule of the second 70S monomer. It has been noticed that CTD plays an important role in dimerizing the 70S monomers, mainly via contacting ribosomal proteins S2 and S18 beside the interaction between S2 of 70S and h26 of the 16S rRNA of the twin 70S. The dimerization role exerted by long HPF-CTD has been observed biochemically, where *L. lactis* CTD along with short HPF induced the 100S formation in *E. coli* ribosomes (Puri et al. 2014).

Despite the sequence similarity between RMF and LHPF-CTD, which accordingly led to the proposal that they might share the same function. The structure rather shows that they do not share the same ribosomal binding site, and that the CTD does not interfere with the SD helix formation as shown for RMF. On the other hand, the linker is assumed to be replacing the role of RMF in Gram-positive bacteria due to its probable binding site which interrupts the Shine Dalgarno helix formation. However, the absence of the linker density, owing to the high flexibility, made it challenging to validate such a function. The *T. thermophilus* 100S structure has provided this evidence since Flygaard and colleagues have successfully resolved most of the linker spreading into the mRNA to the Shine Dalgarno helix location at the 30S back (Flygaard et al. 2018). Moreover, biochemical assays were performed by Beckert and coworkers (Beckert et al. 2017) on the linker to show its essentiality in ribosomal binding and 100S formation, both length and sequence wise.

Regardless of the conservation of the LHPF mediated 100S mechanisms in Gram-positive bacteria, the structural studies illustrate species-specific variations. For instance in *B. subtilis* (Beckert et al. 2017), *L. lactis* (Franken et al. 2017) and *S. aureus* (Khusainov et al. 2017; Matzov et al. 2017), the HPF-CTD dimerization brings the two small subunits into contact, leading to an interaction between ribosomal proteins uS2 and bS18 on the opposing monomers, as well as creating surface interface between uS2 and h26 of the 16S rRNA. However, in *T. thermophilus* (Flygaard et al. 2018) the interaction between h26 and uS2 is lost due to the short length of h26. In addition, the contact between h40 and HPF-CTD observed in *S. aureus* is absent from *Thermus*, albeit the length of h40 is comparable to that in other species. Furthermore, ribosomal rotations have been observed in cases of *S. aureus* and *L. lactis*, resulting in closed and open conformations in terms of the space between the two small subunits. This in turn displays different intra-species interaction patterns in the 30S-30S interface. Thus, the key drive for dimerization is the interaction between the two CTDs via hydrophobic, and with stacking interactions.

A recent cryo-EM structure of the 100S isolated from *E. coli* cells at the stationary phase has presented the counterpart mechanism of hibernation from Gram-negative bacteria (Beckert et al. 2018). The structure reveals the binding site of RMF to be alternately allocated from the previously proposed crystal structure of *T. thermophilus* bound to *E. coli* factors (Polikanov, Blaha, and Steitz 2012). RMF is found to be binding in the area of the Shine Dalgarno helix, thus disrupting translation initiation, while the previously noted RMF location in the crystal structure has been shown to be occupied by the inactive compact conformation of protein S21 which is absent in *T. thermophilus*. This could be due to the fact that the crystal structure was performed using a heterologous system; that is to say *Thermus* ribosomes bound to *E. coli* factors knowing that *Thermus* 100S is mediated by long HPF homologue. The density corresponding for the short HPF has been identified on the 30S at the channel between the head and the body, interfering with the mRNA, anticodon stem loops of the tRNAs, as well as initiation factors. This concerted action of RMF mediated 90S followed by maturation into 100S via HPF binding leads to the final product of inactively translating 100S. It is remarkable that short HPF (SHPF) shares sequence similarity and overlapping binding sites with the 100S antagonistic factor, YfiA. Its binding is analogous to SHPF in addition to an extending CTD, which sterically hinders not only SHPF but also RMF binding, thus inhibiting protein translation on 70S.

The combined biochemical and structural studies on hibernating ribosomes from Gram-positive bacteria suggests a mechanistic outline for the 100S formation. Cell exposure to environmental stresses induce the secondary messengers level including (p)ppGpp and cAMP. These messengers then maintain the cell homeostasis during harsh conditions via stress response up-regulation. Among the up-regulated genes is the long HPF forming a dimer in solution, as shown experimentally using size exclusion chromatography. The dimerized HPF binds to the 70S, and owing to the length and flexibility of the linker, the second 70S is recruited forming the 100S. The LHPF-NTD share sequence homology, hence the binding site with SHPF and YfiA followed by the linker passing down the mRNA channel connecting to the CTD on the 30S back. The NTD and the linker collectively block translation via interfering with initiation factors and the Shine Dalgarno helix, respectively, whereas the CTD works on stabilizing the dimerization via developing interactions between the 30S-30S interface.

In spite of the intensive structural studies performed on the 100S, several issues are still not addressed. The physiological role of the 100S is still controversial and not well understood. Different studies have related the 100S formation to persistence, virulence, easy recovery, as

well as protection against degradation. A recent study has shed light on GTPase HflX as an inducer of 100S dissociation (Basu and Yap 2017), however the deletion did not dramatically increase the disome fraction. This, in turn, suggests the presence of other pathways that still remain to be unraveled. Another important question is the exact step in the translation process at which the hibernation factors bind and induce 100S formation. This question has been raised as a result of the detection of LHPF bound 30S in exponentially growing *S. aureus* cells. Further biochemical and structural studies need to be applied in order to provide an answer to the still uncovered areas in the mechanism of ribosome hibernation in bacteria. This could in turn result into a great improvement in the field of producing antimicrobials, in addition to overcoming the increasing problem of developing persistence and antibiotic resistance.

4.3. Publication 4: Structural basis for antibiotic resistance mediated by the *Bacillus subtilis* ABCF ATPase VmlR

ABCF proteins represent a subfamily of the highly distributed ABC superfamily. In contrast to the majority of the proteins belonging to the ABC subfamilies that are composed of two ATP binding cassettes (ABC) in addition to two transmembrane domains (TMD), the ABCF proteins are lacking the TMDs. ARE ABCF are a subclass of the ABCF proteins which play an important role in developing resistance toward different antibiotics. They have been detected in disease causing bacteria together with bacteria producing antibiotics. Concomitant with the increasing demand for new antibiotics, studying bacterial mechanisms involved in conferring antibiotic resistance are becoming of great interest.

Two cryo-EM structures focusing on the mode of action of ARE ABCF proteins have been recently published. Su and coworkers (Su et al. 2018) have studied the cryo-EM structure of *P. aeruginosa* MsrE, an ARE ABCF protein known to confer resistance to macrolides and streptogramin B, in complex with *T. thermophilus* ribosomes using nonhydrolyzable ATP (AMP-PNP) at a resolution of 3.6 Å. The second cryo-EM by Crowe-McAuliffe (Crowe-McAuliffe et al. 2018) has reported the structure of *B. subtilis* VmlR-EQ_2, an ARE ABCF protein which develops resistance to Streptogramin A, lincosamides and pleuromutilins, using *B. subtilis* 70S stalled in presence of telithromycin and ATP at 3.5 Å.

Both structures are in agreement with the binding mode, for both MsrE and VmlR, where they bind on the ribosomal E-site with the linker domain being extended toward the PTC. These structures have solved the long controversy about the mechanism underlying the resistance by AREs as well as disapproving the old hypothesis (Ross et al. 1990), that favors

the efflux of the antibiotics by ARE as they were mistaken for the function of the ABC transporters. But, this hypothesis has always been questionable due to the absence of TMDs in the ARE subfamily. These studies suggest that resistance takes place via displacing the bound drug on the ribosome by inducing conformational changes, rather than antibiotic efflux. The rearrangements taking place could also explain the prevention of antibiotic rebinding following their fall off the ribosome.

The VmlR-EQ_2 mutant replaces the E129 and E432 glutamates into glutamine, this yields a protein incapable of hydrolyzing ATP. This is based on the assumption that ATP hydrolysis is a pre-requisite for the dissociation of the VmlR off the ribosome, in a similar fashion to the non ARE ABCF protein EttA, and thus can stabilize the protein binding on the ribosome for a relatively longer time. This is in a way similar to the usage of a non-hydrolysable ATP form used for the MsrE structure. Both structures have further suggested the importance of ATP hydrolysis in recycling the ARE ABCF protein. Moreover, the MsrE-EQ_2 mutant has shown a reduced resistance profile that highlights the ATP hydrolysis significance in mediating resistance.

The structural studies have also shed light on an important aspect regarding the different antibiotic resistance profiles exhibited by the different AREs. Different contacts with the PTC have been detected for VmlR in comparison with MsrE, owing to the differences in the length and sequence of the linker domain of both proteins. The linker has been shown to be very crucial in determining the resistance profiles, where mutations in the Vga(A) linker has led to changes in the antibiotic resistance conferred by the protein. Last but not least the structure of VmlR complex has an extra density for the C- terminal extension (CTE) following the second nucleotide binding domain which has been shown to reside on the 30S in the Shine Dalgarno-anti Shine Dalgarno cavity. The CTE, although being absent in MsrE, has shown to be functionally essential for conferring resistance in VmlR. Despite of the high conservation among ARE ABCF subfamily, they still have enough differences enough to mediate resistance against different antibiotic spectrum. Thus, more structural studies are required to cover the different mode of actions of ARE proteins in conferring resistance toward different antibiotics.

5. References

Adamczyk, A. J., and A. Warshel. 2011. 'Converting structural information into an allosteric-energy-based picture for elongation factor Tu activation by the ribosome', *Proc Natl Acad Sci U S A*, 108: 9827-32.

Aevarsson, A., E. Brazhnikov, M. Garber, J. Zheltonosova, Y. Chirgadze, S. Alkaradaghi, L.A. Svensson, and A. Liljas. 1994. 'Three-dimensional structure of the ribosomal translocase: Elongation factor G from *Thermus thermophilus*', *EMBO J.*, 13: 3669-77.

Agafonov, D. E., V. A. Kolb, and A. S. Spirin. 2001. 'Ribosome-associated protein that inhibits translation at the aminoacyl-tRNA binding stage', *EMBO Rep.*, 2: 399-402.

Agirrezabala, X., I. S. Fernandez, A. C. Kelley, D. G. Carton, V. Ramakrishnan, and M. Valle. 2013. 'The ribosome triggers the stringent response by RelA via a highly distorted tRNA', *EMBO Rep*, 14: 811-6.

Agrawal, RK, MR Sharma, MC Kiel, G Hirokawa, TM Booth, CMT Spahn, RA Grassucci, A Kaji, and J. Frank. 2004. 'Visualization of ribosome-recycling factor on the *Escherichia coli* 70S ribosome: Functional implications', *Proc. Natl Acad. Sci. USA*, 101: 8900–05.

Aiso, T., H. Yoshida, A. Wada, and R. Ohki. 2005. 'Modulation of mRNA stability participates in stationary-phase-specific expression of ribosome modulation factor', *J Bacteriol*, 187: 1951-8.

Akanuma, G., Y. Kazo, K. Tagami, H. Hiraoka, K. Yano, S. Suzuki, R. Hanai, H. Nanamiya, Y. Kato-Yamada, and F. Kawamura. 2016. 'Ribosome dimerization is essential for the efficient regrowth of Bacillus subtilis', *Microbiology*, 162: 448-58.

Ali, I. K., L. Lancaster, J. Feinberg, S. Joseph, and H. F. Noller. 2006. 'Deletion of a conserved, central ribosomal intersubunit RNA bridge', *Mol Cell*, 23: 865-74.

Allen, GS, A Zavialov, R Gursky, M Ehrenberg, and J Frank. 2005. 'The cryo-EM structure of a translation initiation complex from Escherichia coli', *Cell*, 121: 703-12.

Aqvist, J., and S. C. Kamerlin. 2015. 'The conformation of a catalytic loop is central to GTPase activity on the ribosome', *Biochemistry*, 54: 546-56.

Arenz, S., M. Abdelshahid, D. Sohmen, R. Payoe, A. L. Starosta, O. Berninghausen, V. Hauryliuk, R. Beckmann, and D. N. Wilson. 2016. 'The stringent factor RelA adopts an open conformation on the ribosome to stimulate ppGpp synthesis', *Nucleic Acids Res*, 44: 6471-81.

Armache, J. P., A. Jarasch, A. M. Anger, E. Villa, T. Becker, S. Bhushan, F. Jossinet, M. Habeck, G. Dindar, S. Franckenberg, V. Marquez, T. Mielke, M. Thomm, O. Berninghausen, B. Beatrix, J. Soding, E. Westhof, D. N. Wilson, and R. Beckmann. 2010. 'Localization of eukaryote-specific ribosomal proteins in a 5.5-A cryo-EM map of the 80S eukaryotic ribosome', *Proc Natl Acad Sci U S A*, 107: 19754-9.

Atkinson, G. C., T. Tenson, and V. Hauryliuk. 2011. 'The RelA/SpoT homolog (RSH) superfamily: distribution and functional evolution of ppGpp synthetases and hydrolases across the tree of life', *PLoS One*, 6: e23479.

Ban, N, P Nissen, J Hansen, P B Moore, and T A Steitz. 2000. 'The complete atomic structure of the large ribosomal subunit at 2.4 Å resolution', *Science*, 289: 905-20.

Barker, M. M., T. Gaal, and R. L. Gourse. 2001. 'Mechanism of regulation of transcription initiation by ppGpp. II. Models for positive control based on properties of RNAP mutants and competition for RNAP', *J. Mol. Biol.*, 305: 689-702.

Barker, M. M., T. Gaal, C. A. Josaitis, and R. L. Gourse. 2001. 'Mechanism of regulation of transcription initiation by ppGpp. I. Effects of ppGpp on transcription initiation in vivo and in vitro', *J. Mol. Biol.*, 305: 673-88.

Basu, A., and M. N. Yap. 2017. 'Disassembly of the Staphylococcus aureus hibernating 100S ribosome by an evolutionarily conserved GTPase', *Proc Natl Acad Sci U S A*, 114: E8165-E73.

Beckert, B., M. Abdelshahid, H. Schafer, W. Steinchen, S. Arenz, O. Berninghausen, R. Beckmann, G. Bange, K. Turgay, and D. N. Wilson. 2017. 'Structure of the Bacillus subtilis hibernating 100S ribosome reveals the basis for 70S dimerization', *EMBO J*, 36: 2061-72.

Beckert, B., M. Turk, A. Czech, O. Berninghausen, R. Beckmann, Z. Ignatova, J. M. Plitzko, and D. N. Wilson. 2018. 'Structure of a hibernating 100S ribosome reveals an inactive conformation of the ribosomal protein S1', *Nat Microbiol*, 3: 1115-21.

Belardinelli, R., H. Sharma, N. Caliskan, C. E. Cunha, F. Peske, W. Wintermeyer, and M. V. Rodnina. 2016. 'Choreography of molecular movements during ribosome progression along mRNA', *Nat Struct Mol Biol*, 23: 342-8.

Beringer, M., C. Bruell, L. Xiong, P. Pfister, P. Bieling, V. I. Katunin, A. S. Mankin, E. C. Bottger, and M. V. Rodnina. 2005. 'Essential mechanisms in the catalysis of peptide bond formation on the ribosome', *J. Biol. Chem.*, 280: 36065-72.

Bieling, P., M. Beringer, S. Adio, and M. V. Rodnina. 2006. 'Peptide bond formation does not involve acid-base catalysis by ribosomal residues', *Nat Struct Mol Biol*, 13: 423-8.

Blanchard, S. C., R. L. Gonzalez, H. D. Kim, S. Chu, and J. D. Puglisi. 2004. 'tRNA selection and kinetic proofreading in translation', *Nat. Struct. Mol. Biol.*, 11: 1008-14.

Blanchard, S. C., H. D. Kim, R. L. Gonzalez, Jr., J. D. Puglisi, and S. Chu. 2004. 'tRNA dynamics on the ribosome during translation', *Proc. Natl. Acad. Sci. USA*, 101: 12893-98.

Bock, L. V., C. Blau, G. F. Schroder, Davydov, II, N. Fischer, H. Stark, M. V. Rodnina, A. C. Vaiana, and H. Grubmuller. 2013. 'Energy barriers and driving forces in tRNA translocation through the ribosome', *Nat Struct Mol Biol*, 20: 1390-6.

Boel, G., P. C. Smith, W. Ning, M. T. Englander, B. Chen, Y. Hashem, A. J. Testa, J. J. Fischer, H. J. Wieden, J. Frank, R. L. Gonzalez, Jr., and J. F. Hunt. 2014. 'The ABC-F protein EttA gates ribosome entry into the translation elongation cycle', *Nat Struct Mol Biol*, 21: 143-51.

Boelens, R., and C.O. Gualerzi. 2002. 'Structure and function of bacterial initiation factors', *Curr. Protein Pept. Sci.*, 3: 107-19.

Bonocora, R. P., C. Smith, P. Lapierre, and J. T. Wade. 2015. 'Genome-Scale Mapping of Escherichia coli sigma54 Reveals Widespread, Conserved Intragenic Binding', *PLoS Genet*, 11: e1005552.

Borg, A., M. Pavlov, and M. Ehrenberg. 2016. 'Complete kinetic mechanism for recycling of the bacterial ribosome', *RNA*, 22: 10-21.

Brenner, S., L. Barnett, E.R. Katz, and F.H.C. Crick. 1967. 'UGA: A third nonsense triplet in the genetic code', *Nat.*, 213: 449-50.

Brenner, S., A.O.W. Stretton, and S. Kaplan. 1965. 'Genetic code: the 'nonsense' triplets for chain termination and their suppression', *Nat.*, 206: 994-98.

Breuner, A., D. Frees, P. Varmanen, A. M. Boguta, K. Hammer, J. Martinussen, and M. Kilstrup. 2016. 'Ribosomal dimerization factor YfiA is the major protein synthesized after abrupt glucose depletion in Lactococcus lactis', *Microbiology*, 162: 1829-39.

Brown, A., I. S. Fernandez, Y. Gordiyenko, and V. Ramakrishnan. 2016. 'Ribosome-dependent activation of stringent control', *Nature*, 534: 277-80.

Bussiere, D. E., S. W. Muchmore, C. G. Dealwis, G. Schluckebier, V. L. Nienaber, R. P. Edalji, K. A. Walter, U. S. Ladror, T. F. Holzman, and C. Abad-Zapatero. 1998. 'Crystal structure of ErmC', an rRNA methyltransferase which mediates antibiotic resistance in bacteria', *Biochemistry*, 37: 7103-12.

Caban, K., M. Pavlov, M. Ehrenberg, and R. L. Gonzalez, Jr. 2017. 'A conformational switch in initiation factor 2 controls the fidelity of translation initiation in bacteria', *Nat Commun*, 8: 1475.

Carter, A. P., W. M. Clemons, Jr., D. E. Brodersen, R. J. Morgan-Warren, T. Hartsch, B. T. Wimberly, and V. Ramakrishnan. 2001. 'Crystal structure of an initiation factor bound to the 30S ribosomal subunit', *Science*, 291: 498-501.

Cashel, M, D R Gentry, V J Hernandez, and D Vinella. 1996. 'Chapter 92: The Stringent Response.' in F.C. Neidhardt, R.I. Curtis, J.L. Ingraham, E.C.C. Lin, K.B. Low, B. Magasanik, W.S. Reznikoff, M. Riley, M. Schaechter and H.E Umbarger (eds.), *Escherichia coli and Salmonella thyphimurium: Cellular and Molecular Biology* (American Society for Microbiology: Washington).

Cashel, M., and J. Gallant. 1969. 'Two compounds implicated in the function of the RC gene of Escherichia coli', *Nature*, 221: 838-41.

Caskey, C. T., W. C. Forrester, W. Tate, and C. D. Ward. 1984. 'Cloning of the *Escherichia coli* release factor 2 gene', *J. Bacteriol.*, 158: 365-68.

Celano, Bruna, Roman T. Pawlik, and Claudio O. Gualerzi. 1988. 'Interaction of Escherichia coli, translation-initiation factor IF-1 with ribosomes', *Eur. J. Biochem.*, 178: 351-5.

Chen, B., G. Boel, Y. Hashem, W. Ning, J. Fei, C. Wang, R. L. Gonzalez, Jr., J. F. Hunt, and J. Frank. 2014. 'EttA regulates translation by binding the ribosomal E site and restricting ribosome-tRNA dynamics', *Nat Struct Mol Biol*, 21: 152-9.

Cornish, P. V., D. N. Ermolenko, H. F. Noller, and T. Ha. 2008. 'Spontaneous intersubunit rotation in single ribosomes', *Mol Cell*, 30: 578-88.

Crick, F. 1970. 'Central dogma of molecular biology', *Nature*, 227: 561-3.

Crowe-McAuliffe, C., M. Graf, P. Huter, H. Takada, M. Abdelshahid, J. Novacek, V. Murina, G. C. Atkinson, V. Hauryliuk, and D. N. Wilson. 2018. 'Structural basis for antibiotic resistance mediated by the Bacillus subtilis ABCF ATPase VmlR', *Proc Natl Acad Sci U S A*, 115: 8978-83.

Cummings, H.S., J.F. Sands, P.C. Foreman, J. Fraser, and J.W.B. Hershey. 1991. 'Structure and Expression of the infA Operon Encoding Translational Initiation Factor-IF1 - Transcriptional Control by Growth Rate', *J Biol Chem*, 266: 16491-98.

Czworkowski, J, J Wang, T A Seitz, and P B Moore. 1994. 'The crystal structure of elongation factor G complexed with GDP, at 2.7 Å resolution', *EMBO J.*, 13: 3661-68.

Dahl, J. L., C. N. Kraus, H. I. Boshoff, B. Doan, K. Foley, D. Avarbock, G. Kaplan, V. Mizrahi, H. Rubin, and C. E. Barry, 3rd. 2003. 'The role of RelMtb-mediated adaptation to stationary phase in long-term persistence of Mycobacterium tuberculosis in mice', *Proc Natl Acad Sci U S A*, 100: 10026-31.

Dalebroux, Z. D., S. L. Svensson, E. C. Gaynor, and M. S. Swanson. 2010. 'ppGpp conjures bacterial virulence', *Microbiol Mol Biol Rev*, 74: 171-99.

Dalebroux, Z. D., and M. S. Swanson. 2012. 'ppGpp: magic beyond RNA polymerase', *Nat Rev Microbiol*, 10: 203-12.

Das, B., R. R. Pal, S. Bag, and R. K. Bhadra. 2009. 'Stringent response in Vibrio cholerae: genetic analysis of spoT gene function and identification of a novel (p)ppGpp synthetase gene', *Mol Microbiol*, 72: 380-98.

Davidson, A. L., E. Dassa, C. Orelle, and J. Chen. 2008. 'Structure, function, and evolution of bacterial ATP-binding cassette systems', *Microbiol Mol Biol Rev*, 72: 317-64, table of contents.

Daviter, T., H. J. Wieden, and M. V. Rodnina. 2003. 'Essential role of histidine 84 in elongation factor Tu for the chemical step of GTP hydrolysis on the ribosome', *J Mol Biol*, 332: 689-99.

Dean, M., A. Rzhetsky, and R. Allikmets. 2001. 'The human ATP-binding cassette (ABC) transporter superfamily', *Genome Res*, 11: 1156-66.

Delcour, A. H. 2009. 'Outer membrane permeability and antibiotic resistance', *Biochim Biophys Acta*, 1794: 808-16.

DeLisa, M. P., C. F. Wu, L. Wang, J. J. Valdes, and W. E. Bentley. 2001. 'DNA microarray-based identification of genes controlled by autoinducer 2-stimulated quorum sensing in Escherichia coli', *J Bacteriol*, 183: 5239-47.

Dennis, P. P., M. Ehrenberg, and H. Bremer. 2004. 'Control of rRNA synthesis in Escherichia coli: a systems biology approach', *Microbiol Mol Biol Rev*, 68: 639-68.

Dennis, PP, and M Nomura. 1974. 'Stringent control of ribosomal protein gene expression in *Escherichia coli*', *Proc. Natl. Acad. Sci. USA*, 71: 3819-23.

Diaconu, M., U. Kothe, F. Schlunzen, N. Fischer, J. M. Harms, A. G. Tonevitsky, H. Stark, M. V. Rodnina, and M. C. Wahl. 2005. 'Structural basis for the function of the ribosomal L7/12 stalk in factor binding and GTPase activation', *Cell*, 121: 991-1004.

Dincbas-Renqvist, V., A. Engstrom, L. Mora, V. Heurgue-Hamard, R. Buckingham, and M. Ehrenberg. 2000. 'A post-translational modification in the GGQ motif of RF2 from *Escherichia coli* stimulates termination of translation', *EMBO J.*, 19: 6900-07.

Dorner, S., C. Panuschka, W. Schmid, and A. Barta. 2003. 'Mononucleotide derivatives as ribosomal P-site substrates reveal an important contribution of the 2'-OH to activity', *Nucleic Acids Res*, 31: 6536-42.

Dunkle, J. A., L. Xiong, A. S. Mankin, and J. H. Cate. 2010. 'Structures of the Escherichia coli ribosome with antibiotics bound near the peptidyl transferase center explain spectra of drug action', *Proc Natl Acad Sci U S A*, 107: 17152-7.

English, B. P., V. Hauryliuk, A. Sanamrad, S. Tankov, N. H. Dekker, and J. Elf. 2011. 'Single-molecule investigations of the stringent response machinery in living bacterial cells', *Proc Natl Acad Sci U S A*, 108: E365-73.

Falagas, M. E., and D. E. Karageorgopoulos. 2008. 'Pandrug resistance (PDR), extensive drug resistance (XDR), and multidrug resistance (MDR) among Gram-negative bacilli: need for international harmonization in terminology', *Clin Infect Dis*, 46: 1121-2; author reply 22.

Falagas, M. E., P. K. Koletsi, and I. A. Bliziotis. 2006. 'The diversity of definitions of multidrug-resistant (MDR) and pandrug-resistant (PDR) Acinetobacter baumannii and Pseudomonas aeruginosa', *J Med Microbiol*, 55: 1619-29.

Fei, J., P. Kosuri, D. D. MacDougall, and R. L. Gonzalez, Jr. 2008. 'Coupling of ribosomal L1 stalk and tRNA dynamics during translation elongation', *Mol Cell*, 30: 348-59.

Feng, B., C. S. Mandava, Q. Guo, J. Wang, W. Cao, N. Li, Y. Zhang, Y. Zhang, Z. Wang, J. Wu, S. Sanyal, J. Lei, and N. Gao. 2014. 'Structural and functional insights into the mode of action of a universally conserved Obg GTPase', *PLoS Biol*, 12: e1001866.

Fischer, N., A. L. Konevega, W. Wintermeyer, M. V. Rodnina, and H. Stark. 2010. 'Ribosome dynamics and tRNA movement by time-resolved electron cryomicroscopy', *Nature*, 466: 329-33.

Fischer, N., P. Neumann, A. L. Konevega, L. V. Bock, R. Ficner, M. V. Rodnina, and H. Stark. 2015. 'Structure of the E. coli ribosome-EF-Tu complex at <3 A resolution by C-corrected cryo-EM', *Nature*, 520: 567-70.

Fleming, A. 2001. 'On the antibacterial action of cultures of a penicillium, with special reference to their use in the isolation of B. influenzae. 1929', *Bull World Health Organ*, 79: 780-90.

Flygaard, R. K., N. Boegholm, M. Yusupov, and L. B. Jenner. 2018. 'Cryo-EM structure of the hibernating Thermus thermophilus 100S ribosome reveals a protein-mediated dimerization mechanism', *Nat Commun*, 9: 4179.

Frank, J., and R. K. Agrawal. 2000. 'A ratchet-like inter-subunit reorganization of the ribosome during translocation', *Nature*, 406: 318-22.

Franken, L. E., G. T. Oostergetel, T. Pijning, P. Puri, V. Arkhipova, E. J. Boekema, B. Poolman, and A. Guskov. 2017. 'A general mechanism of ribosome dimerization revealed by single-particle cryo-electron microscopy', *Nat Commun*, 8: 722.

Freistroffer, D.V., M.Y. Pavlov, J. MacDougall, R.H. Buckingham, and M. Ehrenberg. 1997. 'Release factor RF3 in *E. coli* accelerates the dissociation of release factors RF1 and RF2 from the ribosome in a GTP-dependent manner', *EMBO J.*, 16: 4126-33.

Frolova, LY, RY Tsivkovskii, GF Sivolobova, NY Oparina, OI Serpinski, VM Blinov, SI Tatkov, and LL Kisselev. 1999. 'Mutations in the highly conserved GGQ motif of class 1 polypeptide release factors abolish the ability of human eRF1 to trigger peptidyl-tRNA hydrolysis', *RNA*, 5: 1014-20.

Fu, Z., S. Kaledhonkar, A. Borg, M. Sun, B. Chen, R. A. Grassucci, M. Ehrenberg, and J. Frank. 2016. 'Key Intermediates in Ribosome Recycling Visualized by Time-Resolved Cryoelectron Microscopy', *Structure*, 24: 2092-101.

Gaca, A. O., J. K. Kajfasz, J. H. Miller, K. Liu, J. D. Wang, J. Abranches, and J. A. Lemos. 2013. 'Basal levels of (p)ppGpp in Enterococcus faecalis: the magic beyond the stringent response', *MBio*, 4: e00646-13.

Gao, H., Z. Zhou, U. Rawat, C. Huang, L. Bouakaz, C. Wang, Z. Cheng, Y. Liu, A. Zavialov, R. Gursky, S. Sanyal, M. Ehrenberg, J. Frank, and H. Song. 2007. 'RF3 induces ribosomal conformational changes responsible for dissociation of class I release factors', *Cell*, 129: 929-41.

Gao, Haixiao, Jayati Sengupta, Mikel Valle, Andrei Korostelev, Narayanan Eswar, Scott M. Stagg, Patrick van Roey, Rajendra K. Agrawal, Stephen C. Harvey, Andrej Sali, Michael S. Chapman, and Joachim Frank. 2003. 'Study of the structural dynamics of the *E. coli* 70S ribosome using real-space refinement', *Cell*, 113: **789–801**.

Gao, N., A. V. Zavialov, M. Ehrenberg, and J. Frank. 2007. 'Specific interaction between EF-G and RRF and its implication for GTP-dependent ribosome splitting into subunits', *J Mol Biol*, 374: 1345-58.

Gao, N., A. V. Zavialov, W. Li, J. Sengupta, M. Valle, R. P. Gursky, M. Ehrenberg, and J. Frank. 2005. 'Mechanism for the disassembly of the posttermination complex inferred from cryo-EM studies', *Mol. Cell*, 18: 663-74.

Gao, W., K. Chua, J. K. Davies, H. J. Newton, T. Seemann, P. F. Harrison, N. E. Holmes, H. W. Rhee, J. I. Hong, E. L. Hartland, T. P. Stinear, and B. P. Howden. 2010. 'Two novel point mutations in clinical Staphylococcus aureus reduce linezolid susceptibility and switch on the stringent response to promote persistent infection', *PLoS Pathog*, 6: e1000944.

Gao, Y. G., M. Selmer, C. M. Dunham, A. Weixlbaumer, A. C. Kelley, and V. Ramakrishnan. 2009. 'The structure of the ribosome with elongation factor G trapped in the posttranslocational state', *Science*, 326: 694-9.

Garrett, R A, and C Rodriguez-Fonseca. 1996. 'The peptidyl transferase center.' in R A Zimmermann and A E Dahlberg (eds.), *Ribosomal RNA - structure, evolution, processing and function in protein biosynthesis* (CRC Press: Boca Raton, FA).

Geiger, T., B. Kastle, F. L. Gratani, C. Goerke, and C. Wolz. 2014. 'Two small (p)ppGpp synthases in Staphylococcus aureus mediate tolerance against cell envelope stress conditions', *J Bacteriol*, 196: 894-902.

Goldstein, J L, and C T Caskey. 1970. 'Peptide chain termination: effect of protein S on ribosomal binding of RFs.', *Proc. Natl. Acad. Sci. USA*, 67: 537-?.

Graf, M., P. Huter, C. Maracci, M. Peterek, M. V. Rodnina, and D. N. Wilson. 2018. 'Visualization of translation termination intermediates trapped by the Apidaecin 137 peptide during RF3-mediated recycling of RF1', *Nat Commun*, 9: 3053.

Gromadski, K. B., and M. V. Rodnina. 2004. 'Kinetic determinants of high-fidelity tRNA discrimination on the ribosome', *Mol Cell*, 13: 191-200.

Guo, Z., and H. F. Noller. 2012. 'Rotation of the head of the 30S ribosomal subunit during mRNA translocation', *Proc Natl Acad Sci U S A*, 109: 20391-4.

Gutell, Robin R., Bryn Weiser, Carl R. Woese, and Harry F. Noller. 1985. 'Comparative anatomy of 16-S-like ribosomal RNA', *Prog. Nucleic Acid Res. Mol. Biol.*

Hansen, J. L., T. M. Schmeing, P. B. Moore, and T. A. Steitz. 2002. 'Structural insights into peptide bond formation', *Proc. Natl. Acad. Sci. USA*, 99: 11670-75.

Harms, J., F. Schluenzen, R. Zarivach, A. Bashan, S. Gat, I. Agmon, H. Bartels, F. Franceschi, and A. Yonath. 2001. 'High resolution structure of the large ribosomal subunit from a mesophilic eubacterium', *Cell*, 107: 679-88.

Haseltine, W. A., and R. Block. 1973. 'Synthesis of guanosine tetra- and pentaphosphate requires the presence of a codon-specific, uncharged transfer ribonucleic acid in the acceptor site of ribosomes', *Proc. Natl Acad. Sci. USA*, 70: 1564-68.

Haugen, S. P., W. Ross, and R. L. Gourse. 2008. 'Advances in bacterial promoter recognition and its control by factors that do not bind DNA', *Nat Rev Microbiol*, 6: 507-19.

Hauryliuk, V., G. C. Atkinson, K. S. Murakami, T. Tenson, and K. Gerdes. 2015. 'Recent functional insights into the role of (p)ppGpp in bacterial physiology', *Nat Rev Microbiol*, 13: 298-309.

Hecht, S. M., J. W. Kozarich, and F. J. Schmidt. 1974. 'Isomeric phenylalanyl-tRNAs. Position of the aminoacyl moiety during protein biosynthesis', *Proc Natl Acad Sci U S A*, 71: 4317-21.

Hede, K. 2014. 'Antibiotic resistance: An infectious arms race', *Nature*, 509: S2-3.

Hirashima, A., and A. Kaji. 1970. 'Factor dependent breakdown of polysomes.', *Biochem. Biophys. Res. Com.*, 41: 877-83.

Hirokawa, G, MC Kiel, A Muto, G Kawai, K Igarashi, H Kaji, and A Kaji. 2002. 'Binding of ribosome recycling factor to ribosomes, comparison with tRNA.', *J. Biol. Chem.*, 277: 35847-52.

Hirokawa, G., M. C. Kiel, A. Muto, M. Selmer, V. S. Raj, A. Liljas, K. Igarashi, H. Kaji, and A. Kaji. 2002. 'Post-termination complex disassembly by ribosome recycling factor, a functional tRNA mimic', *EMBO J.*, 21: 2272-81.

Hogg, T., U. Mechold, H. Malke, M. Cashel, and R. Hilgenfeld. 2004. 'Conformational antagonism between opposing active sites in a bifunctional RelA/SpoT homolog modulates (p)ppGpp metabolism during the stringent response', *Cell*, 117: 57-68.

Hui, Anna, and Boer Herman A. De. 1987. 'Specialized ribosome system: preferential translation of a single mRNA species by a subpopulation of mutated ribosomes in *Escherichia coli*', *Proc. Natl Acad. Sci. USA.*, 84: 4762-66.

Hussain, T., J. L. Llacer, B. T. Wimberly, J. S. Kieft, and V. Ramakrishnan. 2016. 'Large-Scale Movements of IF3 and tRNA during Bacterial Translation Initiation', *Cell*, 167: 133-44 e13.

Indrisiunaite, G., M. Y. Pavlov, V. Heurgue-Hamard, and M. Ehrenberg. 2015. 'On the pH dependence of class-1 RF-dependent termination of mRNA translation', *J Mol Biol*, 427: 1848-60.

Irving, S. E., and R. M. Corrigan. 2018. 'Triggering the stringent response: signals responsible for activating (p)ppGpp synthesis in bacteria', *Microbiology*, 164: 268-76.

Ito, K, T Fujiwara, T Toyoda, and Y Nakamura. 2002. 'Elongation factor G participates in ribosome disassembly by interacting with ribosome recycling factor at their tRNA-mimicry domains.', *Mol. Cell*, 9: 1263-72.

Ito, K., M. Uno, and Y. Nakamura. 1998. 'Single amino acid substitution in prokaryote polypeptide release factor 2 permits it to terminate translation at all three stop codons', *Proc Natl Acad Sci USA*, 95: 8165-9.

———. 2000. 'A tripeptide 'anticodon' deciphers stop codons in messenger RNA', *Nature*, 403: 680-84.

Izutsu, K., A. Wada, and C. Wada. 2001. 'Expression of ribosome modulation factor (RMF) in *Escherichia coli* requires ppGpp', *Genes Cells*, 6: 665-76.

Jacob, W. F., M. Santer, and A. E. Dahlberg. 1987. 'A single base change in the Shine-Dalgarno region of 16S rRNA of Escherichia coli affects translation of many proteins', *Proc Natl Acad Sci U S A*, 84: 4757-61.

Jacques, N., and M. Dreyfus. 1990. 'Translation Initiation in *Escherichia coli* - Old and New Questions', *Molecular Microbiology*, 4: 1063-67.

Janosi, L., I. Shimizu, and A. Kaji. 1994. 'Ribosome recycling factor (ribosome releasing factor) is essential for bacterial growth', *Proc. Natl Acad. Sci. USA*, 91: 4249-53.

Jin, H., A. C. Kelley, D. Loakes, and V. Ramakrishnan. 2010. 'Structure of the 70S ribosome bound to release factor 2 and a substrate analog provides insights into catalysis of peptide release', *Proc Natl Acad Sci U S A*, 107: 8593-98.

Jin, H., A. C. Kelley, and V. Ramakrishnan. 2011. 'Crystal structure of the hybrid state of ribosome in complex with the guanosine triphosphatase release factor 3', *Proc. Natl Acad. Sci. U S A*: Epub.

Jishage, M., K. Kvint, V. Shingler, and T. Nystrom. 2002. 'Regulation of sigma factor competition by the alarmone ppGpp', *Genes Dev*, 16: 1260-70.

Kasai, K., T. Nishizawa, K. Takahashi, T. Hosaka, H. Aoki, and K. Ochi. 2006. 'Physiological analysis of the stringent response elicited in an extreme thermophilic bacterium, Thermus thermophilus', *J Bacteriol*, 188: 7111-22.

Kato, T., H. Yoshida, T. Miyata, Y. Maki, A. Wada, and K. Namba. 2010. 'Structure of the 100S ribosome in the hibernation stage revealed by electron cryomicroscopy', *Structure*, 18: 719-24.

Katunin, V. I., A. Savelsberg, M. V. Rodnina, and W. Wintermeyer. 2002. 'Coupling of GTP hydrolysis by elongation factor G to translocation and factor recycling on the ribosome', *Biochemistry*, 41: 12806-12.

Kazemi, M., J. Socan, F. Himo, and J. Aqvist. 2018. 'Mechanistic alternatives for peptide bond formation on the ribosome', *Nucleic Acids Res*, 46: 5345-54.

Kerr, I. D. 2004. 'Sequence analysis of twin ATP binding cassette proteins involved in translational control, antibiotic resistance, and ribonuclease L inhibition', *Biochem Biophys Res Commun*, 315: 166-73.

Khusainov, I., Q. Vicens, R. Ayupov, K. Usachev, A. Myasnikov, A. Simonetti, S. Validov, B. Kieffer, G. Yusupova, M. Yusupov, and Y. Hashem. 2017. 'Structures and dynamics of hibernating ribosomes from Staphylococcus aureus mediated by intermolecular interactions of HPF', *EMBO J*, 36: 2073-87.

Kiel, MC, VS Raj, H Kaji, and A Kaji. 2003. 'Release of ribosome-bound ribosome recycling factor by elongation factor G.', *J. Biol. Chem.*, 278: 48041-50.

Kim, D. F., and R. Green. 1999. 'Base-pairing between 23S rRNA and tRNA in the ribosomal A site', *Mol Cell*, 4: 859-64.

Kim, K. K., K. Min, and S. W. Suh. 2000. 'Crystal structure of the ribosome recycling factor from *Escherichia coli*', *EMBO J.*, 19: 2362-70.

Kitani, T., K. Yoda, T. Ogawa, and T. Okazaki. 1985. 'Evidence that discontinuous DNA replication in Escherichia coli is primed by approximately 10 to 12 residues of RNA starting with a purine', *J Mol Biol*, 184: 45-52.

Klaholz, B. P., T. Pape, A. V. Zavialov, A. G. Myasnikov, E. V. Orlova, B. Vestergaard, M. Ehrenberg, and M. Van Heel. 2003. 'Structure of the Escherichia coli ribosomal termination complex with release factor 2', *Nature*, 421: 90-94.

Klaholz, BP, AG Myasnikov, and M Van Heel. 2004. 'Visualization of release factor 3 on the ribosome during termination of protein synthesis', *Nature*, 427: 862-65.

Klevens, R. M., M. A. Morrison, J. Nadle, S. Petit, K. Gershman, S. Ray, L. H. Harrison, R. Lynfield, G. Dumyati, J. M. Townes, A. S. Craig, E. R. Zell, G. E. Fosheim, L. K. McDougal, R. B. Carey, S. K. Fridkin, and Mrsa Investigators Active Bacterial Core surveillance. 2007. 'Invasive methicillin-resistant Staphylococcus aureus infections in the United States', *JAMA*, 298: 1763-71.

Kline, B. C., S. L. McKay, W. W. Tang, and D. A. Portnoy. 2015. 'The Listeria monocytogenes hibernation-promoting factor is required for the formation of 100S ribosomes, optimal fitness, and pathogenesis', *J Bacteriol*, 197: 581-91.

Kohanski, M. A., D. J. Dwyer, and J. J. Collins. 2010. 'How antibiotics kill bacteria: from targets to networks', *Nat Rev Microbiol*, 8: 423-35.

Kohler, R., R. A. Mooney, D. J. Mills, R. Landick, and P. Cramer. 2017. 'Architecture of a transcribing-translating expressome', *Science*, 356: 194-97.

Korostelev, A., H. Asahara, L. Lancaster, M. Laurberg, A. Hirschi, J. Zhu, S. Trakhanov, W. G. Scott, and H. F. Noller. 2008. 'Crystal structure of a translation termination complex formed with release factor RF2', *Proc Natl Acad Sci U S A*, 105: 19684-9.

Korostelev, Andrei, Jianyu Zhu, Haruichi Asahara, and Harry F. Noller. 2010. 'Recognition of the amber UAG stop codon by release factor RF1', *The EMBO journal*, 29: 2577-85.

Kothe, U., H. J. Wieden, D. Mohr, and M. V. Rodnina. 2004. 'Interaction of helix D of elongation factor Tu with helices 4 and 5 of protein L7/12 on the ribosome', *J Mol Biol*, 336: 1011-21.

Koutmou, K. S., M. E. McDonald, J. L. Brunelle, and R. Green. 2014. 'RF3:GTP promotes rapid dissociation of the class 1 termination factor', *RNA*, 20: 609-20.

Krasny, L., and R. L. Gourse. 2004. 'An alternative strategy for bacterial ribosome synthesis: Bacillus subtilis rRNA transcription regulation', *EMBO J*, 23: 4473-83.

Krasny, L., H. Tiserova, J. Jonak, D. Rejman, and H. Sanderova. 2008. 'The identity of the transcription +1 position is crucial for changes in gene expression in response to amino acid starvation in Bacillus subtilis', *Mol Microbiol*, 69: 42-54.

Kriel, A., A. N. Bittner, S. H. Kim, K. Liu, A. K. Tehranchi, W. Y. Zou, S. Rendon, R. Chen, B. P. Tu, and J. D. Wang. 2012. 'Direct regulation of GTP homeostasis by (p)ppGpp: a critical component of viability and stress resistance', *Mol Cell*, 48: 231-41.

Krokowski, D., F. Gaccioli, M. Majumder, M. R. Mullins, C. L. Yuan, B. Papadopoulou, W. C. Merrick, A. A. Komar, D. Taylor, and M. Hatzoglou. 2011. 'Characterization of hibernating ribosomes in mammalian cells', *Cell Cycle*, 10: 2691-702.

Kruger, M. K., S. Pedersen, T. G. Hagervall, and M. A. Sorensen. 1998. 'The modification of the wobble base of tRNAGlu modulates the translation rate of glutamic acid codons in vivo', *J Mol Biol*, 284: 621-31.

Kuhlenkoetter, S., W. Wintermeyer, and M. V. Rodnina. 2011. 'Different substrate-dependent transition states in the active site of the ribosome', *Nature*, 476: 351-4.

La Teana, A., C. O. Gualerzi, and A. E. Dahlberg. 2001. 'Initiation factor IF 2 binds to the alpha-sarcin loop and helix 89 of *Escherichia coli* 23S ribosomal RNA', *RNA*, 7: 1173-79.

Lancaster, L., M.C. Kiel, A. Kaji, and H.F. Noller. 2002. 'Orientation of ribosome recycling factor from directed hydroxyl radical probing', *Cell*, 111: 129-40.

Landick, R., J. Carey, and C. Yanofsky. 1985. 'Translation activates the paused transcription complex and restores transcription of the trp operon leader region', *Proc Natl Acad Sci U S A*, 82: 4663-7.

Laurberg, M., H. Asahara, A. Korostelev, J. Zhu, S. Trakhanov, and H. F. Noller. 2008. 'Structural basis for translation termination on the 70S ribosome', *Nature*, 454: 852-57.

Lenart, J., V. Vimberg, L. Vesela, J. Janata, and G. Balikova Novotna. 2015. 'Detailed mutational analysis of Vga(A) interdomain linker: implication for antibiotic resistance specificity and mechanism', *Antimicrob Agents Chemother*, 59: 1360-4.

Levy, S. B. 1992. 'Active efflux mechanisms for antimicrobial resistance', *Antimicrob Agents Chemother*, 36: 695-703.

Li, W., E. Bouveret, Y. Zhang, K. Liu, J. D. Wang, and J. C. Weisshaar. 2016. 'Effects of amino acid starvation on RelA diffusive behavior in live Escherichia coli', *Mol Microbiol*, 99: 571-85.

Liang, S. T., Y. C. Xu, P. Dennis, and H. Bremer. 2000. 'mRNA composition and control of bacterial gene expression', *J Bacteriol*, 182: 3037-44.

Lin, J., M. G. Gagnon, D. Bulkley, and T. A. Steitz. 2015. 'Conformational changes of elongation factor G on the ribosome during tRNA translocation', *Cell*, 160: 219-27.

Loveland, A. B., E. Bah, R. Madireddy, Y. Zhang, A. F. Brilot, N. Grigorieff, and A. A. Korostelev. 2016. 'Ribosome*RelA structures reveal the mechanism of stringent response activation', *Elife*, 5.

Loveland, A. B., G. Demo, N. Grigorieff, and A. A. Korostelev. 2017. 'Ensemble cryo-EM elucidates the mechanism of translation fidelity', *Nature*, 546: 113-17.

Magiorakos, A. P., A. Srinivasan, R. B. Carey, Y. Carmeli, M. E. Falagas, C. G. Giske, S. Harbarth, J. F. Hindler, G. Kahlmeter, B. Olsson-Liljequist, D. L. Paterson, L. B. Rice, J. Stelling, M. J. Struelens, A. Vatopoulos, J. T. Weber, and D. L. Monnet. 2012. 'Multidrug-resistant, extensively drug-resistant and pandrug-resistant bacteria: an international expert proposal for interim standard definitions for acquired resistance', *Clin Microbiol Infect*, 18: 268-81.

Magnusson, L. U., A. Farewell, and T. Nystrom. 2005. 'ppGpp: a global regulator in Escherichia coli', *Trends Microbiol*, 13: 236-42.

Maguire, B. A., A. D. Beniaminov, H. Ramu, A. S. Mankin, and R. A. Zimmermann. 2005. 'A protein component at the heart of an RNA machine: the importance of protein l27 for the function of the bacterial ribosome', *Mol Cell*, 20: 427-35.

Maki, Y., H. Yoshida, and A. Wada. 2000. 'Two proteins, YfiA and YhbH, associated with resting ribosomes in stationary phase *Escherichia coli*', *Genes Cells*, 5: 965-74.

Maracci, C., F. Peske, E. Dannies, C. Pohl, and M. V. Rodnina. 2014. 'Ribosome-induced tuning of GTP hydrolysis by a translational GTPase', *Proc Natl Acad Sci U S A*, 111: 14418-23.

Maracci, C., I. Wohlgemuth, and M. V. Rodnina. 2015. 'Activities of the peptidyl transferase center of ribosomes lacking protein L27', *RNA*, 21: 2047-52.

Matzov, D., S. Aibara, A. Basu, E. Zimmerman, A. Bashan, M. F. Yap, A. Amunts, and A. E. Yonath. 2017. 'The cryo-EM structure of hibernating 100S ribosome dimer from pathogenic Staphylococcus aureus', *Nat Commun*, 8: 723.

McLennan, A. G. 2013. 'Substrate ambiguity among the nudix hydrolases: biologically significant, evolutionary remnant, or both?', *Cell Mol Life Sci*, 70: 373-85.

Melnikov, S., A. Ben-Shem, N. Garreau de Loubresse, L. Jenner, G. Yusupova, and M. Yusupov. 2012. 'One core, two shells: bacterial and eukaryotic ribosomes', *Nat. Struct. Mol. Biol.*, 19: 560-67.

Mikuni, O., K. Ito, J. Moffat, K. Matsumura, K. McCaughan, T. Nobukuni, W. Tate, and Y. Nakamura. 1994. 'Identification of the *prfC* gene, which encodes peptide-chain-release factor 3 of *Escherichia coli*', *Proc. Natl Acad. Sci. USA*, 91: 5798-802.

Milon, P., C. Maracci, L. Filonava, C. O. Gualerzi, and M. V. Rodnina. 2012. 'Real-time assembly landscape of bacterial 30S translation initiation complex', *Nat Struct Mol Biol*, 19: 609-15.

Mitkevich, V. A., A. Ermakov, A. A. Kulikova, S. Tankov, V. Shyp, A. Soosaar, T. Tenson, A. A. Makarov, M. Ehrenberg, and V. Hauryliuk. 2010. 'Thermodynamic characterization of ppGpp binding to EF-G or IF2 and of initiator tRNA binding to free IF2 in the presence of GDP, GTP, or ppGpp', *J Mol Biol*, 402: 838-46.

Moazed, D., and H. F. Noller. 1989. 'Intermediate states in the movement of transfer RNA in the ribosome', *Nature*, 342: 142-48.

Moazed, D., R.R. Samaha, C. Gualerzi, and H.F. Noller. 1995. 'Specific protection of 16 S rRNA by translational initiation factors', *J. Mol. Biol.*, 248: 207-10.

Mohr, D., W. Wintermeyer, and M. V Rodnina. 2002. 'GTPase activation of elongation factors Tu and G on the ribosome', *Biochemistry*, 41: 12520-28.

Munro, J. B., R. B. Altman, N. O'Connor, and S. C. Blanchard. 2007. 'Identification of two distinct hybrid state intermediates on the ribosome', *Mol. Cell*, 25: 505-17.

Munro, J. B., R. B. Altman, C. S. Tung, K. Y. Sanbonmatsu, and S. C. Blanchard. 2010. 'A fast dynamic mode of the EF-G-bound ribosome', *EMBO J.*, 29: 770-81.

Nakagawa, S., Y. Niimura, K. Miura, and T. Gojobori. 2010. 'Dynamic evolution of translation initiation mechanisms in prokaryotes', *Proc Natl Acad Sci U S A*, 107: 6382-7.

Nakano, H., T. Yoshida, S. Uchiyama, M. Kawachi, H. Matsuo, T. Kato, A. Ohshima, Y. Yamaichi, T. Honda, H. Kato, Y. Yamagata, T. Ohkubo, and Y. Kobayashi. 2003. 'Structure and binding mode of a ribosome recycling factor (RRF) from mesophilic bacterium', *J. Biol. Chem.*, 278: 3427-36.

Nanamiya, H., K. Kasai, A. Nozawa, C. S. Yun, T. Narisawa, K. Murakami, Y. Natori, F. Kawamura, and Y. Tozawa. 2008. 'Identification and functional analysis of novel (p)ppGpp synthetase genes in Bacillus subtilis', *Mol Microbiol*, 67: 291-304.

Narlikar, G.J., and D. Herschlag. 1997. 'Mechanistic aspects of enzymatic catalysis: Lessons from comparison of RNA and protein enzymes', *Annu Rev Biochem*, 66: 19-59.

Nissen, P., J. Hansen, N. Ban, P. B. Moore, and T. A. Steitz. 2000. 'The structural basis of ribosome activity in peptide bond synthesis', *Science*, 289: 920-30.

Nissen, P., J. A. Ippolito, N. Ban, P. B. Moore, and T. A. Steitz. 2001. 'RNA tertiary interactions in the large ribosomal subunit: the A-minor motif', *Proc. Natl. Acad. Sci. USA*, 98: 4899-903.

Nissen, P., M. Kjeldgaard, S. Thirup, G. Polekhina, L. Reshetnikova, B. F. Clark, and J. Nyborg. 1995. 'Crystal structure of the ternary complex of Phe-tRNAPhe, EF-Tu, and a GTP analog', *Science*, 270: 1464-72.

Noller, H. F., M. M. Yusupov, G. Z. Yusupova, A. Baucom, and J. H. D Cate. 2002. 'Translocation of tRNA during protein synthesis', *FEBS Letter*, 514: 11-16.

Noller, H.F. 1991. 'Ribosomal RNA and Translation', *Annu. Rev. Biochem.*, 60: 191-227.

Noller, Harry F., and et al. 1981. 'Secondary structure model for 23S ribosmal RNA', *Nucleic Acids Res.*, 9: 6167-89.

Nystrom, T. 2004. 'Growth versus maintenance: a trade-off dictated by RNA polymerase availability and sigma factor competition?', *Mol Microbiol*, 54: 855-62.

Ogle, J. M., D. E. Brodersen, W. M. Clemons Jr, M. J. Tarry, A. P. Carter, and V. Ramakrishnan. 2001. 'Recognition of cognate transfer RNA by the 30S ribosomal subunit', *Science*, 292: 897-902.

Ogle, J. M., F. V. Murphy, M. J. Tarry, and V. Ramakrishnan. 2002. 'Selection of tRNA by the ribosome requires a transition from an open to a closed form', *Cell*, 111: 721-32.

Ooga, T., Y. Ohashi, S. Kuramitsu, Y. Koyama, M. Tomita, T. Soga, and R. Masui. 2009. 'Degradation of ppGpp by nudix pyrophosphatase modulates the transition of growth phase in the bacterium Thermus thermophilus', *J Biol Chem*, 284: 15549-56.

Ortiz, J. O., F. Brandt, V. R. Matias, L. Sennels, J. Rappsilber, S. H. Scheres, M. Eibauer, F. U. Hartl, and W. Baumeister. 2010. 'Structure of hibernating ribosomes studied by cryoelectron tomography in vitro and in situ', *J Cell Biol*, 190: 613-21.

Pallesen, J., Y. Hashem, G. Korkmaz, R. K. Koripella, C. Huang, M. Ehrenberg, S. Sanyal, and J. Frank. 2013. 'Cryo-EM visualization of the ribosome in termination complex with apo-RF3 and RF1', *Elife*, 2: e00411.

Pape, T., W. Wintermeyer, and M. Rodnina. 1999. 'Induced fit in initial selection and proofreading of aminoacyl-tRNA on the ribosome', *EMBO J*, 18: 3800-7.

Pedersen, Steen. 1984. 'Escherichia coli ribosomes translate in vivo with variable rate', *Embo J*, 3: 2895-8.

Peil, L., A. L. Starosta, J. Lassak, G. C. Atkinson, K. Virumae, M. Spitzer, T. Tenson, K. Jung, J. Remme, and D. N. Wilson. 2013. 'Distinct XPPX sequence motifs induce ribosome stalling, which is rescued by the translation elongation factor EF-P', *Proc Natl Acad Sci U S A*, 110: 15265-70.

Peschke, U., H. Schmidt, H. Z. Zhang, and W. Piepersberg. 1995. 'Molecular characterization of the lincomycin-production gene cluster of Streptomyces lincolnensis 78-11', *Mol Microbiol*, 16: 1137-56.

Peske, F., S. Kuhlenkoetter, M. V. Rodnina, and W. Wintermeyer. 2014. 'Timing of GTP binding and hydrolysis by translation termination factor RF3', *Nucleic Acids Res*, 42: 1812-20.

Petry, S, DE Brodersen, FV 4th Murphy, CM Dunham, M Selmer, MJ Tarry, AC Kelley, and V Ramakrishnan. 2005. 'Crystal structures of the ribosome in complex with release factors RF1 and RF2 bound to a cognate stop codon', *Cell*, 123: 1255-66.

Philippon, A., R. Labia, and G. Jacoby. 1989. 'Extended-spectrum beta-lactamases', *Antimicrob Agents Chemother*, 33: 1131-6.

Polacek, N., M. Gaynor, A. Yassin, and A. S. Mankin. 2001. 'Ribosomal peptidyl transferase can withstand mutations at the putative catalytic nucleotide', *Nature*, 411: 498-501.

Polikanov, Y. S., G. M. Blaha, and T. A. Steitz. 2012. 'How hibernation factors RMF, HPF, and YfiA turn off protein synthesis', *Science*, 336: 915-8.

Polikanov, Y. S., T. A. Steitz, and C. A. Innis. 2014. 'A proton wire to couple aminoacyl-tRNA accommodation and peptide-bond formation on the ribosome', *Nat Struct Mol Biol*, 21: 787-93.

Potrykus, K., and M. Cashel. 2008. '(p)ppGpp: still magical?', *Annu Rev Microbiol*, 62: 35-51.

Potrykus, K., H. Murphy, N. Philippe, and M. Cashel. 2011. 'ppGpp is the major source of growth rate control in E. coli', *Environ Microbiol*, 13: 563-75.

Prabhakar, A., M. C. Capece, A. Petrov, J. Choi, and J. D. Puglisi. 2017. 'Post-termination Ribosome Intermediate Acts as the Gateway to Ribosome Recycling', *Cell Rep*, 20: 161-72.

Primm, T. P., S. J. Andersen, V. Mizrahi, D. Avarbock, H. Rubin, and C. E. Barry, 3rd. 2000. 'The stringent response of Mycobacterium tuberculosis is required for long-term survival', *J Bacteriol*, 182: 4889-98.

Proshkin, S., A. R. Rahmouni, A. Mironov, and E. Nudler. 2010. 'Cooperation between translating ribosomes and RNA polymerase in transcription elongation', *Science*, 328: 504-8.

Prossliner, T., K. Skovbo Winther, M. A. Sorensen, and K. Gerdes. 2018. 'Ribosome Hibernation', *Annu Rev Genet*, 52: 321-48.

Puri, P., T. H. Eckhardt, L. E. Franken, F. Fusetti, M. C. Stuart, E. J. Boekema, O. P. Kuipers, J. Kok, and B. Poolman. 2014. 'Lactococcus lactis YfiA is necessary and sufficient for ribosome dimerization', *Mol Microbiol*, 91: 394-407.

Quiggle, K., G. Kumar, T. W. Ott, E. K. Ryu, and S. Chladek. 1981. 'Donor site of ribosomal peptidyltransferase: investigation of substrate specificity using 2'(3')-O-(N-acylaminoacyl)dinucleoside phosphates as models of the 3' terminus of N-acylaminoacyl transfer ribonucleic acid', *Biochemistry*, 20: 3480-85.

Ramakrishnan, V. 2002. 'Ribosome structure and the mechanism of translation', *Cell*, 108: 557-72.

Ramrath, D. J., L. Lancaster, T. Sprink, T. Mielke, J. Loerke, H. F. Noller, and C. M. Spahn. 2013. 'Visualization of two transfer RNAs trapped in transit during elongation factor G-mediated translocation', *Proc Natl Acad Sci U S A*, 110: 20964-9.

Ratje, A. H., J. Loerke, A. Mikolajka, M. Brunner, P. W. Hildebrand, A. L. Starosta, A. Donhofer, S. R. Connell, P. Fucini, T. Mielke, P. C. Whitford, J. N. Onuchic, Y. Yu, K. Y. Sanbonmatsu, R. K. Hartmann, P. A. Penczek, D. N. Wilson, and C. M. Spahn. 2010. 'Head swivel on the ribosome facilitates translocation by means of intra-subunit tRNA hybrid sites', *Nature*, 468: 713-16.

Rawat, U. B., A. V. Zavialov, J. Sengupta, M. Valle, R. A. Grassucci, J. Linde, B. Vestergaard, M. Ehrenberg, and J. Frank. 2003. 'A cryo-electron microscopic study of ribosome-bound termination factor RF2', *Nature*, 421: 87-90.

Rawat, U., H. Gao, A. Zavialov, R. Gursky, M. Ehrenberg, and J. Frank. 2006. 'Interactions of the release factor RF1 with the ribosome as revealed by cryo-EM', *J Mol Biol*, 357: 1144-53.

Ray, P. N., and M. L. Pearson. 1975. 'Functional inactivation of bacteriophage lambda morphogenetic gene in RNA', *Nature*, 253: 647-50.

Rheinberger, H-J, H Sternbach, and K H Nierhaus. 1981. 'Three tRNA binding sites on *Escherichia coli* ribosomes', *Proc. Natl. Acad. Sci. USA*, 78: 5310-14.

Richter, D. 1976. 'Stringent factor from *Escherichia coli* directs ribosomal binding and release of uncharged tRNA', *Proc. Natl Acad. Sci. USA*, 73: 707-11.

Rodnina, M. V. 2018. 'Translation in Prokaryotes', *Cold Spring Harb Perspect Biol*, 10.

Rodnina, M. V., M. Beringer, and W. Wintermeyer. 2007. 'How ribosomes make peptide bonds', *Trends Biochem Sci*, 32: 20-6.

Rodnina, M. V., N. Fischer, C. Maracci, and H. Stark. 2017. 'Ribosome dynamics during decoding', *Philos Trans R Soc Lond B Biol Sci*, 372.

Rodnina, M. V., A. Savelsbergh, V. I. Katunin, and W. Wintermeyer. 1997. 'Hydrolysis of GTP by elongation factor G drives tRNA movement on the ribosome', *Nature*, 385: 37-41.

Rodnina, M.V., T. Pape, R. Fricke, L. Kuhn, and W. Wintermeyer. 1996. 'Initial binding of the elongation factor Tu center dot GTP center dot aminoacyl-tRNA complex preceding codon recognition on the ribosome', *J Biol Chem*, 271: 646-52.

Ross, J. I., E. A. Eady, J. H. Cove, W. J. Cunliffe, S. Baumberg, and J. C. Wootton. 1990. 'Inducible erythromycin resistance in staphylococci is encoded by a member of the ATP-binding transport super-gene family', *Mol Microbiol*, 4: 1207-14.

Rowen, L., and A. Kornberg. 1978. 'Primase, the dnaG protein of Escherichia coli. An enzyme which starts DNA chains', *J Biol Chem*, 253: 758-64.

Rymer, R. U., F. A. Solorio, A. K. Tehranchi, C. Chu, J. E. Corn, J. L. Keck, J. D. Wang, and J. M. Berger. 2012. 'Binding mechanism of metalNTP substrates and stringent-response alarmones to bacterial DnaG-type primases', *Structure*, 20: 1478-89.

Saikrishnan, K, SK Kalapala, U Varshney, and M Vijayan. 2005. 'X-ray structural studies of Mycobacterium tuberculosis RRF and a comparative study of RRFs of known structure. Molecular plasticity and biological implications', *J. Mol. Biol.*, 345: 29-38.

Salsi, E., E. Farah, Z. Netter, J. Dann, and D. N. Ermolenko. 2015. 'Movement of elongation factor G between compact and extended conformations', *J Mol Biol*, 427: 454-67.

Samaha, R R, R Green, and H F Noller. 1995. 'A base pair between tRNA and 23S rRNA in the peptidyl transferase center of the ribosome', *Nature*, 377: 309-14.

Sanbonmatsu, K. Y., S. Joseph, and C. S. Tung. 2005. 'Simulating movement of tRNA into the ribosome during decoding', *Proc Natl Acad Sci U S A*, 102: 15854-9.

Santos, N., J. Zhu, J. P. Donohue, A. A. Korostelev, and H. F. Noller. 2013. 'Crystal structure of the 70S ribosome bound with the Q253P mutant form of release factor RF2', *Structure*, 21: 1258-63.

Savelsbergh, A., D. Mohr, B. Wilden, W. Wintermeyer, and M. V. Rodnina. 2000. 'Stimulation of the GTPase activity of translation elongation factor G by ribosomal protein L7/12', *J. Biol. Chem.*, 275: 890-94.

Savelsbergh, A., M. V. Rodnina, and W. Wintermeyer. 2009. 'Distinct functions of elongation factor G in ribosome recycling and translocation', *RNA*, 15: 772-80.

Schluenzen, F, A Tocilj, R Zarivach, J Harms, M Gluehmann, D Janell, A Bashan, H Bartels, Ilana Agmon, F Franceschi, and A Yonath. 2000. 'Structure of functionally activated small ribosomal subunit at 3.3 A resolution', *Cell*, 102: 615-23.

Schlünzen, F., R. Zarivach, J. Harms, A. Bashan, A. Tocilj, R. Albrecht, A. Yonath, and F. Franceschi. 2001. 'Structural basis for the interaction of antibiotics with the peptidyl transferase centre in eubacteria', *Nature*, 413: 814-21.

Schmeing, T. M., K. S. Huang, D. E. Kitchen, S. A. Strobel, and T. A. Steitz. 2005. 'Structural insights into the roles of water and the 2' hydroxyl of the P site tRNA in the peptidyl transferase reaction', *Mol. Cell*, 20: 437-48.

Schmeing, T. M., K. S. Huang, S. A. Strobel, and T. A. Steitz. 2005. 'An induced-fit mechanism to promote peptide bond formation and exclude hydrolysis of peptidyl-tRNA', *Nature*, 438: 520-24.

Schmeing, T. M., and V. Ramakrishnan. 2009. 'What recent ribosome structures have revealed about the mechanism of translation', *Nature*, 461: 1234-42.

Schmeing, T. M., A. C. Seila, J. L. Hansen, B. Freeborn, J. K. Soukup, S. A. Scaringe, S. A. Strobel, P. B. Moore, and T. A. Steitz. 2002. 'A pre-translocational intermediate in protein synthesis observed in crystals of enzymatically active 50S subunits', *Nat. Struct. Biol.*, 9: 225-30.

Schmeing, T. M., R. M. Voorhees, A. C. Kelley, Y. G. Gao, F. V. th Murphy, J. R. Weir, and V. Ramakrishnan. 2009. 'The crystal structure of the ribosome bound to EF-Tu and aminoacyl-tRNA', *Science*, 326: 688-94.

Schuwirth, BS, MA Borovinskaya, CW Hau, W Zhang, A Vila-Sanjurjo, JM Holton, and JH Cate. 2005. 'Structures of the bacterial ribosome at 3.5 Å resolution', *Science*, 310: 827-34.

Schwarz, S., J. Shen, K. Kadlec, Y. Wang, G. Brenner Michael, A. T. Fessler, and B. Vester. 2016. 'Lincosamides, Streptogramins, Phenicols, and Pleuromutilins: Mode of Action and Mechanisms of Resistance', *Cold Spring Harb Perspect Med*, 6.

Scolnick, E, R Tompkins, T Caskey, and M Nirenberg. 1968. 'Release factors differing in specificity for terminator codons', *Proc. Natl Acad. Sci. USA*, 61: 768-74.

Scott, M., C. W. Gunderson, E. M. Mateescu, Z. Zhang, and T. Hwa. 2010. 'Interdependence of cell growth and gene expression: origins and consequences', *Science*, 330: 1099-102.

Selmer, M, S Al-Karadaghi, G Hirakawa, A Kaji, and A Liljas. 1999. 'Crystal structure of *Thermotoga maritima* ribosome recycling factor: A tRNA mimic', *Science*, 286: 2349-52.

Selmer, M., CM Dunham, FV 4th Murphy, A Weixlbaumer, S Petry, AC Kelley, JR Weir, and V. Ramakrishnan. 2006. 'Structure of the 70S ribosome complexed with mRNA and tRNA', *Science*, 313: 1935-42.

Semenkov, Y., T. Shapkina, V. Makhno, and S. Kirillov. 1992. 'Puromycin Reaction for the A-Site-Bound Peptidyl-Transfer RNA', *FEBS Lett*, 296: 207-10.

Seo, H. S., M. Kiel, D. Pan, V. S. Raj, A. Kaji, and B. S. Cooperman. 2004. 'Kinetics and thermodynamics of RRF, EF-G, and thiostrepton interaction on the Escherichia coli ribosome', *Biochemistry*, 43: 12728-40.

Seyfzadeh, M., J. Keener, and M. Nomura. 1993. 'spoT-dependent accumulation of guanosine tetraphosphate in response to fatty acid starvation in Escherichia coli', *Proc Natl Acad Sci U S A*, 90: 11004-8.

Sharkey, L. K., T. A. Edwards, and A. J. O'Neill. 2016. 'ABC-F Proteins Mediate Antibiotic Resistance through Ribosomal Protection', *MBio*, 7.

Sharma, H., S. Adio, T. Senyushkina, R. Belardinelli, F. Peske, and M. V. Rodnina. 2016. 'Kinetics of Spontaneous and EF-G-Accelerated Rotation of Ribosomal Subunits', *Cell Rep*, 16: 2187-96.

Sharma, M. R., A. Donhofer, C. Barat, V. Marquez, P. P. Datta, P. Fucini, D. N. Wilson, and R. K. Agrawal. 2010. 'PSRP1 is not a ribosomal protein, but a ribosome-binding factor that is recycled by the ribosome-recycling factor (RRF) and elongation factor G (EF-G)', *J Biol Chem*, 285: 4006-14.

Sharma, M. R., D. N. Wilson, P. P. Datta, C. Barat, F. Schluenzen, P. Fucini, and R. K. Agrawal. 2007. 'Cryo-EM study of the spinach chloroplast ribosome reveals the structural and functional roles of plastid-specific ribosomal proteins', *Proc Natl Acad Sci U S A*, 104: 19315-20.

Sharma, P. K., Y. Xiang, M. Kato, and A. Warshel. 2005. 'What are the roles of substrate-assisted catalysis and proximity effects in peptide bond formation by the ribosome?', *Biochemistry*, 44: 11307-14.

Shaw, J. J., and R. Green. 2007. 'Two distinct components of release factor function uncovered by nucleophile partitioning analysis', *Mol Cell*, 28: 458-67.

Shcherbakova, K., H. Nakayama, and N. Shimamoto. 2015. 'Role of 100S ribosomes in bacterial decay period', *Genes Cells*, 20: 789-801.

Shimada, T., H. Yoshida, and A. Ishihama. 2013. 'Involvement of cyclic AMP receptor protein in regulation of the rmf gene encoding the ribosome modulation factor in Escherichia coli', *J Bacteriol*, 195: 2212-9.

Shine, J., and L . Dalgarno. 1974. 'The 3'-terminal sequence of *E. coli* 16S rRNA: Complementarity to nonsense triplets and ribosome binding sites.', *Proc. Natl Acad. Sci. USA*, 71: 1342-46.

Sievers, A., M. Beringer, M. V. Rodnina, and R. Wolfenden. 2004. 'The ribosome as an entropy trap', *Proc. Natl. Acad. Sci. U S A*, 101: 7897-901.

Simonetti, A., S. Marzi, A. G. Myasnikov, A. Fabbretti, M. Yusupov, C. O. Gualerzi, and B. P. Klaholz. 2008. 'Structure of the 30S translation initiation complex', *Nature*, 455: 416-20.

Singal, B., A. M. Balakrishna, W. Nartey, M. S. S. Manimekalai, J. Jeyakanthan, and G. Gruber. 2017. 'Crystallographic and solution structure of the N-terminal domain of the Rel protein from Mycobacterium tuberculosis', *FEBS Lett*, 591: 2323-37.

Spirin, A. S. 1969. 'A model of the functioning ribosome: locking and unlocking of the ribosome subparticles', *Cold Spring Harb Symp Quant Biol*, 34: 197-207.

Sprink, T., D. J. Ramrath, H. Yamamoto, K. Yamamoto, J. Loerke, J. Ismer, P. W. Hildebrand, P. Scheerer, J. Burger, T. Mielke, and C. M. Spahn. 2016. 'Structures of ribosome-bound initiation factor 2 reveal the mechanism of subunit association', *Sci Adv*, 2: e1501502.

Srivatsan, A., and J. D. Wang. 2008. 'Control of bacterial transcription, translation and replication by (p)ppGpp', *Curr Opin Microbiol*, 11: 100-5.

Stark, H., M. V. Rodnina, J. Rinkeappel, R. Brimacombe, W. Wintermeyer, and M. Vanheel. 1997. 'Visualization of Elongation Factor Tu On the Escherichia Coli Ribosome', *Nature.*, 389: 403-06.

Starosta, A. L., J. Lassak, K. Jung, and D. N. Wilson. 2014. 'The bacterial translation stress response', *FEMS Microbiol Rev*, 38: 1172-201.

Steinchen, Wieland, and Gert Bange. 2016. 'The magic dance of the alarmones (p)ppGpp', *Molecular microbiology*, 101: 531-44.

Stringer, E. A., P. Sarkar, and U. Maitra. 1977. 'Function of initiation factor 1 in the binding and release of initiation factor 2 from ribosomal initiation complexes in Escherichia coli', *J Biol Chem*, 252: 1739-44.

Su, W., V. Kumar, Y. Ding, R. Ero, A. Serra, B. S. T. Lee, A. S. W. Wong, J. Shi, S. K. Sze, L. Yang, and Y. G. Gao. 2018. 'Ribosome protection by antibiotic resistance ATP-binding cassette protein', *Proc Natl Acad Sci U S A*, 115: 5157-62.

Subramanian, A. R., B. D. Davis, and R. J. Beller. 1969. 'The ribosome dissociation factor and the ribosome-polysome cycle', *Cold Spring Harb Symp Quant Biol*, 34: 223-30.

Subramanian, A. R., E. Z. Ron, and B. D. Davis. 1968. 'A factor required for ribosome dissociation in Escherichia coli', *Proc Natl Acad Sci U S A*, 61: 761-7.

Subramanian, AR, and BD Davis. 1973. 'Release of 70 S ribosomes from polysomes in *Escherichia coli*.', *J. Mol. Biol.*, 74: 45-56.

Sun, D., G. Lee, J. H. Lee, H. Y. Kim, H. W. Rhee, S. Y. Park, K. J. Kim, Y. Kim, B. Y. Kim, J. I. Hong, C. Park, H. E. Choy, J. H. Kim, Y. H. Jeon, and J. Chung. 2010. 'A metazoan ortholog of SpoT hydrolyzes ppGpp and functions in starvation responses', *Nat Struct Mol Biol*, 17: 1188-94.

Tagami, K., H. Nanamiya, Y. Kazo, M. Maehashi, S. Suzuki, E. Namba, M. Hoshiya, R. Hanai, Y. Tozawa, T. Morimoto, N. Ogasawara, Y. Kageyama, K. Ara, K. Ozaki, M. Yoshida, H. Kuroiwa, T. Kuroiwa, Y. Ohashi, and F. Kawamura. 2012. 'Expression of a small (p)ppGpp synthetase, YwaC, in the (p)ppGpp(0) mutant of Bacillus subtilis triggers YvyD-dependent dimerization of ribosome', *Microbiologyopen*, 1: 115-34.

Thompson, J., D. F. Kim, M. O'Connor, K. R. Lieberman, M. A. Bayfield, S. T. Gregory, R. Green, H. F. Noller, and A. E. Dahlberg. 2001. 'Analysis of mutations at residues A2451 and G2447 of 23S rRNA in the peptidyltransferase active site of the 50S ribosomal subunit', *Proc. Natl Acad. Sci. USA*, 98: 9002-07.

Tissières, A, JD Watson, D Schlessinger, and BR Hollingworth. 1959. 'Ribonucleoprotein particles from *Escherichia coli*', *J. Mol. Biol.*, 1: 221-33.

Tourigny, D. S., I. S. Fernandez, A. C. Kelley, and V. Ramakrishnan. 2013. 'Elongation factor G bound to the ribosome in an intermediate state of translocation', *Science*, 340: 1235490.

Toyoda, T., O. F. Tin, K. Ito, T. Fujiwara, T. Kumasaka, M. Yamamoto, M. B. Garber, and Y. Nakamura. 2000. 'Crystal structure combined with genetic analysis of the *Thermus thermophilus* ribosome recycling factor shows that a flexible hinge may act as a functional switch', *RNA*, 6: 1432-44.

Trobro, S., and J. Aqvist. 2009. 'Mechanism of the translation termination reaction on the ribosome', *Biochemistry*, 48: 11296-303.

Ueta, M., R. L. Ohniwa, H. Yoshida, Y. Maki, C. Wada, and A. Wada. 2008. 'Role of HPF (hibernation promoting factor) in translational activity in Escherichia coli', *J Biochem*, 143: 425-33.

Ueta, M., C. Wada, T. Daifuku, Y. Sako, Y. Bessho, A. Kitamura, R. L. Ohniwa, K. Morikawa, H. Yoshida, T. Kato, T. Miyata, K. Namba, and A. Wada. 2013. 'Conservation of two distinct types of 100S ribosome in bacteria', *Genes Cells*, 18: 554-74.

Ueta, M., C. Wada, and A. Wada. 2010. 'Formation of 100S ribosomes in Staphylococcus aureus by the hibernation promoting factor homolog SaHPF', *Genes Cells*, 15: 43-58.

Ueta, M., A. Yoshida, C. Wada, T. Baba, H. Mori, and A. Wada. 2005. 'Ribosome binding proteins YhbH and YfiA have opposite functions during 100S formation in the stationary phase of *Escherichia coli*', *Genes Cells*, 10: 1103-12.

Valle, M., J. Sengupta, N. K. Swami, R. A. Grassucci, N. Burkhardt, K. H. Nierhaus, R. K. Agrawal, and J. Frank. 2002. 'Cryo-EM reveals an active role for aminoacyl-tRNA in the accommodation process', *EMBO J.*, 21: 3557-67.

Valle, M., A. Zavialov, J. Sengupta, U. Rawat, M. Ehrenberg, and J. Frank. 2003. 'Locking and unlocking of ribosomal motions', *Cell*, 114: 123-34.

Vestergaard, B, LB Van, GR Andersen, J Nyborg, RH Buckingham, and M Kjeldgaard. 2001. 'Bacterial polypeptide release factor RF2 is structurally distinct from eukaryotic eRF1', *Mol. Cell*, 8: 1375-82.

Vinella, D., C. Albrecht, M. Cashel, and R. D'Ari. 2005. 'Iron limitation induces SpoT-dependent accumulation of ppGpp in Escherichia coli', *Mol Microbiol*, 56: 958-70.

Voorhees, R. M., and V. Ramakrishnan. 2013. 'Structural basis of the translational elongation cycle', *Annu. Rev. Biochem.*, 82: 203-36.

Voorhees, R. M., T. M. Schmeing, A. C. Kelley, and V. Ramakrishnan. 2010. 'The mechanism for activation of GTP hydrolysis on the ribosome', *Science*, 330: 835-38.

Voorhees, R. M., A. Weixlbaumer, D. Loakes, A. C. Kelley, and V. Ramakrishnan. 2009. 'Insights into substrate stabilization from snapshots of the peptidyl transferase center of the intact 70S ribosome', *Nat Struct Mol Biol*, 16: 528-33.

Wada, A., K. Igarashi, S. Yoshimura, S. Aimoto, and A. Ishihama. 1995. 'Ribosome modulation factor: Stationary growth phase-specific inhibitor of ribosome functions from *Escherichia coli*', *Biochem. Biophys. Res. Commun.*, 214: 410-17.

Wada, A., Y. Yamazaki, N. Fujita, and A. Ishihama. 1990. 'Structure and probable genetic location of a ribosome modulation factor associated with 100S ribosomes in stationary-phase *Escherichia coli* cells', *Proc. Natl Acad. Sci. U S A*, 87: 2657-61.

Wallin, G., and J. Aqvist. 2010. 'The transition state for peptide bond formation reveals the ribosome as a water trap', *Proc Natl Acad Sci U S A*, 107: 1888-93.

Wallin, G., S. C. Kamerlin, and J. Aqvist. 2013. 'Energetics of activation of GTP hydrolysis on the ribosome', *Nat Commun*, 4: 1733.

Wasserman, M. R., J. L. Alejo, R. B. Altman, and S. C. Blanchard. 2016. 'Multiperspective smFRET reveals rate-determining late intermediates of ribosomal translocation', *Nat Struct Mol Biol*, 23: 333-41.

Weinger, J. S., K. M. Parnell, S. Dorner, R. Green, and S. A. Strobel. 2004. 'Substrate-assisted catalysis of peptide bond formation by the ribosome', *Nat. Struct. Mol. Biol.*, 11: 1101-06.

Weiss, R. B., J. P. Murphy, and J. A. Gallant. 1984. 'Genetic screen for cloned release factor genes', *J Bacteriol*, 158: 362-4.

Weixlbaumer, A, H Jin, C Neubauer, RM Voorhees, S Petry, AC Kelley, and V Ramakrishnan. 2008. 'Insights into translational termination from the structure of RF2 bound to the ribosome', *Science*, 322: 953-6.

Wendrich, T. M., G. Blaha, D. N. Wilson, M. A. Marahiel, and K. H. Nierhaus. 2002. 'Dissection of the mechanism for the stringent factor RelA', *Mol. Cell*, 10: 779-88.

Wexselblatt, E., I. Kaspy, G. Glaser, J. Katzhendler, and E. Yavin. 2013. 'Design, synthesis and structure-activity relationship of novel Relacin analogs as inhibitors of Rel proteins', *Eur J Med Chem*, 70: 497-504.

Wexselblatt, E., Y. Oppenheimer-Shaanan, I. Kaspy, N. London, O. Schueler-Furman, E. Yavin, G. Glaser, J. Katzhendler, and S. Ben-Yehuda. 2012. 'Relacin, a novel antibacterial agent targeting the Stringent Response', *PLoS Pathog*, 8: e1002925.

Williamson, J. R. 2009. 'The ribosome at atomic resolution', *Cell*, 139: 1041-3.

Wilson, D. N., F. Schluenzen, J. M. Harms, T. Yoshida, T. Ohkubo, R. Albrecht, J. Buerger, Y. Kobayashi, and P. Fucini. 2005. 'X-ray crystallography study on ribosome recycling: the mechanism of binding and action of RRF on the 50S ribosomal subunit', *EMBO J.*, 24: 251-60.

Wilson, K. S., and H. F. Noller. 1998. 'Mapping the position of translational elongation factor EF-G in the ribosome by directed hydroxyl radical probing', *Cell*, 92: 131-9.

Wimberly, B. T., D. E. Brodersen, W. M. Clemons, R. J. Morgan-Warren, A. P. Carter, C. Vonrhein, T. Hartsch, and V. Ramakrishnan. 2000. 'Structure of the 30S ribosomal subunit', *Nature*, 407: 327-39.

Winther, K. S., M. Roghanian, and K. Gerdes. 2018. 'Activation of the Stringent Response by Loading of RelA-tRNA Complexes at the Ribosomal A-Site', *Mol Cell*, 70: 95-105 e4.

Wohlgemuth, I., M. Beringer, and M. V. Rodnina. 2006. 'Rapid peptide bond formation on isolated 50S ribosomal subunits', *EMBO Rep*, 7: 699-703.

Wool, I.G., A. Gluck, and Y. Endo. 1992. 'Ribotoxin Recognition of Ribosomal RNA and a Proposal for the Mechanism of Translocation', *Trends Biochem Sci*, 17: 266-69.

Woolstenhulme, C. J., S. Parajuli, D. W. Healey, D. P. Valverde, E. N. Petersen, A. L. Starosta, N. R. Guydosh, W. E. Johnson, D. N. Wilson, and A. R. Buskirk. 2013. 'Nascent peptides that block protein synthesis in bacteria', *Proc Natl Acad Sci U S A*, 110: E878-87.

Xiao, H., M. Kalman, K. Ikehara, S. Zemel, G. Glaser, and M. Cashel. 1991. 'Residual guanosine 3',5'-bispyrophosphate synthetic activity of relA null mutants can be eliminated by spoT null mutations', *J. Biol. Chem.*, 266: 5980-90.

Yang, X., and EE Ishiguro. 2001. 'Involvement of the N terminus of ribosomal protein L11 in regulation of the RelA protein of *Escherichia coli*', *J. Bacteriol.*, 183: 6532-37.

Yoshida, H, Y Maki, H Kato, H Fujisawa, K Izutsu, C Wada, and A Wada. 2002. 'The ribosome modulation factor (RMF) binding site on the 100S ribosome of *Escherichia coli*', *J. Biochem. (Tokyo)*, 132: 983-89.

Yoshida, H., and A. Wada. 2014. 'The 100S ribosome: ribosomal hibernation induced by stress', *Wiley Interdiscip Rev RNA*, 5: 723-32.

Yoshida, T, S Oka, S Uchiyama, H Nakano, T Kawasaki, T Ohkubo, and Y Kobayashi. 2003. 'Characteristic domain motion in the ribosome recycling factor revealed by 15N NMR relaxation experiments and molecular dynamics simulations.', *Biochemistry*, 42: 4101-07.

Yoshida, T., S. Uchiyama, H. Nakano, H. Kashimori, H. Kijima, T. Ohshima, Y. Saihara, T. Ishino, H. Shimahara, K. Yokose, T. Ohkubo, A. Kaji, and Y. Kobayashi. 2001. 'Solution structure of the ribosome recycling factor from Aquifex aeolicus', *Biochemistry*, 40: 2387-96.

Youngman, E. M., J. L. Brunelle, A. B. Kochaniak, and R. Green. 2004. 'The active site of the ribosome is composed of two layers of conserved nucleotides with distinct roles in peptide bond formation and peptide release', *Cell*, 117: 589-99.

Yusupova, G. Z., M. M. Yusupov, J. H. Cate, and H. F. Noller. 2001. 'The path of messenger RNA through the ribosome', *Cell*, 106: 233-41.

Zavialov, A. V., R. H. Buckingham, and M. Ehrenberg. 2001. 'A posttermination ribosomal complex is the guanine nucleotide exchange factor for peptide release factor RF3', *Cell*, 107: 115-24.

Zavialov, A. V., L. Mora, R. H. Buckingham, and M. Ehrenberg. 2002. 'Release of peptide promoted by the GGQ motif of class 1 release factors regulates the GTPase activity of RF3', *Mol. Cell*, 10: 789-98.

Zhou, J., L. Lancaster, J. P. Donohue, and H. F. Noller. 2014. 'How the ribosome hands the A-site tRNA to the P site during EF-G-catalyzed translocation', *Science*, 345: 1188-91.

Zhou, Y. N., and D. J. Jin. 1998. 'The rpoB mutants destabilizing initiation complexes at stringently controlled promoters behave like "stringent" RNA polymerases in Escherichia coli', *Proc Natl Acad Sci U S A*, 95: 2908-13.

Zhouravleva, G., L. Frolova, X. Legoff, R. Leguellec, S. Ingevechtomov, L. Kisselev, and M. Philippe. 1995. 'Termination of translation in eukaryotes is governed by two interacting polypeptide chain release factors, eRF1 and eRF3', *EMBO J.*, 14: 4065-72.

Zoldak, G., L. Redecke, D. I. Svergun, P. V. Konarev, C. S. Voertler, H. Dobbek, E. Sedlak, and M. Sprinzl. 2007. 'Release Factors 2 from Escherichia coli and Thermus thermophilus: structural, spectroscopic and microcalorimetric studies', *Nucleic Acids Res*.

Zucker, Frank H., and John W. B. Hershey. 1986. 'Binding of Escherichia coli protein synthesis initiation factor IF1 to 30S ribosomal subunits measured by fluorescence polarization', *Biochemistry*, 25: 3682-90.

6. Publications

2018

1. Caillan Crowe-McAuliffe, Michael Graf, Paul Huter, Hiraku Takada, **Maha Abdelshahid**, Jiří Novacek, Victoriia Murina, Gemma C. Atkinson, Vasili Hauryliuk, and Daniel N. Wilson. 2018. Structural basis for antibiotic resistance mediated by the *Bacillus subtilis* ABCF ATPase VmlR.

   Proc Natl Acad Sci U S A**,** 115: 8978-83.

2. Patrick Pausch, **Maha Abdelshahid**, Wieland Steinchen, Heinrich Schäfer, Fabio Lino Gratani, Sven-Andreas Freibert, Christiane Wolz, Kürşad Turgay, Daniel N. Wilson and Gert Bange. Stringent response control by bifunctional RelA enzyme in the presence and absence of the ribosome.

   Manuscript ready for submission

2017

3. Bertrand Beckert*, **Maha Abdelshahid***, Heinrich Schafer, WIeland Steinchen, Stefan Arenz, Otto Berninghausen, Roland Beckmann, Gert Bange, Kürşad Turgay, and Daniel N. Wilson. 2017. Structure of the *Bacillus subtilis* hibernating 100S ribosome reveals the basis for 70S dimerization.

   EMBO J**,** 36: 2061-72.

2016

4. Stefan Arenz*, **Maha Abdelshahid***, Daniel Sohmen*, Roshani Payoe, Agata L. Starosta, Otto Berninghausen, Vasili Hauryliuk, Roland Beckmann, and Daniel N. Wilson. 2016. The stringent factor RelA adopts an open conformation on the ribosome to stimulate ppGpp synthesis.

   Nucleic Acids Res**,** 44: 6471-81.

* These authors contributed equally to this work

Structural basis for antibiotic resistance mediated by the *Bacillus subtilis* ABCF ATPase VmlR

Caillan Crowe-McAuliffe[a], Michael Graf[a], Paul Huter[a], Hiraku Takada[b,c], Maha Abdelshahid[a], Jiří Nováček[d], Victoriia Murina[b], Gemma C. Atkinson[b], Vasili Hauryliuk (Василий Гаврилюк)[b,c,e], and Daniel N. Wilson[a,1]

[a]Institute for Biochemistry and Molecular Biology, University of Hamburg, 20146 Hamburg, Germany; [b]Department of Molecular Biology, Umeå University, 90187 Umeå, Sweden; [c]Laboratory for Molecular Infection Medicine Sweden, Umeå University, 90187 Umeå, Sweden; [d]Central European Institute of Technology, Masaryk University, 62500 Brno, Czech Republic; and [e]Institute of Technology, University of Tartu, 50411 Tartu, Estonia

Edited by Peter B. Moore, Yale University, New Haven, CT, and approved July 23, 2018 (received for review May 17, 2018)

Many Gram-positive pathogenic bacteria employ ribosomal protection proteins (RPPs) to confer resistance to clinically important antibiotics. In *Bacillus subtilis*, the RPP VmlR confers resistance to lincomycin (Lnc) and the streptogramin A (S_A) antibiotic virginiamycin M (VgM). VmlR is an ATP-binding cassette (ABC) protein of the F type, which, like other antibiotic resistance (ARE) ABCF proteins, is thought to bind to antibiotic-stalled ribosomes and promote dissociation of the drug from its binding site. To investigate the molecular mechanism by which VmlR confers antibiotic resistance, we have determined a cryo-electron microscopy (cryo-EM) structure of an ATPase-deficient *B. subtilis* VmlR-EQ_2 mutant in complex with a *B. subtilis* ErmDL-stalled ribosomal complex (SRC). The structure reveals that VmlR binds within the E site of the ribosome, with the antibiotic resistance domain (ARD) reaching into the peptidyltransferase center (PTC) of the ribosome and a C-terminal extension (CTE) making contact with the small subunit (SSU). To access the PTC, VmlR induces a conformational change in the P-site tRNA, shifting the acceptor arm out of the PTC and relocating the CCA end of the P-site tRNA toward the A site. Together with microbiological analyses, our study indicates that VmlR allosterically dissociates the drug from its ribosomal binding site and exhibits specificity to dislodge VgM, Lnc, and the pleuromutilin tiamulin (Tia), but not chloramphenicol (Cam), linezolid (Lnz), nor the macrolide erythromycin (Ery).

ABC ATPase | cryo-EM | ribosome | antibiotic resistance | VmlR

The ribosome is one of the major targets in the cell for antibiotics, including many clinically important antibiotic classes, for example the streptogramins, lincosamides, pleuromutilins, and macrolides (reviewed in refs. 1 and 2). However, the ever-increasing emergence of multidrug resistant bacteria is rendering our current antibiotic arsenal obsolete. Therefore, it is important to understand the mechanisms that bacteria employ to obtain antibiotic resistance to develop improved antimicrobial agents to overcome these mechanisms. Two important antibiotic resistance strategies employed by bacteria include antibiotic efflux and ribosome protection, both of which can be mediated by members of the large family of ATP-binding cassette (ABC) proteins. ABC proteins involved in drug efflux include membrane-bound transporters that use energy to pump the antibiotic out of the cell. By contrast, ABC proteins of the subclass F (ABCF) do not contain transmembrane domains to anchor them to the membrane and instead confer resistance by binding to the ribosome and chasing the antibiotic from its binding site (reviewed in ref. 3).

Antibiotic resistance (ARE) ABCF proteins are widespread in Gram-positive bacteria but also found in some Gram-negative bacteria (3, 4). ARE-ABCF proteins can be chromosomally and/or plasmid-encoded and are found in many clinically relevant pathogenic bacteria, including *Staphylococcus aureus*, *Enterococcus faecalis*, *Listeria monocytogenes*, and *Escherichia coli* (3, 4). To date, all ARE-ABCF proteins confer resistance to antibiotics that bind to the large ribosomal subunit (LSU), either at the peptidyl-transferase center (PTC) or adjacent to the PTC in the ribosomal exit tunnel. ARE-ABCF proteins can be divided into distinct classes on the basis of their resistance profiles (3, 4). For example, the Vga/Lsa/Sal/Vml class confers resistance to streptogramin A (S_A) antibiotics, lincosamides, and sometimes pleuromutilins, whereas the Msr class confers resistance to streptogramin B (S_B) antibiotics, macrolides, and sometimes ketolides. In *Enterococci*, the ARE-ABCF OptrA has been reported to confer resistance to oxazolidinones and chloramphenicols (5). Several studies have demonstrated that ARE-ABCFs are RPPs that confer resistance by displacing the drug from its binding site on the ribosome (6, 7), analogous to the displacement of tetracycline from the ribosome mediated by the RPPs TetM/TetO (8).

ARE-ABCF proteins comprise two ABC nucleotide-binding domains (NBD1 and NBD2) that are separated by a helical linker and, depending on the species, may have an additional "Arm" subdomain inserted within NBD1 as well as a C-terminal extension (CTE) (4). The ATPase activity of ARE-ABCF proteins is essential for their function since mutations of the catalytic glutamate in NBD1 or NBD2 lead to a loss of the ability of VgaA to confer resistance to VgM (6, 9). Consistently, the inhibition of ribosomal transpeptidation (transfer of fMet from the P-site tRNA to puromycin) that results from the presence of Lnc

Significance

The recent increase in multidrug-resistant pathogenic bacteria is limiting the utility of our current arsenal of clinically important antibiotics. The development of improved antibiotics would therefore benefit from a better understanding of the current resistance mechanisms employed by bacteria. Many Gram-positive bacteria, including pathogenic *Staphylococcus aureus* and *Enterococcus faecalis*, utilize ribosome protection proteins to confer resistance to medically relevant antibiotics, such as streptogramins A, lincosamides, and pleuromutilins. We have employed cryo-electron microscopy to reveal the structural basis for how the *Bacillus subtilis* VmlR protein binds to the ribosome to confer resistance to the streptogramin A antibiotic virginiamycin M, the lincosamide lincomycin, and the pleuromutilin tiamulin.

Author contributions: G.C.A., V.H., and D.N.W. designed research; C.C.-M., H.T., J.N., and G.C.A. performed research; M.A. and V.M. contributed new reagents/analytic tools; C.C.-M., M.G., P.H., H.T., V.H., and D.N.W. analyzed data; and C.C.-M. and D.N.W. wrote the paper.

The authors declare no conflict of interest.

This article is a PNAS Direct Submission.

Data deposition: The atomic coordinates have been deposited in the Protein Data Bank, www.wwpdb.org (PDB ID codes 6HA1 and 6HA8). The cryo-EM maps have been deposited in the Electron Microscopy Data Bank (EMDB ID codes EMD-0176 and EMD-0177).

[1]To whom correspondence should be addressed. Email: daniel.wilson@chemie.uni-hamburg.de.

This article contains supporting information online at www.pnas.org/lookup/suppl/doi:10.1073/pnas.1808535115/-/DCSupplemental.

Published online August 20, 2018.

is relieved by VgaA, but not the catalytically inactive VgaA-EQ_2 mutant (4). Similarly, transpeptidation was restored by VgaA in the presence of ATP, but not ADP or nonhydrolysable ATP analogs (4).

ARE-ABCFs are closely related to energy-dependent translational throttle A (EttA), an ABCF protein that binds within the ribosomal E site to regulate translation in response to energy levels in the cell (10, 11). A recent cryo-electron microscopy (cryo-EM) structure of the *Pseudomonas aeruginosa* ARE-ABCF MsrE bound to the *Thermus thermophilus* 70S ribosome revealed that MsrE, like EttA, binds in the E site and has an extended interdomain linker that reaches toward the PTC of the ribosome (7). Large variations in sequence and length are observed within the interdomain linker between different classes of ARE-ABCFs (*SI Appendix*, Fig. S1), and mutations within a loop at the tip of the interdomain linker can alter the antibiotic specificity of the ARE-ABCF proteins (6, 7, 12, 13). Furthermore, VgaA variants where the interdomain linker is truncated cannot restore the ribosomal transpeptidation in the presence of lincomycin (4). While the MsrE-70S structure provides insight into how the Msr class confers resistance to macrolide antibiotics (7), structural insight into how the Vga/Lsa/Sal/Vml class confers resistance to PTC-targeting antibiotics has been lacking.

Here, we have determined a cryo-EM structure of *Bacillus subtilis* VmlR bound to a stalled ribosome complex (SRC) at 3.5-Å resolution, revealing that VmlR, like EttA and MsrE, binds within the E site of the ribosome. The interdomain linker of VmlR accesses the PTC of the ribosome by inducing a noncanonical conformation of the P-site tRNA where the acceptor arm is disengaged from the PTC and the CCA end is shifted toward the A site. While the interdomain linker of VmlR directly encroaches the binding site of PTC-targeting antibiotics, we observe specificity in the VmlR resistance profile, such that VmlR confers resistance to VgM, Lnc, and Tia, but not to Cam, Lnz, or Ery. We also identify a VmlR-F237A variant that exhibits altered specificity, conferring resistance to Lnc and Tia, but not to VgM. Our combined structural and mutagenesis analyses suggest that VmlR dislodges VgM, Lnc, and Tia using an indirect allosteric, rather than a direct steric, mechanism of action.

Results

Generation of a *B. subtilis* VmlR–70S Ribosome Complex. Initially, we in vitro-reconstituted complexes between wild-type VmlR (previously called ExpZ) and tight-coupled *B. subtilis* 70S ribosomes in the presence of the nonhydrolysable ATP analog ADPNP. Despite observing binding in pelleting assays, no density for VmlR was observed in low-resolution cryo-EM reconstructions, suggesting that the VmlR–ribosome interaction was not stable. A previous study employed an ATPase-deficient form of EttA (EttA-EQ_2) to trap and visualize the factor in the ATP form on the ribosome using cryo-EM (11). Therefore, we generated an equivalent ATPase-deficient VmlR-EQ_2 variant where Glu129 in NBD1 and Glu432 in NBD2 were mutated to Gln129 and Gln432, respectively. A low-resolution cryo-EM reconstruction of the VmlR–EQ_2–70S complex revealed density for VmlR in the E site of the 70S ribosomes bearing a tRNA in the P site. Unfortunately, this represented a small percentage of the population, as the P-site tRNAs were only present as contaminants that remained bound to the tight-coupled ribosomes despite the purification process. To increase the ribosomal occupancy of the P-site tRNAs, and thus promote binding of VmlR, we replaced 70S ribosomes with stalled ribosome complexes (SRCs), as used previously to visualize RelA (14) and TetM (15) on the ribosome. To generate the SRCs, translation of an ErmDL stalling peptide in the presence of the ketolide telithromycin was carried out, leading to ribosomes stalled with a short seven-amino acid peptidyl-tRNA decoding the seventh codon of the mRNA (16). In contrast to our previous studies, we performed translation in the *E. coli* PURE system using *B. subtilis* rather than *E. coli* 70S ribosomes (17), thus enabling a homogeneous *B. subtilis* VmlR-EQ_2-SRC to be generated. Since VmlR does not confer resistance to the macrolide class of antibiotics (18), we rationalized that using the ErmDL-SRC may also contribute to trapping VmlR on the ribosome. We did not attempt to generate Lnc or VgM SRCs as substrates for VmlR binding, since our past experience in forming TetM-SRC revealed that the presence of the drug (in this case, tetracycline) only generated additional sample heterogeneity due to competition for binding between TetM and tetracycline (19).

Cryo-EM Structure of a *B. subtilis* VmlR-EQ_2-SRC. Cryo-EM data for the *B. subtilis* VmlR-EQ_2-SRC was collected on a Titan Krios transmission electron microscope (TEM) with a Falcon III direct electron detector (DED) and processed with RELION 2.1 (20). After 2D classification, a total of 159,722 ribosomal particles were sorted into two major populations, both of which contained a P-site tRNA but differed with respect to the presence (18–21%, 28,972–33,392) or absence (43%, 68,652 particles) of VmlR-EQ_2 (Fig. 1 and *SI Appendix*, Fig. S2*A*). The cryo-EM maps of the VmlR-EQ_2-SRC (Fig. 1*A*) and P-tRNA-SRC could be refined to yield final average resolutions of 3.5 Å and 3.1 Å, respectively (*SI Appendix*, Fig. S2 *B–D*). Molecular models for the *B. subtilis* 70S ribosome were based on a previous model of a *B. subtilis* MifM-SRC (21), which could be improved to include side chains for the proteins of the SSU due to the better resolution (*SI Appendix*, Table S1). The VmlR model was initially based on a homology model generated using the crystal structure of EttA (10) as a template (Fig. 1*B*). The density for the C-terminal extension (CTE) that is absent in EttA and MsrE was modeled as two α-helices connected by a short linker to the NBD2 (Fig. 1*B*), which is consistent with secondary structure predictions; however, the quality of the density map only permitted the backbone to be traced. By contrast, the interdomain linker between NBD1 and NBD2, which we refer to as the antibiotic resistance domain (ARD), was well-resolved and could be modeled de novo (*SI Appendix*, Fig. S2*E*), presumably because the ARD is sandwiched between the 23S rRNA of the LSU and the acceptor arm of the P-site tRNA (Fig. 1*A*). Clear density was observed for two molecules of ATP bound within the active sites formed by NBD1 and NBD2 (Fig. 1*C*), in agreement with the ability of the VmlR-EQ_2 to bind, but not hydrolyze, ATP. Consistently, previous studies have shown that EQ mutations in either NBD lead to a loss in the ability of VgaA to confer resistance to VgM (9). NBD1 and NBD2 of VmlR-EQ_2 adopt a closed conformation on the ribosome, similar to that observed for the ABC multidrug resistance protein 1 (MRP1) (22) as well as the modeled ATP conformation of EttA (10, 11), but distinct from the open conformation observed for the free state of ABCE1 (23) (*SI Appendix*, Fig. S3 *A–C*).

Binding Site of VmlR on the 70S Ribosome. VmlR binds within the E site of the 70S ribosome (Fig. 1*A*), analogously to EttA (11) (*SI Appendix*, Fig. S3 *D–F*). The NBD1 of VmlR directly contacts and stabilizes an open conformation of the L1 stalk (Fig. 2*A*), which is similar but distinct from that observed in the presence of EttA due to the EttA "Arm" being absent in VmlR (*SI Appendix*, Fig. S2 *D–F*). NBD1 of VmlR also establishes interactions with H68 of the 23S rRNA as well as ribosomal protein bL33 (Fig. 2 *A* and *B*). The ARD, linking NBD1 and NBD2, comprises two long α-helices that span from the E site across the interface of the LSU inserting the ARD loop into the PTC (Fig. 2 *A* and *B*). Helix α2 of the ARD runs parallel to H74-H75 and forms multiple contacts with the backbone of nucleotides within these helices, whereas helix α1 interacts predominantly with the acceptor arm of the P-site tRNA (Fig. 2*A*). The elbow region of the P-site tRNA is contacted by NBD2, which establishes additional interactions with ribosomal protein uL5 of the LSU (Fig. 2 *A* and *B*) and h41-42 of the 16S rRNA located within the head of the SSU (Fig. 2*C*). The CTE of VmlR, which has no equivalent in EttA, extends from NBD2 where a short linker guides the CTE between a cleft created by ribosomal proteins uS7 and uS11 on the SSU head and positions the two CTE α-helices into the

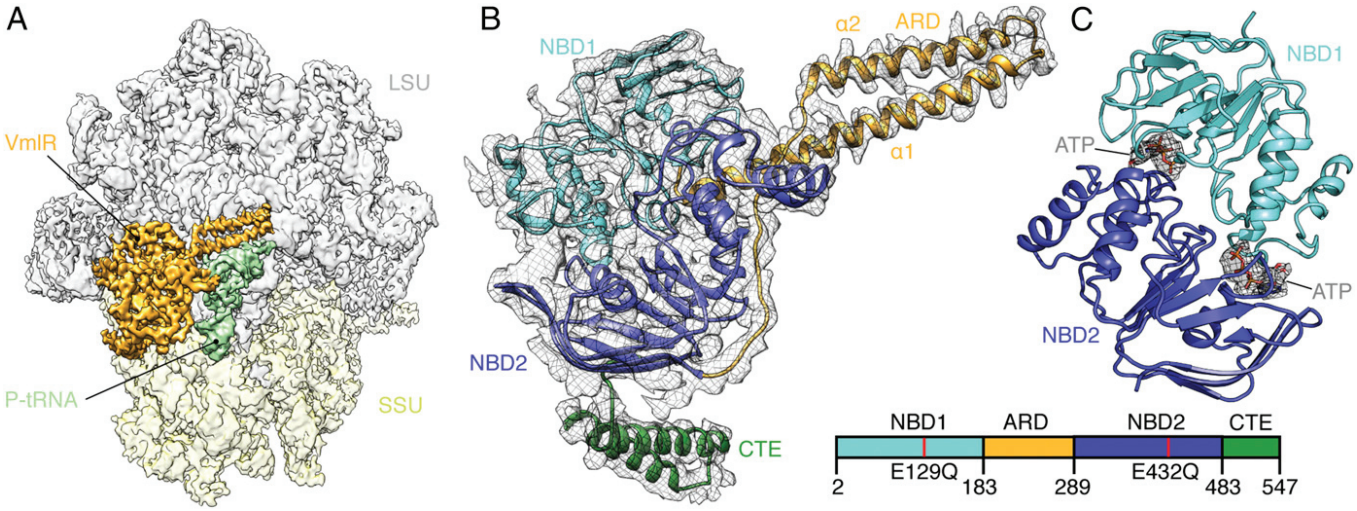

Fig. 1. Structure of VmlR–ribosome complex. (*A*) Cryo-EM map with isolated densities for VmlR (orange), P/V-tRNA (pale green), small subunit (SSU, yellow), and large subunit (LSU, gray). (*B*) Electron density (gray mesh) with molecular model for VmlR, colored according to domains as represented in the schematic (*Bottom Right*): nucleotide binding domain 1 (NBD1, cyan), antibiotic-resistance domain (ARD, orange), nucleotide binding domain 2 (NBD2, blue), and C-terminal extension (CTE, green). (*C*) Molecular model for NBD1 (cyan) and NBD2 (blue) of VmlR with isolated electron density (gray mesh) for the modeled ATP nucleotides (sticks).

Shine–Dalgarno (SD)–anti-SD cavity located on the SSU platform (Fig. 2*C*). This interaction is likely to be important for VmlR function since a VmlR variant lacking the CTE loses its ability to confer antibiotic resistance (*SI Appendix*, Fig. S4 *A–D*), as observed previously for VgaA (9).

VmlR Stabilizes a Noncanonical P/V-tRNA Conformation. Binding of VmlR to the ribosome and accommodation of the ARD at the PTC of the LSU requires the P-site tRNA to be displaced from its canonical position and adopt a noncanonical state, which we term the P/V-tRNA (Fig. 3*A*). The ARD of VmlR is 27 amino acids longer than the equivalent region in EttA (Fig. 3 *A–C*), explaining why binding of EttA does not affect the conformation of the P-site tRNA, nor encroach on the PTC (Fig. 3*B*). Compared with the canonical P-site tRNA position, the elbow region of the P/V-tRNA is shifted by ∼10 Å away from the PTC toward the E site and is likely to be stabilized via interactions with the NBD2 of VmlR (Fig. 3*C*). As a consequence, the CCA end of the P/V-tRNA is redirected by 37 Å into the A site, where it overlaps with the binding site of the acceptor arm of a canonical A-site tRNA, but not with an A/T-tRNA state (Fig. 3*D*). This suggests that the VmlR-stabilized P/V-tRNA would allow delivery of aminoacyl-tRNA to the ribosome by EF-Tu but prevent the subsequent accommodation at the A site of the PTC. It should be noted that the density for the CCA end of the P/V-tRNA was poorly resolved and the nascent chain was not observed (*SI Appendix*, Fig. S5*A*), indicative of high flexibility and consistent with local resolution calculations (*SI Appendix*, Fig. S5*B*). Although we cannot exclude that the nascent chain was hydrolyzed by VmlR, we do not believe this is likely since the

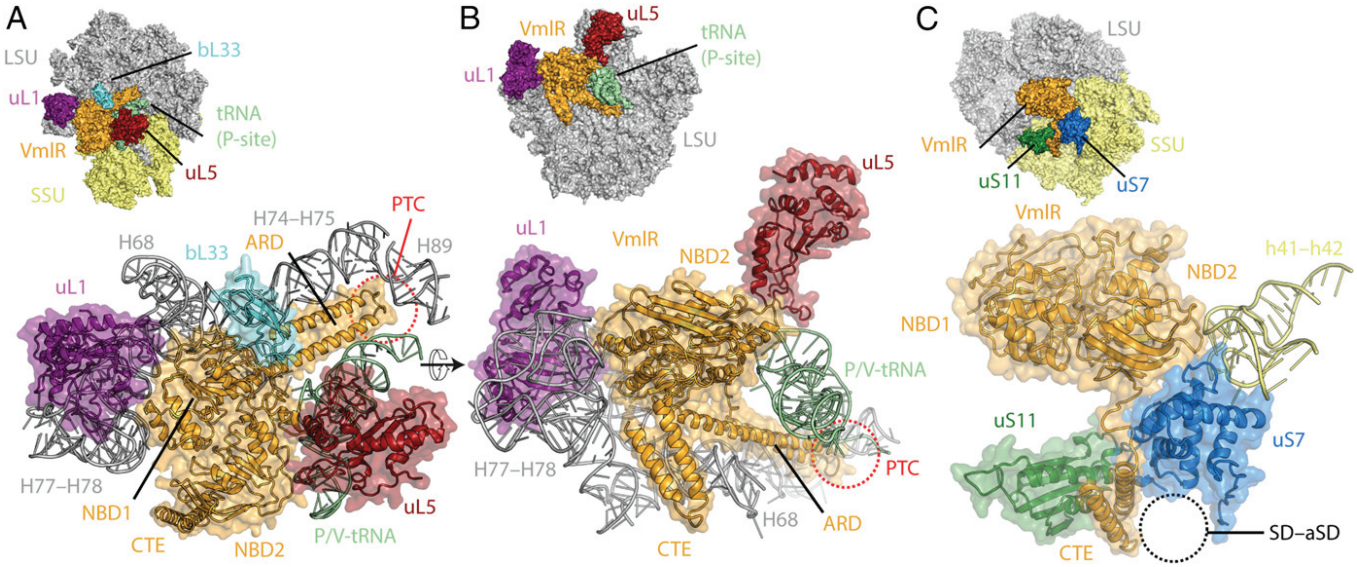

Fig. 2. Interaction of VmlR with the ribosome. (*A–C*) *Inset* and zoom showing VmlR (orange) interaction P/V-tRNA (green) and components of the large subunit (LSU, gray); 23S rRNA helices H68, H74-H75; and H89 (gray) and ribosomal proteins uL1 (magenta), uL5 (red), and bL33 (cyan) (*A* and *B*) and components of the small subunit (SSU, yellow), including 16S rRNA helices h41-42 and ribosomal proteins uS7 (blue) and uS11 (green) (*C*).

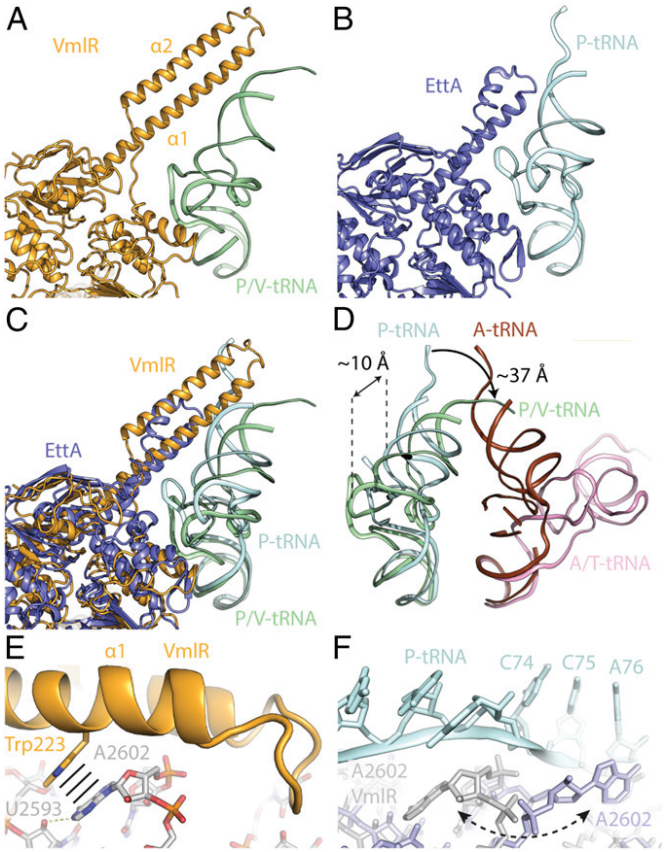

Fig. 3. Comparison of VmlR and EttA on the ribosome. (*A–C*) Relative position of VmlR (orange) and P/V-tRNA (green) (*A*), EttA (blue, PDB ID code 3J5S) (11) and P-tRNA (cyan) (*B*), and superimposition of *A* and *B* (*C*). (*D*) Comparison of P/V-tRNA (green), P-tRNA (cyan), A-tRNA (brown) (39), and A/T-tRNA (pink, PDB ID code 4V5G) (40). (*E*) Stacking interaction (indicated by black lines) of Trp223 of VmlR (orange) with 23S rRNA nucleotide A2602 (gray), which forms hydrogen bonds (dashed lines) with U2593. (*F*) Conformation of VmlR bound conformation of A2602 (gray) compared with the A2602 (slate) conformation in the pretranslocation state conformation (39) with P-tRNA (cyan) and A-tRNA (data not shown).

related VgaA has no detectable peptidyl-tRNA hydrolysis activity (4).

By contrast, the canonical P-site tRNA was well-resolved in the cryo-EM map of the P-tRNA-SRC and the nascent chain could be visualized extending down the ribosomal tunnel toward the telithromycin-binding site (*SI Appendix*, Fig. S5 *E* and *F*). Therefore, binding of VmlR to the ribosome can disengage the P-site tRNA from the PTC despite the presence of the oligopeptidyl-tRNA. Compared with the P-tRNA-SRC, binding of VmlR induces a 3.4° rotation of the SSU body and 4.1° swivel of the SSU head (*SI Appendix*, Fig. S5 *G* and *H*), which may also contribute to destabilizing the P-site tRNA. Displacement of the P-site tRNA from the PTC by the ARD of VmlR leads to a rearrangement in 23S rRNA nucleotide A2602 (*E. coli* numbering is used for rRNA nucleotides) (Fig. 3 *E* and *F*). In the VmlR-SRC, the nucleobase of A2602 stacks upon Trp223 within helix α1 of the ARD of VmlR and forms potential hydrogen bond interactions with U2593 (Fig. 3*E*). By contrast, the VmlR position of A2602 is flipped by 180° compared with the canonical A2602 that interacts with the CCA end of the P-site tRNA (Fig. 3*F*). Therefore, in addition to stabilizing VmlR on the ribosome, flipping of A2602 may also be necessary to clear the way for the transition from the P to the P/V-tRNA state.

VmlR and Resistance to PTC-Targeting Antibiotics. At the PTC, the binding position of helix α1 of the ARD of VmlR overlaps that of the CCA end of a P-site tRNA, whereas the ARD loop and specifically Phe237 extends into the A-site pocket where the aminoacyl moiety of the A-site tRNA normally resides (Fig. 4 *A* and *B*). The A-site pocket is also the binding site of PTC-targeting antibiotics, such as VgM, Lnc, Tia, Cam, and Lnz, whereas S_B antibiotics, such as VgS, and macrolides, such as Ery, bind deeper within the ribosomal tunnel (Fig. 4 *B–D*). While VmlR has been shown to confer resistance to VgM and Lnc, but not to VgS or the macrolides Ery, oleandomycin, and spiramycin (18), the effect on other PTC-targeting antibiotics remains unknown. To test this, we monitored growth of a wild-type (WT) *B. subtilis* strain containing VmlR as well as a *B. subtilis* strain where the *vmlR* gene was inactivated (Δ*vmlR*), in the presence of increasing concentrations of the relevant antibiotics. Growth was also monitored for a Δ*vmlR* strain that was complemented by inserting the *vmlR* gene into the *thrC* locus under the control of an IPTG-inducible promoter. In agreement with previous findings (18), VmlR conferred resistance to VgM and Lnc, but not to Ery (Fig. 4*E* and *SI Appendix*, Fig. S4 *A–C*). In addition, we could also demonstrate that VmlR conferred resistance to Tia, as expected based on the steric overlap between Phe237 of VmlR and the drug, but surprisingly not to Cam or Lnz, which also sterically overlap with VmlR (Fig. 4*E* and *SI Appendix*, Fig. S4 *C–E*).

This observation, coupled with the incomplete conservation of Phe237 (*SI Appendix*, Fig. S1), led us to generate VmlR variants where Phe237 was mutated to Ala (VmlR-F237A) or Val (VmlR-F237V). Growth experiments revealed that the VmlR-F237V retained a WT-like activity profile, conferring resistance to VgM, Lnc, and Tia, but not Ery, Cam, and Lnz (Fig. 4*E* and *SI Appendix*, Fig. S6). By contrast, the VmlR-F237A variant displayed altered specificity, conferring resistance to Lnc and Tia, but not to VgM (Fig. 4*E* and *SI Appendix*, Fig. S6). The retention of resistance activity of the VmlR-F237V variant suggested that VmlR does not employ direct steric interference to dislodge the drug from the binding site at the PTC, but rather an indirect allosteric mechanism. This prompted us to analyze whether the binding of VmlR induced any specific conformational changes within PTC nucleotides that could mediate dissociation of antibiotics from the ribosome. Comparing the PTC conformation in the VmlR-SRC with structures of ribosomes bound with VgM (24), Lnc (25), and Tia (26) revealed the most significant difference for U2585, which is stacked upon by Tyr240 of VmlR, thereby preventing other conformations being adopted that interact with the drugs (Fig. 4 *F–H* and *SI Appendix*, Fig. S7 *F–I*). In addition, shifted conformations were also observed for U2506 and A2062 that may be influenced indirectly by VmlR binding (Fig. 4 *F–H* and *SI Appendix*, Fig. S7 *F–K*).

Discussion

Together with the available literature and the insights gained from the VmlR-EQ_2-SRC structure, we present a model for the mechanism of action of VmlR (Fig. 5) and discuss how it relates to other ARE-ABCF proteins. First, our structure revealed that VmlR recognizes and binds to antibiotic-stalled ribosomes with vacant E sites (Fig. 5 *A* and *B*). We envisage two main scenarios when this can occur during translation, namely, directly following initiation when the E site is free and only an initiator fMet-tRNA is bound in the P site, or subsequent to E-tRNA release from a posttranslocation state during elongation (27). Although a pretranslocational state also has a free E site, we do not believe this is a substrate for VmlR since the relevant PTC-targeting antibiotics prevent A-site tRNA binding and, thereby, block the pretranslocation state from forming. The VmlR-EQ_2-SRC structure suggests that VmlR binds to antibiotic-stalled ribosomes in the ATP conformation with the NBDs adopting a closed conformation (Fig. 5*B*). Binding of VmlR, which is facilitated by important CTE–30S interactions, induces a slight rotation of the SSU relative to the LSU and disengages the P-site tRNA from the PTC, leading to stabilization of a noncanonical P/V-tRNA state (Fig. 5*B*). The VmlR-EQ_2-SRC structure

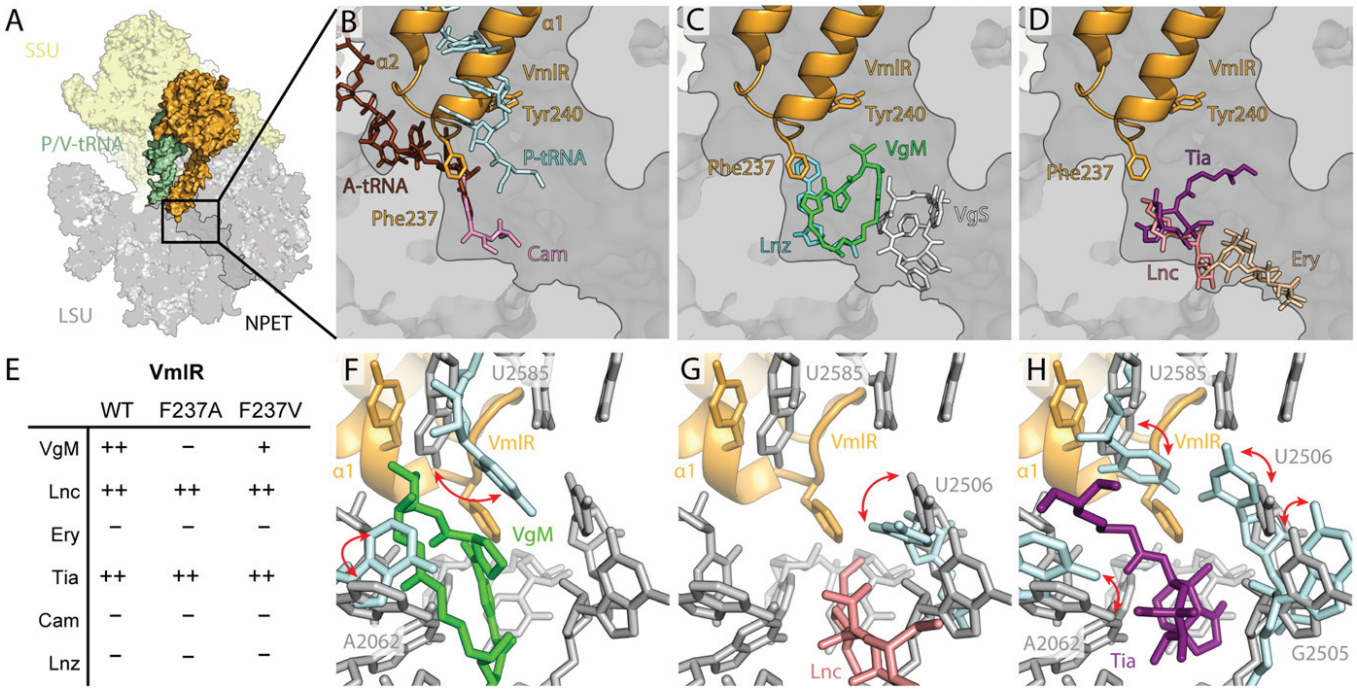

Fig. 4. Interaction of VmlR at the peptidyltransferase center. Overview of VmlR (orange) and P/V-tRNA (green) on the ribosome (SSU, yellow; LSU, gray) (*A*) with transverse section of the LSU to reveal the nascent polypeptide exit tunnel (NPET) with VmlR (orange) superimposed (*B–D*) against A-site tRNA (brown) and P-site tRNA (cyan) from a pretranslocation state (39) and chloramphenicol (Cam, pink, PDB ID code 4V7U) (41) (*B*); virginiamycin M (VgM, green) and S (VgS, white) (PDB ID code 1YIT) (24) and linezolid (Lnz, cyan, PDB ID code 3DLL) (42) (*C*); lincomycin (Lnc, salmon, PDB ID code 5HKV) (25), tiamulin (Tia, purple, PDB ID code 1XBP) (26), and erythromycin (Ery, tan, PDB ID code 4V7U) (41) (*D*). (*E*) Summary of antibiotic resistance conferred by WT VmlR as well as VmlR variants F237A and F237V complementing a Δ*vmlR* strain of *B. subtilis* (see also *SI Appendix*, Fig. S6 *A–F*). (*F–H*) The conformation of selected 23S rRNA nucleotides (gray sticks) at the PTC in the presence of VmlR (orange) superimposed with with different nucleotide (cyan) conformations (indicated by red arrows) when virginiamycin M (VgM, green, PDB ID code 1YIT) (24) (*F*), lincomycin (Lnc, pink, PDB ID code 5HKV) (25) (*G*), and tiamulin (Tia, purple, PDB ID code 1XBP) (26) (*H*) are bound to the ribosome.

revealed that VmlR could even disengage short oligopeptidyl-tRNAs from the PTC, although it remains unclear whether longer peptidyl-tRNA will be refractory to the action of VmlR or other ARE-ABCFs. By inducing a P/V-tRNA state, the ARD of VmlR can access the PTC of the ribosome where it indirectly dislodges the PTC-targeting antibiotics from their binding sites (Fig. 5*B*). This presumably occurs because VmlR induces allosteric conformational changes within PTC nucleotides that comprise the drug-binding site; however, the transition of the P-tRNA to the P/V-tRNA may also contribute to drug dissociation. Surprisingly, our results suggest that VmlR can promote dissociation of some PTC inhibitors, such as VgM, Lnc, and Tia, but not others, such as Cam and Lnz. While we also observe some conformational differences between the PTC bond with VmlR or Cam/Lnz (*SI Appendix*, Fig. S7 *J* and *K*), we note that Cam and Lnz display strong nascent chain-dependent stalling (28), which may preclude VmlR from acting on these stalled complexes, but this needs to be investigated further.

Transpeptidation experiments in the presence and absence of VgaA/Lsa and Lnc indicate that ATP hydrolysis is critical for recycling of ARE-ABCFs (4), suggesting that VmlR-ADP is the low-affinity form that dissociates from the ribosome following drug release (Fig. 5*B*). Moreover, since processive transpeptidation reactions require VmlR-ADP release, the observed

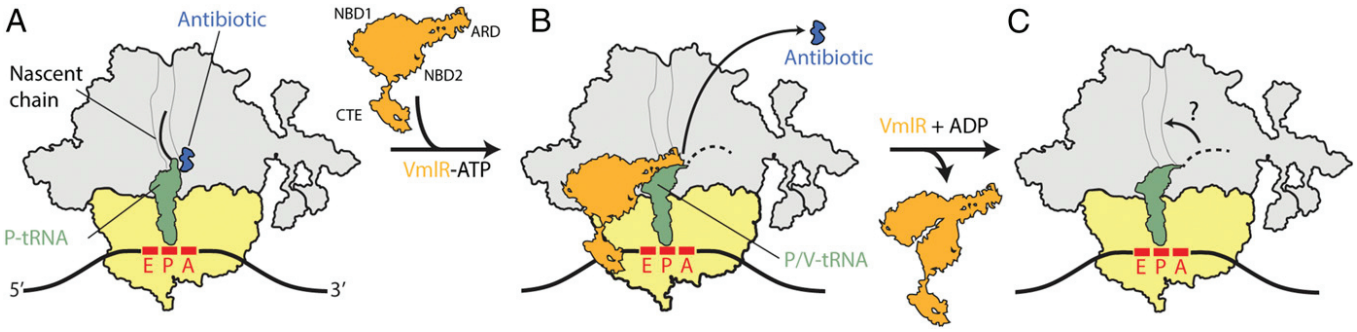

Fig. 5. Model for ribosome protection by VmlR. (*A*) Antibiotic-stalled ribosomes with a peptidyl-tRNA in the P site are recognized by the ABCF ATPase VmlR, which binds to the E site of the ribosome with a closed ATP-bound conformation. (*B*) Binding of VmlR induces a shifted P/V-tRNA conformation in the ribosome allowing the ARD of VmlR to access the peptidyl-transferase center (PTC) and dislodge the drug from its binding. (*C*) Hydrolysis of ATP to ADP leads to dissociation of VmlR from the ribosome, which may allow the peptidyl-tRNA to accommodate back on the ribosome with the nascent chain inserting into the NPET and translation to continue. In *B* and *C*, the dashes line extending from the P/V-tRNA represents a flexible nascent chain.

transpeptidation in the presence of ATP (4) indicates that the P/V-tRNA can reaccommodate at the P site of the PTC (Fig. 5*C*). The transpeptidation experiments were performed with fMet-tRNA (4), thus it is still unclear whether reaccommodation at the PTC can occur with longer peptidyl-tRNAs.

Before submission of this manuscript, a cryo-EM structure was reported of *P. aeruginosa* MsrE in complex with a *T. thermophilus* 70S ribosome bearing a deacylated $tRNA^{fMet}$ in the P site (7). At the time of revision, the cryo-EM map and model were still unavailable, therefore a comparison can only be made based on the publication figures, which are in good overall agreement with the structure and interpretation of the *B. subtilis* VmlR-EQ_2-SRC reported here. The two main differences appear to be that (*i*) MsrE lacks the CTE and therefore also lacks the associated SSU interactions that are available for VmlR, and (*ii*) the ARD loop differs in sequence and length between MsrE and VmlR (*SI Appendix*, Fig. S1) and therefore the interactions at the PTC are likewise distinct. While the ARD loop of MsrE is longer and reaches to the macrolide binding site (7), the VmlR loop is shorter and approaches only the PTC-targeting antibiotics, which is consistent with the respective antibiotic resistance profiles of these proteins.

Materials and Methods

The *B. subtilis* VmlR-EQ_2-SRC was generated by incubating recombinant *B. subtilis* VmlR-EQ_2 protein in the presence of ATP with *B. subtilis* ErmDL-SRC, which were essentially prepared as described (29, 30). Cryo-EM data collection was performed on a Titan Krios 300 kV TEM equipped with a Falcon III DED (FEI). Images of individual ribosome particles were aligned using MotionCor2 (31) and then particles were selected automatically using Gautomatch (https://www.mrc-lmb.cam.ac.uk/kzhang/). All images were processed using RELION 2.1 (20). Final reconstructions were corrected for the modulation transfer function and sharpened by applying a negative B factor estimated by RELION 2.1 (20). The average resolution of reconstructions was determined using the "gold-standard" criterion ($FSC_{0.143}$) (32). ResMap was used for local resolution estimation (33), and the final volumes were locally filtered using SPHIRE (34). Molecular models were fitted and adjusted using Coot (35) and refined in Phenix (36). Model validation was carried out using the MolProbity server (37), and the final model statistics are presented in *SI Appendix*, Table S1. All figures were generated using PyMOL (Schrödinger, LLC) and/or Chimera (38). Further details can be found in the *SI Appendix*, *Material and Methods*. The cryo-EM maps and models for the VmlR- and P-tRNA-SRC are deposited in the EMDatabank (EMD-0177 and EMD-0176) and RCSB Protein Data Bank (6HA8 and 6HA1), respectively.

ACKNOWLEDGMENTS. We thank Susanne Rieder for expert technical assistance and Seki Takahiro for generating the Δ*vmlR* strain. This research was supported by Deutsche Forschungsgemeinschaft Grants FOR1805 and WI3285/8-1 (to D.N.W.), Swedish Research Council Grants 2013-4680 (to V.H.) and 2015-04746 (to G.C.A.), the Ragnar Söderberg Foundation (V.H.), Carl Tryggers stiftelse CTS 34 (G.C.A.), Jeanssons stiftelse (G.C.A.), and from the Umeå Centre for Microbial Research (UCMR): postdoctoral grant 2017 (to H.T.) and Gender Policy Support 2017 (to G.C.A.). iNEXT, project number 5966, was funded by the Horizon 2020 program of the European Union. Czech Infrastructure for Integrative Structural Biology research infrastructure project LM2015043 funded by Ministry of Education, Youth, and Sports of the Czech Republic is gratefully acknowledged for the financial support of the measurements at the CF Cryo-electron Microscopy and Tomography Central European Institute of Technology, Masaryk University. This article reflects only the author's view, and the European Commission is not responsible for any use that may be made of the information it contains.

1. Wilson DN (2014) Ribosome-targeting antibiotics and bacterial resistance mechanisms. *Nat Rev Microbiol* 12:35–48.
2. Lin J, Zhou D, Steitz TA, Polikanov YS, Gagnon MG (2018) Ribosome-targeting antibiotics: Modes of action, mechanisms of resistance, and implications for drug design. *Annu Rev Biochem* 87:451–478.
3. Sharkey LKR, O'Neill AJ (2018) Antibiotic resistance ABC-F proteins: Bringing target protection into the limelight. *ACS Infect Dis* 4:239–246.
4. Murina V, Kasari M, Hauryliuk V, Atkinson GC (2018) Antibiotic resistance ABCF proteins reset the peptidyl transferase centre of the ribosome to counter translational arrest. *Nucleic Acids Res* 46:3753–3763.
5. Wang Y, et al. (2015) A novel gene, *optrA*, that confers transferable resistance to oxazolidinones and phenicols and its presence in *Enterococcus faecalis* and *Enterococcus faecium* of human and animal origin. *J Antimicrob Chemother* 70:2182–2190.
6. Sharkey LK, Edwards TA, O'Neill AJ (2016) ABC-F proteins mediate antibiotic resistance through ribosomal protection. *MBio* 7:e01975.
7. Su W, et al. (2018) Ribosome protection by antibiotic resistance ATP-binding cassette protein. *Proc Natl Acad Sci USA* 115:5157–5162.
8. Nguyen F, et al. (2014) Tetracycline antibiotics and resistance mechanisms. *Biol Chem* 395:559–575.
9. Jacquet E, et al. (2008) ATP hydrolysis and pristinamycin IIA inhibition of the Staphylococcus aureus Vga(A), a dual ABC protein involved in streptogramin A resistance. *J Biol Chem* 283:25332–25339.
10. Boël G, et al. (2014) The ABC-F protein EttA gates ribosome entry into the translation elongation cycle. *Nat Struct Mol Biol* 21:143–151.
11. Chen B, et al. (2014) EttA regulates translation by binding the ribosomal E site and restricting ribosome-tRNA dynamics. *Nat Struct Mol Biol* 21:152–159.
12. Novotna G, Janata J (2006) A new evolutionary variant of the streptogramin A resistance protein, $Vga(A)_{LC}$, from *Staphylococcus haemolyticus* with shifted substrate specificity towards lincosamides. *Antimicrob Agents Chemother* 50:4070–4076.
13. Lenart J, Vimberg V, Vesela L, Janata J, Balikova Novotna G (2015) Detailed mutational analysis of Vga(A) interdomain linker: Implication for antibiotic resistance specificity and mechanism. *Antimicrob Agents Chemother* 59:1360–1364.
14. Arenz S, et al. (2016) The stringent factor RelA adopts an open conformation on the ribosome to stimulate ppGpp synthesis. *Nucleic Acids Res* 44:6471–6481.
15. Arenz S, Nguyen F, Beckmann R, Wilson DN (2015) Cryo-EM structure of the tetracycline resistance protein TetM in complex with a translating ribosome at 3.9-Å resolution. *Proc Natl Acad Sci USA* 112:5401–5406.
16. Sothiselvam S, et al. (2014) Macrolide antibiotics allosterically predispose the ribosome for translation arrest. *Proc Natl Acad Sci USA* 111:9804–9809.
17. Chiba S, et al. (2011) Recruitment of a species-specific translational arrest module to monitor different cellular processes. *Proc Natl Acad Sci USA* 108:6073–6078.
18. Ohki R, Tateno K, Takizawa T, Aiso T, Murata M (2005) Transcriptional termination control of a novel ABC transporter gene involved in antibiotic resistance in *Bacillus subtilis*. *J Bacteriol* 187:5946–5954.
19. Dönhöfer A, et al. (2012) Structural basis for TetM-mediated tetracycline resistance. *Proc Natl Acad Sci USA* 109:16900–16905.
20. Kimanius D, Forsberg BO, Scheres SH, Lindahl E (2016) Accelerated cryo-EM structure determination with parallelisation using GPUs in RELION-2. *eLife* 5:e18722.
21. Sohmen D, et al. (2015) Structure of the *Bacillus subtilis* 70S ribosome reveals the basis for species-specific stalling. *Nat Commun* 6:6941.
22. Johnson ZL, Chen J (2018) ATP binding enables substrate release from multidrug resistance protein 1. *Cell* 172:81–89.e10.
23. Barthelme D, et al. (2011) Ribosome recycling depends on a mechanistic link between the FeS cluster domain and a conformational switch of the twin-ATPase ABCE1. *Proc Natl Acad Sci USA* 108:3228–3233.
24. Tu D, Blaha G, Moore PB, Steitz TA (2005) Structures of MLS_BK antibiotics bound to mutated large ribosomal subunits provide a structural explanation for resistance. *Cell* 121:257–270.
25. Matzov D, et al. (2017) Structural insights of lincosamides targeting the ribosome of *Staphylococcus aureus*. *Nucleic Acids Res* 45:10284–10292.
26. Schlünzen F, Pyetan E, Fucini P, Yonath A, Harms JM (2004) Inhibition of peptide bond formation by pleuromutilins: The structure of the 50S ribosomal subunit from *Deinococcus radiodurans* in complex with tiamulin. *Mol Microbiol* 54:1287–1294.
27. Choi J, Puglisi JD (2017) Three tRNAs on the ribosome slow translation elongation. *Proc Natl Acad Sci USA* 114:13691–13696.
28. Marks J, et al. (2016) Context-specific inhibition of translation by ribosomal antibiotics targeting the peptidyl transferase center. *Proc Natl Acad Sci USA* 113:12150–12155.
29. Arenz S, et al. (2014) Drug sensing by the ribosome induces translational arrest via active site perturbation. *Mol Cell* 56:446–452.
30. Arenz S, et al. (2014) Molecular basis for erythromycin-dependent ribosome stalling during translation of the ErmBL leader peptide. *Nat Commun* 5:3501.
31. Zheng SQ, et al. (2017) MotionCor2: Anisotropic correction of beam-induced motion for improved cryo-electron microscopy. *Nat Methods* 14:331–332.
32. Scheres SH, Chen S (2012) Prevention of overfitting in cryo-EM structure determination. *Nat Methods* 9:853–854.
33. Kucukelbir A, Sigworth FJ, Tagare HD (2014) Quantifying the local resolution of cryo-EM density maps. *Nat Methods* 11:63–65.
34. Moriya T, et al. (2017) High-resolution single particle analysis from electron cryo-microscopy images using SPHIRE. *J Vis Exp* e55448.
35. Emsley P, Cowtan K (2004) Coot: Model-building tools for molecular graphics. *Acta Crystallogr D Biol Crystallogr* 60:2126–2132.
36. Adams PD, et al. (2010) PHENIX: A comprehensive Python-based system for macromolecular structure solution. *Acta Crystallogr D Biol Crystallogr* 66:213–221.
37. Chen VB, et al. (2010) MolProbity: All-atom structure validation for macromolecular crystallography. *Acta Crystallogr D Biol Crystallogr* 66:12–21.
38. Pettersen EF, et al. (2004) UCSF Chimera–A visualization system for exploratory research and analysis. *J Comput Chem* 25:1605–1612.
39. Polikanov YS, Steitz TA, Innis CA (2014) A proton wire to couple aminoacyl-tRNA accommodation and peptide-bond formation on the ribosome. *Nat Struct Mol Biol* 21:787–793.
40. Schmeing TM, et al. (2009) The crystal structure of the ribosome bound to EF-Tu and aminoacyl-tRNA. *Science* 326:688–694.
41. Dunkle JA, Xiong L, Mankin AS, Cate JH (2010) Structures of the *Escherichia coli* ribosome with antibiotics bound near the peptidyl transferase center explain spectra of drug action. *Proc Natl Acad Sci USA* 107:17152–17157.
42. Wilson DN, et al. (2008) The oxazolidinone antibiotics perturb the ribosomal peptidyl-transferase center and effect tRNA positioning. *Proc Natl Acad Sci USA* 105:13339–13344.

PNAS
www.pnas.org

Supplementary Information for

Structural basis for antibiotic resistance mediated by the *Bacillus subtilis* ABCF ATPase VmlR

Caillan Crowe-McAuliffe, Michael Graf, Paul Huter, Hiraku Takada, Maha Abdelshahid, Jiří Nováček, Victoriia Murina, Gemma C. Atkinson, Vasili Hauryliuk, Daniel N. Wilson

Daniel N. Wilson
Email: Daniel.Wilson@chemie.uni-hamburg.de

This PDF file includes:

MATERIALS AND METHODS

Protein expression and purification

VmlR-EQ_2 in pET21b was synthesized by Eurofins. The resulting sequence encoded for a protein identical to GenBank record WP_003234144.1, except for the presence of an N-terminal hexahistidine tag and with glutamates 129 and 432 mutated to glutamines. *E. coli* BL21 (DE3) was used for protein expression. An 800 mL culture was grown at 37°C to OD_{600} ~0.5, and protein expression was induced 1 mM IPTG for 5 h at 22°C. Cells were harvested at 8,000 × *g* for 10 min at 4°C. All subsequent steps were performed at 4°C or on ice. The pellet was washed with 50 mM sodium-phosphate (pH 8.0), 300 mM NaCl, and stored at −80°C. The pellet was thawed and resuspended in 30 mL buffer A (20 mM HEPES/KOH [pH 7.8], 200 mM NH_4Ac, 10 mM $Mg(OAc)_2$, 5 mM 2-mercaptoethanol) with 300 mM NaCl, protease inhibitor cocktail (Complete ultra EDTA-free, Roche), and 0.2 µL DNase I (Thermo). Cells were lysed with three passages through an EmulsiFlex-C3 cell homogeniser (AVESTIN, Inc, Ottawa, Canada) and the lysate was centrifuged at 15,000 × *g* for 10 min. Tween 20 was added to a concentration of 0.01% and the supernatant was applied to 0.5 mL pre-washed cobalt resin (TALON, Clontech). After binding for 90 min with gentle agitation, the resin was washed with 150 mL wash buffer (buffer A with 300 mM NaCl, 10 mM imidazole, and 5 mM 2-mercaptoethanol). Protein was eluted in 1 mL fractions with buffer A with 300 mM imidazole. Elution fractions 1-4 were centrifuged at 21,000 × *g* for 10 min, the supernatants pooled, and the resulting fraction purified by gel filtration over a HiPrep 16/600 75 pg column (GE Healthcare). The buffer used for gel filtration was buffer A supplemented with 0.5 mM EDTA. Elution fractions were centrifuged at 21,000 × *g* for 10 min, concentrated in a centrifugal concentrator (Ultra 4, 10 kDa MWCO, Amicon) and aliquots of the supernatant were snap-frozen in liquid N_2 and stored at -80°C.

Generation and purification of ErmDL-SRC

The ErmDL-SRC was generated based on the disome approach, as previously described (1, 2). The *2XermDL* construct contained a T7 promoter followed by a strong ribosome binding site (RBS) spaced by 7 nucleotides (nts) to the ATG start codon of the first *ermDL* cistron. A linker of 22 nts separated the stop codon of the first *ermDL* cistron and the start codon of the second *ermDL* cistron. The linker also comprised the strong RBS 7 nts upstream of the ATG start codon of the second *ermDL* cistron, enabling initiation of translation independent from the first *ermDL* cistron. With the exception of an R8K mutation, each *ermDL* cistron encoded amino acids 1-14 corresponding to the ErmDL leader peptide (Entry code P62188) present on the macrolide resistance plasmid pE194. The complete sequence of *2XermDL* construct is: 5′-*TAATACGACTCACTATAGGG*AGTTTTATAA**GGAGG**AAAAAATATGACACACTC
AATGAGA**CTT**AAGTTCCCAACTTTGAACCAGTAAAGTTTTATAA**GGAGG**AAA
AAATATGACACACTCAATGAGA**CTT**AAGTTCCCAACTTTGAACCAGTAA-3′
(T7 promoter, italics; RBS, bold; ErmDL ORF, shaded grey with CTT codon in P-site of stalled ribosome shown in bold; annealing site for complementary DNA oligonucleotide, underlined).

In vitro translation of the *ermDL* construct was performed using purified *Bacillus subtilis* 70S and the PURExpress delta ribosome Kit (NEB). Translation reactions were

analyzed on sucrose density gradients (10-55% sucrose in buffer containing 50 mM HEPES-KOH, pH 7.4, 100 mM KOAc, 25 mM $Mg(OAc)_2$, 6 mM β-mercaptoethanol, 100 μM telithromycin and 1x Complete EDTA-free Protease Inhibitor cocktail (Roche)) by centrifugation at 154,693 × *g* (SW-40 Ti, Beckman Coulter) for 3 h at 4°C. For ErmDL-SRC purification, disome fractions were collected using a Gradient Station (Biocomp) with an Econo UV Monitor (Biorad) and a FC203B Fraction Collector (Gilson). Purified ErmDL-SRC disomes were concentrated by centrifugation at 88,760 × *g* for 4 h at 4°C (TLA120.2 rotor, Beckman Coulter). To obtain monosomes of the ErmDL-SRC, a short DNA oligonucleotide (5′-ttcctccttataaaact-3′, Metabion) was annealed to the linker between the *ermDL* cistrons, generating a DNA-RNA hybrid that could be cleaved by RNase H (NEB) treatment in buffer A at 25°C for 1 h. After cleavage of the disomes, ErmDL-SRC monosomes were again purified and concentrated by centrifugation at 88,760 × *g* for 4 h at 4°C (TLA120.2 rotor, Beckman Coulter).

Grid preparation

Samples containing 2.5 pmol ErmDL-SRC, 12.5 pmol VmlR-EQ_2, 100 μM ATP, 10 μM telithromycin were prepared in 20 μL of buffer B (20 mM HEPES/KOH [pH 7.8], 100 mM NH_4Ac, 10 mM $Mg(OAc)_2$, 5 mM 2-mercaptoethanol). N-dodecyl β-D-maltoside was added to a final concentration of 0.1 % (v/v). (The final reaction contained 0.035% DMSO from the telithromycin stock). Reactions were incubated for 15 min at 22°C and then held at 4°C as samples were applied to 2 nm precoated Quantifoil R3/3 holey-carbon-supported grids and vitrified using a Vitrobot Mark IV (FEI, Netherlands).

Data collection and Processing

Images were collected with a Titan Krios TEM equipped with a Falcon III direct electron detector (FEI, Netherlands) at 300 kV using a pixel size of 1.061 Å and an under-defocus range of −0.8 to −1.6 μm. Micrographs were recorded as 39 frames, each with a dose of 1.425 $e^-/Å^2$. Micrographs were aligned and dose-weighted with MotionCor2 (3) and the CTF of every micrograph was determined using GCTF (4). Template-free particle picking was performed using Gautomatch (http://www.mrc-lmb.cam.ac.uk/kzhang/) resulting in 286,701 particles. Manual inspection of thrice-decimated particle after 2D classification resulted in 159,722 particles that were further used for 3D-refinement using an *E. coli* ribosome filtered to 70 Å as an initial reference. The resulting volume was used as a reference for 3D classification yielding four different classes. The class containing VmlR and P-tRNA was subjected to focused sorting, using a spherical mask encompassing the P- and E-sites. Volumes of interest were then refined using undecimated particles. Final reconstructions were corrected for the modulation transfer function and sharpened by applying a negative B-factor estimated by RELION-2.1 (5). The average resolution of reconstructions was determined using the "gold-standard" criterion (FSC = 0.143) (6). ResMap was used for local resolution estimation (7). The final volumes were locally filtered using SPHIRE (8).

Modelling

A homology model of VmlR was created using the deposited structure of ABCF protein EttA (PDB ID 3J5S) (9) as a template for SWISS-MODELLER (10). The homology model was fitted into density with UCSF Chimera (11) using the command 'fit in map',

and manually adjusted with Coot (12). The well-resolved ARD helices could be modelled *de novo*, while residues 486–547 of the CTE of VmlR were modelled as polyalanine. The model of the *B. subtilis* 70S ribosome was derived from PDB ID 3J9W (13). For the less well resolved L1 protein, a homology model was created based on the *E. coli* L1 protein (PDB ID 5AFI) (14) using SWISS-MODELLER (10). The resulting model was rigid body fitted into the cryo-EM density using UCSF Chimera (11). ATP molecules and the *E. coli* Leu-tRNA were obtained from PDB ID 6BHU (15) and PDB ID 4WSM (16), respectively, and subjected to refinement as necessary. The atomic coordinates were refined using phenix.real_space refine (17) with restraints obtained by phenix.secondary_structure_restraints (17). Statistics for the model were obtained using Molprobity (18).

Figure preparation

Figures showing atomic models and electron densities were generated using either UCSF Chimera (11) or PyMol Molecular Graphic Systems (Schrödinger) and assembled with Adobe Illustrator. Growth curves were prepared with Igor Pro.

Construction of *B. subtilis* strains

Strain VHB5 [*trpC2* Δ*vmlR*] was constructed using the marker-free deletion technique (19) with wild type *B. subtilis* strain 168. First, three linear ≈500 nt-long DNA fragments were amplified by PCR using genomic DNA as a template: one located upstream of the *vmlR* ORF (primers VmlR-A-F and VmlR-A-R; see **Table S2** for sequences), one downstream of the *vmlR* ORF (primers VmlR-B-F and VmlR-B-R) and one within the *vmlR* ORF (primers VmlR-C-F and VmlR-C-R). Second, the TMO310 *mazF* cassette was amplified by PCR using primers chpA-R and pAPNC-F. The cassette contains i) the *mazF* toxin ORF under the control of an IPTG-inducible promoter (P_{spac}), ii) the *lacI* ORF for expression of Lac repressor controlling the P_{spac}, and iii) the spectinomycin resistance marker (*spc*). All four PCR products described above were used simultaneously as the template for PCR amplification using primers VmlR-A-F and VmlR-C-R. The resultant long PCR fragment was used to transform the *B. subtilis* strain 168. *vmlR* deletion mutants were selected by spectinomycin resistance, followed by a second selection step on IPTG plates to identify marker-less *vmlR* deletion mutants lacking the *mazF* toxin ORF, yielding the VHB5 strain.

To construct the VHB44 [trpC2 Δ*vmlR thrC::*$P_{hyspnak}$*-vmlR kmR*] strain untagged VmlR under the control of an IPTG-inducible P*hy-spank* promotor, a PCR product encoding *vmlR* was PCR-amplified from the VHp62 plasmid (pAPNC-*vmlR-HTF*) using the primers PhyvmlR_F and PhyvmlR_R. The second PCR fragment encoding a kanamycin-resistance marker, a polylinker downstream of the P*hy-spank* promoter and the *lac* repressor ORF – all inserted in the middle of the *thrC* gene – was PCR-amplified from pHT009 plasmid using primers pHT002_F and pHT002_R. The two fragments were ligated using the NEBuilder HiFi DNA Assembly master mix (New England BioLabs, Ipswich, MA) yielding the pHT009-*vmlR* plasmid which was used to transform the VHB5 [*trpC2* Δ*vmlR*] strain. Selection for kanamycin resistance yielded the desired VHB44 strain.

A QuikChange Multi Site-Directed Mutagenesis Kit (Agilent Technologies) was used to mutate the *vmlR* gene expressed from the pHT009-*vmlR* plasmid. Sequences of

the primers used to generate plasmids pHT009-*vmlRF237A* (F237A), pHT009-*vmlRF237V* (F237V), and pHT009-*vmlRΔCTE* (491STOPx2) are provided in the **Table S2**. To generate pHT009-*vmlRΔCTE,* two consecutive stop codons (TGATAA) were introduced after codon 491 (GAA). VHB5 [*trpC2* Δ*vmlR*] strain was transformed with the plasmids listed above yielding upon selection for kanamycin resistance strains [*trpC2* Δ*vmlR thrC::*$P_{hyspnak}$*-vmlRF237A kmR*], VHB89 [*trpC2* Δ*vmlR thrC::*$P_{hyspnak}$*-vmlRF237V kmR*], and VHB88 [*trpC2* Δ*vmlR thrC::*$P_{hyspnak}$*-vmlRΔCTE kmR*].

Antibiotic sensitivity testing

B. subtilis strains were pre-grown on LB plates either supplemented with 1 mM IPTG (VHB44 strain) or lacking the inducer (wt 168 and VHB5 strains) overnight at 30˚C. Fresh individual colonies were used to inoculate filtered LB medium in the presence and absence of 1 mM IPTG, and OD_{600} adjusted to 0.01. The cultures were seeded on a 100-well honeycomb plate (Oy Growth Curves AB Ltd, Helsinki, Finland), and plates incubated in a Bioscreen C (Labsystems, Helsinki, Finland) at 37°C with continuous medium shaking. After 90 min ($OD_{600} \approx 0.1$), antibiotics were added and growth was followed for an additional 6 hours.

Sequence alignments

To compare the sequence of the ARD domain among VmlR orthologs and other ABCF AREs, we generated a multiple sequence alignment using MAFFT v7.164b (20). VmlR-like proteins in the ARE2 family of ABCFs were retrieved from the ABCF database (21); VgaALC, LsaA, SalA, MsrE and OptrA were downloaded from The Comprehensive Antibiotic Resistance Database (CARD) (22), and EttA from Uniprot (23).

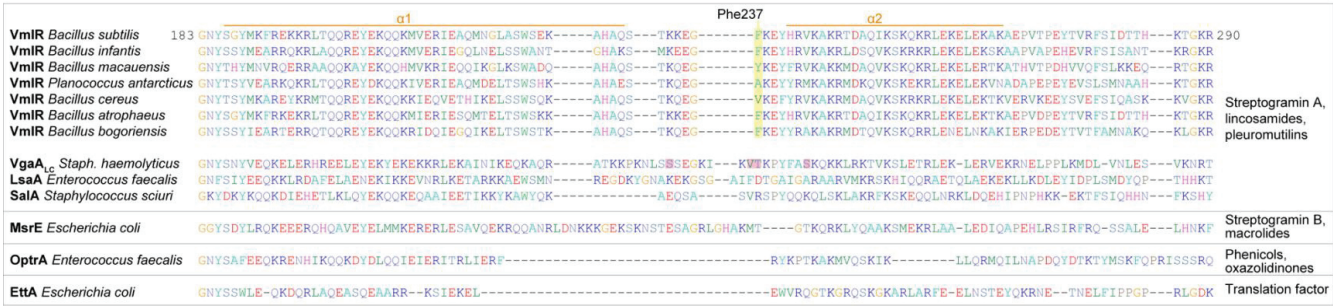

Figure S1. Sequence alignment of selected ARE-ABCF proteins. VmlR, a selection of uncharacterized proteins closely related to vmlR, as well as other AREs with known specificities, were aligned with MAFFT as described in the methods. A portion of an alignment spanning the interdomain linker region was selected for analysis. Helices α1 and α2 and Phe237 from *Bacillus subtilis* VmlR are indicated. Accession identifiers for sequences from top to bottom: *Bacillus subtilis* VmlR (Uniprot P39115), *Bacillus infantis NRRL B-14911* (NCBI YP_008607708.1), *Bacillus macauensis ZFHKF-1* (NCBI WP_007203347.1), *Planococcus antarcticus DSM 14505* (NCBI WP_006828374.1), *Bacillus cereus m1293* (NCBI WP_000675965.1), *Bacillus atrophaeus 1942* (NCBI YP_003971957.1), *Bacillus bogoriensis ATCC BAA-922* (NCBI WP_026673438.1), VgaA$_{LC}$ [*Staphylococcus haemolyticus*] (CARD gb|ABH10964.1), MsrE [*Escherichia coli*] (CARD gb|YP_724476.1), LsaA [*Enterococcus faecalis*] (CARD gb|AAT46077.1), SalA [*Staphylococcus sciuri subsp. sciuri*] (CARD gb|AGN74946), OptrA [*Enterococcus faecalis*] (CARD gb|AKA86814)

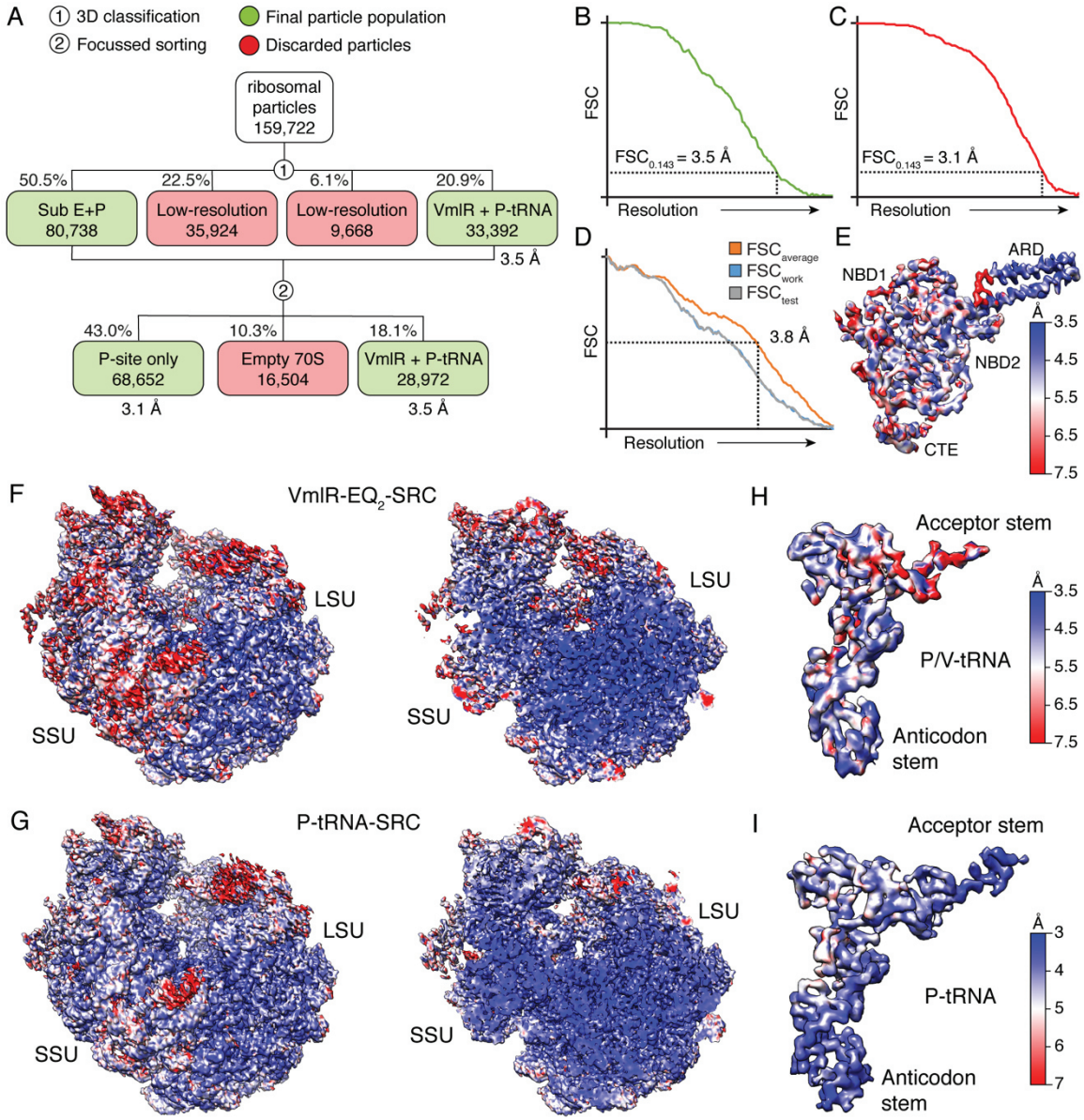

Figure S2. Processing of the cryo-EM data of VmlR-ribosome complex. (**A**) Following 2D classification, 159,722 ribosomal particles were subjected to 3D classification, sorting the particles into four distinct classes, with one defined population containing VmlR and P/V-tRNA (20.9%, 33,392 particles), a population with sub-stoichiometric P-tRNA and two poorly resolved subpopulations that were discarded (red). Focused sorting was implemented yielding three classes, one bearing P-tRNA only (60.2%, 68,652 particles), one vacant 70S class (14.5%, 16,504 particles) and a defined population containing VmlR and P/V-tRNA (25.4%, 28,972 particles). (**B-C**) Fourier Shell Correlation ($FSC_{0.143}$; green) of the (**B**) VmlR-SRC (green) and (**C**) P-tRNA-SRC (red), with the resolution at FSC=0.143 indicated with a dashed line (**D**) $FSC_{average}$ (orange) and self and cross-validated correlations FSC_{work} (red) and FSC_{test} (green), respectively, shown for VmlR-70S complex. (**E**) Isolated density of VmlR from the cryo-EM map of the VmlR-ribosome complex colored according to local resolution. (**F**) Overview and (**G**) transverse section of the cryo-EM map of the VmlR-SRC colored

according to local resolution. (**H-I**) Isolated density of (**H**) P/V-tRNA from the VmlR-SRC and (**I**) P-tRNA from the P-tRNA-SRC colored according to local resolution. (**A**) Following 2D classification, 159,722 ribosomal particles were subjected to 3D classification, sorting the particles into four distinct classes, with one defined population containing VmlR and P/V-tRNA (20.9%, 33,392 particles), a population with sub-stoichiometric P-tRNA and two poorly resolved subpopulations that were discarded (red). Focused sorting was implemented yielding three classes, one bearing P-tRNA only (60.2%, 68,652 particles), one vacant 70S class (14.5%, 16,504 particles) and a defined population containing VmlR and P/V-tRNA (25.4%, 28,972 particles). (**B-C**) Fourier Shell Correlation ($FSC_{0.143}$; green) of the (**B**) VmlR-SRC (green) and (**C**) P-tRNA-SRC (red), with the resolution at FSC=0.143 indicated with a dashed line (**D**) $FSC_{average}$ (orange) and self and cross-validated correlations FSC_{work} (red) and FSC_{test} (green), respectively, shown for VmlR-70S complex. (**E**) Isolated density of VmlR from the cryo-EM map of the VmlR-ribosome complex colored according to local resolution. (**F**) Overview and (**G**) transverse section of the cryo-EM map of the VmlR-SRC colored according to local resolution. (**H-I**) Isolated density of (**H**) P/V-tRNA from the VmlR-SRC and (**I**) P-tRNA from the P-tRNA-SRC colored according to local resolution.

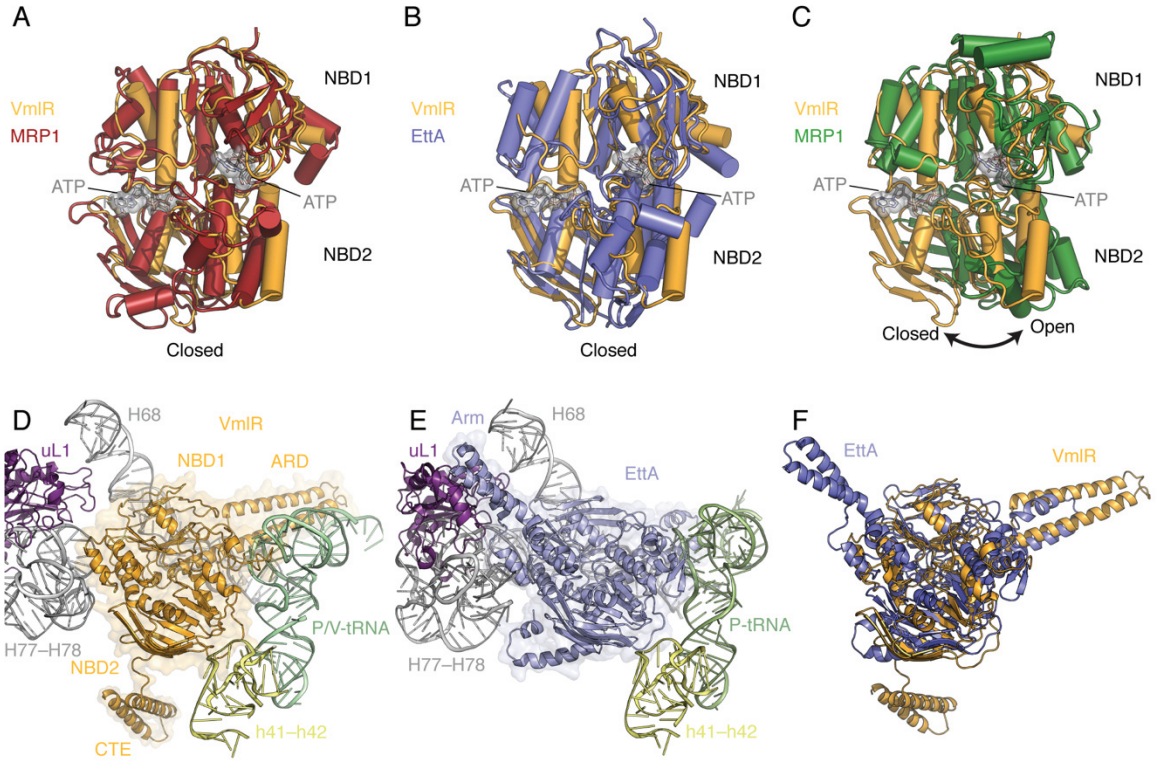

Figure S3. Conformation of the VmlR NBDs with respect to other ABC proteins. (**A-C**) Alignment (based on NBD1) of the closed conformation ABC domains of VmlR (orange) with (**A**) the closed conformations of multi-drug transporter MRP1 (red, PDB ID 6BHU) (15), (**B**) EttA (blue, PDB ID 3J5S) (9) as well as (**C**) the open conformation observed for ABCE1 (green, PDB ID 5LL6) (24). (**D-F**) Comparison of the binding site of VmlR (**D**) and EttA (**E**) on the ribosome. (F) Superimposition of ribosome-bound VmlR (orange) and EttA (blue) from (**D**) and (**E**), respectively.

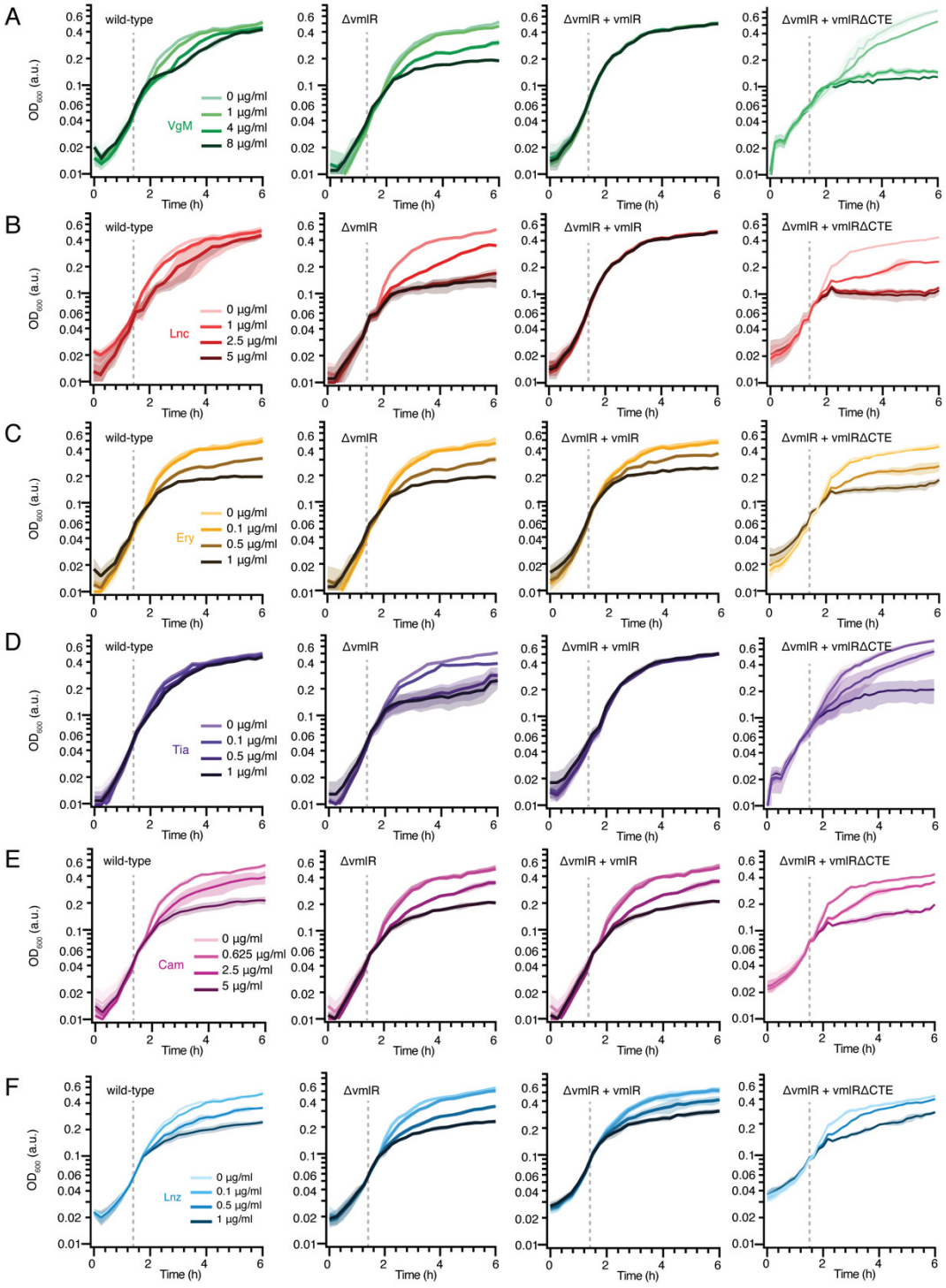

Figure S4. Antibiotic resistance conferred by VmlR and VmlRΔCTE *in vivo*. (**A-F**) Growth curves of wild-type *B. subtilis*, *vmlR*-knockout (Δ*vmlR*) alone, and complemented by wildtype VmlR (Δ*vmlR* + *vmlR*) VmlR-ΔCTE grown in the presence of increasing concentrations of (**A**) virginiamycin M1 (VgM), (**B**) lincomycin (Lnc), (**C**) erythromycin (Ery), (**D**) tiamulin (Tia), (**E**) chloramphenicol (Cam) and (**F**) linezolid (Lnz). Cells were diluted to an OD_{600} value of 0.01 and grown in LB (with IPTG for the

complemented cells) at 37°C with shaking. After 90 minutes antibiotics were added at the indicated concentrations (dashed line) and growth was measured for a further 6 h.

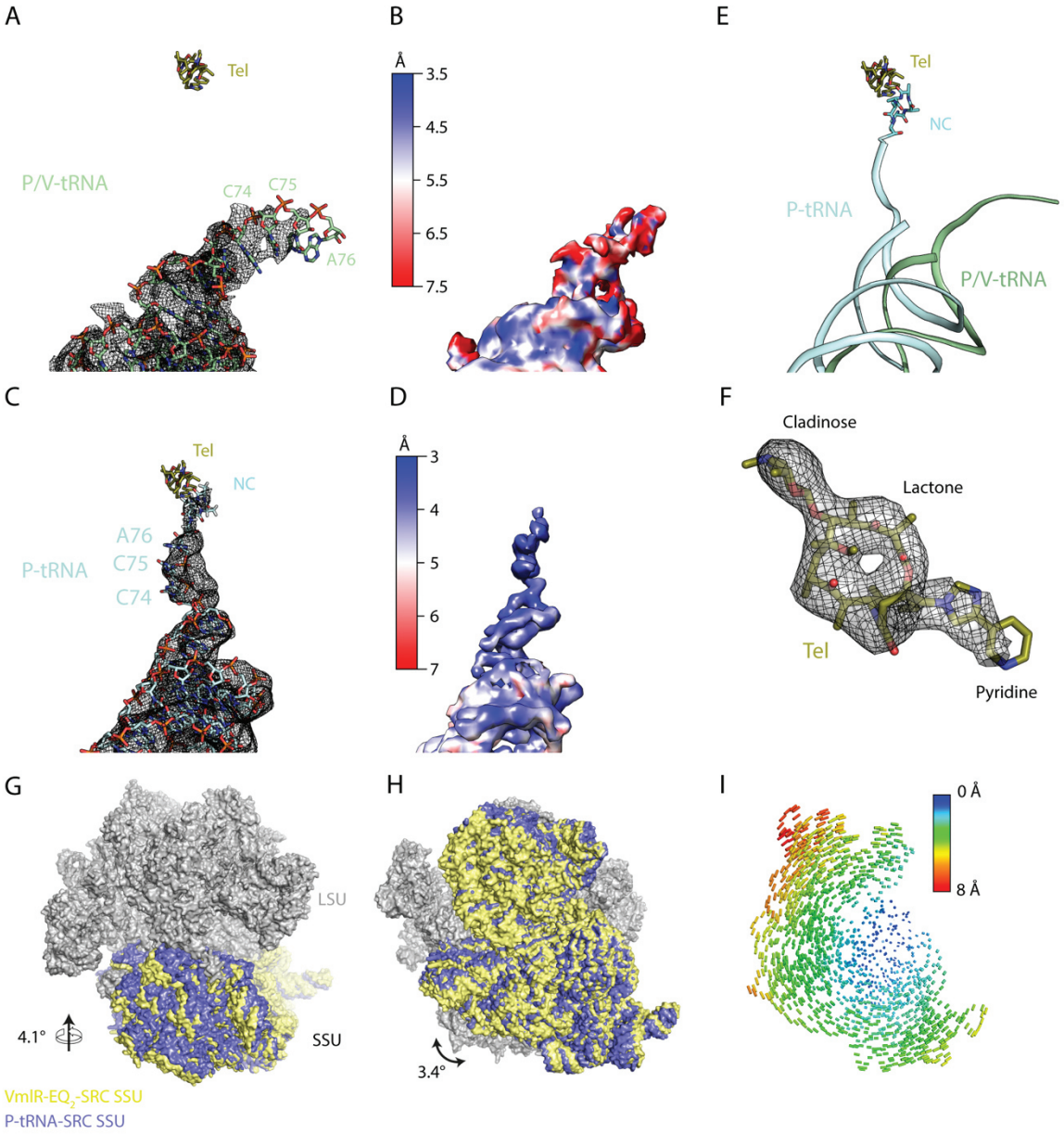

Figure S5. VmlR induces a P/V-site tRNA and subunit rotation. (**A**) Isolated cryo-EM electron density (grey mesh) for the P/V-tRNA (model in green sticks) from the VmlR-EQ_2-SRC. (**B**) Isolated cryo-EM electron density for the P/V-tRNA, as in (A), but coloured according to local resolution. (**C**) Isolated cryo-EM electron density (grey mesh) for the P-tRNA (model in cyan sticks) and ErmDL nascent chain (NC model in cyan sticks) from the P-tRNA-SRC. (**D**) Isolated cryo-EM electron density for the P-tRNA, as in (**C**), but colored according to local resolution. (**E**) Superimposition of P/V-tRNA (green ribbon) and ErmBL nascent chain (cyan) with P-tRNA (cyan ribbon). In (**A-E**), the binding site of telithromycin (Tel) is shown for reference. (**F**) Isolated cryo-EM electron density (grey mesh) for telithromycin (Tel, khaki sticks) from the P-tRNA-SRC, with cladinose, lactone ring and pyridine heterocycle indicated. (**G-H**) Alignment based on the LSU (grey) of the structures of the VmlR-EQ2-SRC (SSU, yellow) and P-tRNA-SRC (blue) revealing a (**G**) 4.1° swivel of the SSU head and (**H**) 3.4° rotation of the SSU

body. (**I**) Illustration of movement of the SSU between the VmlR-EQ2-SRC and P-tRNA-SRC. The length and color of the lines correspond to the degree of movement between each phosphate group in of the SSU between the VmlR-EQ2-SRC and P-tRNA-SRC structures. The view is the same as in (**H**).

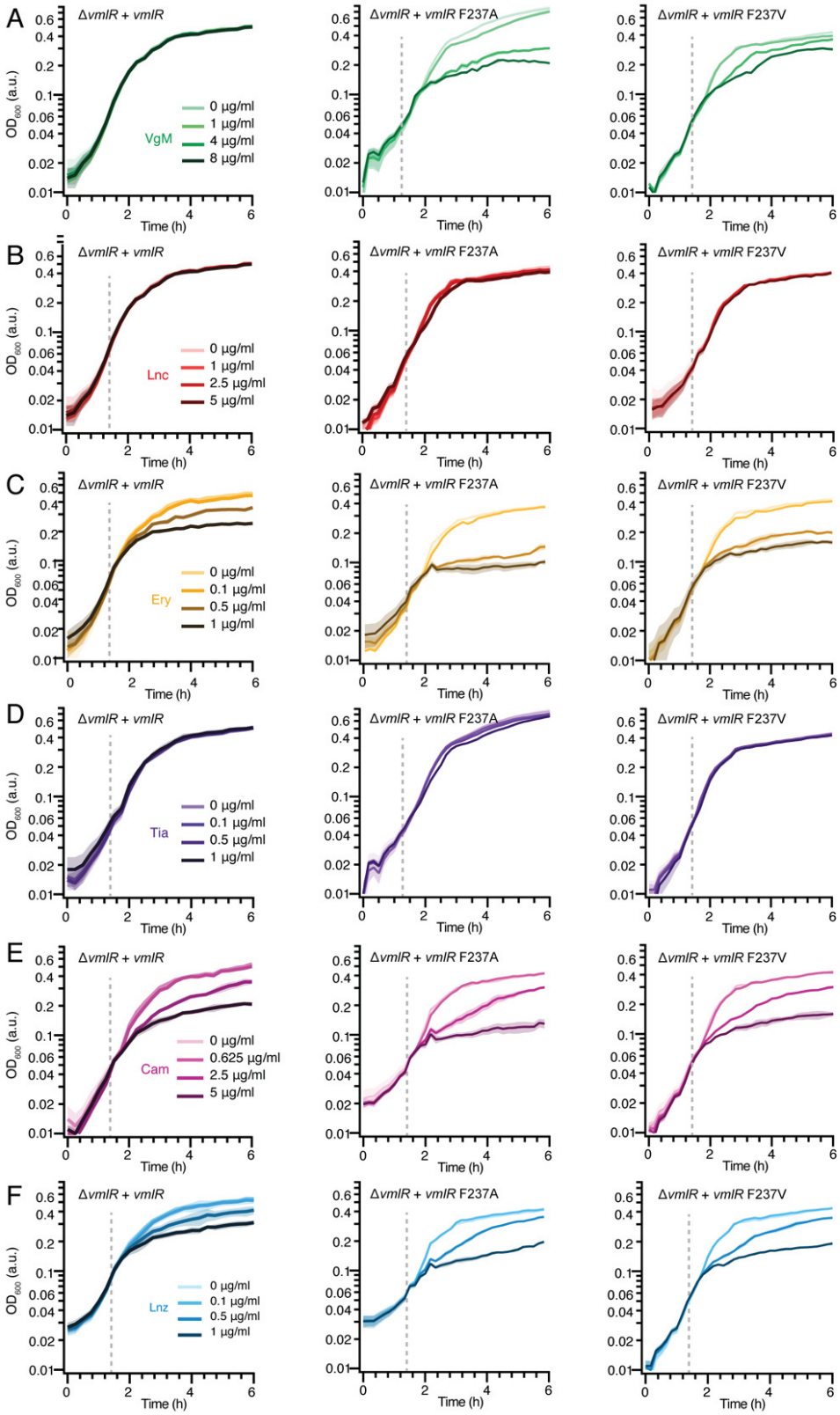

Figure S6. Antibiotic resistance conferred by VmlR variants *in vivo*. (**A-F**) Growth curves of *vmlR*-knockout (Δ*vmlR*) complemented by wildtype VmlR (Δ*vmlR* + *vmlR*, same panels as in Figure S4), or VmlR variants VmlR-F237A or VmlR-F237V grown in

the presence of increasing concentrations of (**A**) virginiamycin M1 (VgM), (**B**) lincomycin (Lnc), (**C**) erythromycin (Ery), (**D**) tiamulin (Tia), (**E**) chloramphenicol (Cam) and (**F**) linezolid (Lnz). Cells were diluted to an OD_{600} value of 0.01 and grown in LB (with IPTG for the complemented cells) at 37°C with shaking. After 90 minutes antibiotics were added at the indicated concentrations (dashed line) and growth was measured for a further 6 h.

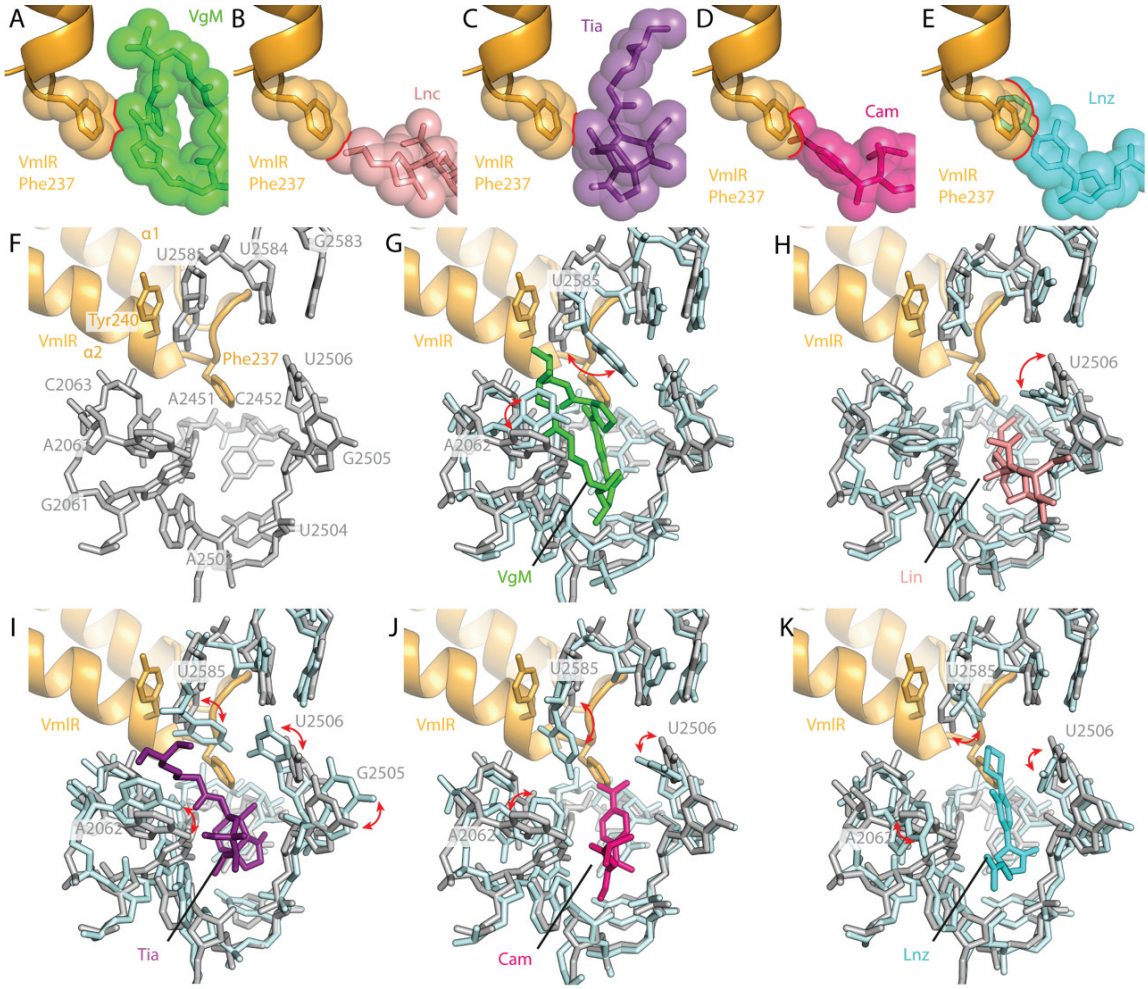

Figure S7. Conformation of the PTC in the presence of VmlR and antibiotics. (**A-E**) Zoom showing steric clash between Phe237 of VmlR with (**A**) virginiamycin M (VgM, green), (**B**) lincomycin (Lnc, salmon), (**C**) tiamulin (Tia, purple), (**D**) chloramphenicol (Cam, pink) and (**E**) linezolid (Lnz, cyan). (**F**) The conformation of selected 23S rRNA nucleotides (grey sticks) at the PTC in the presence of VmlR (orange). Tyr240 within the ARD of VmlR stacks upon U2585. (**G-K**) Superimposition of (**F**) with 23S rRNA nucleotides (cyan) that comprise the binding site of (**G**) virginiamycin M (VgM, green, PDB ID 1YIT) (25), (**H**) lincomycin (Lin, pink, PDB ID 5HKV) (26) and (**I**) tiamulin (Tia, purple, PDB ID 1XBP) (27), (**J**) chloramphenicol (Cam, pink, PDB ID 4V7U) (28), and (**K**) linezolid (Lnz, cyan, PDB ID 3DLL) (29). Conformational differences of 23S rRNA nucleotides between VmlR and antibiotic structures are highlighted with red arrows. Note that for (B) lincomycin (Lin, pink, PDB ID 5HKV) (26), the nucleobase of U2585 is not present in the model.

Table S1. Cryo-EM data collection, refinement and validation statistics

	VmlR-SRC (EMD ID EMD-0177, PDB 6HA8)	P-tRNA-SRC (EMD ID EMD-0176, PDB 6HA1)
Data collection		
Microscope	FEI Titan Krios	FEI Titan Krios
Camera	Falcon III	Falcon III
Magnification	131,951	131,951
Voltage (kV)	300	300
Electron dose (e^{-}/Å^2)	55.5	55.5
Defocus range (μm)	-0.8 to -1.6	-0.8 to -1.6
Pixel size (Å)	1.061	1.061
Initial particles (no.)	159,722	159,722
Final particles (no.)	33,392	68,652
Model composition		
Nonhydrogen atoms	146,414	140,834
Protein residues	6,053	5,300
RNA bases	4,610	4,622
Refinement		
Average resolution (Å)	3.5	3.1
Map CC (around atoms)	0.77	0.79
Map CC (whole unit cell)	0.75	0.79
Map sharpening *B* factor (Å^2)	-88.20	-88.14
R.m.s. deviations		
Bond lengths (Å)	0.010	0.007
Bond angles (°)	1.3	1.1
Validation		
MolProbity score	1.96 (100th percentile for structures 3.50Å ± 0.25Å)	1.92 (100th percentile for structures 3.10Å ± 0.25Å)
Clashscore	7.68 (80th percentile for structures ≥ 3Å)	7.12 (98th percentile for structures ≥ 2.85Å)
Poor rotamers (%)	0.87%	0.90%
Ramachandran plot		
Favored (%)	90.36 %	90.67 %
Allowed (%)	9.15 %	8.77 %
Disallowed (%)	0.49 %	0.56 %

Table S2. Primers used for construction of *B. subtilis* strains

VmlR-A-F	CATATGAAATACCGCAAAACAAG
VmlR-A-R	CAATGCCGCTTGAACTTTCTCCC-CCATATCCCTCGCTTTAAAGGGAG
VmlR-B-F	GGGAGAAAGTTCAAGCGGCATTG
VmlR-B-R	GCTTGAGTCAATTCCGCTGTCGCATAACGTCAGGAACTTGGACG
VmlR-C-F	CAAAATTAACGTACTGATTGGGTAGGATCCGCGGCTTGAGGATCAGACGCT GATTG
VmlR-C-R	CTGTCCCAGAATGATGTTCAGTAATG
chpA-R	CGCGGATCCTACCCAATCAGTACGTTAATTTTG
pAPNC-F	CGACAGCGGAATTGACTCAAGC
PhyvmlR_F	CGGATAACAATTAAGCTTAGTCGACGAAGGAGAGAGCGATAATGGCCGGC AAAGAGATCGTAACA
PhyvmlR_R	GTTTCCACCGAATTAGCTTGCATGCTTAGTCTTTTTTGTCTTGATGATCCAGC TCTTTTATTC
pHT002_R	GTCGACTAAGCTTAATTGTTATCCGCTCACAATTACACACATTATGCC
pHT002_F	GCATGCAAGCTAATTCGGTGGAAACGAGGTCATC
F237A	CTCAATCGACGAAAAAGGAAGGGGCTAAAGAATATCACCGGGTAAAAG
F237V	TCGACGAAAAAGGAAGGGGTTAAAGAATATCACCGGG
491STOPx2	CAGTTAAACGACGTTCCTTCAGAATGATAAGAGCGGGAGGAGC

References

1. Arenz S, *et al.* (2014) Drug sensing by the ribosome induces translational arrest via active site perturbation. *Mol Cell* 56(3):446-452.
2. Arenz S, *et al.* (2014) Molecular basis for erythromycin-dependent ribosome stalling during translation of the ErmBL leader peptide. *Nat Commun* 5:3501.
3. Zheng SQ, *et al.* (2017) MotionCor2: anisotropic correction of beam-induced motion for improved cryo-electron microscopy. *Nat Methods* 14(4):331-332.
4. Zhang K (2016) Gctf: Real-time CTF determination and correction. *J Struct Biol* 193(1):1-12.
5. Kimanius D, Forsberg BO, Scheres SH, & Lindahl E (2016) Accelerated cryo-EM structure determination with parallelisation using GPUs in RELION-2. *Elife* 5.
6. Scheres SH & Chen S (2012) Prevention of overfitting in cryo-EM structure determination. *Nat Methods* 9(9):853-854.
7. Kucukelbir A, Sigworth FJ, & Tagare HD (2014) Quantifying the local resolution of cryo-EM density maps. *Nat Methods* 11(1):63-65.
8. Moriya T, *et al.* (2017) High-resolution single particle analysis from electron cryo-microscopy images using SPHIRE. *J Vis Exp* (123).
9. Chen B, *et al.* (2014) EttA regulates translation by binding the ribosomal E site and restricting ribosome-tRNA dynamics. *Nat Struct Mol Biol* 21(2):152-159.
10. Bienert S, *et al.* (2017) The SWISS-MODEL Repository—new features and functionality. *Nucleic Acids Res* 45(D1):D313-D319.
11. Pettersen EF, *et al.* (2004) UCSF Chimera - A visualization system for exploratory research and analysis. *J Comput Chem* 25(13):1605-1612.
12. Emsley P & Cowtan K (2004) Coot: Model-building tools for molecular graphics. *Acta Crystallographica Section D - Biological Crystallography* 60:2126-2132.
13. Sohmen D, *et al.* (2015) Structure of the *Bacillus subtilis* 70S ribosome reveals the basis for species-specific stalling. *Nat Commun* 6:6941.
14. Fischer N, *et al.* (2015) Structure of the *E. coli* ribosome-EF-Tu complex at <3 Å resolution by C-corrected cryo-EM. *Nature* 520(7548):567-570.
15. Johnson ZL & Chen J (2018) ATP binding enables substrate release from Multidrug Resistance Protein 1. *Cell* 172(1-2):81-89 e10.
16. Rozov A, Demeshkina N, Westhof E, Yusupov M, & Yusupova G (2015) Structural insights into the translational infidelity mechanism. *Nat Commun* 6:7251.
17. Adams PD, *et al.* (2010) PHENIX: a comprehensive Python-based system for macromolecular structure solution. *Acta Crystallogr D Biol Crystallogr* 66(Pt 2):213-221.
18. Chen VB, *et al.* (2010) MolProbity: all-atom structure validation for macromolecular crystallography. *Acta Crystallogr D Biol Crystallogr* 66(Pt 1):12-21.
19. Morimoto T, Ara K, Ozaki K, & Ogasawara N (2011) A simple method for introducing marker-free deletions in the *Bacillus subtilis* genome. *Methods Mol Biol* 765:345-358.

20. Katoh K & Standley DM (2013) MAFFT multiple sequence alignment software version 7: improvements in performance and usability. *Mol Biol Evol* 30(4):772-780.
21. Murina V, Kasari M, Reith M, Hauryliuk V, & Atkinson GC (2017) ABCF ATPases involved in protein synthesis, ribosome assembly and antibiotic resistance: structural and functional diversification across the tree of life. *bioRvix*: 10.1101/220046. Posted November 16, 2017.
22. Jia B*, et al.* (2017) CARD 2017: expansion and model-centric curation of the comprehensive antibiotic resistance database. *Nucleic Acids Res*:gkw1004.
23. Consortium U (2018) UniProt: the universal protein knowledgebase. *Nucleic Acids Res* 45(5):2699.
24. Karcher A, Schele A, & Hopfner KP (2008) X-ray structure of the complete ABC enzyme ABCE1 from *Pyrococcus abyssi*. *J Biol Chem* 283(12):7962-7971.
25. Tu D, Blaha G, Moore P, & Steitz T (2005) Structures of MLS_BK antibiotics bound to mutated large ribosomal subunits provide a structural explanation for resistance. *Cell* 121(2):257-270.
26. Matzov D*, et al.* (2017) Structural insights of lincosamides targeting the ribosome of *Staphylococcus aureus*. *Nucleic Acids Res* 45(17):10284-10292.
27. Schlunzen F, Pyetan E, Fucini P, Yonath A, & Harms J (2004) Inhibition of peptide bond formation by pleuromutilins: the structure of the 50S ribosomal subunit from *Deinococcus radiodurans* in complex with tiamulin. *Mol Microbiol* 54(5):1287-1294.
28. Dunkle JA, Xiong L, Mankin AS, & Cate JH (2010) Structures of the *Escherichia coli* ribosome with antibiotics bound near the peptidyl transferase center explain spectra of drug action. *Proc Natl Acad Sci U S A* 107(40):17152-17157.
29. Wilson DN*, et al.* (2008) The oxazolidinone antibiotics perturb the ribosomal peptidyl-transferase center and effect tRNA positioning. *Proc Natl Acad Sci U S A* 105(36):13339-13344.

Stringent response control by a bifunctional RelA enzyme in the presence and absence of the ribosome

Patrick Pausch[1], Maha Abdelshahid[2], Wieland Steinchen[1], Heinrich Schäfer[3], Fabio Lino Gratani[4], Sven-Andreas Freibert[5], Christiane Wolz[4], Kürşad Turgay[3*], Daniel N. Wilson[2,*] and Gert Bange[1,*]

[1] Center for Synthetic Microbiology & Dep. Of Chemistry, Hans-Meerwein-Strasse, C07, Philipps-University Marburg, Marburg, Germany

[2] Institute for Biochemistry and Molecular Biology, University of Hamburg, Hamburg, Germany.

[3] University of Hannover, Institute for Microbiology, Herrenhäuser Strasse 2, Hannover, Germany

[4] Interfaculty Institute of Microbiology and Infection Medicine, University of Tübingen, Tübingen, Germany

[5] Center for Synthetic Microbiology & Institute für Cytobiology und Cytopathology, Philipps-University Marburg, Marburg, Germany

*Correspondence: Gert.Bange@synmikro.uni-marburg.de, Daniel.Wilson@chemie.uni-hamburg.de and Turgay@ifmb.uni-hannover.de

Abstract

The stringent response enables metabolic adaptation of bacteria upon environmental changes and to stress conditions. RelA/SpoT Homologue (RSH)-type enzymes produce and degrade the pleiotropically acting second messenger nucleotides (p)ppGpp. Bifunctional Rel enzymes synthesize (p)ppGpp in the context of ribosomes stalled by deacyl-tRNA and degrade (p)ppGpp in their absence. Here we show by cryo-EM that the C-terminal domain (CTD) of Rel interacts with the ribosome to enable (p)ppGpp synthesis by its catalytic N-terminal domain (NTD). In the absence of the ribosome, Rel forms a symmetric homodimer through contacts of its NTD and the deacyl-tRNA binding site of its CTD. Our study shows how the relative orientation of CTD and NTD controls the reciprocal activities of (p)ppGpp-synthesis and -hydrolysis. Relative domain arrangement of Rel is tightly controlled by homodimerization, deacyl-tRNA and the ribosome. Thus, our study provides an in-depth molecular view on the Rel/RelA-dependent mechanism of the stringent response.

Metabolic adaptation upon alteration of environmental conditions, emerging cellular stress and nutrient limitation is essential for the fitness of living organisms. Most bacteria and the chloroplasts of plants employ the stringent response (SR) in order to adjust transcription, translation and metabolic pathways for control over growth and cell proliferation, but also pathogenicity[1,2]. At the heart of the SR, RelA/SpoT Homologue (RSH)-type proteins sense stress and control the cellular levels of the pleiotropically acting second messenger alarmones (p)ppGpp[1,2].

Nutrient limitation (i.e. amino acid starvation) is sensed by the RSH-type proteins Rel/RelA recognizing uncharged tRNAs in context of translationally stalled ribosome complexes (SRCs) to synthesize (p)ppGpp[3–5]. Rel/RelA is a multi-domain protein that can be divided into N-terminal and C-terminal domains (NTD and CTD, respectively) (**Fig. 1a**). The NTD consists of the hydrolase (Hyd) subdomain, which degrades (p)ppGpp to GTP/GDP and pyrophosphate (PP_i) in the absence of stress, and the synthetase (Syn) subdomain that catalyzes (p)ppGpp synthesis by transfer of PP_i from ATP to the 3'-OH ribose of GTP/GDP when stalled ribosomes and uncharged tRNAs are sensed[5–7]. The CTD comprises four subdomains, the TGS (ThrRS, GTPase and SpoT), AH (Alpha Helical), RIS (Ribosome Inter-Subunit) and ACT (Aspartate kinase, Chorismate mutase, TyrA) (**Fig. 1a**). The enzymatic activities of the NTD are regulated by the CTD such that in the absence of the ribosome, the CTD inhibits (p)ppGpp synthesis by the NTD[8–11] and this autoinhibition is relieved in the presence of the ribosome[4,5,12–15]. Noteworthy, the Hyd subdomain is inactive in RelA, but functional in Rel proteins, hence RelA is referred to as monofunctional and Rel is classified as a bifunctional long RSH-type protein (**Fig. 1a**). Bifunctional Rel proteins are widely conserved in Gram-positive bacteria of the phylum Firmicutes, such as the model organism *Bacillus subtilis*, but also pathogenic representatives, such as *Mycobacterium tuberculosis*, *Listeria monocytogenes* and *Staphylococcus aureus*. In Gram-negative bacteria, such as *Escherichia coli* and *Vibrio cholera*, a second long RSH-type protein, the bifunctional protein SpoT, complements monofunctional RelA[16]. In contrast to Rel/RelA, SpoT does not interact with ribosomes, but was shown to be responsive to fatty acid biosynthesis stress via TGS-mediated interaction with the acyl-carrier protein ACP[17]. Noteworthy, SpoT has also been implied to be regulated by depletion of the 6S RNA[18] and it has been shown that hydrolysis activity is suppressed in the presence of deacyl-tRNAs[19].

Structural data for long RSH-type proteins is available for the monofunctional *E. coli* RelA on the ribosome[13–15] and for the NTDs of the bifunctional *Streptococcus dysgalactiae* and *M. tuberculosis* Rel proteins[20,21]. Three cryo-EM studies of *E. coli* RelA bound to the ribosome in the presence of deacyl-tRNA recently revealed that RelA adopts an elongated 'open' conformation to stimulate alarmone production by disrupting the autoinhibitory interaction of the CTD with the NTD[13–15]. In this extended conformation, RelA recognizes the uncharged CCA 3′-end of the A/R-tRNA (30S A-site/RelA-bound) via the TGS subdomain and positions the NTD near the 30S spur for alarmone production. The TGS is C-terminally followed by the AH subdomain, which wraps around the A/R-tRNA and connects to the 50S and 30S bridging RIS domain. The extreme C-terminal ACT subdomain folds back towards the A/R-tRNA and is buried in a cavity within the 50S subunit, formed by the A-site finger, helix 89, L16 and the P-site tRNA[13–15]. Exactly how RelA is capable of entering the ribosome to associate in this intricate conformation is unclear, but recent data suggests that RelA associates with the ribosome as a preformed RelA•deacyl-tRNA complex[22]. Upon dissociation from the ribosome and deacyl-tRNA, Rel was suggested to fall back in an inhibited NTD-CTD approximated 'closed' conformation[23], which might also involve oligomerization of Rel[8,24]. The crystal structure of NTD of *S. dysgalactiae* Rel revealed that it can adopt two conformations, namely, the Syn 'ON' / Hyd 'OFF' state and the Syn 'OFF' / Hyd 'ON' state for either alarmone synthesis, or breakdown, respectively[20]. Based on these conformations, a reciprocal regulation of the antagonistic catalytic activities has been proposed that might involve a ligand-induced signal transmission between the Syn and Hyd active sites[20]. However, an evaluation of this proposal is difficult because no structural data have visualized how the CTD could regulate the bifunctional activity of the NTD in the absence of the ribosome. Moreover, no structural information of a bifunctional Rel protein in the context of a stalled ribosome is available.

Therefore, we set out to obtain a comprehensive structural and functional characterization of the bifunctional Rel protein from *B. subtilis* to dissect its regulation in the presence and the absence of the ribosome.

Results

Cryo-EM structure of the B. subtilis Rel•stalled ribosomal complex

To ascertain whether *B. subtilis* Rel protein binds to the ribosome analogously to the bifunctional *E. coli* RelA protein, we assembled and analyzed a *B. subtilis* Rel•stalled ribosomal complex (Rel•SRC) using single particle cryo-EM, similarly to that described previously for the *E. coli* RelA•SRC[14]. The *B. subtilis* SRC was obtained using a disome purification protocol based on a dicistronic mRNA encoding an R8K variant of the ErmDL stalling leader peptide (**Supplementary Fig. 1**). The *B. subtilis* Rel•SRCs were formed by incubating the *B. subtilis* ErmDL-R8K•SRC with deacyl $tRNA^{Lys}$ and purified recombinant *B. subtilis* Rel protein in the presence of GDP and the non-hydrolysable ATP analogue α, β-methylene-ATP. The cryo-EM data for the *B. subtilis* Rel•SRC were collected on a Titan Krios with a Falcon II direct electron detector. From a total of 650,054 ribosomal particles, 3D classification revealed a diverse array of ribosome subpopulations containing only P-tRNA (8.9%), E-tRNA (12.5%), both P- and E-tRNAs (25.3%), as well as A- and P-tRNAs with (33.4%) and without (9.1%) E-tRNA (**Supplementary Fig. 2**). Despite this vast heterogeneity, it was also possible to obtain a small subpopulation (10.3%) that contained P- and E-tRNAs, as well as A/R-tRNA and Rel bound within the ribosomal A-site (**Supplementary Fig. 2**). This subpopulation could be further refined to yield a final cryo-EM map of the *B. subtilis* Rel•SRC (**Fig. 1b**) with an average resolution of 4.5 Å (**Supplementary Fig. 3a**) and local resolution reaching to 3.8 Å within the core of the ribosome (**Supplementary Fig. 3b,c**). Local resolution calculations for the A/R-tRNA and Rel ranged from 5-7 Å (**Supplementary Fig. 3d,e**), consistent with the high flexibility of the A/R-tRNA and Rel within the ribosomal binding site, as observed previously for the *E. coli* RelA•ribosome complexes[13–15]. The resolution allowed an unambiguous rigid body fit of homology models for the *B. subtilis* Rel TGS, RIS and ACT subdomains to the cryo-EM density, together with the A/R-tRNA (**Supplementary Fig. 3**). The density for the AH linker connecting the TGS and RIS of *B. subtilis* Rel was relatively well-resolved and most consistent with the conformation observed in the *E. coli* RelA model from Loveland *et al*., 2016[13] (**Supplementary Fig. 3**). The overall conformation of *B. subtilis* Rel and the A/R-tRNA on the *B. subtilis* 70S ribosome is analogous to that observed previously for the

E. coli RelA•ribosome complexes[13–15]. (**Figure 1c,d**). Also the individual domains of *B. subtilis* Rel appear to establish a similar set of contacts with the ribosome, such that the TGS interacts with the CCA-end of the deacyl A/R-tRNA and with h5/h15 of the small subunit, the ACT interacts with H38, L16 and H43 of the large subunit, and the RIS bridges both subunits by interaction with H38 and S19 (**Supplementary Fig. 4**). The NTD was poorly ordered in the *B. subtilis* Rel•SRC, but additional density could be seen when the map was filtered to 12 Å in a similar but distinct position to that observed previous for the *E. coli* RelA•ribosome complexes[13–15] (**Supplementary Fig. 5**). Hence, (p)ppGpp synthesis might be triggered by detraction of the inhibitory CTD from the NTD upon ribosome contact, which was also suggested for the *Ec*RelA protein[14,15]. Taken together, our structural analysis suggests that the regulation of bi- and monofunctional RSH-type proteins, Rel and RelA, by the SRC seems very similar.

Crystal structure of B. subtilis RelΔRIS-ACT

To understand how the CTD regulates the NTD in the absence of the ribosome, we determined the crystal structure of Rel in the absence of the ribosome. Because crystallization of full-length Rel was unsuccessful, we employed a C-terminally truncated Rel lacking the RIS and ACT subdomains. Both the RIS and ACT subdomains were previously shown to be dispensable for regulating Rel activity in absence of the ribosome[11]. The protein was purified by Ni-ion affinity and size exclusion chromatography (SEC). On SEC, RelΔRIS-CT migrated with an apparent molecular weight (MW) of a homodimer, when compared to MW standards and the Rel-NTD (**Fig. 2a and Supplementary Fig. 7**). The crystal structure of *Bs*RelΔRIS-CT was determined by molecular replacement using the structure of *Sd*Rel-NTD (PDB 1VJ7[20], chain B) and refined to a resolution of 3.95 Å (**Table 1**). The resolution was sufficient to enable the secondary structure elements of the Syn, Hyd, TGS and AH subdomains of Rel to be unambiguously placed with high confidence into the electron density map (**Supplementary Fig. 6a,b**). The structure shows a nucleotide-free Rel in an elongated conformation in which the TGS contacts the Syn subdomain via an interface involving α-helix 14 and β-strands 7/8 of the Syn and TGS, respectively (**Fig. 2b**). Further inspection of the crystal packing showed that a Rel homodimer, as suggested by SEC (**Fig. 2a**), is formed across the crystallographic two-fold axis (**Fig. 2c and Supplementary Fig. 6a,b**). Within the symmetric Rel

homodimer, each monomer contacts the other through interactions between the TGS-AH subdomains and the NTD (**Fig. 2c,d**). The loop connecting helices α17 and α18 of the TGS of one monomer interacts with the loop connecting helix α12 and strand β3 of the Syn of the other, and *vice versa* (**Fig. 2e**). Helices α19 and α20 of the AH subdomain of one monomer binds into an extended surface cavity formed by helices α1/α3 of the Hyd and helix α15 and the sheet β3/4 of the Syn of the other (hereafter referred to as: NTD-cleft), and *vice versa* (**Fig. 2e**). It is important to note that the N-terminus of Rel interacts with the α-helical bundle (AHb) of the AH subdomain. Taken together, our structure of the Rel homodimer shows that the CTDs of each monomer are involved in stabilizing the homodimer via the NTDs in the absence of the ribosome. Of note; the Rel homodimer would not allow binding of deacyl-tRNA, because the deacyl-tRNA binding site is masked by the opposing monomer (**Fig. 2d**).

Rel forms a homodimer

Our structure of the Rel homodimer shows that the NTD interacts with the TGS-AH subdomains. Indeed, an *in vitro* pull-down assay employing an N-terminally GST-tagged NTD shows its ability to interact with the TGS-AH (**Fig. 3a**). The NTD-CTD interaction is highly salt-sensitive, consistent with the structure showing that this interaction is mainly comprised of polar contacts (**Fig. 2d**). Moreover, our GST pull-down assay shows that the presence of the ATP and GTP substrates, as well as the product pppGpp, have no impact on the NTD-CTD interaction (**Supplementary Fig. 8**). To quantify the interaction strength between the two Rel monomers within the homodimer, we employed Bio Layer Interferometry (BLI) allowing the determination of the dissociation constant (K_D) and the contributing k_{on} and k_{off} values (**Fig 3b and Supplementary Fig. 9 and Supplementary Tab. 2**). Full-length Rel and RelΔRIS-CT interacted with biologically relevant dissociation constants (K_D) of ≈ 10.6 ± 0.2 μM and ≈ 4.9 ± 0.01 μM, respectively, which suggested that the ACT and RIS domains are not required for homodimerization. No relevant self-interaction of TGS-AH subdomain was observed (i.e. K_D of ≈ 129 ± 7 μM), suggesting that that the TGS-AH does not interact in solution. Although our analysis suggested a self-interaction of the NTD with a K_D of ≈ 43.1 ± 3.3 μM, comparison of the k_{on} (≈ 7.5 ± 0.5 $M^{-1}s^{-1}$) and k_{off} ($3.2x10^{-4}$ ± $7.5x10^{-6}$ s^{-1}) showed that any NTD homodimer formed is extremely short lived. The structure of the Rel homodimer also suggested that the NTD should be

capable of interacting with the TGS-AH, firstly, via the TGS *in cis*, and, secondly, via the TGS-AH *in trans*. Indeed, analysis of the interaction between the NTD and TGS-AH revealed two K_Ds in the low µM-range ($K_D1 \approx 4.8 \pm 0.1$ µM and $K_D2 \approx 10.7 \pm 0.2$ µM) and a stoichiometry of one NTD to two TGS-AH.

To test our predictions *in vivo*, we also performed Bacterial two-Hybrid (B2H) assays. Again, self-interaction was observed for the full-length Rel and RelΔRIS-CT, whereas self-interaction was not observed for the TGS-AH domain (**Fig. 3c**). In contrast to our SEC (Fig.2a), the Rel structure (Fig. 2b-e) and the BLI results (Fig. 3c), we also observed self-interaction for the NTD in the B2H assay. It might be that the B2H-tags (i.e. T25 and T18) change the k_{off} observed in the BLI, and thus enable a longer lifespan of a NTD homodimer sufficient to activate the reporter. Whether factors exist that stabilize a putative NTD homodimer in the cellular context is therefore possible, but requires further investigation. Taken together, our experiments show that Rel forms a symmetric homodimer stabilized through extensive interactions between the NTD and CTD of both monomers.

Ribosome-dependent domain reorganization of Rel

Next, we wanted to understand the conformational differences between the structure of Rel associated with the ribosome compared to its free homodimeric form. Structural comparison of the two states showed that the TGS and AH subdomains are rotated by ~90° and shifted by up to ~125 Å (AH bundle) and ~50 Å (TGS) (**Fig. 4**). The comparison further revealed that rearrangement of α-helix 7 and α-helix 16 that connect the NTD and CTD, hereafter called joint helices, is accompanied by the association of the TGS at α-helix 14 of the Syn subdomain (**Fig. 4**). Moreover, α-helix 20 (α20) of the AH subdomain is straighter in the Rel homodimer than in the ribosome-bound Rel. The bending of α20 in the ribosome-bound state seems to be induced by the A/R-tRNA, and would be antagonistic for Rel homodimer formation (**Fig. 4**). Therefore, straightening of α20 in the absence of the SRC should allow accommodation of the AH domain at the NTD-cleft for homodimer formation (**Fig. 2c**). Taken together, our structural comparison of Rel in the presence and absence of the SRC shows that the CTD undergoes major conformational rearrangements relative to the NTD.

Repression of the synthetase in the Rel homodimer

To delineate conformational changes upon TGS and AH association to the NTD, we superimposed the Rel homodimer structure with the NTD of the ribosome-bound *Ec*RelA[13] and to the bifunctional *Sd*Rel-NTD[20] in the Hyd 'OFF' / Syn 'ON' (PDB 1VJ7; chain A) and Hyd 'ON' / Syn-'OFF' (PDB 1VJ7; chain B) states. Superimposition of the NTDs according to the central three α-helical bundle (C3HB; α8-α10), which is situated between the Syn and Hyd domains and does not rearrange upon ribosome release, revealed that our structure adopts a conformation matching the Hyd 'ON' / Syn 'OFF' state described for the isolated *Sd*Rel-NTD (**Fig. 5**). This observation is supported by the root mean square deviation (r.m.s.d.) values for the NTDs compared to *Bs*Rel-NTD, showing that the closest matching structure is *Sd*Rel-NTD chain B in the Hyd 'ON' / Syn 'OFF' configuration (r.m.s.d.s: *Sd*Rel-NTD chain A: 1.107; SdRel-NTD chain B: 0.649; *Ec*RelA-NTD: 1.065)

Association of the TGS and AH to helix α14 and the central mixed β-sheet (mβs) of the Syn domain leads to an orchestrated movement of α14, α15 and the mβs along the helix α12, resulting in displacement of the catalytic loop and helix α13, which are essential for magnesium binding and association of ATP for PP_i transfer to GTP/GDP[20] (**Fig. 5**). Interestingly, helix α11 that connects the Syn core to the C3HB was previously suggested not to undergo a conformational rearrangement during the activity switch[20]. The reasoning for this proposal was that helix α11 seemed to be locked via its covalent and van der Waals association to helix α10 of the C3HB[20]. However, in our structure, helices α11 and α13 follow the displacement of helix α12, which as a consequence reorganizes and restricts the active site (**Fig. 5**). Association of CTD and NTD also results in reorganization of the joint helices, which leads to insertion of the loop connecting α16 and TGS (lid-loop) into the Syn active site (**Figs. 4 and 5**). Both rearrangements should render the Syn domain inactive and prevent (p)ppGpp synthesis in absence of the ribosome.

Activation of the hydrolase in the Rel homodimer

Juxtaposed to the Syn, the Hyd domain is stabilized through interactions of the N-terminus of Rel and the AH′ domain of the dimer partner (see above, **Fig. 5**). AH association to the N-terminus and helix α1 leads to relocation of helix α1 towards the center of the structure, stabilizing the Hyd domain by placement of helices α2-α5 in a

comparable configuration to that observed in the hydrolase 'ON' state described by Hogg *et al.*[20] (**Fig. 5**). Helices α3 and α4 harbor the catalytic motifs critical for the coordination of the manganese cofactor, substrate-binding and catalysis[2,20]. Based on the structure of the *Sd*Rel-NTD[20], hydrolase activation was previously suggested to involve stabilization of the loop connecting helices α8 and α9, which is also stabilized in our structure as evident by the pronounced electron density for the loop (**Supplementary Fig. 6c**). Furthermore, the joint helix α7 is relocated from a helix α6 proximal position, as observed in the *Sd*Rel Hyd 'OFF' state[20], towards helix α9 (**Fig. 5**). The linker connecting α6 and α7 is in turn stabilized in proximity to the active center. Coordinated movement of the joint helices α7 and α16 in concert with the association of the TGS and AH might therefore enable the synchronized regulation of the opposing synthetase and hydrolase activities of the NTD.

The TGS/Syn interface and the joint helices are the critical determinants of Rel regulation

To ascertain that the critical CTD elements that regulate Rel in the absence of the ribosome reside within TGS and AH domain, we successively truncated Rel domain-wise from its C-terminus and assayed its pppGpp synthetase and hydrolase activities using our previously described HPLC-based assay[25] (**Fig. 6a,b**). As expected, full-length Rel showed a low pppGpp synthetic and a strong pppGpp hydrolytic activity (**Fig. 6b**), showing that Rel is in the Syn 'OFF' / Hyd 'ON' state when not bound to the ribosome. This situation did not change with the successive truncation of the ACT, RIS and the α-helical bundle of the AH subdomain (AHb) (**Fig. 6b**). Moreover, deletion of the AHb-interacting N-terminal residues, alanine 2 to threonine 8, also did not affect the activities. However, when the AH (ΔAH-CT) and especially AH and TGS (NTD) subdomains were removed, we observed inhibition of the pppGpp hydrolytic activity and concomitant stimulation of the pppGpp synthetic activity. These findings illustrate that the TGS and AH domains are critical for maintaining the Syn 'OFF' / Hyd 'ON' state of Rel, and their removal leads to an inversion into the Syn 'ON' / Hyd 'OFF' state.

Next, we analyzed the impact of the lid-loop on Rel activity by mutating the lid-loop glutamate 380 and phenylalanine 381 and into alanine (E380A/F381A). This Rel variant exhibited a mild increase in pppGpp synthesis and decrease in pppGpp hydrolysis compared to the full length Rel (**Fig. 6b**). By contrast, when we varied

arginine 125 and methionine 127 within the joint helix α7 (R125A/M127A), we observed the opposite effect with a pronounced repression of hydrolase and activation of synthetase activities, respectively (**Fig. 6b**). These results demonstrate the importance of the joint helix for synchronizing the synthetase and hydrolase activities of Rel.

To analyze the impact of the interface formed by the AH domain and the NTD-cleft *in trans*, we introduced charge-reversing mutations E65R, F330R, E334R alone as well as in combination (E65R/F330R/E334R). In our GST pull-down assay, these GST-immobilized NTD variants displayed a loss of interaction with a TGS-AH domain fragment (**Fig. 6c**). However, neither the single amino acid variants, nor the combination, affected regulation of Rel (**Fig. 6b**). By contrast, when we exchanged residues Y279 or G283 that reside in the interface connecting the Syn and TGS *in cis*, we could not only detect a loss of NTD/TGS-AH interaction in our GST pull-down assay (**Fig. 6c**), but both variants also showed a pronounced loss of pppGpp hydrolytic activity (**Fig. 6b**). While the synthetase activity of the G283E mutant was strongly stimulated, the Y279E variant was incapable of synthesizing (p)ppGpp, likely due to a destabilized Syn subdomain (**Fig. 6b**). Taken together, our data show that the TGS subdomain primarily regulates the NTD activities *in cis*, and the joint helices α7 and α16 synchronize the reciprocal activities within the NTD. The *in trans* interaction of the AH subdomain with the NTD cleft is important for homodimer stability, however, apparently not important for the regulation of activity.

In vivo dissection of Rel

To substantiate our structural and biochemical findings, we evaluated our Rel variants *in vivo* using the cell growth-reducing property of (p)ppGpp[1,2] and a *B. subtilis* strain lacking all (p)ppGpp synthetases and hydrolases (named: (p)ppGpp0 (BHS_214)). We then introduced the *rel* mutants *in trans* into the *amy* locus under the control of an IPTG inducible promoter. IPTG-induced production and growth analysis revealed that the *rel* knockout can be functionally complemented by *rel in trans*, as well as by Rel lacking the 8 N-terminal residues (ΔN8) or lacking the RIS and ACT subdomains (ΔRIS-CT) (**Fig. 7a**). By contrast, we observed a prominent reduction in growth (lack of complementation) when we further truncated Rel by removing the AH and TGS subdomains (ΔAH and NTD in **Fig. 7a**), which is in excellent agreement with the *in vitro* assays (**Fig. 6b**). Similarly, the Rel-

R125E/M127E (joint helix α7), Y279E and G283E variants (TGS/Syn interface *in cis*) also showed severe growth defects consistent with a deregulated NTD as observed in the *in vitro* experiments (**Fig. 7a and 6b**). Moreover, the E380A/F381A as well as E65R, F330R, E334R and their combination (E65R/F330R/E334R) did not show growth inhibition, in line with our biochemical assays (**Figs. 7a and 6b**).

We further assessed the Rel variant production as well as the presence of (p)ppGpp by indirectly monitoring the production levels of the ribosome hibernation promoting factor (HPF, previously called YvyD), the synthesis of which correlates with the cellular (p)ppGpp concentration[26,27] (**Fig. 7b**). Western blotting revealed that all complementing Rel variants were synthesized at levels comparable to the wildtype (**Fig. 7b**). In addition, the production of HPF was strongly induced when CTD truncations of Rel involve the AH and TGS, as well as for R125E/M127E, Y279E and G283E Rel variants (**Fig. 7b**), consistent with an elevated intracellular (p)ppGpp level. Interestingly, the Y279E variant appeared to synthesize (p)ppGpp *in vivo* (**Fig. 7b**), but was deficient in (p)ppGpp synthesis *in vitro* (**Fig. 6b**). A possible explanation might be that the Syn fold is stabilized within context of the intracellular environment. In conclusion, the results suggest that the critical regulative elements mainly reside within the TGS and joint helices (α7, α16) and are in agreement with the growth phenotypes (**Fig 7a**) and *in vitro* data (**Fig. 6b**).

Discussion

Ribosome interaction of mono- and bifunctional RelA/Rel enzymes

During the SR, the (p)ppGpp synthetase activities of the monofunctional RelA as well as of the bifunctional Rel are activated through their association to ribosomes stalled by uncharged tRNAs in the ribosomal A-site. Consistent with the high (39%) sequence identity between the bifunctional *B. subtilis* Rel and monofunctional *E. coli* RelA proteins, we also observed a high similarity between the structure of the bifunctional *B. subtilis* Rel•SRC determined here and previous structures of monofunctional *E. coli* RelA•SRCs[13–15]. Importantly, we observed that on the ribosome, the bifunctional *B. subtilis* Rel protein also adopts an open conformation where the conserved CTD interacts with the A/R-tRNA as well as components of the small and large ribosomal subunits, analogously to those observed between the

ribosome and the monofunctional *E. coli* RelA[13–15]. Therefore, our findings suggest that the ribosome-dependent activation of the Syn activity of bifunctional Rel proteins utilizes an analogous mechanism to that observed for monofunctional RelA proteins, namely, by adopting an open conformation on the ribosome to relieve the autoinhibition of the CTD on the NTD.

One major difference between Rel and RelA is that the Rel protein contains a functional Hyd domain whereas RelA has an inactive 'pseudo' Hyd domain. Therefore, ribosome binding in the case of bifunctional Rel proteins leads not only to stimulation of the synthetase activity, but also inactivation of the Hyd domain. In the structure of the *B. subtilis* Rel•SRC determined here, the NTD exhibited a high degree of flexibility, suggesting no obvious stabilizing interactions existing with the ribosome (**Supplementary Fig. 5**). Therefore, we favour a model whereby activation of Syn allosterically inactivates the Hyd[20], rather than inactivation of the Hyd via additional interactions with components of the ribosome. In this regard, we note that the sarcin-ricin loop (SRL) of the ribosome, which is involved in activation of the GTPase activity of translation factors such as EF-Tu and EF-G, has been cross-linked to the NTD of RelA[22]. This observation led to the suggestion that the SRL may be involved in activation of (p)ppGpp synthesis of RelA[22]. However, our structure does not support any stable interaction between the NTD and the SRL and, moreover, α-sarcin, a toxin which cleaves and inactivates the SRL, was recently reported to have no effect on the ribosome-stimulated (p)ppGpp synthesis of RelA[28]. Taken together, we propose that the Syn activity of the bifunctional Rel proteins is activated by adopting an open conformation on the ribosome, as observed also for monofunctional RelA proteins[13–15], and the Hyd subdomain is inactivated allosterically.

Rel forms a homodimer in the absence of the ribosome

Our structural and functional analysis of Rel shows that the protein forms a symmetric homodimer. The homodimer interface is established between the NTD of one monomer and the TGS-AH domains of the other, and *vice versa* (**Fig. 1c,d**). One consequence of the homodimer structure is that in the full-length Rel protein the ACT/RIS domains of one monomer come into close proximity to the N-terminus of the other monomer, and *vice versa* (**Fig. 8**). A previously observed decrease in fluorescence resonance energy transfer (FRET) between the NTD and CTD of Rel

upon tRNA addition is in agreement with the homodimer architecture of our structure[23]. Although an isolated ACT subdomain structure suggested a role in homodimerization (PDB-ID: 2KO1), our structure clearly shows that the ACT subdomains cannot self-interact in the context of the full-length homodimer. Truncation of the ACT (and RIS) subdomains did not weaken the affinity of the monomers for each other in our BLI experiments, supporting the idea that homodimerization is independent of the RIS/ACT domains. Taken together, our Rel structure, *in vitro* and *in vivo* analysis have revealed for the first time how an NTD-CTD interaction mediates homodimer formation.

Regulation of Rel in the cellular context

Our crystal structure shows that the TGS-AH subdomains form *in trans* interactions with the NTD across the homodimer interface. Moreover, the TGS subdomain forms *in cis* contacts with the Syn subdomain of the NTD. Our functional analysis shows that the *in trans* contacts are essential for homodimer formation, but seem to play no major role on the regulation of the catalytic activities of the NTD. In the context of the homodimer, the NTD is in a Hyd 'ON' / Syn 'OFF' configuration as previously postulated by Hilgenfeld and coworkers from the structure of an isolated *Sd*NTD[20]. Based on the *Sd*NTD structures, the authors suggested that the C3HB couples the Hyd and Syn subdomains via the catalytic elements to reciprocally regulate their activities[20]. Our Rel crystal structure, supported by our functional studies, now shows that previously unrecognized elements, namely the 'joint helices', transmit the relative orientation of the TGS as part of the CTD to the NTD, and thereby regulates the reciprocal enzymatic activities of Rel. This *in cis* interaction of the TGS-Syn subdomains is crucial for this regulation, as supported by our *in vitro* and *in vivo* experiments.

Interestingly, the TGS-AH/NTD *in trans* interaction does not contribute to the regulation of the enzymatic activities, raising the question as to the biological function of this interface and the dimerization of Rel. The symmetric arrangement of the Rel homodimer and the accompanying *in trans* interactions lead to a masking of the tRNA binding site at the TGS-AH domain by the NTD. This observation suggests that homodimerization might modulate interaction of Rel with deacyl-tRNA. Following this idea, binding of deacyl-tRNA would then compete with homodimerization, and eventually lead to dissolution of the Rel homodimer. In our model, binding of the

deacyl-tRNA would have no impact on the Hyd 'ON' / Syn 'OFF' configuration, which solely relies on the TGS/Syn interaction *in cis*. Thereby, Rel could be prevented from futile (p)ppGpp synthesis in the absence of the ribosome. This idea is supported by the observation that RelA is not activated by association to deacyl-tRNA, but requires the presence of both, the ribosome and the deacyl-tRNA[4]. Hence, the hypothetical deacyl-tRNA induced dimer dissociation results in a Rel•deacyl-tRNA complex 'primed' for future interaction with a ribosome, which displays a matching A-site codon. Indeed, recently *E. coli* RelA was shown to require the association of deacyl-tRNA prior to its interaction with the ribosome[22].

In summary, we propose the following model for the regulation of Rel (**Fig. 8**): In the absence of stress, translating ribosomes are provided with aa-tRNAs by EF-Tu•aa-tRNA•GTP ternary complexes for protein biosynthesis and Rel resides in a homodimeric Hyd 'ON' / Syn 'OFF' state to degrade (p)ppGpp (**Fig. 8**, left). Upon accumulation of deacyl-tRNAs (indicative for amino acid starvation), the Rel homodimer dissociates and binds deacyl tRNA to form Rel•deacyl-tRNA complexes, which are 'primed' for binding to cognate ribosomes (**Fig. 8**, middle). Upon recognition of a cognate ribosome, the preformed Rel•deacyl-tRNA complex associates to the SRC and switches into the Syn 'ON' and Hyd 'OFF' state for (p)ppGpp synthesis (**Fig. 8**, right).

Methods

Cloning, expression, and purification for heterologous production of Rel

B. subtilis rel gene fragments were amplified by PCR from *B. subtilis* 168 genomic DNA and cloned into pET24d (Novagen) between the *Nco*I and *Bam*HI sites to generate expression constructs (see table M1, M2 for primers and plasmids). Mutagenesis of *rel* was performed via overlap extension PCR and subsequent cloning as described above. The *rel*-Hyd-Syn fragment sequence was subcloned from pET24d into pGAT (N-terminal GST) using *Nco*I and *Xho*I, or amplified by PCR from full-length mutant genes for cloning into pGAT. Constructs were transformed in *E. coli* BL21(DE3) (Novagen) for overexpression. Cells were inoculated into two liters of LB medium, supplemented with 25 g lactose, ampicillin (100 mg/l) or kanamycin

(50 mg/l) depending on the selection marker and incubated at 30 °C over night under rigorous shaking (180 revolutions per minute (rpm)). Cells were harvested by centrifugation (3,500 x g, 20 min, 4 °C) and resuspended in 20 ml lysis buffer (20 mM HEPES-NaOH, pH 8.0, 500 mM NaCl, 40 mM imidazole) before lysis in a M-110L Microfluidizer (Microfluidics). The lysate was cleared at 47,850 x g for 20 min at 4 °C and the supernatant was applied onto two pre-equilibrated 1 ml HisTrap FF columns (GE Healthcare) for Ni-NTA affinity chromatography. After a wash step with 15 column volumes (CV) of lysis buffer, proteins were eluted with three CV of elution buffer (20 mM HEPES-NaOH, pH 8.0, 500 mM NaCl, 500 mM imidazole). Proteins were concentrated to 1 ml and further purified by size exclusion chromatography using a HiLoad 16/600 Superdex 200 column (GE Healthcare) equilibrated in size exclusion buffer (20 mM HEPES-NaOH, pH 7.5, 500 mM NaCl). For the purification of RelA variants used for the enzymatic activity assay, buffers were supplemented with an additional amount of 500 mM NaCl and 5% glycerol. The main peak fractions were concentrated and concentrations were determined by measuring the absorbance at 280 nm (wavelength) using a NanoDrop Lite Spectrophotometer. Proteins were flash frozen in liquid nitrogen and stored at -80 °C up to two weeks.

Purification of B. subtilis 70S ribosomes

The *B. subtilis* 70S ribosomes were prepared following a procedure described in [29], with some modifications. Cells (*B. subtilis* strain 168) were grown overnight in LB (Luria-Bertani) liquid medium using baffled flasks at 37°C with shaking (220 rpm). A volume of 6L of LB medium was inoculated at a 1:100 dilution with an overnight culture and cells were grown to an OD_{600} of 1.5. Cells were harvested by centrifugation at 5000 × *g* for 15 min at 4°C (Sorvall, SLC 6000 rotor) and the cell pellet was resuspended in buffer A (20 mM HEPES (pH 7.4), 30 mM NH_4Cl, 10 mM $Mg(OAc)_2$, 6 mM β-mercaptoethanol and 1x Complete EDTA-free Protease Inhibitor cocktail (Roche)). Cells were then disrupted using the microfluidizer (Microfluidics), followed by centrifugation at 30,000 × *g* for 30 min at 4°C to remove cellular debris (Sorvall, SS-34 rotor). The supernatant was then centrifuged at 151,457 × g (Type 45 Ti, Beckman Coulter) for 4.5 h at 4°C. The crude ribosome pellet was resuspended in 5 mL of cold buffer A and loaded onto a 10-50% sucrose gradient (total of 100 A_{260}/ml per tube) followed by centrifugation at 89,454 ×g using an SW28 rotor (Beckman Coulter) for 4 h at 4°C. The fractions corresponding to the 70S ribosomes

were collected using a Gradient Station (Biocomp) with an Econo UV Monitor (Biorad) and a FC203B Fraction Collector (Gilson). The collected fractions were then pooled together and the 70S ribosomes pelleted at 92,159 × g for 2.5 h at 4°C using a TLA-110 rotor (Beckman Coulter). The 70S pellet was re-suspended in buffer A followed by concentration determination and then aliquots were snap-frozen in liquid nitrogen and stored at -80°C.

Generation and purification of the B. subtilis SRC

The *B. subtilis* stalled ribosome complex (SRC) was generated based on the disome approach similar to that used previously for the *E. coli* RelA•SRC[14] (**Supplementary Fig. 1**). However, the *2XermCL* construct used for the *E. coli* RelA•SRC did not work efficiently with *B. subtilis* ribosomes (data not shown) and was therefore replaced by a construct based on the ErmDL leader peptide (Uniprot entry code P62188) derived from the macrolide resistance plasmid pE194. The *ermDL* sequences used in the *2XermDL* construct were modified from the original sequence by substitution of the 8th codon CGT (Arg) with AAG (Lys). The *2XermDL* construct was then synthesized (Eurofins, Germany) such that it contained a T7 promoter followed by a strong ribosome binding site (RBS) spaced by seven nucleotides to the ATG (AUG start codon) of the first *ermDL_R8K* cistron. A linker of 22 nts separated the stop codon of the first *ermDL_R8K* cistron and the start codon of the second *ermDL_R8K* cistron. The linker also comprised the strong RBS seven nucleotides upstream of the ATG start codon of the second *ermDL_R8K* cistron, enabling initiation of translation independent from the first *ermDL_R8K* cistron. The complete sequence of *2XermDL_R8K* construct is:

5′-

*TAATACGACTCACTATAGGG*AGTTTTATAA**GGAGG**AAAAAATATGACACACTCAA TGAGA**CTT**AAGTTCCCAACTTTGAACCAGTAAAGTTTTATAA**GGAGG**AAAAAATA TGACACACTCAATGAGA**CTT**AAGTTCCCAACTTTGAACCAGTAA-3′

(T7 promoter, italics; RBS, bold; ErmDL ORF, underlined with CTT codon in P-site of stalled ribosome shown in bold; Annealing site for complementary DNA oligonucleotide, underlined). *In vitro* translation of the *ermDL_R8K* construct was performed using 12 µg of *ermDL_R8K* PCR product, 100 µM telithromycin dissolved in DMSO (0.3% final DMSO concentration) as well as 600 pmoles of purified *B. subtilis* 70S ribosomes in 250 µL reaction of the PURExpress delta ribosome kit

(NEB). Translation reactions were analyzed on sucrose density gradients (10-55% sucrose in buffer A (50 mM HEPES-KOH, pH 7.4, 100 mM KOAc, 25 mM $Mg(OAc)_2$, 6 mM β-mercaptoethanol, 100 µM telithromycin and 1x Complete EDTA-free Protease Inhibitor cocktail (Roche)) by centrifugation at 154,693 × *g* (SW40 rotor, Beckman Coulter) for 3 h at 4°C. For ErmDL_R8K•70S complex purification, disome fractions were collected using a Gradient Station (Biocomp) with an Econo UV Monitor (Biorad) and a FC203B Fraction Collector (Gilson). Purified ErmDL_R8K disomes were concentrated by centrifugation at 88,760 × *g* for 4 h at 4°C (TLA120.2 rotor, Beckman Coulter). To obtain monosomes of the ErmDL_R8K•70S complex, a short DNA oligonucleotide (5′-ttcctccttataaaact-3′, Metabion) was annealed to the linker between the *ermDL_R8K* cistrons, generating a DNA-RNA hybrid that could be cleaved by RNase H (NEB) treatment in buffer A at 25°C for 1 h. After cleavage of the disomes, ErmDL_R8K•70S complex monosomes were again purified and concentrated by centrifugation at 88,760 × *g* for 4 h at 4°C (TLA120.2 rotor, Beckman Coulter).

Generation of the B. subtilis Rel• SRC

The *B. subtilis* Rel•SRC was assembled similarly to that used previously for the *E. coli* RelA•SRC[14] (**Supplementary Fig. 1**). The *B. subtilis* Rel•SRC was formed using a final concentration of 0.125 µM ErmDL_R8K•70S complex monosomes, 0.625 µM *B. subtilis* Rel (N-terminal His_6-tag), 0.625 µM $tRNA^{Lys}$ (Sigma-Aldrich), 500 µM α, β-methylene-ATP (Sigma-Aldrich), 500 µM GDP and 10 µM telithromycin. All components were pre-dissolved in buffer A and the reaction was incubated at 37°C for 20 min.

Cryo-electron microscopy and single particle reconstruction

A total of 5 A_{260}/ml of the *B. subtilis* Rel•SRC was applied to 2 nm pre-coated Quantifoil R3/3 holey carbon supported grids and vitrified using a Vitrobot Mark IV (FEI, Netherlands). Data collection was performed using EM-TOOLS (TVIPS GmbH) on a Titan Krios transmission electron microscope equipped with a Falcon II direct electron detector (FEI) at 300 kV at a pixel size of 1.084 Å and a defocus range of 0.7-2.2 µm. Ten frames (dose per frame of 2.4 $e^-/Å^2$) were aligned using Motion Correction software[30]. Power-spectra, defocus values and astigmatism were

determined with CTFIND4 software[31]. Micrographs showing Thon rings beyond 4 Å were manually inspected for good areas and power-spectra quality. Automatic particle picking was performed on 4,411 micrographs using Gautomatch (http://www.mrc-lmb.cam.ac.uk/kzhang/) and *E. coli* 70S as a template[14]. 2-dimensional class averaging was performed to exclude non-ribosomal particles and then single particles were processed using RELION 2.1[32]. 650,054 particles were first subjected to 3D refinement using *B. subtilis* 70S ribosome as reference structure[33]. This was followed by 3D classification using RELION into 10 classes with 6 distinct subpopulations (**Supplementary Fig. 2**). Only subpopulation 1 (67,047 particles) had stoichiometric density for Rel and was further refined to yield a final reconstruction with an average resolution (at 0.143 FSC) of 4.5 Å (**Supplementary Fig. 3a**) with local resolution reaching to 3.8 Å (**Supplementary Fig. 3b-c**) within the core of the ribosomal subunits. The other subpopulations 2-6 did not contain density for Rel, but rather had various combinations of A-, P- and E-site tRNAs (**Supplementary Fig. 2**).

Molecular model of the B. subtilis Rel•SRC

Homology models of the *B. subtilis* Rel TGS, RIS and ACT subdomains were generated using Swiss-model[34] and could be unambiguously rigid body-fitted using UCSF Chimera[35] into the electron density of the cryo-EM map of the *B. subtilis* Rel•SRC (**Supplementary Fig. 3d-i**). The homology model for the TGS, ACT, and RIS subdomains of *B. subtilis* Rel were based on *E. coli* RelA•70S complex (PDB ID 5IQR[15]). TGS (residues 390-469), RIS (residues 585-655) and ACT (residues 656-731) correlated with *E. coli* template model residues 404-505, 594-662, 663-744 respectively. In order to yield the best fit, each domain was fitted individually as a rigid body into the locally filtered density of the *B. subtilis* Rel•SRC (**Supplementary Fig. 3d-i**). The homology model for the AH subdomain of *B. subtilis* Rel was based on the AH subdomain from the *E. coli* RelA in the *E. coli* RelA•70S complex (PDB ID 5KPX[13]) (**Supplementary Fig. 3h**). The models for A/R-tRNA, P-tRNA and E-tRNA were taken from the *E. coli* RelA•70S complex (PDB ID 5IQR[15]) and also fitted as rigid-bodies into the cryo-EM map of the *B. subtilis* Rel•SRC complex (**Supplementary Fig. 3e**). The models for the *B. subtilis* ribosomal subunits were based on the PDB IDs 3J9W[33] and 6HA1[36].

Crystallization, data collection, and structure determination

Purified *Bs*RelΔRIS-CT was concentrated to an absorbance at 280 nm of 20 AU (NanoDrop Lite Spectrophotometer), corresponding to an estimated concentration of 22.2 mg/ml, and subjected to crystallization by sitting drop vapor-diffusion at 20 °C. Tetragonal bipyramidal crystals grew within one day in drops containing 1 µl *Bs*RelΔRIS-CT and 1 µl crystallization buffer (1 M Lithium chloride, 0.1 M Bicine pH 9.0, 10% PEG6000 (w/v), final pH 9.0). Crystals were transferred into crystallization buffer containing 20% (v/v) glycerol as cryo-protectant, subsequently flash frozen and stored in liquid nitrogen. Diffraction data was collected at beamline ID29 of the European Synchrotron Radiation Facility (ESRF), Grenoble, France[37]. Data was processed with the XDS program package for data reduction[38]. Merging and scaling was performed using the AIMLESS program as implemented in the CCP4 package[39]. The *Bs*RelΔRIS-CT dataset was solved by molecular replacement using the *Sd*Rel-NTD crystal structure (PDB-ID: 1VJ7[20], chain B) via the CCP4 implemented program Phaser[40]. Coot[41] in combination with Refmac5 (CCP4 package) and phenix.refine (PHENIX package) was used for iterative model building and refinement[42]. Figures were prepared in PyMol.

Crystallographic and cryo-EM data availability

Cryo-EM maps have been deposited in the EMDB under accession codes XXX and XXX. Coordinates for the crystal structure of *Bs*Rel have been deposited at the PDB under the accession code 6HJ9.

GST pull-down

50 µl Glutathione Sepharose 4B beads (GE Healthcare) were washed with 1 ml binding buffer (50 mM Tris-HCl, pH 8.0, 500 mM NaCl). The beads were resuspended in 500 µl binding buffer and 4 nmol GST-NTD protein was added for the coupling reaction to the beads for 20 min at 4 °C on a turning wheel. Beads were washed twice with 1 ml binding buffer. After discarding of the binding buffer, 1 ml pull down buffer (50 mM Tris-HCl, pH 8.0, 5 mM $MgCl_2$, 100 mM NaCl) was added to the beads. For the GST pull down in dependence of the NaCl concentration, pull down buffers with 500 mM, 300 mM, 200 mM and 100 mM NaCl were used. For the GST pull down in dependence of the presence of nucleotides, the buffer contained 50 mM Tris-HCl, pH 8.0, 5 mM $MgCl_2$, 100 mM NaCl and nucleotides (ATP, GTP and/or

pppGpp) each at a concentration of 1 mM. Subsequently, 8 nmol of the TGS-AH fragment was added and the beads were incubated for 20 min at 4 °C on a turning wheel to allow for complex formation. Beads were washed three times with the respective pull down buffer and proteins were eluted in 50 µl elution buffer (20 mM GSH, 50 mM Tris-NaOH, pH 8.0, 500 mM NaCl) for 3 min at 20 °C. Finally, beads were pelleted in a tabletop centrifuge at 17300 x g for 3 min at 20° C and 15 µl of the eluate was analyzed on SDS-PAGE (15 % PAA). Band intensity was quantified by ImageJ[43].

Bacterial two-hybrid assay

Full-length and truncated versions of *B. subtilis rel* were subcloned from pET24d_His-*Bsrel* into BamHI digested plasmids, pUT18C and pKT25 (Euromedex) by Gibson assembly using oligonucleotides listed in Table M3. Bacterial two-hybrid experiments were performed as described previously[44]. Briefly, for each interaction experiment, *E. coli* BTH101 (containing a RelA mutation) was co-transformed with two plasmids (pUT18C and pKT25 derivatives) selected on LB agar plates supplemented with 50 µg/ml kanamycin and 100 µg/ml ampicillin. Each interaction measurement is based on analyses of 6 independently isolated colonies from freshly transformed cells. Clones were inoculated in LB containing 5 mM IPTG and grown at 30 °C overnight in a 24-well plate. OD_{600} was determined and 200 µl of each culture transferred to 800 µl of Z-buffer (8 g of Na_2HPO_4 x $12H_2O$, 3.125 g of NaH_2PO_4 x H_2O, 0.375 g of KCl, 0.123 g of $MgSO_4$ x $7H_2O$ dissolved in 500 ml distilled water, adjusted to pH 7, 1.35 ml β-mercaptoethanol is freshly added). 1 drop of 0.01% SDS and 2 drops of chloroform were added and 50 µl of the upper phase transferred to 150 µl of Z-buffer in a 96-well plate. For each sample 40 µl of ortho-Nitrophenyl-β-galactosidase (ONPG, 4 mg/ml final concentration) was added and A_{420} measured in 30 intervals using microtiter plate reader Infinite M200 Pro (Tecan). The relative β-galactosidase activity for each sample was determined by (OD_{420} at time t2 - OD_{420} at time t1)/ t2 – t1 (sec)/OD600. The time points t2 and t1 were chosen from the linear part of the kinetic.

Analytical size exclusion

Proteins were purified by Ni-NTA and size exclusion chromatography, as described above. Due to the co-precipitation of Rel with cellular RNA species during protein

purification which might affect the migration behavior of Rel on SEC, we employed the H420E RelΔRIS-CT variant in the analytical SEC that does not interact and therefore do not co-precipitate with tRNA, as also recently observed for the *Ec*RelA H432E variant[22]. Analytical size exclusion chromatography was performed using a Superdex 200 Increase 10/300 GL column (GE Healthcare) pre-equilibrated in size exclusion buffer (20 mM HEPES-NaOH, pH 7.5, 500 mM NaCl, 5% glycerol). The calculated apparent molecular weights were derived from the calibration curve obtained from the Gel Filtration Calibration Kit (LMW, HMW; GE life sciences) according to the manufacturers protocol.

Bio Layer Interferometry

The Rel-H420E protein and its truncation variants were purified as described above. All binding steps were performed in 20 mM HEPES-NaOH, pH 7.5, 500 mM NaCl, 200 µM $MnCl_2$ on an Octet K2 System (Pall ForteBio). Ligand proteins were biotinylated using EZ-Link Sulfo-NHS-Biotin (Thermo Scientific #21217 LOT TD261836). The respective protein was incubated with a 2-fold molar excess of EZ-Link for 20 min. Subsequently, the protein was desalted using a Zeba Spin Column (Thermo Scientific #89882 LOT TA262955). The biotinylated proteins were immobilized on Super Streptavidin (SSA) Biosensors (Pall ForteBio) by preparing 200 µl of a 50 µM solution in a black 96-well plate (Greiner) and a loading step for 900 s followed by a washing step for 30 s. The analyte was titrated form 30 µM to 3.75 µM in a 1:1 dilution series in 200 µl final volume. Measurements were repeated at least twice for each of the four concentrations. Association and dissociation was both measured for 600 s (except for delta_RIS-CT both was measured for 900 s). Baseline was recorded prior and after association/dissociation for 120 s in 20 mM HEPES-NaOH, pH 7.5, 500 mM NaCl, 200 µM $MnCl_2$. For each measurement a reference was recorded omitting the analyte in solution. For K_D determination, the reference curves were subtracted from the sample curves. Subsequently, the binding and dissociation curves were fit to standard 1:1, 2:1 or 1:2 global binding models using the Pall ForteBio analysis software (specified in **Supplementary Figure 9**).

Alarmone preparation, and Rel activity assay

pppGpp was produced as described previously[45]. All Rel-H420E variants were purified as described above. Assays for pppGpp hydrolytic and synthetic activity of

Rel were carried out in 20 mM Tris-HCl, pH 7.5, 50 mM NaCl, 1 mM $MnCl_2$ and 10 mM $MgCl_2$. 5 µM of Rel or its variants (see table M2) were incubated at 37°C in presence of 1 mM of pppGpp for 10 min (hydrolysis) or 1 mM ATP and 1 mM GTP for 60 min (synthesis). The reactions were stopped by adding two volume parts of chloroform followed by thorough mixing for 15 seconds subsequent incubation at 95°C for 15 seconds and flash-freezing in liquid nitrogen. While thawing, the samples were centrifuged (17300 *x g*, 30 min, 4°C) and the aqueous phase analyzed by HPLC on an Agilent 1100 Series system (Agilent technologies) equipped with a C18 column (EC 250/4.6 Nucleodur HTec 3 µM; Macherey-Nagel). Nucleotides were eluted isocratically with a buffer containing 50 mM KH_2PO_4, 50 mM K_2HPO_4, 10 mM TPAB (tetrapentylammonium bromide) and 25% (v/v) acetonitrile and detected at 260 nm wavelength in agreement with standards. pppGpp hydrolytic activity of Rel was estimated by quantification of pppGpp. pppGpp synthetic activity of Rel was estimated by quantification of AMP released equimolar to the alarmone pppGpp during the reaction. All measurements were performed in duplicates.

Cloning, strain construction, and B. subtilis growth assay

ywaC^{E154V} and *yjbM*^{E139V} mutations were introduced markerless into *B. subtilis 168* cells by successive transformation and recombination of plasmids pMAD-ywaC^{E154V} and pMAD-yjbM^{E139V} prior to transformation of *rel* constructs[46,47], yielding strain BHS_204. The *rel* gene was amplified from *B. subtilis 168* genomic DNA and cloned into pDR111[48] using the *Sal*I and *Sph*I restriction sites. Mutagenesis of *rel* was performed via overlap extension PCR and subsequent cloning as described above. Rel variants bearing the H77A, D78A or E324V mutation were first cloned in pMAD and subsequently amplified and cloned into pDR111. To generate pDR111-rel$^{H77A\ D78A\ E324V}$, a C-terminal fragment carrying E324V was amplified using primers 44, 63 and used as a megaprimer in a second reaction with primer 42 with rel$^{H77A\ D78A}$ as template. The resulting plasmids (for primers and plasmids see table M3-5) were linearized by digestion with *Sca*I and transformed into naturally competent BHS204 (*ywaC*^{E154V} *yjbM*^{E139V}) cells. Transformants were selected on 100 µg/ml spectinomycin and checked for loss of α-amylase activity. The resulting strains were subsequently transformed with a PCR-amplified fragment encoding *ΔrelA::erm*[12] and selected on 1 µg/ml erythromycin, 25 µg/ml lincomycin to generate the pppGpp^0 strain background. PCR and DNA sequencing confirmed the identity of the generated plasmids and

strains. Strains were grown in synthetic medium[49] supplemented with 0.5 % casamino acids (CAA) at 37 °C with orbital shaking at 200 rpm. At OD600 of 0.3, the medium was supplemented with 1 mM IPTG. After 30 min, cells were harvested by centrifugation at 3680 xg for 5 min. Cells were resuspended in buffer TE (10 mM TRIS-HCl pH 8.0, 1 mM EDTA) and disrupted by sonication. 8 µg total cleared protein extract was analysed by SDS-PAGE and western blotting according. Polyclonal antibodies raised against *Bs*Hpf (Pineda Antibody Service), *Bs*RelA-NTD (1-387) or rabbit IgG conjugated with HRP (Carl Roth, Karlsruhe, Germany) were used in 5000-fold dilutions. Signals were detected using a ChemoStar imaging system (Intas, Göttingen, Germany).

For the growth assay on agar plates, stationary-phase cultures were adjusted to an OD600 of 1.0 and serially diluted in 0.9 % NaCl. 5 µl cell suspension was spotted on LB agar plates with or without 1 mM IPTG. Plates were incubated at 37 °C over night (18 h).

Table M1 | **Primers used for cloning of heterologous expression vectors**

ID	Name	sequence (5′-3′)
0	Bs*rel*-BamHI-rev	TAATGGATCCTTAGTTCATGACGCGGCGCAC
1	Bs*rel*-NcoI-for	TTAACCATGGCGAACGAACAAGTATTG
2	Bs*rel*-H6-BamHI-rev	TAATGGATCCTTAATGGTGATGGTGATGGTGGTTCATGACGCGGCGCAC
3	Bs*rel*-H6-NcoI-for	TTAACCATGGGCCACCATCACCATCACCATAACGAACAAGTATTG
4	Bs*rel*-H6-392-NcoI-for	TTAACCATGGGCCACCATCACCATCACCATGACATGGTGTATGTCTTTAC
5	Bs*rel*-647-H6-BamHI-rev	TAATGGATCCTTAGTGATGGTGATGGTGATGTTCCCACTCTACCGGG
6	Bs*rel*-556-H6-BamHI-rev	TAATGGATCCTTAATGGTGATGGTGATGGTGCTTTCTCTCTTTTTCTG
7	Bs*rel*-556-BamHI-rev	TAATGGATCCTTACTTTCTCTCTTTTTCTG
8	Bs*rel*-495-H6-BamHI-rev	TAATGGATCCTTAATGGTGATGGTGATGGTGCTCACGGCCTTTTTCGAC
9	Bs*rel*-455-H6-BamHI-rev	TAATGGATCCTTAATGGTGATGGTGATGGTGCTTAGAGGTGAGAATTTC
10	Bs*rel*-387-H6-BamHI-rev	TAATGGATCCTTAATGGTGATGGTGATGGTGTGCATCTGTCGATTC
11	Bs*rel*-387-BamHI-rev	TAATGGATCCTTATGCATCTGTCGATTC

12	Bs*rel*-9-NcoI-for	TTAACCATGGCCGAGCAAGTTATAG
13	Bs*rel*-R125A-M127A-for	GCGGAAAATCATGCCAAAGCGTTTGTCGCTATG
14	Bs*rel*-R125A-M127A-rev	CATAGCGACAAACGCTTTGGCATGATTTTCCGC
15	Bs*rel*-R125E-M127E-for	GCGGAAAATCATGAGAAAGAGTTTGTCGCTATG
16	Bs*rel*-R125E-M127E-rev	CATAGCGACAAACTCTTTCTCATGATTTTCCGC
17	Bs*rel*-H420E-for	CTTACCGGATTGAATCTGAAATCGGC
18	Bs*rel*-H420E-rev	GCCGATTTCAGATTCAATCCGGTAAG
19	Bs*rel*-E380A-F381A-for	GATGCAGAAGCAGCTATGGAATCGC
20	Bs*rel*-E380A-F381A-rev	GCGATTCCATAGCTGCTTCTGCATC
21	Bs*rel*-E65R-for	CGTTGATCTTCGTATGGACCCTTC
22	Bs*rel*-E65R-rev	GAAGGGTCCATACGAAGATCAACG
23	Bs*rel*-F330R-for	GATCCGCACCCGTGAAATGCATG
24	Bs*rel*-F330R-rev	CATGCATTTCACGGGTGCGGATC
25	Bs*rel*-E334R-for	GAAATGCATCGTATAGCGGAATAC
26	Bs*rel*-E334R-rev	GTATTCCGCTATACGATGCATTTC
27	Bs*rel*-G283E-for	CGCGGTGCTTGAAATCATTCACAC
28	Bs*rel*-G283E-rev	GTGTGAATGATTTCAAGCACCGCG
29	Bs*rel*-Y279E-for	CATAAAGGACTGCGAAGCGGTGCTTGGC
30	Bs*rel*-Y279E-rev	GCCAAGCACCGCTTCGCAGTCCTTTATG
31	Bs*rel*-387-XhoI-rev	TAATCTCGAGTTAAATTTTGAGCGATTCC

790 **Table M2** | **Heterologous expression vectors**

plasmid	**cloning primers**	**product**	**purpose**	**source**
pET24d_His-*Bs*Rel	3, 0	*Bs*Rel-His_6-1-743	Cryo-EM	this work
pET24d_*Bs*Rel-ΔRIS-CT	1, 6	*Bs*Rel-1-556-His_6	crystallization	this work
pET24d_*Bs*Rel-NTD	2, 11	*Bs*Rel-His_6-1-387	cloning	this work
pGAT_*Bs*Rel-NTD	subcloned	GST-*Bs*Rel-His_6-1-387	pull-down	this work
pET24d_*Bs*Rel-TGS-AH	4, 7	*Bs*Rel-His_6-392-556	pull-down	this work
pET24d_*Bs*Rel	1, 2	*Bs*Rel-1-743-H420E-His_6	*in vitro*	this work
pET24d_*Bs*Rel-ΔACT	1, 5, 17, 18	*Bs*Rel-1-647-H420E-His_6	*in vitro*	this work
pET24d_*Bs*Rel-ΔRIS-CT	1, 6, 17, 18	*Bs*Rel-1-556-H420E-His_6	*in vitro*	this work
pET24d_*Bs*Rel-ΔAHb-CT	1, 8, 17, 18	*Bs*Rel-1-495-H420E-His_6	*in vitro*	this work
pET24d_*Bs*Rel-ΔAH-CT	1, 9, 17, 18	*Bs*Rel-1-455-H420E-His_6	*in vitro*	this work

pET24d_*Bs*Rel-NTD	1, 10	*Bs*Rel-1-387-His_6	*in vitro*	this work
pET24d_*Bs*Rel-ΔN8	12, 2, 17, 18	*Bs*Rel-9-743-H420E-His_6	*in vitro*	this work
pET24d_*Bs*Rel-R125A-M127A	1, 2, 13, 14, 17, 18	*Bs*Rel-1-743-R125A/M127A/H420E-His_6	*in vitro*	this work
pET24d_*Bs*Rel-R125E-M127E	1, 2, 15, 16, 17, 18	*Bs*Rel-1-743-R125E/M127E/H420E-His_6	*in vitro*	this work
pET24d_*Bs*Rel-E380A-F381A	1, 2, 19, 20, 17, 18	*Bs*Rel-1-743-E380A/F381A/H420E-His_6	*in vitro*	this work
pET24d_*Bs*Rel-E65R	1, 2, 21, 22, 17, 18	*Bs*Rel-1-743-E65R/H420E-His_6	*in vitro*	this work
pET24d_*Bs*Rel-F330R	1, 2, 23, 24, 17, 18	*Bs*Rel-1-743-E380A/F381A/H420E-His_6	*in vitro*	this work
pET24d_*Bs*Rel-E334R	1, 2, 25, 26, 17, 18	*Bs*Rel-1-743-F330R/H420E-His_6	*in vitro*	this work
pET24d_*Bs*Rel-E65R-F330R-E334R	1, 2, 21-26, 17, 18	*Bs*Rel-1-743-E65R/F330R/E334R/H420E-His_6	*in vitro*	this work
pET24d_*Bs*Rel-Y279E	1, 2, 29, 30, 17, 18	*Bs*Rel-1-743-Y279E /H420E-His_6	*in vitro*	this work
pET24d_*Bs*Rel-G283E	1, 2, 27, 28, 17, 18	*Bs*Rel-1-743-G283E /H420E-His_6	*in vitro*	this work
pGAT_*Bs*Rel-NTD-E65R	2, 31, ampl. from pET24d_*Bs*Rel-E65R	GST-*Bs*Rel-His_6-1-387-E65R	pull-down	this work
pGAT_*Bs*Rel-NTD-F330R	2, 31, ampl. from pET24d_*Bs*Rel-F330R	GST-*Bs*Rel-His_6-1-387-F330R	pull-down	this work
pGAT_*Bs*Rel-NTD-E334R	2, 31, ampl. from pET24d_*Bs*Rel-E334R	GST-*Bs*Rel-His_6-1-387-E334R	pull-down	this work
pGAT_*Bs*Rel-NTD-E65R-F330R-E334R	2, 31, ampl. from pET24d_*Bs*Rel-E65R-F330R-E334R	GST-*Bs*Rel-His_6-1-387-E65R-F330R-E334R	pull-down	this work
pGAT_*Bs*Rel-NTD-Y279E	2, 31, ampl. from pET24d_*Bs*Rel-Y279E	GST-*Bs*Rel-His_6-1-387-Y279E	pull-down	this work
pGAT_*Bs*Rel-NTD-G283E	2, 31, ampl. from pET24d_*Bs*Rel-G283E	GST-*Bs*Rel-His_6-1-387-G283E	pull-down	this work

Table M3 | Primers used for cloning of bacterial two-hybrid vectors

ID	Name	sequence (5′-3′)
32	Bs*rel*- pUT18c-for	tgcaggtcgactctagagATGGCGAACGAACAAGTATTGAC

33	Bs*rel*- pUT18c-rev	tcgagctcggtacccgggTTAGTTCATGACGCGGCGC
34	Bs*rel*- pKT25-for	gcagggtcgactctagagATGGCGAACGAACAAGTATTGAC
35	Bs*rel*- pKT25-rev	gttacttaggtacccgggTTAGTTCATGACGCGGCGC
36	Bs*rel*-NTD-pUT18c-rev	tcgagctcggtacccgggTTAAATTTTGAGCGATTCCA
37	Bs*rel*-NTD-pKT25-rev	gttacttaggtacccgggTTAAATTTTGAGCGATTCCA
38	Bs*rel*-NTD-TGS-AH-pUT18c-rev	tcgagctcggtacccgggTTACTTTCTCTCTTTTTCTGTTAGGCG
39	Bs*rel*-NTD-TGS-AH-pKT25-rev	gttacttaggtacccgggTTACTTTCTCTCTTTTTCTGTTAGGCG
40	Bs*rel*-TGS-AH-pUT18c-for	tgcaggtcgactctagagGACATGGTGTATGTCTTTACGCC
41	Bs*rel*-TGS-AH-pKT25-for	gcagggtcgactctagagGACATGGTGTATGTCTTTACGCC

Table M4 | **Bacterial two-hybrid vectors**

plasmid	primers	insert	purpose	source
pCG774 (pUT18C)	32, 33	*Bs*Rel	Bacterial two-hybrid	this work
pCG775 (pKT25)	34, 35	*Bs*Rel	Bacterial two-hybrid	this work
pCG776 (pUT18C)	32, 36	*Bs*Rel(1-387)	Bacterial two-hybrid	this work
pCG777 (pKT25)	34, 37	*Bs*Rel(1-387)	Bacterial two-hybrid	this work
pCG778 (pUT18C)	32, 38	*Bs*Rel(1-556)	Bacterial two-hybrid	this work
pCG779 (pKT25)	34, 39	*Bs*Rel(1-556)	Bacterial two-hybrid	this work
pCG780 (pUT18C)	40, 38	*Bs*Rel(392-556)	Bacterial two-hybrid	this work
pCG781 (pKT25)	41, 39	*Bs*Rel(392-556)	Bacterial two-hybrid	this work

795

Table M5 | **Primers used for cloning of *B. subtilis* vectors**

ID	Name	sequence (5′-3′)
42	SalI_SD_Bs*rel*_for	ACGCGTCGACTTGGGGGATGTATGATGGCGAACGAACAAGTATTG
43	SalI_SD2_Bs*rel*_for	ACGCGTCGACAGGATGGTGCTGAATATGGCGAACGAACAAGTATTG
44	SphI_Bs*rel*_rev	ACATGCATGCTTAGTTCATGACGCGGCGCAC

45	SalI_SD2_Bs*rel*_ΔN8	ACGCGTCGACAGGATGGTGCTGAATATGGCCGAGCAAGTTAT AGATAAAGCAC
46	sphI_Bs*rel*_ΔRIS-CT	ACATGCATGCTTACTTTCTCTCTTTTTCTGTTAGGC
47	sphI_Bs*rel*_ΔAH-CT	ACATGCATGCTTACTTAGAGGTGAGAATTTCAACG
48	sphI_Bs*rel*_ΔTGS-CT	ACATGCATGCTTAAATTTTGAGCGATTCCATAAATTC
49	rel_R125E-M127E_for	CAGGCGGAAAATCATGAAAAAGAATTTGTCGCTATGGCTC
50	rel_R125E-M127E_rev	GAGCCATAGCGACAAATTCTTTTTCATGATTTTCCGCCTG
51	Bs*rel*_E380A-F381A_for	CGACAGATGCAGAAGCAGCAATGGAATCGCTCA
52	Bs*rel*_E380A-F381A_rev	TGAGCGATTCCATTGCTGCTTCTGCATCTGTCG
53	Bs*yjbM*-flk1-EcoRI-F	TTAAGAATTCCCGCCCTGTAAATCTTATTT
54	Bs*yjbM* -flk1-R	TCCCATTGTTTGTCATCCATCATACATCCCCCAATTCCGA
55	Bs*yjbM* -flk2-F	AAGGAAGCGAGCAACAATAGGTAAAGGGGAAGAAGAGCA
56	Bs*yjbM* -flk2-NcoI-R	AATTCCATGGGTGCTGCCTGATGGAGTTGA
57	Bs*yjbM* -E139V-F	GAAAAGCATGTTCTCGTAGTAATACAGATCCGTACAC
58	Bs*yjbM* -E139V-R	GTGTACGGATCTGTATTACTACGAGAACATGCTTTTC
59	Bs*ywaC* -EcoRI-F	TTAAGAATTCATGGATTTATCTGTAACAC
60	Bs*ywaC* +fla-NcoI-R	TTAACCATGGAATCCAGCCGTACGGCTGC
61	Bs*ywaC* -E154V-F	GTCAAAGCAGTAATTC
62	Bs*ywaC* -E154V-R	GAATTACTGCTTTGAC
63	BsRelA-F330R-E334R-F	ATCCGCACCCGTGAAATGCATCGTATAGCGGAATAC
64	BsRelA-F330R-E334R-R	GTATTCCGCTATACGATGCATTTCACGGGTGCGGAT

Table M6 | **Primers used for sequencing of *B. subtilis* vectors and strains**

ID	Name	sequence (5′-3′)
65	*rel*_up_for	GTGTGCTGTCTGTTGTGAGC
66	*rel*_do_rev	CAAAACGGCAAAACTGCTCG
67	*ywaC*_seq	GAACCTTGCAGCAGACAGGG
68	*ywaC*_do_rev	CTATGACGCCAAACCTGTCG
69	*ywaC*_up_for	TTGCCTATGGATCCAGATCGC
70	*yjbM*_up_for	CTGATACCTCTGAAAGCTGC
71	*yjbM*_do_rev	CCTTATTGTAGGCTGTGCTG
72	*yjbM*_seq	GCAAACTATGGAGAAGAAATGG
73	P_{spac}seq	GTTGACTTTATCTACAAGGTGTGGC
74	*lacI*_rev	CGGCATACTCTGCGACATCG
75	*rel*_intra_seq	TACGATTTGTTGGCTGTCCG

Table M7 | ***B. subtilis* strains**

strain	detail	genotype	source
B. subtilis	wildtype	trpC2	Spizizen,

168			1958[46]
BHS_204	*ywaC, yjbM* inactive	trpC2 *ywaC*(E154V) *yjbM*(E139V)	this work
BHS_214	(p)ppGpp^0, *rel* knockout	trpC2 *ywaC*(E154V) *yjbM*(E139V) rel::erm	this work
BHS_624	(p)ppGpp^0, *rel* knockout, *rel* dead-Syn expression	trpC2 amyE::Phy-rel E324V spec ywaC(E154V) yjbM(E139V) rel::erm	this work
BHS_625	(p)ppGpp^0, *rel* knockout, *rel* dead-Hyd expression	trpC2 amyE::Phy-rel H77A D78A spec ywaC(E154V) yjbM(E139V) rel::erm	this work
BHS_752	(p)ppGpp^0, *rel* knockout, *rel* dead-Syn+Hyd expression	trpC2 amyE::Phy-rel H77A D78A E324V spec ywaC(E154V) yjbM(E139V) rel::erm	this work
BHS_923	(p)ppGpp^0, *rel* knockout, *rel* complementation	trpC2 amyE::Phy-rel spec ywaC(E154V) yjbM(E139V) rel::erm	this work
BHS_924	(p)ppGpp^0, *rel* knockout, *rel*ΔN8 expression	trpC2 amyE::Phy-rel 9-734 spec ywaC(E154V) yjbM(E139V) rel::erm	this work
BHS_926	(p)ppGpp^0, *rel* knockout, *rel*ΔRIS-CT expression	trpC2 amyE::Phy-rel 1-556 spec ywaC(E154V) yjbM(E139V) rel::erm	this work
BHS_928	(p)ppGpp^0, *rel* knockout, *rel*ΔAH-CT expression	trpC2 amyE::Phy-rel 1-455 spec ywaC(E154V) yjbM(E139V) rel::erm	this work
BHS_929	(p)ppGpp^0, *rel* knockout, *rel*NTDexpression	trpC2 amyE::Phy-rel 1-387 spec ywaC(E154V) yjbM(E139V) rel::erm	this work
BHS_930	(p)ppGpp^0, *rel* knockout, *rel*-R125E/M127E expression	trpC2 amyE::Phy-rel R125E M127E spec ywaC(E154V) yjbM(E139V) rel::erm	this work
BHS_931	(p)ppGpp^0, *rel* knockout, *rel*-E380A/F381A expression	trpC2 amyE::Phy-rel E380A F381A spec ywaC(E154V) yjbM(E139V) rel::erm	this work
BHS_979	(p)ppGpp^0, *rel* knockout, *rel*-E65R expression	trpC2 amyE::Phy-rel E65R spec ywaC(E154V) yjbM(E139V) rel::erm	this work
BHS_980	(p)ppGpp^0, *rel* knockout, *rel*-Y279E expression	trpC2 amyE::Phy-rel Y279E spec ywaC(E154V) yjbM(E139V) rel::erm	this work
BHS_981	(p)ppGpp^0, *rel* knockout, *rel*-G283 expression	trpC2 amyE::Phy-rel G283 spec ywaC(E154V) yjbM(E139V) rel::erm	this work
BHS_982	(p)ppGpp^0, *rel* knockout, *rel*-F330R expression	trpC2 amyE::Phy-rel F330R spec ywaC(E154V) yjbM(E139V) rel::erm	this work
BHS_983	(p)ppGpp^0, *rel* knockout, *rel*-E334R expression	trpC2 amyE::Phy-rel E334R spec ywaC(E154V) yjbM(E139V) rel::erm	this work
BHS_985	(p)ppGpp^0, *rel* knockout, *rel*-E65R F330R E334R expression	trpC2 amyE::Phy-rel E65R F330R E334R spec ywaC(E154V) yjbM(E139V) rel::erm	this work

Table M8 | *B. subtilis* vectors

plasmid	Cloning primers	source
pDR111-rel	43, 44	this work
pDR111-relΔN8	44, 45	this work
pDR111-relΔRIS-CT 1-556	43, 46	this work
pDR111-relΔAH-CT 1-469	43, 47	this work
pDR111-relNTD 1-387	43, 48	this work
pDR111-rel R125E M127E	43, 44, 49, 50	this work
pDR111-rel E380A F381A	43, 44, 51, 52	this work
pDR111-rel E65R	43, 44, 21, 22	this work
pDR111-rel F330R	43, 44, 23, 24	this work
pDR111-rel E334R	43, 44, 25, 26	this work
pDR111-rel E65R F330R E334R	43, 44, 21, 22, 63, 64	this work
pDR111-rel Y279E	43, 44, 29, 30	this work
pDR111-rel G283E	43, 44, 27, 28	this work
pDR111-rel E380A	43, 44	this work
pDR111-rel E324V	52, 44	this work
pDR111-rel H77A D78A	42, 44	this work
pDR111-rel H77A D78A E324V	42, 44	this work
pMAD-ywaCE154V	59 - 62	this work
pMAD-yjbME139V	53 - 58	this work

References

1. Hauryliuk, V., Atkinson, G. C., Murakami, K. S., Tenson, T. & Gerdes, K. Recent functional insights into the role of (p)ppGpp in bacterial physiology. *Nat. Rev. Microbiol.* **13,** 298–309 (2015).
2. Steinchen, W. & Bange, G. The magic dance of the alarmones (p)ppGpp. *Mol. Microbiol.* **101,** 531–544 (2016).
3. Wendrich, T. M., Blaha, G., Wilson, D. N., Marahiel, M. A. & Nierhaus, K. H. Dissection of the Mechanism for the Stringent Factor RelA. *Mol. Cell* **10,** 779–788 (2002).
4. Jenvert, R. K. & Schiavone, L. H. Characterization of the tRNA and ribosome-dependent pppGpp-synthesis by recombinant stringent factor from Escherichia coli. *FEBS J.* **272,** 685–695 (2005).
5. Haseltine, W. A. & Block, R. Synthesis of Guanosine Tetra- and Pentaphosphate Requires the Presence of a Codon-Specific , Uncharged Transfer Ribonucleic Acid in the Acceptor Site of Ribosomes. *Proc. Natl. Acad. Sci.* **70,** 1564–1568 (1973).
6. Haseltine, W. A. & Weber, K. MSI and MSII made on Ribosome in Idling Step of Protein Synthesis. *Nature* **238,** 381–384 (1972).
7. Sy, J. & Lipmann, F. Identification of the Synthesis of Guanosine Tetraphosphate (MS I) as Insertion of a Pyrophosphoryl Group into the 3'-

Position in Guanosine 5’-Diphosphate. *Proc. Natl. Acad. Sci.* **70,** 306–309 (1973).
8. Gropp, M., Strausz, Y., Gross, M. & Glaser, G. A. D. Regulation of Escherichia coli RelA Requires Oligomerization of the C-Terminal Domain. **183,** 570–579 (2001).
9. Schreibers, G. *et al.* Overexpression of the relA Gene in Escherichia coli *. *J. Biol. Chem.* **266,** 3760–3767 (1991).
10. Mechold, U., Murphy, H., Brown, L. & Cashel, M. Intramolecular Regulation of the Opposing (p) ppGpp Catalytic Activities of Rel Seq , the Rel / Spo Enzyme from Streptococcus equisimilis. **184,** 2878–2888 (2002).
11. Jain, V., Saleem-batcha, R., China, A. & Chatterji, D. Molecular dissection of the mycobacterial stringent response protein Rel. *Protein Sci.* **15,** 1449–1464 (2006).
12. Wendrich, T. M. & Marahiel, M. A. Cloning and characterization of a relA / spoT homologue from Bacillus subtilis. *Mol. Microbiol.* **26,** 65–79 (1997).
13. Loveland, A. B. *et al.* Ribosome.RelA structures reveal the mechanism of stringent response activation. *Elife* **5,** 1–23 (2016).
14. Arenz, S. *et al.* The stringent factor RelA adopts an open conformation on the ribosome to stimulate ppGpp synthesis. *Nucleic Acids Res.* **44,** 6471–6481 (2016).
15. Brown, A., Fernández, I. S., Gordiyenko, Y. & Ramakrishnan, V. Ribosome-dependent activation of stringent control. *Nature* **534,** 277–80 (2016).
16. Atkinson, G. C., Tenson, T. & Hauryliuk, V. The RelA / SpoT Homolog (RSH) Superfamily : Distribution and Functional Evolution of ppGpp Synthetases and Hydrolases across the Tree of Life. *PLoS One* **6,** e23479 (2011).
17. Battesti, A. & Bouveret, E. Acyl carrier protein / SpoT interaction , the switch linking SpoT-dependent stress response to fatty acid metabolism. *Mol. Microbiol.* **62,** 1048–1063 (2006).
18. Neusser, T., Polen, T., Geissen, R. & Wagner, R. Depletion of the non-coding regulatory 6S RNA in E . coli causes a surprising reduction in the expression of the translation machinery. *BMC Genomics* **11,** (2010).
19. Richter, D. & Zellbiochemie, A. Uncharged tRNA Inhibits Guanosine 3’,5’-Bis (Diphosphate) 3’-Pyrophosphohydrolase [ppGppase], the spoT Gene Product, from Escherichia coli. *Mol. Gen. Genet.* **327,** 325–327 (1980).
20. Hogg, T., Mechold, U., Malke, H., Cashel, M. & Hilgenfeld, R. Conformational antagonism between opposing active sites in a bifunctional RelA/SpoT homolog modulates (p)ppGpp metabolism during the stringent response. *Cell* **117,** 57–68 (2004).
21. Singal, B. *et al.* Crystallographic and solution structure of the N-terminal domain of the Rel protein from Mycobacterium tuberculosis. *FEBS Lett.* **591,** 2323–2337 (2017).
22. Winther, K. S., Roghanian, M. & Gerdes, K. Activation of the Stringent Response by Loading of RelA-tRNA Complexes at the Ribosomal A-Site. *Mol. Cell* **70,** 95–105 (2018).
23. Jain, V., Saleem-batcha, R. & Chatterji, D. Synthesis and hydrolysis of pppGpp in mycobacteria : A ligand mediated conformational switch in Rel. *Biophys. Chem.* **127,** 41–50 (2007).
24. Yang, X. & Ishiguro, E. E. Dimerization of the RelA protein of Escherichia coli. *Biochem. Cell Biol.* **79,** 729–736 (2001).
25. Steinchen, W. *et al.* Catalytic mechanism and allosteric regulation of an oligomeric (p) ppGpp synthetase by an alarmone. *Proc. Natl. Acad. Sci.* **112,**

1–6 (2015).
26. Tagami, K. *et al.* Expression of a small (p) ppGpp synthetase , YwaC , in the (p) ppGpp 0 mutant of Bacillus subtilis triggers YvyD-dependent dimerization of ribosome. *Microbiologyopen* **1,** 115–134 (2012).
27. Beckert, B. *et al.* Structure of the Bacillus subtilis hibernating 100 S ribosome reveals the basis for 70 S dimerization. *EMBO J.* **36,** 2061–2072 (2017).
28. Kudrin, P. *et al.* The ribosomal A-site finger is crucial for binding and activation of the stringent factor RelA. *Nucleic Acids Res.* **46,** 1973–1983 (2018).
29. Mehta, P., Woo, P., Venkataraman, K. & Karzai, A. W. HHS Public Access. *Methods Mol. Biol.* **905,** 273–289 (2012).
30. Li, N. *et al.* Cryo-EM structures of the late-stage assembly intermediates of the bacterial 50S ribosomal subunit. *Nucleic Acids Res.* **41,** 7073–7083 (2013).
31. Rohou, A. & Grigorieff, N. CTFFIND4 : Fast and accurate defocus estimation from electron micrographs. *J. Struct. Biol.* **192,** 216–221 (2015).
32. Scheres, S. H. W. RELION : Implementation of a Bayesian approach to cryo-EM structure determination. *J. Struct. Biol.* **180,** 519–530 (2012).
33. Sohmen, D. *et al.* Structure of the Bacillus subtilis 70S ribosome reveals the basis for species-specific stalling. *Nat. Commun.* **6,** 1–10 (2015).
34. Biasini, M. *et al.* SWISS-MODEL : modelling protein tertiary and quaternary structure using evolutionary information. *Nucleic Acids Res.* **42,** 252–258 (2018).
35. Pettersen, E. F. *et al.* UCSF Chimera — A Visualization System for Exploratory Research and Analysis. *J. Comput. Chem.* **25,** 1605–1612 (2004).
36. Crowe-McAuliffe, C. *et al.* Structural basis for antibiotic resistance mediated by the Bacillus subtilis ABCF ATPase VmlR. *Proc. Natl. Acad. Sci.* (2018). doi:10.1073/pnas.1808535115
37. Gabadinho, J. *et al.* MxCuBE : a synchrotron beamline control environment customized for macromolecular crystallography experiments. *Synchrotron Rediation* **1,** 700–707 (2010).
38. Kabsch, W. XDS. *Acta Crystallogr. Sect. D* **D66,** 125–132 (2010).
39. Winn, M. D. *et al.* Overview of the CCP 4 suite and current developments. *Acta Crystallogr. Sect. D* **4449,** 235–242 (2011).
40. Mccoy, A. J. *et al.* Phaser crystallographic software. *Appl. Crystallogr.* 658–674 (2007). doi:10.1107/S0021889807021206
41. Emsley, P. & Cowtan, K. Coot : model-building tools for molecular graphics. *Acta Crystallogr. Sect. D* 2126–2132 (2004). doi:10.1107/S0907444904019158
42. Adams, P. D. *et al.* PHENIX : a comprehensive Python-based system for macromolecular structure solution. *Acta Crystallogr. Sect. D* **D66,** 213–221 (2010).
43. Schneider, C. A., Rasband, W. S. & Eliceiri, K. W. HISTORICAL commentary NIH Image to ImageJ : 25 years of image analysis. *Nat. Methods* **9,** 671–675 (2012).
44. Battesti, A. & Bouveret, E. The bacterial two-hybrid system based on adenylate cyclase reconstitution in Escherichia coli. *Methods* **58,** 325–334 (2012).
45. Steinchen, W. *et al.* Structural and mechanistic divergence of the small (p) ppGpp synthetases RelP and RelQ. *Sci. Rep.* **8,** 1–10 (2018).
46. Spizizen, J. Transformation Of Biochemically Deficient Strains Of Bacillus Subtilis By Deoxyribonucleate. *Proc. Natl. Acad. Sci.* **44,** 1072–1078 (1968).
47. Arnaud, M., Chastanet, A. & Debarbouille, M. New Vector for Efficient Allelic Replacement in Naturally Gram-Positive Bacteria. *Appl. Environ. Microbiol.* **70,** 6887–6891 (2004).

48. Ben-Yehuda, S., Rudner, D. Z. & Losick, R. RacA , a Bacterial Protein That Anchors Chromosomes to the Cell Poles. *Science (80-.).* **299,** 532–537 (2003).
49. Stülke, J., Hanschke, R. & Michael, H. Temporal activation of beta-glucanase synthesis in Bacillus subtilis is mediated by the GTP pool. *J. Gen. Microbiol.* **139,** 2041–2045 (1993).

Acknowledgements

G.B., K.T. and D.N.W. are grateful for financial support from the DFG priority program SPP1879. C.W. is grateful for financial support of the DFG (TRR34). G.B. and P.P. acknowledge the excellent support by the European Synchrotron Radiation Facility (ESRF), Grenoble, France. G.B. and W.S. acknowledge the generous support of M. A. Marahiel in the beginning of the project. We thank Susanne Reider, Otto Berninghausen and Roland Beckmann (University of Munich, Germany) for help with data collection. We gratefully acknowledge the Core facility “protein biochemistry and protein spectroscopy”, Marburg. We thank Isabel Samp for excellent technical assistance.

Author contributions

P.P. purified proteins, performed the pull-down assays and determined the crystal structure. M.A. performed the cryo-EM analysis. W.S. performed the biochemical activity assay. H.S. performed *in vivo* experiments. F.L.G. performed the bacterial 2-hybrid experiment. S.-A.F. and P.P. performed the Bio Layer Interferometry analysis. All authors contributed to the experimental design and analyzed the data. P.P., K.T., D.N.W. and G.B. wrote the manuscript.

Competing interest

The authors declare that they have no competing interests.

Materials and correspondence

crystallography and *in vitro*: G.B., Gert.Bange@synmikro.uni-marburg.de;
cryo-EM: D.N.W., Daniel.Wilson@chemie.uni-hamburg.de;
in vivo: K.T., Turgay@ifmb.uni-hannover.de.

965 # Tables

Table 1: Crystallographic table RelΔRIS-CT

Data collection	
Space group	P 4_3 2_1 2
Cell dimensions	
a, *b*, *c* (Å)	130.152
	130.152
	157.621
α, β, γ (°)	90.00
	90.00
	90.00
Energy (Å)	0.979
Resolution (Å)	46.82 - 3.95
	(4.09 - 3.95)
No. unique reflections	12293 (1147)
Redundancy	14.2 (13.2)
Completeness (%)	99.28 (93.74)
I / **σ**I	10.04 (1.13)
R_{merge}	0.156 (1.890)
R_{pim}	0.043 (0.528)
CC(1/2)	0.996 (0.492)
Refinement	
Reflections	12293 (1138)
Reflections (R_{free})	1206 (94)
R_{work}	26.01
R_{free}	27.25
No. atoms	4369
Macromolecule	4368
Ligand	1
Water	0
R.m.s deviations	
Bond lengths (Å)	0.004
Bond angles (°)	0.93
Ramachandran (%)	
Preferred	95.1
Allowed	4.9
Outliers	0.00
Rotamer outliers (%)	0.84

*Statistics for the highest-resolution shell are shown in parentheses.

Figures

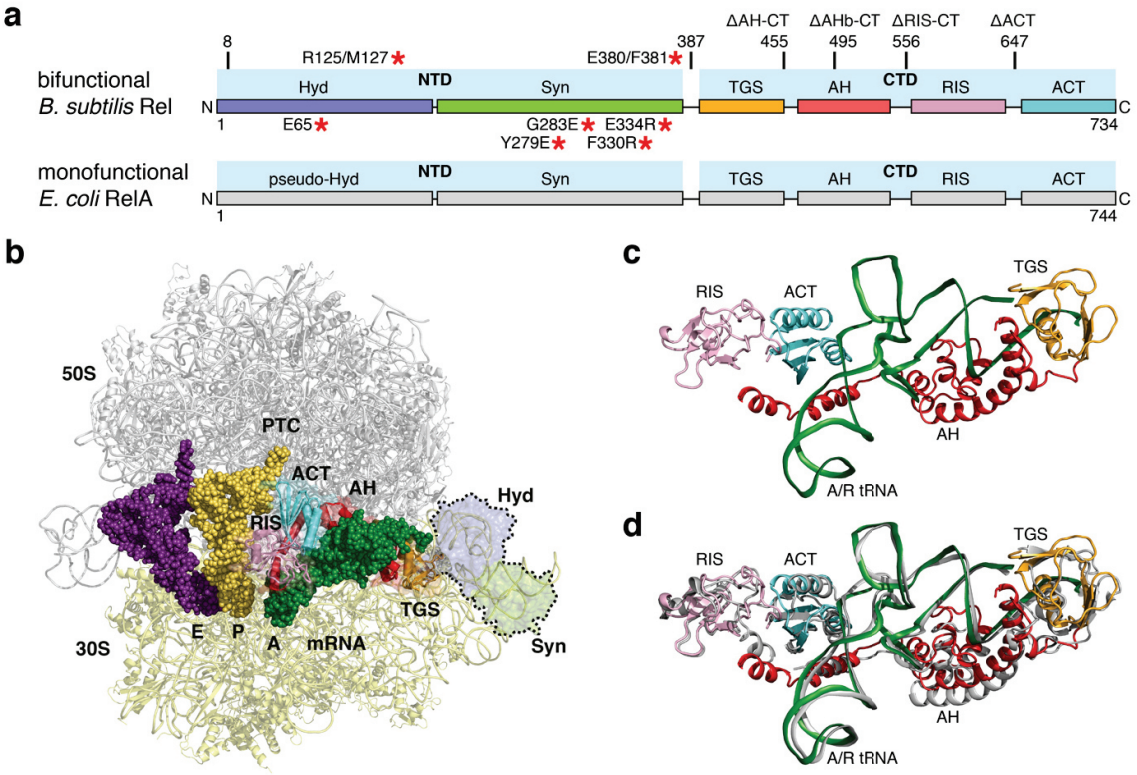

Figure 1 | Cryo-EM structure of the *B. subtilis* Rel•SRC. a, Domain architecture of *Bs*Rel and *Ec*RelA. The domains of *Bs*Rel are colored coded blue (Hyd), green (Syn), orange (TGS), red (AH), pink (RIS) and light blue (ACT). Boundaries of Rel truncations employed in this study are indicated. *Ec*RelA is shown grey below. **b,** Cryo-EM structure of the *Bs*Rel•SRC. The 50S (grey) and 30S (beige) and *Bs*Rel (coloring as in panel a) are shown in cartoon representation. The dot-framed transparent region indicates the estimated configuration of the NTD. The A/R-tRNA (green), P-tRNA (yellow) and E-tRNA (purple) are shown in sphere representation. **c**, isolated view on the *Bs*Rel•A/R-tRNA conformation on the ribosome and **d,** comparison to the conformation observed for *Ec*Rel•A/R-tRNA on the ribosome[13] (grey).

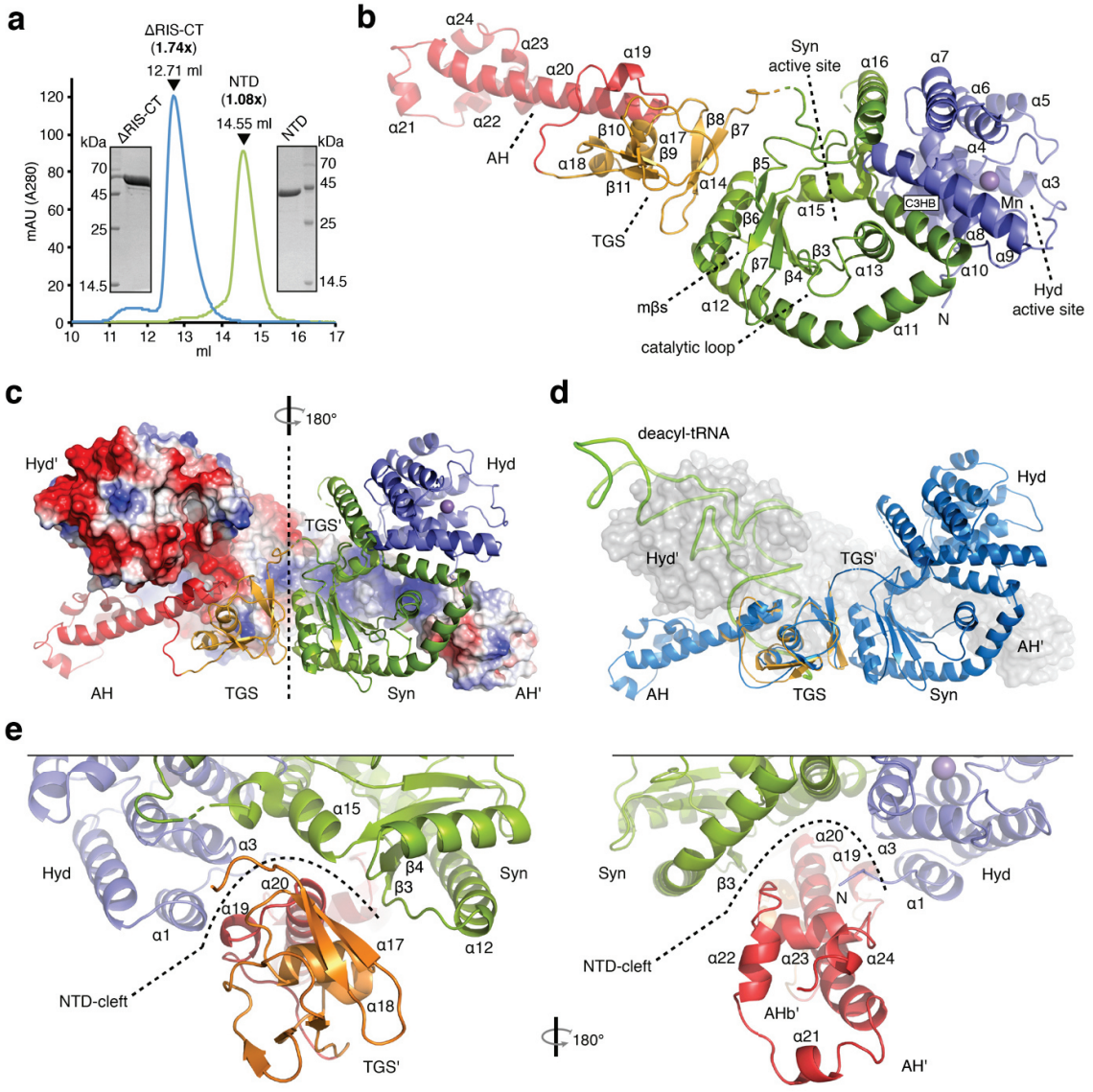

Figure 2 | **Crystal structure of *B. subtilis* RelΔRIS-CT. a,** Analytical SEC of RelΔRIS-CT (blue) and Rel-NTD (green). The corresponding SDS-PAGEs are shown adjacent to the respective peaks. **b,** Crystal structure of RelΔRIS-CT (cartoon representation). Color-coding of the individual domains as in Fig 1a. **c,** RelΔRIS-CT homodimer. The symmetry mate RelΔRIS-CT is shown in charged surface representation. **d,** Superimposition of the RelΔRIS-CT (blue cartoon) TGS domain with the TGS (orange cartoon) bound to the A/R-tRNA (green backbone), as observed at the ribosome. The symmetry mate dimer partner RelΔRIS-CT is shown in a grey surface representation. **e,** close-up view of the *in trans* TGS-AH/NTD interface in two, 180° rotated, views.

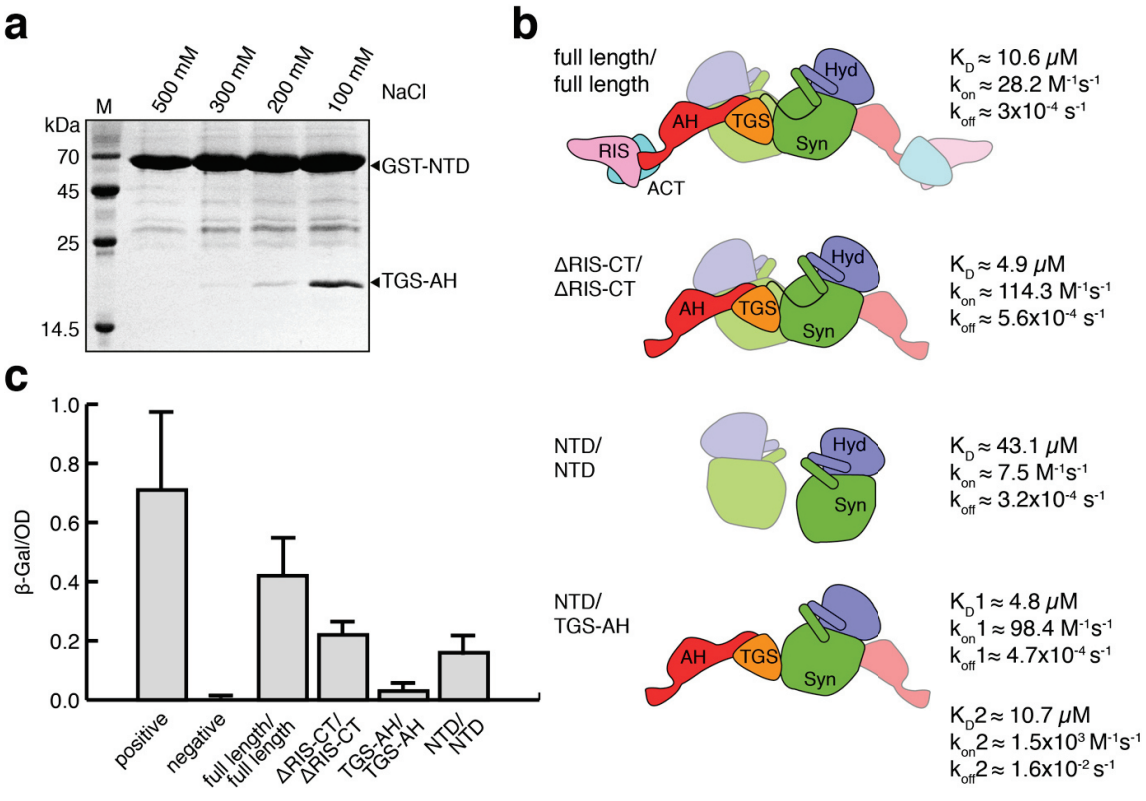

Figure 3 | **Homodimerization of Rel. a,** GST pull-down assaying the salt-dependent interaction of the GST-NTD and the TGS-AH. **b,** Bio Layer Interferometry of Rel variants. The color code is as in Fig. 1a. Only interactions with a K_D < 50 µM are shown. Data, fit and detailed interaction parameters are given in Supplementary Tab. 2 and Supplementary Fig. 9. **c,** Bacterial two-hybrid assay of different Rel variants. The signal is given in miller units. Error bars indicate standard deviation of six independent biological replicates.

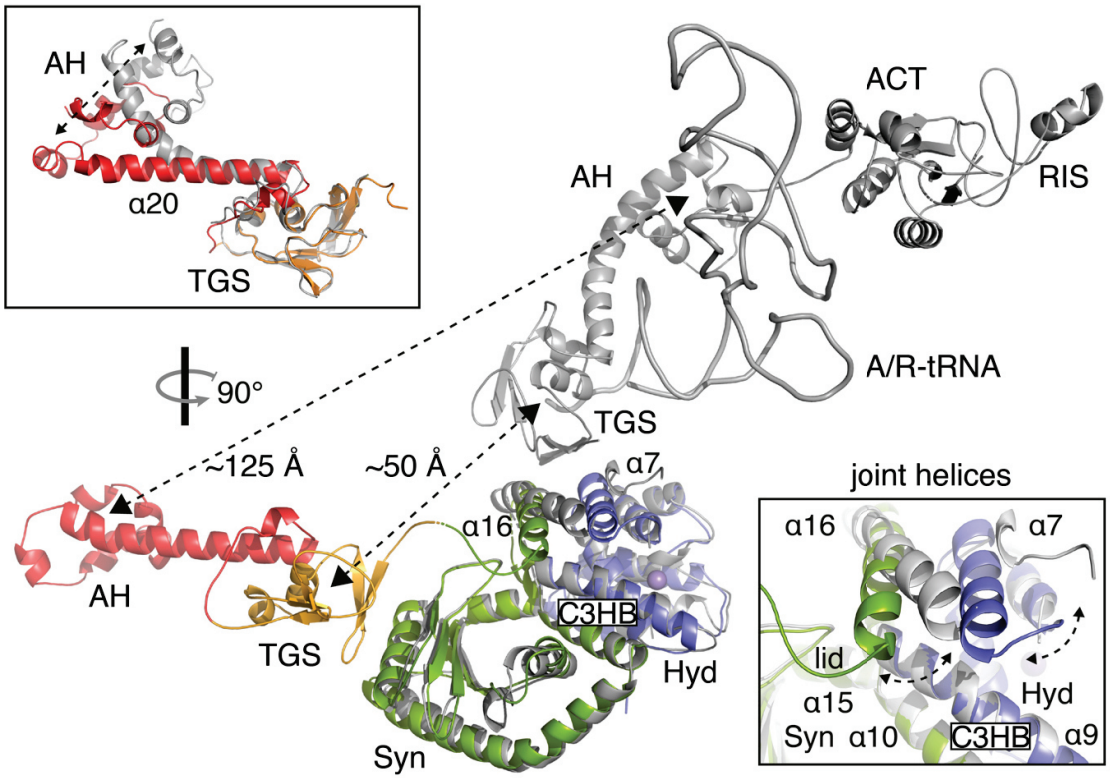

Figure 4 | **Conformational dynamics of Rel. a,** Shown is the ribosome free conformation of *Bs*Rel (colored cartoon; this study) aligned via the NTD to ribosome-bound state of *Ec*RelA (grey cartoon; PDB-ID: 5KPV[13]). Arrows indicate observed rearrangements of the TGS and AH domains. The rearrangement of the AH domain and the joint helices is emphasized in the framed panels.

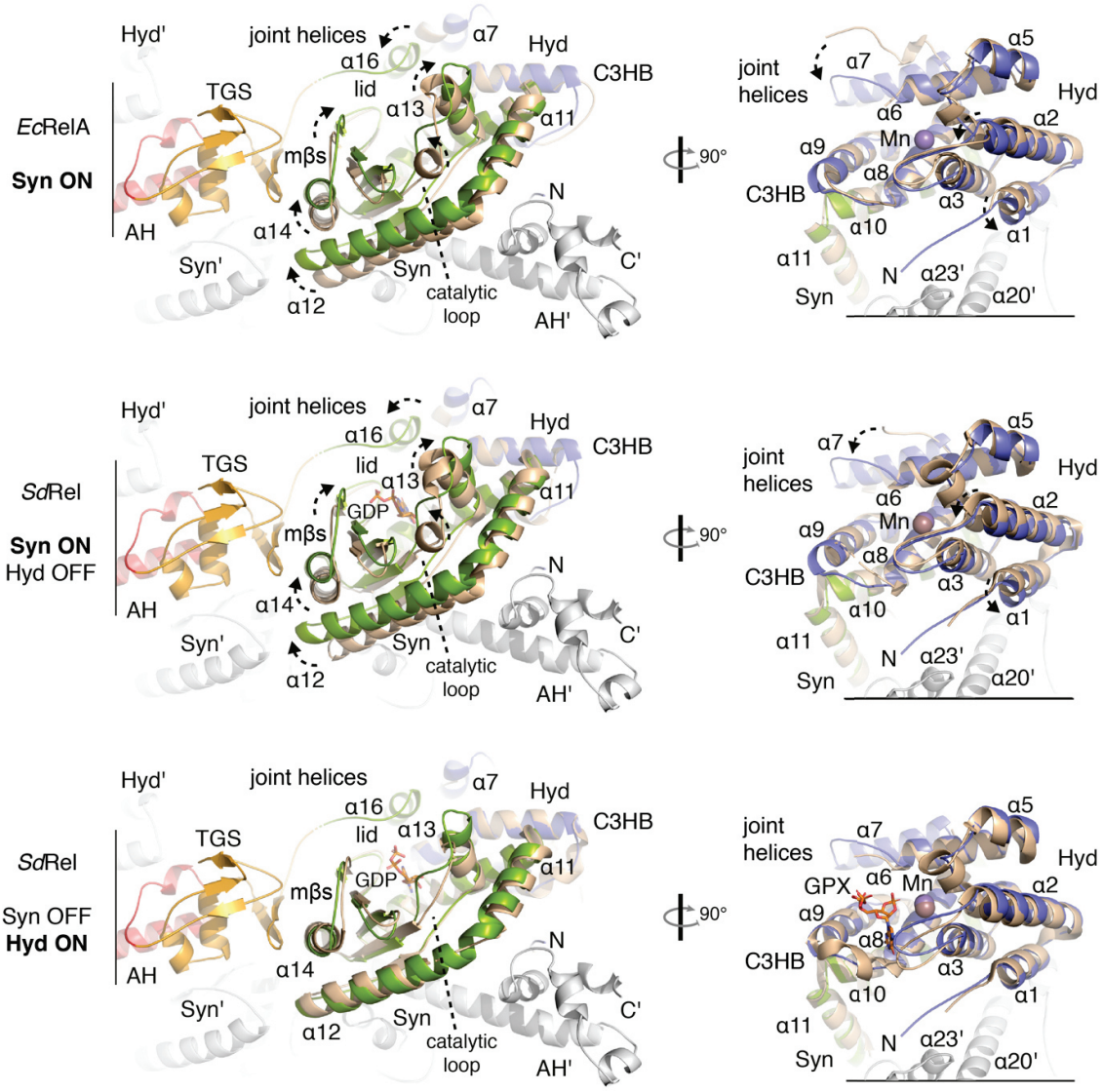

1045 **Figure 5 | NTD of *Bs*Rel is in the Hyd 'ON' and Syn 'OFF' state.** Superimposition of *Bs*RelΔRIS-CT (colored cartoon representation; this study) and the NTDs (beige cartoon representation) of *Ec*RelA (upper panel; PDB-ID: 5KPV[13]) and *Sd*Rel (chain A (middle) and chain B (lower panel)) according to the C3HB in two 90° rotated views; PDB-ID 1VJ7[20]). The symmetry mate dimer partner of *Bs*RelΔRIS-CT is 1050 shown in a grey cartoon representation. Arrows indicate observed structural rearrangements in the NTD.

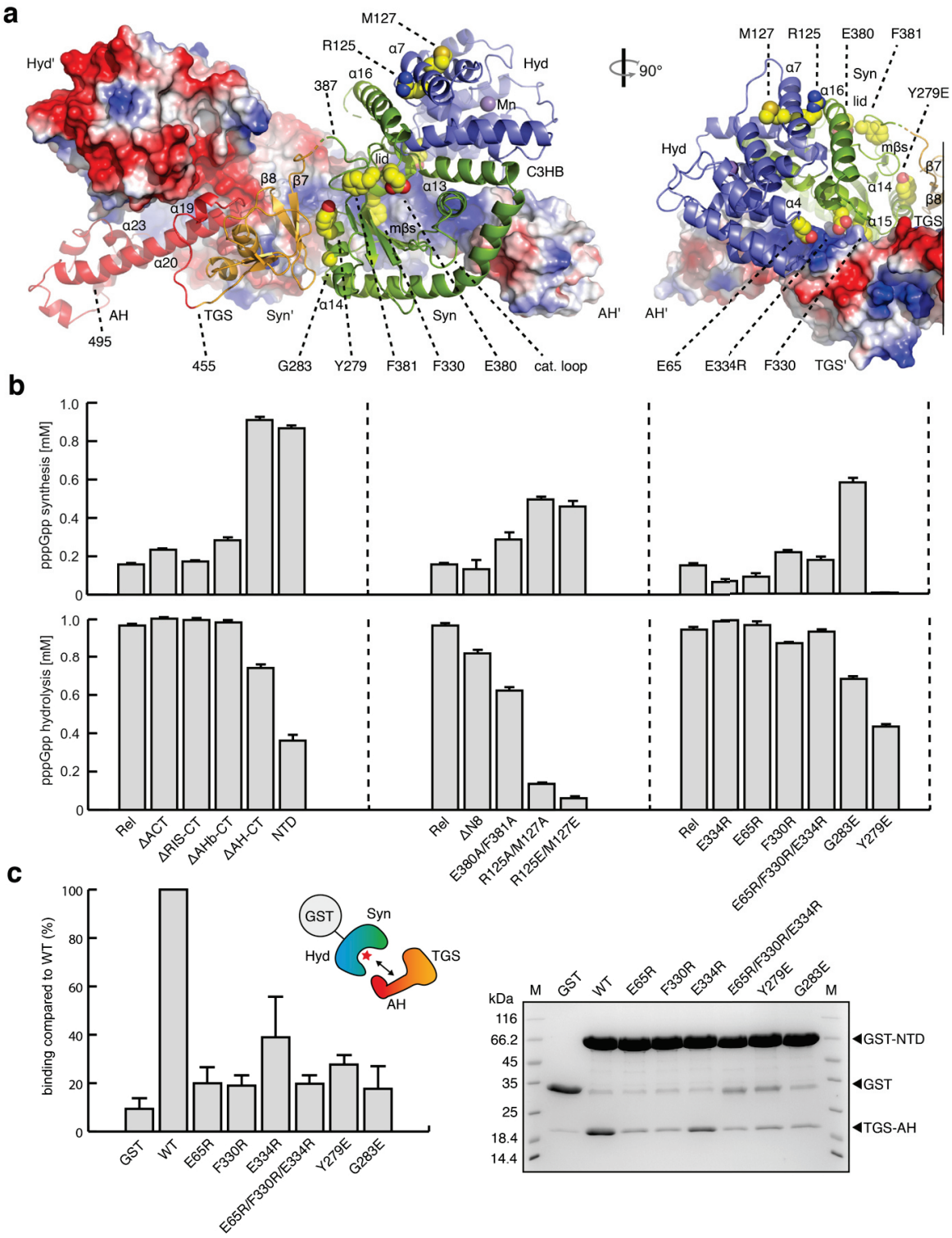

1055 **Figure 6** | ***In vitro*** **dissection of Rel regulation. a,** Crystal structure of Rel indicating the analyzed truncation and amino acid substitution variants. **b,** *in vitro* pppGpp synthesis (upper panel) and hydrolysis (lower panel) activity of Rel variants. Error bars indicate standard deviations derived from two individual measurements. **c,** GST pull-down assaying the interaction of wildtype and NTD variants with the TGS-

AH. *Left*: relative interaction strengths compared to WT-NTD, as derived from four individual experiments and by TGS-AH band intensity quantification with the ImageJ program. Error bars indicate standard deviations. Right: Representative SDS-Page of the pull-down assay.

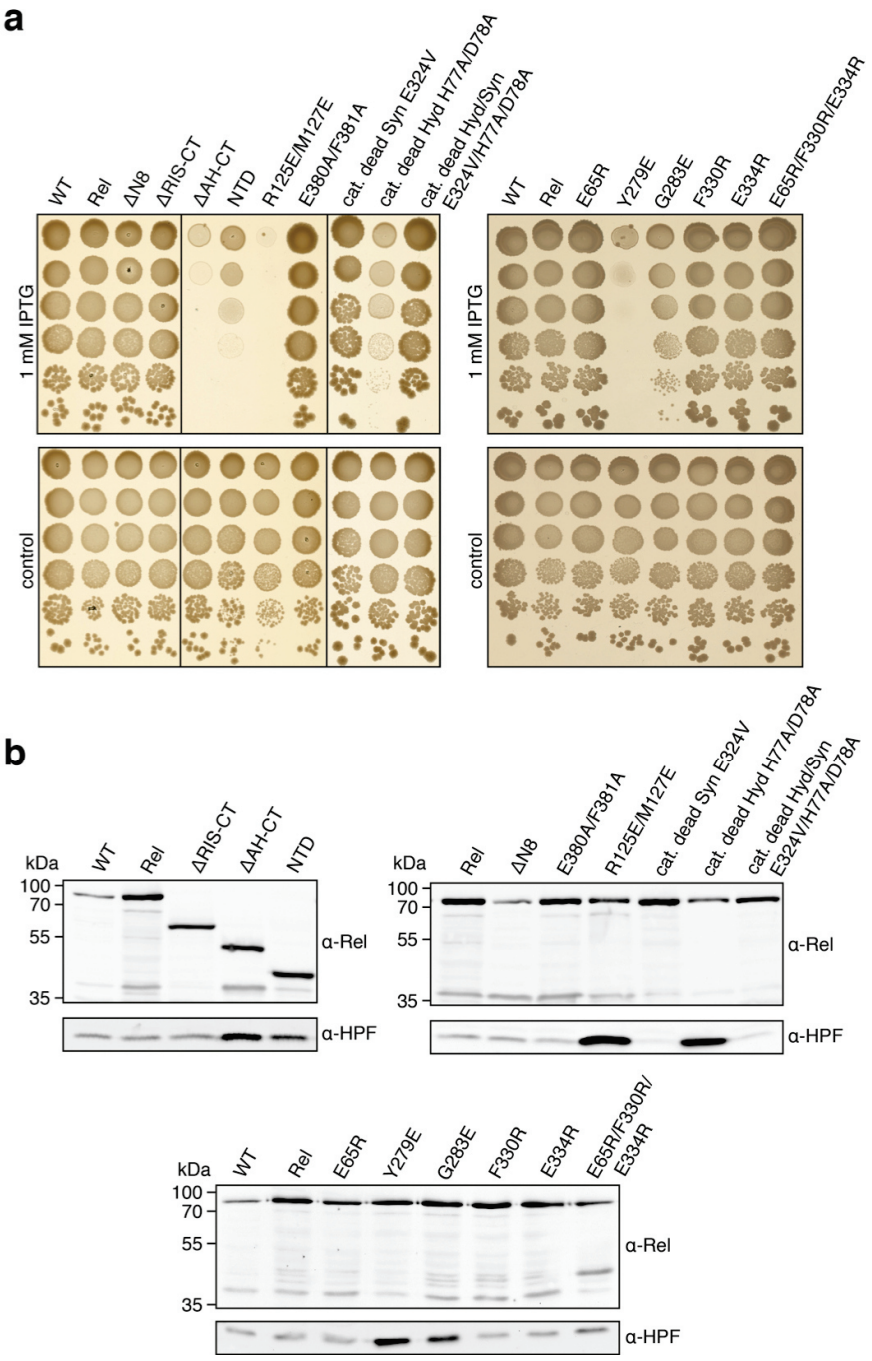

1075

Figure 7 | ***In vivo*** **dissection of Rel regulation. a,** *In vivo* growth assay of *rel*-mutant expressing *B. subtilis* pppGpp^0 strains. "cat. dead" refers to variants of Rel in which Syn (E324V), Hyd (H77A/D78A) or both were catalytically inactivated. The produced Rel variants are indicated above. *Upper panel*: IPTG induced *rel*-mutant
1080 expression. *Lower panel*: Control without IPTG induction. Growth reduction is indicative of high levels of (p)ppGpp. **b,** Western blots assaying the production of Rel variants (upper panels, α-Rel) and the (p)ppGpp induced production of the ribosome hibernation factor HPF (lower panels, α-HPF).

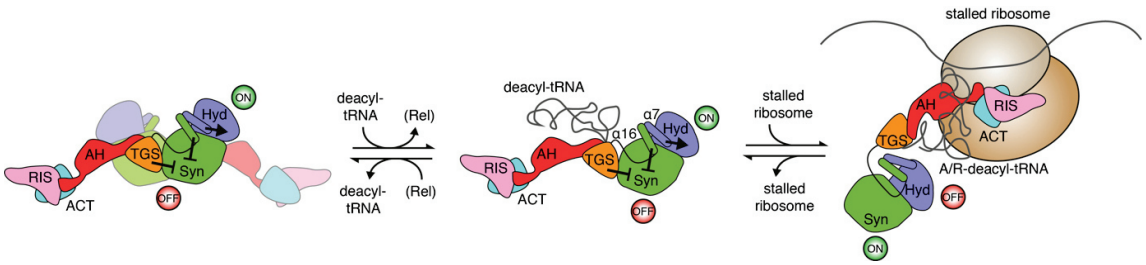

Figure 8 | Model of Rel regulation. During relaxed conditions, i.e. high availability of amino acids and low abundance of deacyl-tRNAs, Rel resides in a homodimeric Hyd 'ON' / Syn 'OFF' state (left). Upon reception of uncharged tRNAs, the Rel•deacyl-tRNA complex is formed to recognize the SRC but remains in the Hyd 'ON' / Syn 'OFF' state (middle). Stringent conditions (amino acid starvation) result in an increase of uncharged tRNAs, priming Rel for interaction with translationally stalled ribosomes that present a matching A-site codon. Accommodation of the CTD in the SRC leads to the activity switch in the NTD for alarmone production and SR signaling (right).

Supplementary Data

Stringent response control by a bifunctional RelA enzyme in the presence and absence of the ribosome

Patrick Pausch[1], Maha Abdelshahid[2], Wieland Steinchen[1], Heinrich Schäfer[3], Fabio Lino Gratani[4], Sven-Andreas Freibert[5], Christiane Wolz[4], Kürşad Turgay[3*], Daniel N. Wilson[2,*] and Gert Bange[1,*]

[1] Center for Synthetic Microbiology & Dep. Of Chemistry, Hans-Meerwein-Strasse, C07, Philipps-University Marburg, Marburg, Germany

[2] Institute for Biochemistry and Molecular Biology, University of Hamburg, Hamburg, Germany.

[3] University of Hannover, Institute for Microbiology, Herrenhäuser Strasse 2, Hannover, Germany

[4] Interfaculty Institute of Microbiology and Infection Medicine, University of Tübingen, Tübingen, Germany

[5] Center for Synthetic Microbiology & Institute für Cytobiology und Cytopathology, Philipps-University Marburg, Marburg, Germany

*Correspondence: Gert.Bange@synmikro.uni-marburg.de, Daniel.Wilson@chemie.uni-hamburg.de and Turgay@ifmb.uni-hannover.de

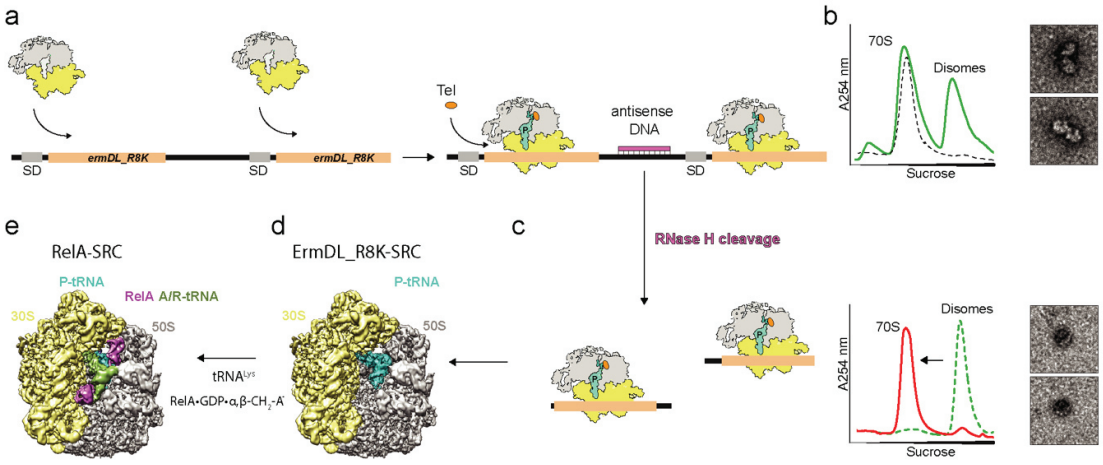

Supplementary Figure 1 | Generation of a *B. subtilis* Rel•70S ribosome complex. a, The bicistronic 2XermDL_R8K mRNA was translated in the presence of 100 μM telithromycin (TEL) in order to generate, **b**, disomes of the ErmDL_R8K stalled ribosomal complex (SRC). **c**, ErmDL_R8K•SRC disomes were converted to monosomes by antisense DNA-mediated RNase H cleavage, as shown by sucrose density gradient centrifugation and negative stain electron microscopy (EM). **d**, The A-site tRNA deficient ErmDL_R8K•SRCs were used as substrate for, **e**, Rel binding in the presence of deacylated $tRNA^{Lys}$, GDP and α, β-methylene-ATP to generate the RelA-SRC.

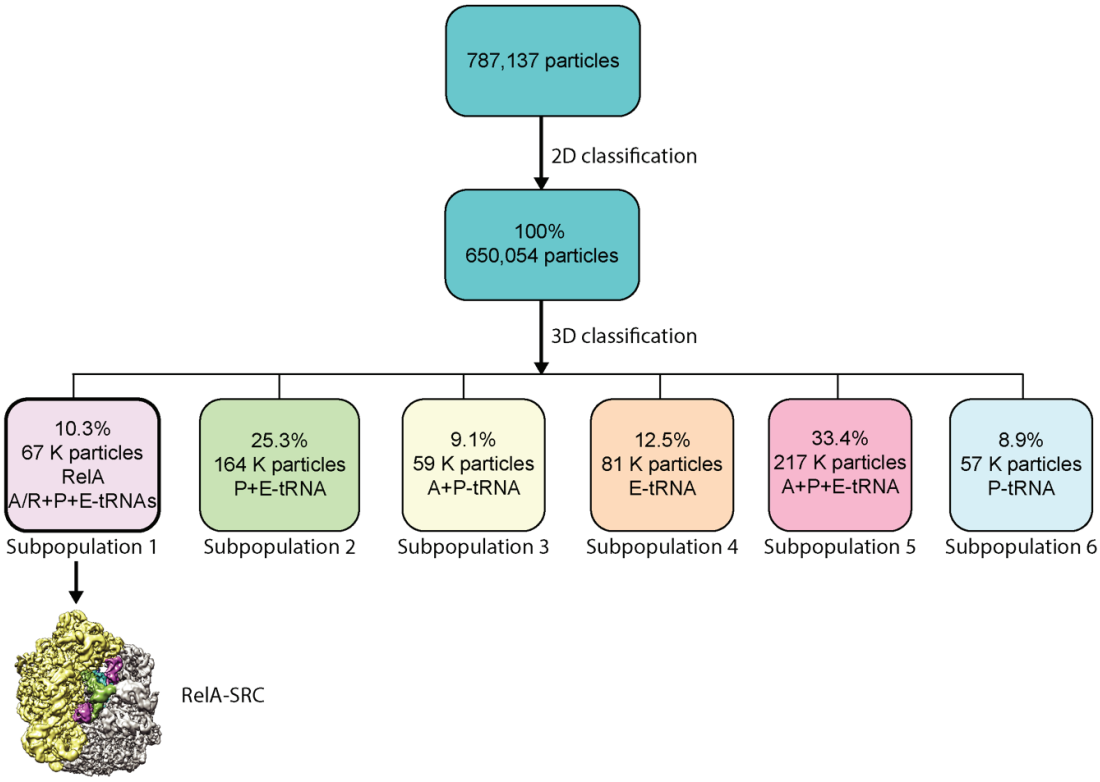

Supplementary Figure 2 | *In silico* sorting scheme of the cryo-EM dataset of the Rel•70S complex. After removal of non-aligning and edge particles from the dataset, 3D classification yielded six distinct subpopulations. The first subpopulation (10.3%; 67,047 particles) contained stoichiometric density for Rel, A/R-tRNA, P-tRNA and E-tRNA and was therefore further refined to obtain a cryo-EM map of the Rel•SRC. The remaining datasets had no density for Rel but contained different combinations of A-, P- and E-tRNAs: Subpopulation two (25.3%; 164,400 particles) contained P-tRNA and E-tRNA, whereas subpopulation three (9.1%; 59,100 particles) contained A-tRNA and P-tRNA. Subpopulation four (12.5%; 81,200 particles) contained only E-tRNA, whereas subpopulation five (33.4%; 217,000 particles) contained A-, P- and E-tRNAs. Subpopulation six (8.9%; 57,800 particles) contained only A-tRNA.

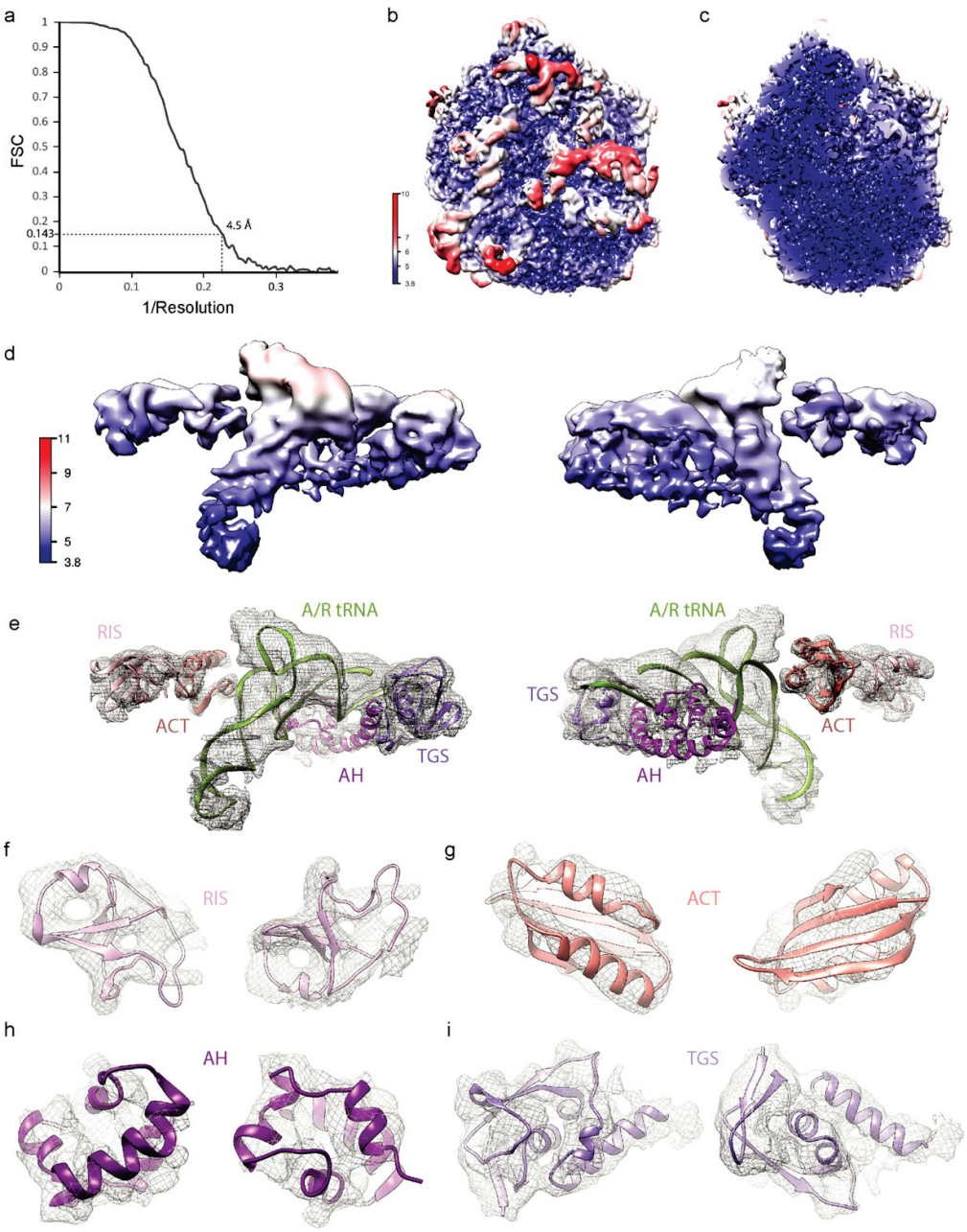

Supplementary Figure 3 | Resolution of the cryo-EM reconstruction of the Rel•70S complex. a, Fourier-shell correlation (FSC) curve of the refined final map, indicating the average resolution of the cryo-EM map of the Rel•70S complex at FSC 0.143 is 4.5 Å. **b**, Overview and, **c**, transverse section of the cryo-EM map of the Rel-70S complex colored according to the local resolution. **d-e**, Cryo-EM density for the Rel and A/R-tRNA, **d**, colored according to local resolution and, **e**, as mesh with fitted models. **f-l**, Cryo-EM density (mesh) with fitted models for, **f**: RIS (pink), **g**: ACT (salmon), **h**: AH (magenta) and, **i**: TGS (purple) subdomains of RelA.

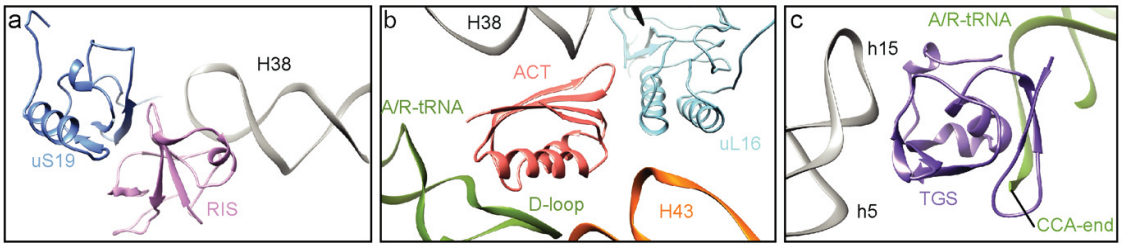

Supplementary Figure 4 | **Interactions of *B. subtilis* Rel with the ribosome and A/R-tRNA. a**, Interaction of RIS (pink) domain of Rel with 23S rRNA helix H38 (grey) of large subunit and uS19 (blue) of small subunit. **b**, Interaction of ACT (salmon) domain of Rel with 23S rRNA H38 (grey) and H43 (orange), uL16 (cyan) of the large subunit as well as the D-loop of the A/R tRNA (olive). **c**, The TGS (purple) domain of Rel appears to interact with the 16S rRNA helices h5 and h15 of the small subunit, as well as the deacylated CCA-end of the A/R-tRNA (olive).

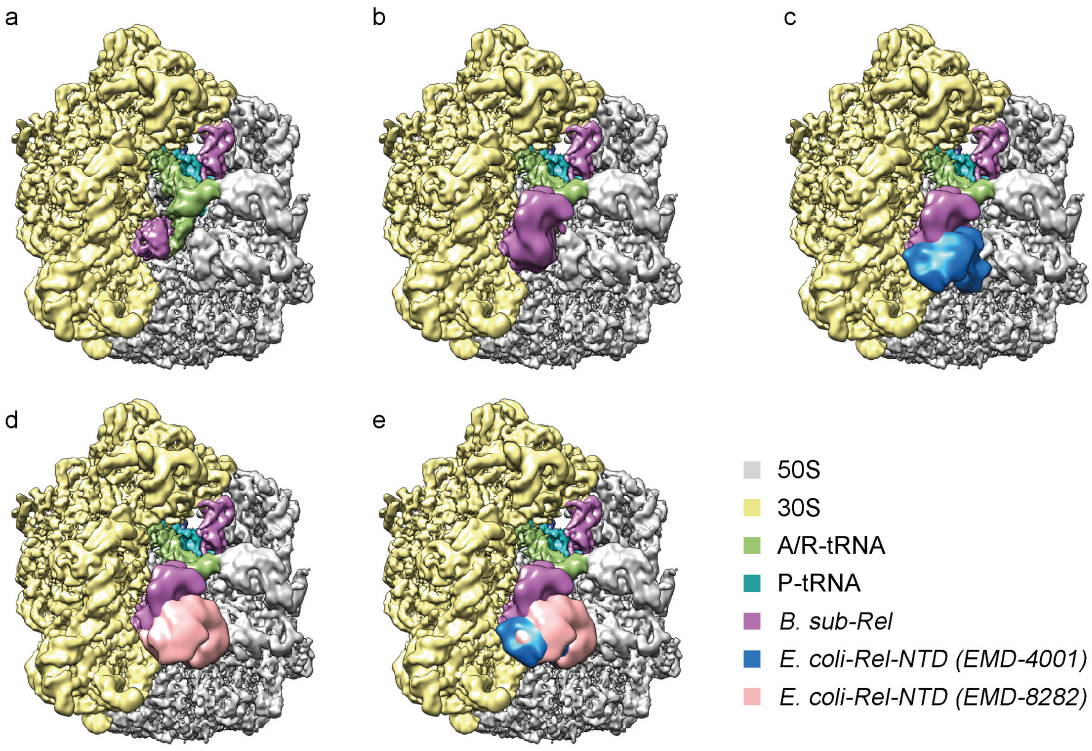

Supplementary Figure 5 | Comparison of NTD of *B. subtilis* Rel and *E. coli* RelA. a-b, Overview of the cryo-EM map of the *B. subtilis* Rel•70S complex. **a**, filtered according to local resolution and, **b**, with isolated cryo-EM density for *B. subtilis* Rel-NTD filtered to 12 Å. **c-e**, Comparison of *B. subtilis* Rel NTD from (**b**) with: **c**, *E. coli* RelA-NTD (blue, EMD-4001), **d**, *E. coli* RelA-NTD (pink, EMD-8282), and **e**, both *E. coli* RelA-NTD (blue, EMD-4001) and *E. coli* RelA-NTD (pink, EMD-8282). In **c-e**, the density for the *E. coli* RelA-NTD was filtered to 12 Å. In **a-e**, the 30S (yellow) and 50S subunit (grey) as well as P-tRNA (cyan), A/R-tRNA (green) and *B. subtilis* Rel (purple) are shown for reference.

Supplementary Table 1 | Cryo-EM data collection and model refinement statistics

Data Collection and Refinement	
Particles	59,987
Pixel size (Å)	1.084
Defocus range (μm)	0.7-2.2
Voltage (kV)	300
Electron dose ($e^-/Å^2$)	28
Model Composition	
Protein residues	6002
RNA bases	4803
Refinement	
Resolution (Å)	4.5
Map sharpening B factor ($Å^2$)	-164
Box size	360x360x360
Validation Proteins	
Poor rotamers (%)	0.92
Ramachandran outliers (%)	1.95
Ramachandran favored (%)	91.77
Bad backbone bonds (%)	0.01
Bad backbone angles (%)	0.08
Validation RNA	
Correct sugar puckers (%)	98.46
Good backbone conformations (%)	76.11
Bad bonds (%)	0.02
Bad angles (%)	0.03
Scores	
MolProbity score	2.12 (69^{th} percentile)
Clash score, all atoms	13.19 (57^{th} percentile)

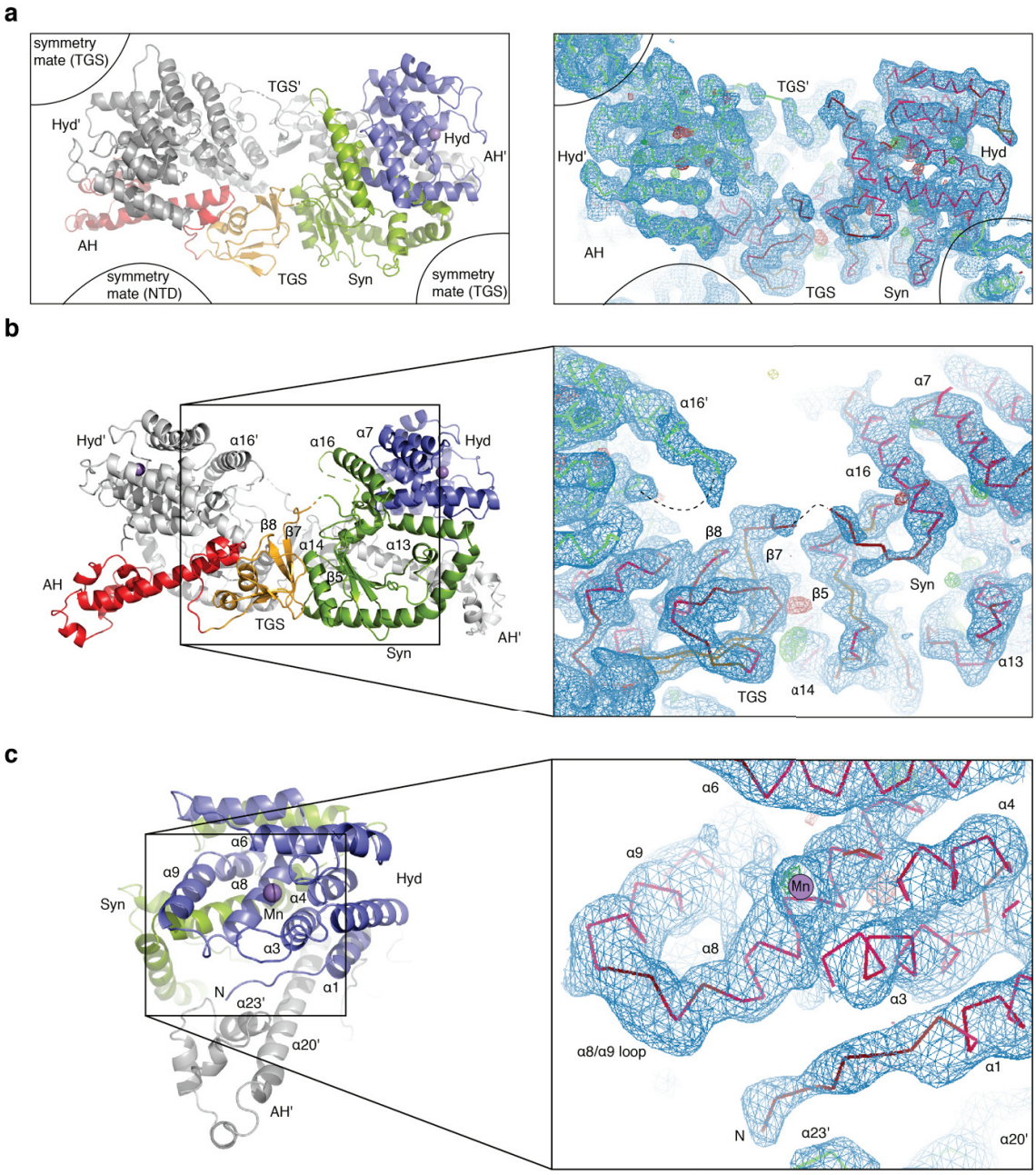

Supplementary Figure 6 | RelΔRIS-CT electron density maps. a, b and c: refined $2F_o$-F_c map at 1.1 σ (blue mesh, right panels) and F_o-F_c map at 4 σ (green mesh indicates positive density, red mesh indicates negative density; right panels) illustrating the observed electron density around the highlighted framed regions (left panels). The structure of RelΔRIS-CT is shown in the left panels in a cartoon representation and colored according to the main text figures (blue Hyd, green Syn, orange TGS and red AH). **a,** crystal packing contacts are highlighted by the framed regions that specify the identity of the contacted domains.

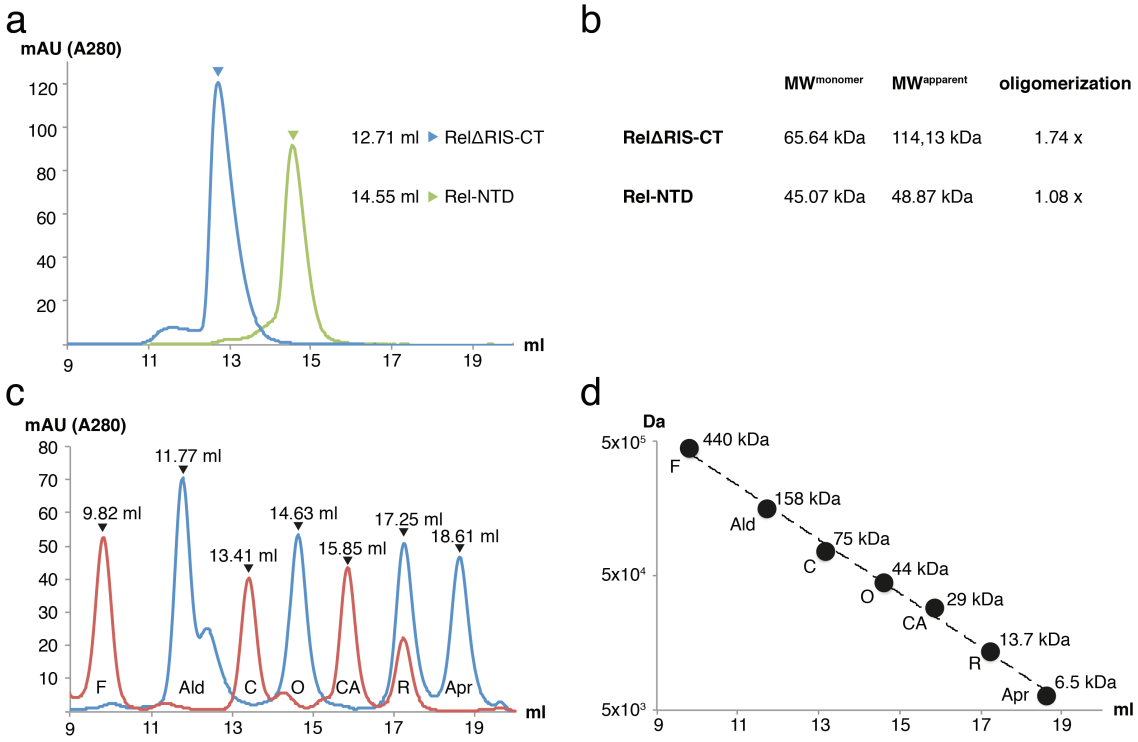

Supplementary Figure 7 | Analytical size-exclusion chromatography. a, SEC profile measured at 280 nm wavelength (Superdex 200, 10/300 GL) of RelΔRIS-CT (blue) and Rel-NTD (green). **b**, calculated molecular weight and oligomerization state according to the calibration standard (**c** and **d**). **c,** calibration standard chromatograms of Ferritin (F), Aldolase (Ald), Conalbumin (C), Ovalbulmin (O), Carb. anh. (CA), RNase A (R), Aprotinin (Apr).

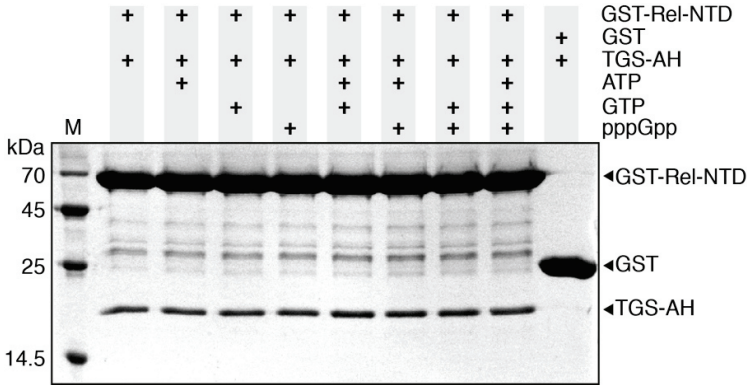

Supplementary Figure 8 | **GST-pulldown in the presence of nucleotides.** Shown is the SDS-PAGE of the GST pull-down (GST-NTD vs. TGS-AH) in dependence of the presence of nucleotides. The elution fractions were loaded according to the scheme shown above.

Supplementary Table 2 | Bio Layer Interferometry interaction parameters

ligand	analyte	K_D1 (μM)	$k_{on}1$ ($M^{-1}s^{-1}$)	$K_{off}1$ (s^{-1})	K_D2 (μM)	$k_{on}2$ ($M^{-1}s^{-1}$)	$K_{off}2$ (s^{-1})
Full length	Full length	10.6 ± 0.2	28.2 ± 0.5	$3x10^{-4}$ ± $4.2x10^{-6}$	82.3 ± 5.2	755.2 ± 43.3	$6.2x10^{-2}$ ± $1.6x10^{-3}$
ΔRIS-CT	ΔRIS-CT	4.9 ± 0.01	114.3 ± 0.2	$5.64x10^{-4}$ ± $1.32x10^{-6}$	-	-	-
TGS-AH	TGS-AH	129 ± 7	106 ± 39.1	0.14 ± $6x10^{-3}$	-	$9.7x10^{-4}$ ± $1.6x10^{-5}$	$9.2x10^{-4}$ ± $2.5x10^{-3}$
NTD	NTD	43.1 ± 0.3	7.5 ± 0.5	$3.2x10^{-4}$ ± $7.5x10^{-6}$	799.2 ± 279.2	93.9 ± 32.7	$7.5x10^{-2}$ ± $2.5x10^{-3}$
TGS-AH	NTD	4.8 ± 0.1	98.4 ± 0.3	$4.7x10^{-4}$ ± $4.7x10^{-6}$	10.7 ± 0.2	$1.5x10^{3}$ ± $2.4x10^{1}$	$1.6x10^{-2}$ ± $2.0x10^{-4}$

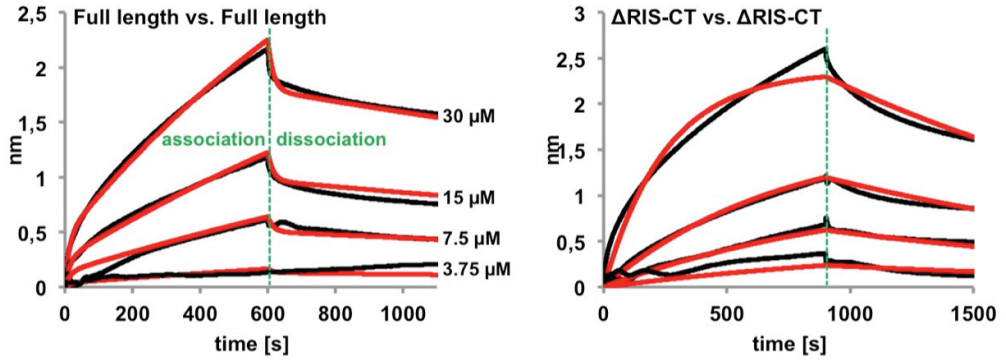

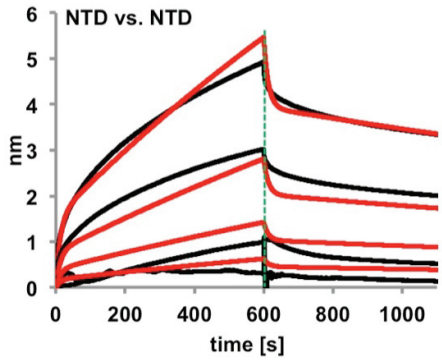

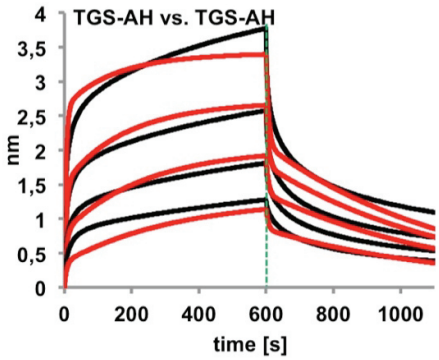

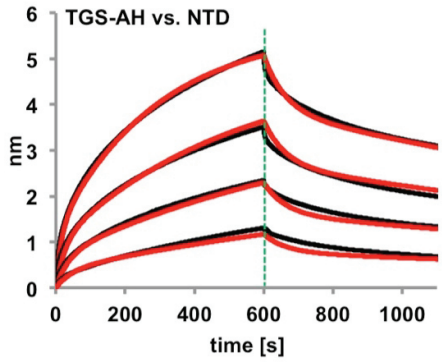

		Steady state analyses			Fit	
ligand	**analyte**	**χ^2**	**R^2**	**R_{max}**	**Model**	**Type**
Full length	Full length	0	1	6.8 ± 0	2:1	global
ΔRIS-CT	ΔRIS-CT	0	1	2.8 ± 0	1:1	global
NTD	NTD	0.37	0.97	52.9 ± 10.9	2:1	global
TGS-AH	TGS-AH	0.22	0.96	5.0 ± 0.6	1:2	global
TGS-AH	NTD	0	1	5.1 ± 0	2:1	global

Supplementary Figure 9 | Bio Layer Interferometry. Experimental data (black) and respective fittings (red) of the four titration steps for each protein couple. Only association and dissociation steps (divided by green dashed line) are shown. Table contains steady state analyses and used fitting parameters.

Published online: May 3, 2017

Article

SOURCE DATA | TRANSPARENT PROCESS

THE EMBO JOURNAL

Structure of the *Bacillus subtilis* hibernating 100S ribosome reveals the basis for 70S dimerization

Bertrand Beckert[1,†], Maha Abdelshahid[1,†], Heinrich Schäfer[2], Wieland Steinchen[3], Stefan Arenz[1], Otto Berninghausen[1], Roland Beckmann[1], Gert Bange[3,*], Kürşad Turgay[2,**] & Daniel N Wilson[1,4,***]

Abstract

Under stress conditions, such as nutrient deprivation, bacteria enter into a hibernation stage, which is characterized by the appearance of 100S ribosomal particles. In *Escherichia coli*, dimerization of 70S ribosomes into 100S requires the action of the ribosome modulation factor (RMF) and the hibernation-promoting factor (HPF). Most other bacteria lack RMF and instead contain a long form HPF (LHPF), which is necessary and sufficient for 100S formation. While some structural information exists as to how RMF and HPF mediate formation of *E. coli* 100S (*Ec*100S), structural insight into 100S formation by LHPF has so far been lacking. Here we present a cryo-EM structure of the *Bacillus subtilis* hibernating 100S (*Bs*100S), revealing that the C-terminal domain (CTD) of the LHPF occupies a site on the 30S platform distinct from RMF. Moreover, unlike RMF, the *Bs*HPF-CTD is directly involved in forming the dimer interface, thereby illustrating the divergent mechanisms by which 100S formation is mediated in the majority of bacteria that contain LHPF, compared to some γ-proteobacteria, such as *E. coli*.

Keywords cryo-EM; hibernation; HPF; RMF; translation
Subject Categories Microbiology, Virology & Host Pathogen Interaction; Protein Biosynthesis & Quality Control; Structural Biology
DOI 10.15252/embj.201696189 | Received 28 November 2016 | Revised 26 March 2017 | Accepted 29 March 2017 | Published online 3 May 2017
The EMBO Journal (2017) 36: 2061–2072

See also: **I Khusainov *et al*** (July 2017) *and* **RL Gonzalez Jr** (July 2017)

Introduction

The translational activity of the bacterial cell is able to respond rapidly to a variety of environmental cues. This is exemplified by the decrease in translational activity observed in bacteria entering into stationary growth phase due to stress conditions, such as nutrient deprivation. Under such circumstances, the decrease in translational activity is correlated with the appearance of 100S particles, which arise due to the dimerization of 70S ribosomes (Wada *et al*, 1990), reviewed by Yoshida and Wada (2014). In *E. coli*, 100S formation requires the presence of the ribosome modulation factor (RMF) and the hibernation-promoting factor (HPF, previously referred to as YhbH; Yamagishi *et al*, 1993; Wada *et al*, 1995; Maki *et al*, 2000; Ueta *et al*, 2005, 2008). Stationary phase *E. coli* cells also express a homolog of HPF (Fig 1A), termed YfiA (also referred to as pY or RaiA), which binds and inactivates 70S ribosomes (Agafonov & Spirin, 2004; Vila-Sanjurjo *et al*, 2004), and is antagonistic to RMF and HPF action by preventing 100S formation (Maki *et al*, 2000; Ueta *et al*, 2005). The hibernation state (Yoshida *et al*, 2002) appears to be important for bacterial survival since inactivation of the *rmf* gene leads to loss of viability in stationary phase cells (Yamagishi *et al*, 1993; Wada *et al*, 2000; Shcherbakova *et al*, 2015) as well as increased sensitivity to osmotic (Garay-Arroyo *et al*, 2000), heat (Niven, 2004), and acid stress (El-Sharoud & Niven, 2007).

Phylogenetic analyses have revealed that the presence of RMF and HPF is restricted to a subset of γ-proteobacteria, including *E. coli*, whereas the majority of other bacteria lack both RMF and YfiA, and instead contain a long form of HPF (LHPF; Fig 1A; Ueta *et al*, 2008, 2013; Yoshida & Wada, 2014). LHPFs comprise an N-terminal domain (NTD) homologous to the short form HPF (SHPF) and a unique C-terminal domain (CTD; Fig 1A), which was proposed to have weak homology with RMF (Ueta *et al*, 2010). LHPFs have been shown to be necessary and sufficient for 100S formation in a variety of different bacteria, including *Staphylococcus aureus* (Ueta *et al*, 2010, 2013; Basu & Yap, 2016), *Lactobacillus paracasei*, *Thermus thermophilus* (Ueta *et al*, 2010, 2013), *Lactococcus lactis* (Puri *et al*, 2014), and *B. subtilis* (Tagami *et al*, 2012; Akanuma *et al*, 2016). Unlike *E. coli* SHPF-100S (*Ec*100S), low levels of LHPF-containing 100S are also observed in exponentially growing cells (Ueta *et al*, 2010, 2013; Akanuma *et al*, 2016). Proteomics studies indicate that expression levels of *Bs*LHPF increase under conditions of nutrient deprivation, but also in response to antibiotics, heat, salt, and ethanol stress (Drzewiecki *et al*, 1998;

1 Gene Center, Department for Biochemistry and Center for integrated Protein Science Munich (CiPSM), University of Munich, Munich, Germany
2 Naturwissenschaftliche Fakultät, Institut für Mikrobiologie, Leibniz Universität Hannover, Hannover, Germany
3 LOEWE Center for Synthetic Microbiology and Faculty of Chemistry, Philipps University Marburg, Marburg, Germany
4 Institute for Biochemistry and Molecular Biology, University of Hamburg, Hamburg, Germany
*Corresponding author. Tel: +49 64 2128 23361; E-mail: gert.bange@synmikro.uni-marburg.de
**Corresponding author. Tel: +49 511 7625241; E-mail: turgay@ifmb.uni-hannover.de
***Corresponding author. Tel: +49 40 4283 82841; E-mail: Daniel.Wilson@chemie.uni-hamburg.de
†These authors contributed equally to this work

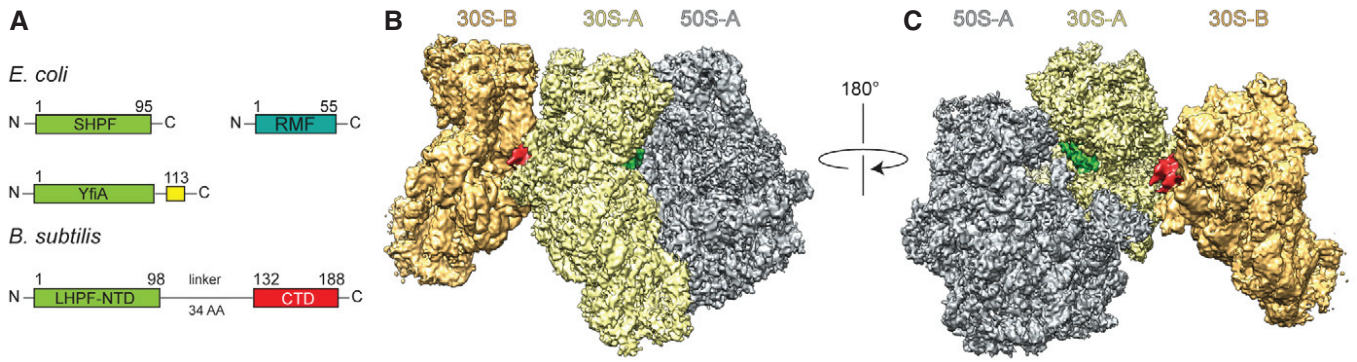

Figure 1. Cryo-EM reconstruction of the *Bs*70S-30S subcomplex.

A Schematic representation of the domain structure of *Escherichia coli* short form HPF (SHPF), RMF, and YfiA (C-terminal extension in yellow) compared to *Bacillus subtilis* long form HPF (LHPF) harboring an N-terminal (NTD, green) and C-terminal domains (CTD, red).

B, C Two views of the cryo-EM map of the *Bs*70S-30S subcomplex, with separated densities for the 30S-A (yellow), 50S-A (gray), 30S-B (orange), and additional densities in green and red.

Reiss *et al*, 2012; Tagami *et al*, 2012). In *Listeria monocytogenes*, LHPF is necessary for tolerance of bacteria to aminoglycoside antibiotics during stationary phase (McKay & Portnoy, 2015) and for optimal fitness and pathogenesis (Kline *et al*, 2015).

Cryo-EM and cryo-electron tomography (cryo-ET) structures of the *Ec*100S have revealed that the 70S monomers interact with each other via the back of the 30S subunits (Kato *et al*, 2010; Ortiz *et al*, 2010), consistent with earlier negative stain images (Wada, 1998; Yoshida *et al*, 2002). Unfortunately, the low resolution (18–38 Å) of these structures was insufficient to resolve the binding positions of the RMF and SHPF proteins within the *Ec*100S (Kato *et al*, 2010; Ortiz *et al*, 2010). However, structures of *E. coli* SHPF and RMF were subsequently determined on the *T. thermophilus* 70S ribosome by X-ray crystallography (Polikanov *et al*, 2012), providing insight into how SHPF and RMF dimerize 70S ribosomes and inactivate translation in γ-proteobacteria. To date, there is, however, little structural information available as to how LHPFs interact with 70S ribosomes to mediate 100S formation in the majority of bacteria other than *E. coli* and its close relatives.

Here we present a cryo-EM structure of the *B. subtilis* 100S particle (*Bs*100S) revealing the binding site for the *Bs*HPF (also referred to as YvyD). The *Bs*HPF-NTD binds in a position overlapping the mRNA, A- and P-tRNAs, analogous to YfiA, SHPF, and the NTD of the LHPF from spinach chloroplasts (Vila-Sanjurjo *et al*, 2004; Sharma *et al*, 2007, 2010; Polikanov *et al*, 2012; Graf *et al*, 2016; Bieri *et al*, 2017), indicating how LHPFs inhibit translation (Ueta *et al*, 2013; Basu & Yap, 2016). Unexpectedly, we observe that the *Bs*HPF-CTD forms a homodimer with the CTD of the *Bs*HPF from the second 70S ribosome, thus providing a structural basis for LHPF-mediated 100S formation. Our findings reveal that 100S formation mediated by RMF and HPF in γ-proteobacteria, such as *E. coli*, is mechanistically unrelated to 100S formation mediated by LHPF in the majority of other bacteria.

Results

Cryo-EM structure of *Bs*100S

*Bs*100S ribosomal particles were isolated from lysates of late exponential phase cells using sucrose density gradient centrifugation (Fig EV1A, see Materials and Methods). Negative stain electron microscopy images of the isolated *Bs*100S revealed the characteristic dimer arrangement of 70S monomers interacting via their 30S subunits (Fig EV1B), as observed previously for *B. subtilis* (Tagami *et al*, 2012), *Lactococcus lactis* (Puri *et al*, 2014), but distinct from *Ec*100S (Wada, 1998; Yoshida *et al*, 2002; Kato *et al*, 2010). The presence of the *Bs*HPF (YvyD) in the *Bs*100S was further confirmed using mass spectrometry. The LHPF-containing 100S particles were then subjected to single particle cryo-EM analysis (see Materials and Methods). Processing of the *Bs*100S was performed by aligning the 70S ribosomes within each 100S to a vacant 70S reference. The box size was maintained large enough so that the majority of the small 30S subunit of the second 70S ribosome in the dimer would also be represented during the reconstruction. The initial reconstructions revealed significant flexibility in the 100S, which was indicated by a stable aligned ribosome (70S-A) with a blurred density for the second 70S ribosome (70S-B). By implementing *in silico* sorting procedures, we were able to obtain a subpopulation of 100S particles with better-defined density for the 70S-B ribosome (Fig EV2). Subsequent refinement yielded a cryo-EM reconstruction of the *Bs*70S-30S subcomplex (Fig 1B and C) with an average resolution of 3.8 Å (Fig EV3A–D and Table EV1). Local resolution calculations indicate that the resolution for the 70S-A monomer ranges in the core between 3.5 and 5.0 Å, whereas, as expected, the resolution for 70S-B is worse, ranging between 5.0 and 10 Å (Fig EV3B and C). The cryo-EM map was fitted with the molecular model of the *B. subtilis* 70S ribosome (Sohmen *et al*, 2015), revealing that the 70S-A monomer adopts a classic non-rotated state, as observed previously (Sohmen *et al*, 2015). Moreover, the swivel of head observed when *E. coli* SHPF and RMF bind to *T. thermophilus* 70S ribosomes (Polikanov *et al*, 2012) is not observed in the *Bs*100S, indicating that dimerization of *B. subtilis* 70S ribosomes, unlike *E. coli*, does not require head movement. After fitting of the 70S models, two unassigned densities remained, one located within the intersubunit space of the 70S-A ribosome and a second located on the back of the 30S platform at the interface of the 70S-A and 70S-B ribosomes (Fig 1B and C).

Binding site of the *Bs*HPF-NTD on the small 30S subunit

The additional map density within the intersubunit space located between the head and body of the 30S subunit was assigned to the N-terminal domain of *Bs*HPF (*Bs*HPF-NTD; Fig 2A). This was based on the high sequence similarity of the *Bs*HPF-NTD with *E. coli* YfiA and HPF (Fig EV1C), both of which were shown to bind to this region of the ribosome (Vila-Sanjurjo *et al*, 2004; Polikanov *et al*, 2012). The local resolution of the *Bs*HPF-NTD ranged between 3.5 and 5.0 Å (Fig EV3F–G), enabling an unambiguous fit of the homology model to the density (Fig 2B). Aligning the *E. coli* SHPF-70S structure (Polikanov *et al*, 2012) to the 70S-A ribosome in the *Bs*100S based on the 16S rRNA revealed the expected similarity in their binding positions (Fig 2C). As noted previously for *E. coli* YfiA and HPF (Vila-Sanjurjo *et al*, 2004; Polikanov *et al*, 2012) and for the NTD of the LHPF from Spinach chloroplast (Sharma *et al*, 2007, 2010; Graf *et al*, 2016; Bieri *et al*, 2017), the binding position of *Bs*HPF-NTD overlaps with the mRNA and anticodon-stem loop regions of tRNAs bound in the ribosomal A- and P-sites (Fig 2D), thus explaining the observed inhibitory effect by LHPFs when added to *in vitro* translation assays (Ueta *et al*, 2013; Basu & Yap, 2016). The *Bs*HPF-NTD is connected by a 34 aa linker to the CTD (Fig 1A). Map density for the linker region was not observed in the cryo-EM map of the *Bs*100S, indicating that it is highly flexible. An exception is the 5–6 aa stretch of the linker region that directly follows the terminal α-helix of the *Bs*HPF-NTD (Fig 2B). Map density for this N-terminal part of the linker passes, analogous to mRNA, through the opening created by the β-hairpin of ribosomal protein S7 and helix h23 of the 16S rRNA, and extends in the general direction of the platform cavity at the back of the 30S subunit (Fig EV4).

*Bs*HPF-CTD is present as a dimer on the small 30S subunit

Given the general direction of the linker, we assigned the additional density located on the back of the 30S platform to the *Bs*HPF-CTD (Fig 3A and B). It was possible to generate a homology model for the *Bs*HPF-CTD based on the deposited crystal structure of the LHPF-CTD from a closely related Firmicute, *Clostridium acetobutylicum* (PDB ID 3KA5; Fig EV1D). Curiously, the *C. acetobutylicum* LHPF-CTD is present as a dimer in the crystal, and it was possible to make an unambiguous rigid body fit of the homology model of the *Bs*HPF-CTD dimer into the unassigned map density of the cryo-EM map (Fig 3C). We note that while the structurally conserved *L. monocytogenes* HPF-CTD (PDB ID 3K2T) appears as a monomer in the asymmetric unit, the homodimer forms across the crystallographic twofold symmetry. This suggests that the LHPF-CTDs are not only dimeric on the ribosome, but are likely to be dimeric in solution. To investigate this further, we performed size-exclusion chromatography (SEC) on the recombinantly expressed and purified wild-type *Bs*HPF and *Bs*HPF variants (see Materials and Methods). Analysis of the full-length *Bs*HPF and the *Bs*HPF-CTD revealed that they have apparent molecular masses of 56 and 14 kDa, respectively, rather than the expected 23 kDa and 8 kDa (Fig 3D–G), indeed suggesting that both proteins are dimeric in solution as well as on the ribosome. The apparent migration behavior of *Bs*HPF on SEC reflects the elongated shape of the dimer as also seen in our cryo-EM structure of the *Bs*100S. Based on the structures of the dimeric *C. acetobutylicum* and *L. monocytogenes*

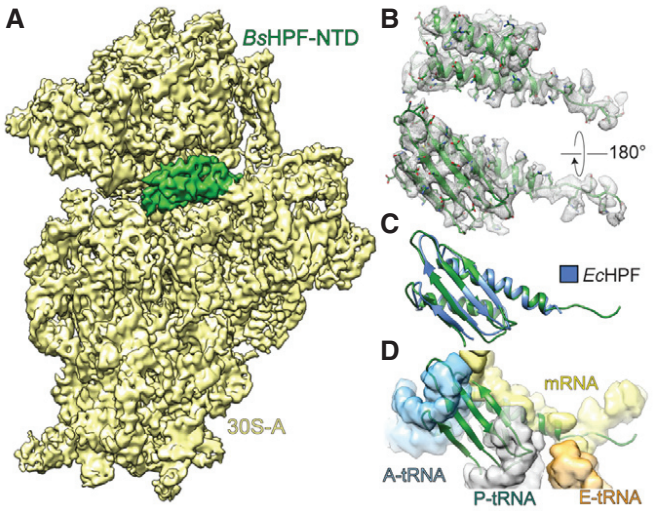

Figure 2. Interaction of the *Bs*HPF-NTD with the ribosome.

A Interface view of cryo-EM map of the 30S-A (yellow) from the *Bs*70S-30S subcomplex with separated *Bs*HPF-NTD density (green).

B Map density (gray mesh) with model of *Bs*HPF-NTD (green).

C, D Comparison of *Bs*HPF-NTD (green) with (C) *Escherichia coli* SHPF (*Ec*HPF, blue; Polikanov *et al*, 2012), and (D) mRNA (yellow surface), A- (cyan), P- (gray), and E-tRNAs (orange; Jenner *et al*, 2011).

LHPF-CTD, we rationalized that the highly conserved Phe160 in the *Bs*HPF-CTD is critical for dimerization (Fig 3H). Phe160 is present within the very hydrophobic dimer interface where it forms stacking interactions with Phe160 of the second monomer (Fig 3H). We predicted that a mutation of Phe160 to Glu (F160E) would disrupt the dimer interface via introduction of a negative charge into the hydrophobic environment. To test this, we also subjected the full-length *Bs*HPF-F160E protein to SEC (Fig 3D and E), revealing that the protein eluted with an apparent molecular mass of 40 kDa, smaller than the 56 kDa observed for the wild-type *Bs*HPF (Fig 3G). Although 40 kDa is larger than the expected size of 22.8 kDa, we believe this is due to retardation of the NTD and subsequent linker. Indeed, a *Bs*HPF variant lacking the CTD (*Bs*HPF-NTD) eluted with an apparent molecular mass of 28 kDa (rather than the expected 13.1 kDa; Fig 3G). This observation is in good agreement with structural information on the NTDs of other hibernation factors showing a non-globular shape (Polikanov *et al*, 2012). Our conclusions based on SEC were also confirmed using static light scattering (SLS), revealing the full-length *Bs*HPF had an absolute molecular mass of 42.8 ± 0.9 kDa, corresponding with a dimer (46 kDa), whereas the mass of the *Bs*HPF-F160E variant (28 ± 2.1 kDa) was more consistent with a monomer (22.8 kDa; Fig 3G). Taken together, our biochemical data clearly show that *Bs*HPF forms a homodimer in solution that is mediated via its CTD.

Dimerization of 70S ribosomes via the *Bs*HPF-CTD

While the limited resolution of the *Bs*HPF-CTD (Fig EV3H and I) does not allow a detailed analysis of the contacts with the ribosomal components to be made, the fitted model nevertheless enables a general description of the interaction mode (Fig 4A). The *Bs*HPF-CTD appears to interact exclusively with ribosomal proteins S2 and

S18 and does not establish contact with the 16S rRNA. Importantly, each *Bs*HPF-CTD monomer contacts S2 from the 70S to which the corresponding *Bs*HPF-NTD is bound, whereas the interaction with the N-terminal extension of S18 is from the second 70S ribosome (Fig 4A). The 100S dimer is also stabilized by direct interactions between the 70S-A and 70S-B monomers (Fig 4A and B). In addition to the contacts established between the N-terminal helix of S2 and the N-terminal extension of S18, the N-terminal β-hairpin and proximal region of the α2-helix of S2 establish a large interaction surface with the stem-loop of helix h26 of the 16S rRNA of the second 70S (Fig 4B). Thus, the dimerization of the HPF-CTDs stabilizes and facilitates direct interaction between the 70S-A and 70S-B monomers in the *Bs*100S. Our findings highlight the importance of the *Bs*HPF-CTD for 70S dimerization, and therefore 100S formation, which is in complete agreement with biochemical studies demonstrating that truncation of the CTD from LHPF leads to loss of 100S formation (Puri *et al*, 2014; Basu & Yap, 2016). Moreover, it was reported that the CTD of the LHPF from *Lactococcus lactis* can dimerize *E. coli* 70S ribosomes, but only when acting in concert with the SHPF from *E. coli* (Puri *et al*, 2014). This observation supports to some extent the previous assertion that the HPF-CTD functions analogously to RMF; an assertion that was partly based on proposed sequence homology between HPF-CTD and RMF (Ueta *et al*, 2010). However, comparison of the structures of *Bs*HPF-CTD with that of RMF on the ribosome (Polikanov *et al*, 2012) reveals that there is no structural similarity in terms of the protein fold and, despite both binding at the platform region at the back of the 30S subunit, there is no overlap in their binding sites on the ribosome (Fig 4C). The binding position of RMF was suggested to inhibit translation by sterically preventing formation of the Shine-Dalgarno-helix (SD-helix) between the 5′ end of the mRNA and the 3′ end of the 16S rRNA (Polikanov *et al*, 2012). In contrast, the HPF-CTD does not overlap with the SD-helix (Fig 4D), although we cannot exclude the possibility that the flexible linker of *Bs*HPF traverses the RMF binding site since it was not visualized in the cryo-EM map.

Importance of the linker–CTD for 100S formation

To assess the importance of the linker and CTD of *Bs*HPF for 100S formation *in vivo*, we generated a *B. subtilis* 168 strain where the *yvyD* gene was inactivated (Δ*Bs*HPF), as confirmed by Western blotting using antibodies specific to *Bs*HPF (Fig 5A). We then re-introduced the wild-type *yvyD* gene, as well as *yvyD* variants, into the *amyE* locus and monitored the IPTG-induced expression of the *Bs*HPFs (Fig 5A). To investigate the importance of the linker between the NTD and CTD of *Bs*HPF, we generated Δ*Bs*HPF strains expressing *Bs*HPF deletion variants lacking 10 aa (*Bs*HPF-LΔ10AA, lacking residues 110–119) or 20 aa (*Bs*HPF-LΔ20AA, lacking residues 105–124) from the central region of the linker (Fig 5A). In addition, we generated a *Bs*HPF variant bearing the F160E mutation in the CTD (*Bs*HPF-F160E), which interferes with homodimerization (Fig 3G). Western blotting of cell extracts from stationary phase bacteria indicated that all *Bs*HPF variants inserted into the *amyE* locus were expressed in the presence of IPTG at similar levels to wild-type *Bs*HPF observed in the parental *Bs*168 strain (Fig 5A). Pelleting experiments indicated that full-length *Bs*HPF co-migrated with the ribosome fraction as expected, as did the *Bs*HPF-LΔ10AA variant (Fig 5B). In contrast, the *Bs*HPF-LΔ20AA

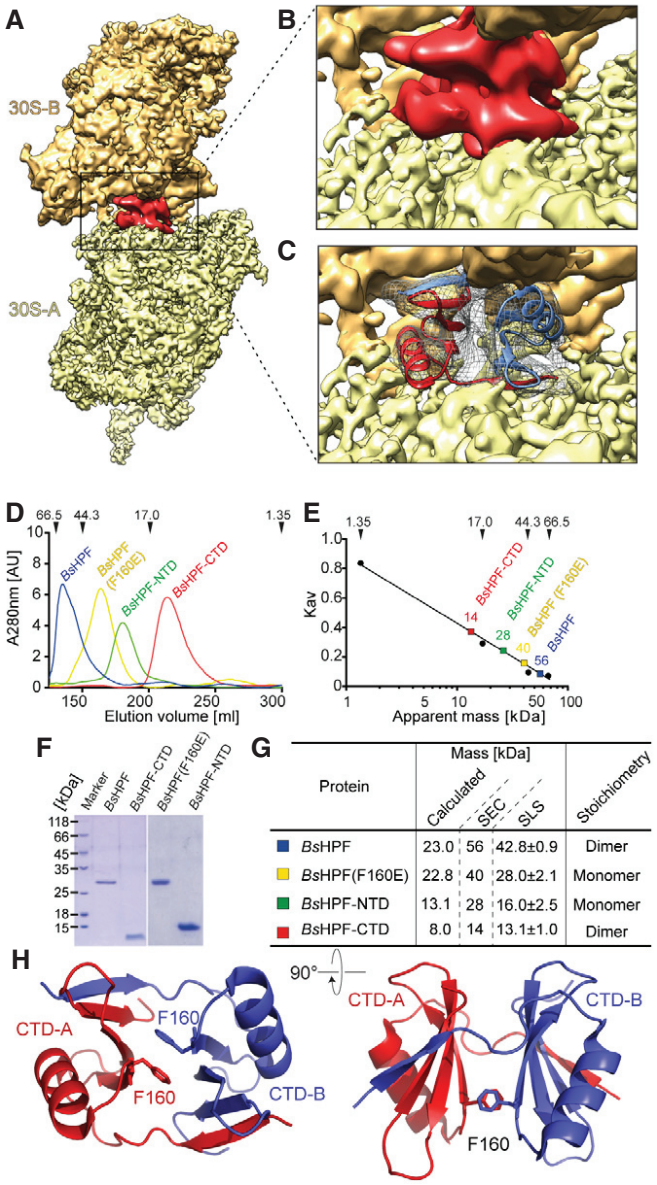

Figure 3. Binding site of dimeric LHPF-CTD on the *Bs*70S-30S subcomplex.

A Cryo-EM map of the 30S-A (yellow) from the *Bs*70S-30S subcomplex with separated LHPF-CTD density (red).

B, C Density (gray mesh) with fitted model of dimeric LHPF-CTD with monomers from 70S-A and 70S-B colored red and blue, respectively.

D Gel-filtration profiles of full-length *Bs*HPF (blue), *Bs*HPF-F160E (yellow), *Bs*HPF-NTD (green), and *Bs*HPF-CTD (red). Arrows indicate the molecular mass in kDa of the size standard.

E Standard curve with estimated molecular masses for full-length *Bs*HPF (blue), *Bs*HPF-F160E (yellow), *Bs*HPF-NTD (green), and *Bs*HPF-CTD (red). Arrows indicate the molecular mass in kDa of the size standard.

F Coomassie-stained SDS–PAGE of the peak fractions containing *Bs*HPF or its variants.

G Table summarizing the actual and apparent molecular mass of proteins in (D-F). Size-exclusion chromatography (SEC) and static light scattering (SLS) determined the apparent and absolute MWs, respectively. "Stoichiometry" indicates whether *Bs*HPF and its variants exist as mono- or homodimer.

H Homology model of the *Bs*HPF-CTD homodimer illustrating the position of Phe160 (F160) at the dimer interface.

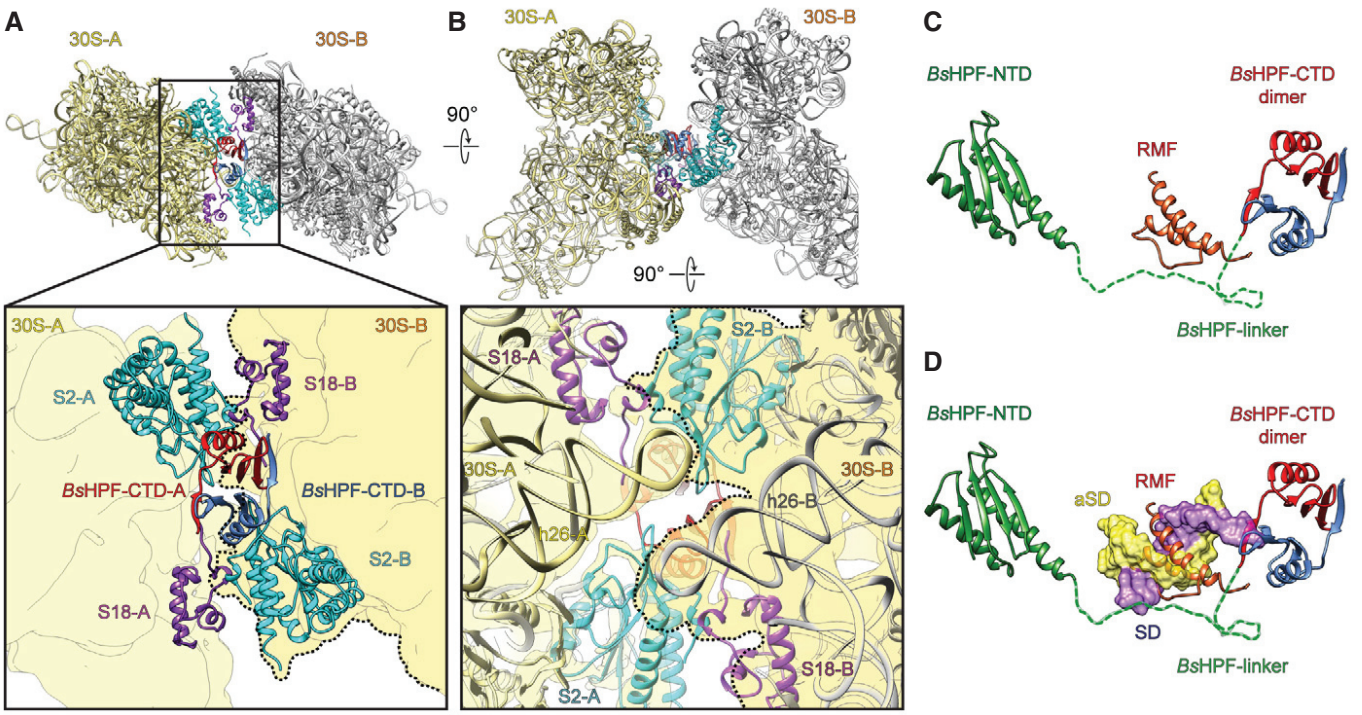

Figure 4. Dimerization interface of the *Bs*70S-30S subcomplex.

A, B Distinct views of the dimer interface between 30S-A (yellow) with *Bs*HPF-CTD-A (red) and 30S-B (gray, darker yellow with dashed line in zoomed panel) with *Bs*HPF-CTD-B (blue). Ribosomal proteins S2 (cyan), S18 (purple), and 16S rRNA are shown only, and the surface outline of the 30S subunit is included schematically for reference.

C, D Binding site of *Bs*HPF-NTD (green) and dimeric *Bs*HPF-CTD (red, blue) relative to (C) RMF (orange; Polikanov *et al*, 2012) and (D) SD–anti-SD helix (yellow-purple surface; Sohmen *et al*, 2015). The dashed line indicates the linker and is shown only to illustrate that the 34 amino acids are more than sufficient to connect the NTD and CTD; however, no density for the linker was observed, suggesting it does not adopt a defined conformation on the ribosome.

and *Bs*HPF-F160E variants had significantly reduced association with the ribosomal pellets (Fig 5B), suggesting that the deletion of 20 aa within the linker or preventing homodimerization via the CTD disrupts the interaction of *Bs*HPF with the ribosome. This is consistent with previous studies using *S. aureus* LHPF where C-terminal truncations of 42 aa (ΔCTD) and 90 aa (Δlinker–CTD) led to progressive loss in ribosome binding (Basu & Yap, 2016).

We next employed sucrose density gradient centrifugation to monitor the formation of 100S ribosomes using the different *Bs*168 strains (Fig 5C–G). As controls, the wild-type *Bs*168 strain was harvested during exponential phase, where a large 70S peak and lots of polysomes were observed, but little or no 100S were evident (Fig 5C). In contrast, a short heat treatment of the wild-type cells led to a complete loss of polysomes and the appearance of a prominent 100S peak (Fig 5C), as observed previously for *B. subtilis* (Akanuma *et al*, 2016). Formation of 100S was never observed in the Δ*Bs*HPF strain (Fig 5C) regardless of the stress conditions tested, in agreement with the strict dependence on *Bs*HPF for 70S dimerization (Akanuma *et al*, 2016). However, when the *yvyD* gene was reintroduced into the *amyE* locus of the Δ*Bs*HPF strain, 100S formation (and loss of polysomes) was observed, but only when *Bs*HPF expression was induced by the presence of IPTG (Fig 5D). No significant increase in the 100S peak, nor reduction in polysomes, was observed when expression of the *Bs*HPF-LΔ20AA variant was induced (Fig 5E), consistent with the lack of ribosome binding (Fig 5B). Surprisingly, similar results were obtained for *Bs*HPF-LΔ10AA (Fig 5F), suggesting that although the *Bs*HPF-LΔ10AA can still bind to the ribosome (Fig 5B), it is impaired in 100S formation. *Bs*HPF variants where the 10 aa or 20 aa were substituted (rather than deleted) by glycine-serine (GS) repeats, creating *Bs*HPF-$(GS)_5$ or *Bs*HPF-$(GS)_{10}$, respectively, also led to both a reduction in ribosome binding and 100S formation (Fig EV4C–E), suggesting that the sequence and not just the length of the linker is critical for *Bs*HPF activity. Lastly, we also monitored 100S formation in the *Bs*168 strain expressing the *Bs*HPF-F160E variant. As expected, no increase in the 100S peak or decrease in the polysome peaks was observed upon *Bs*HPF-F160E induction (Fig 5G), indicating that *Bs*HPF-CTD homodimerization is necessary for 100S formation.

Further support for the loss of activity of the *Bs*HPF-LΔ20AA and *Bs*HPF-F160E variants comes from growth assays. Compared to the wild-type *Bs*168 strain, the Δ*Bs*HPF strain exhibits a lag phase when stationary phase cells are diluted into fresh media (Fig 5H), as reported previously (Akanuma *et al*, 2016). The lag phenotype can be restored by expression of wild-type *Bs*HPF, but not by *Bs*HPF-LΔ20AA and *Bs*HPF-F160E variants (Fig 5H). Curiously, the *Bs*HPF-LΔ10AA variant also rescued the growth phenotype (Fig 5H), suggesting that ribosome binding rather than

Published online: May 3, 2017
The EMBO Journal

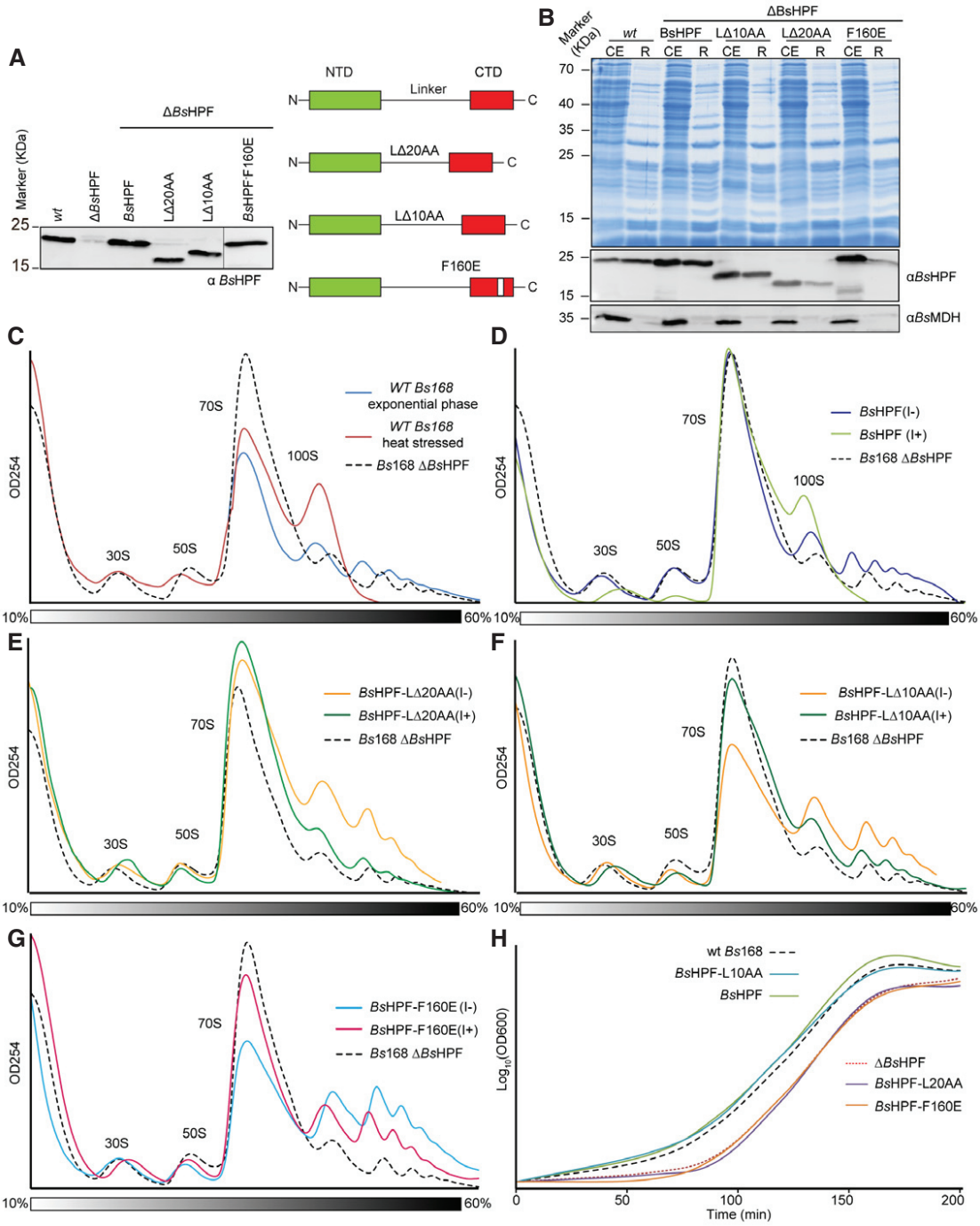

Figure 5. Monitoring 100S formation *in vivo* for *Bs*HPF variants.

A Western blot using antibodies raised against *Bs*HPF to assess the levels of *Bs*HPF in cell extracts of wild-type *Bs*168 (wt), Δ*Bs*HPF, and Δ*Bs*HPF strains expressing either wild-type *Bs*HPF or *Bs*HPF-LΔ20AA, *Bs*HPF-LΔ10AA, *Bs*HPF-F160E variants.

B Coomassie (above) and Western blot of cell extracts (CE) and ribosome pelleted fractions (R) of the wild-type *Bs*168 (wt) strain or the Δ*Bs*HPF strains expressing either wild-type *Bs*HPF, *Bs*HPF-LΔ10AA, *Bs*HPF-LΔ20AA, and *Bs*HPF-F160E.

C Sucrose gradient profiles of cell extracts from the wild-type *Bs*168 (wt) strain in exponential phase (blue) or heat stressed (red), compared with the extract from the *Bs*168 Δ*Bs*HPF strain (dashed line).

D–G Sucrose gradient profiles of cell extracts from the (D) *Bs*168 Δ*Bs*HPF amyE::*Bs*HPF strain, (E) *Bs*168 Δ*Bs*HPF amyE::*Bs*HPF-LΔ20AA strain, (F) *Bs*168 Δ*Bs*HPF amyE::*Bs*HPF-LΔ10AA strain, and (G) *Bs*168 Δ*Bs*HPF amyE::*Bs*HPF-F160E strain in the absence (I−) or presence (I+) of IPTG. The dashed line of the *Bs*168 Δ*Bs*HPF strain from (C) is shown for reference.

H Growth curves illustrating the recovery from stationary phase of the wild-type *Bs*168 (wt), Δ*Bs*HPF, and Δ*Bs*HPF strains expressing either wild-type *Bs*HPF or *Bs*HPF-LΔ20AA, *Bs*HPF-LΔ10AA, *Bs*HPF-F160E variants.

Source data are available online for this figure.

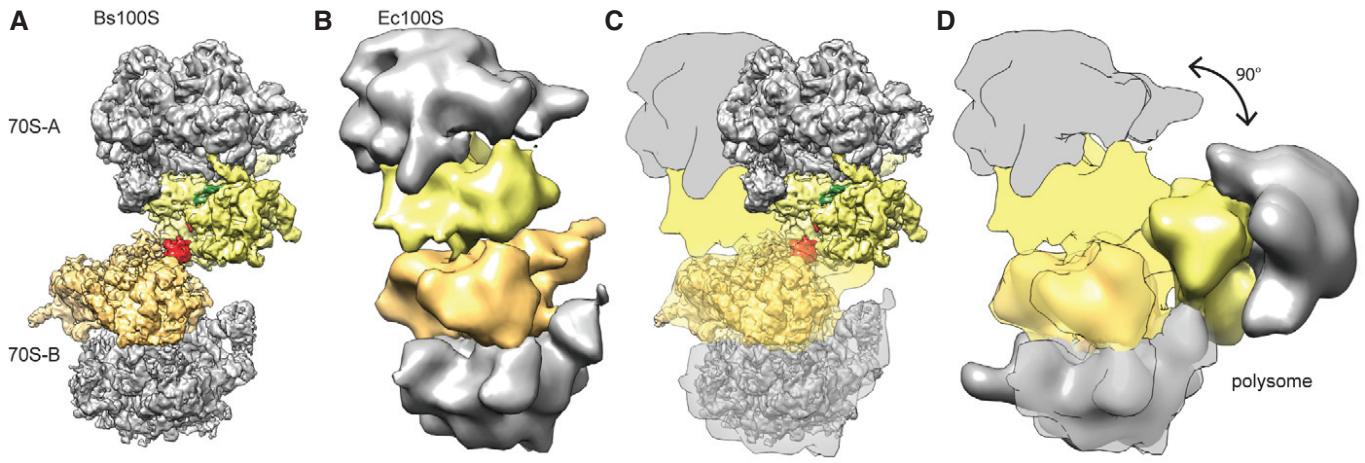

Figure 6. Spatial organization of *Bs*100S, *Ec*100S, and polysomes.

A–D Comparison of the 70S-A and 70S-B monomer arrangement in (A) *Bs*100S, compared with (B, C) *Ec*100S (Ortiz *et al*, 2010) and (D) *Escherichia coli* polysomes (Brandt *et al*, 2009). The 30S-A (yellow), 30S-B (orange), 50S (gray), *Bs*HPF-NTD (green), and *Bs*HPF-CTD (red) are colored for reference, and schematics of the *Ec*100S are presented in (C) and (D) for ease of comparison.

100S formation may be important for efficient stationary phase recovery.

Distinct arrangement of 70S monomers in the *Bs*100S

In order to obtain a reconstruction of the complete *Bs*100S particle to compare with previous *Ec*100S reconstructions, we also reprocessed the cryo-EM data using a larger box size that completely encompassed both 70S monomers (Fig EV2). Despite the inherent flexibility between the 70S monomers, we were able to obtain a reconstruction of the *Bs*100S (Fig 6A) with an average resolution of 6.2 Å (Fig EV5A–C). The relative orientation of the 70S-A and 70S-B monomers within the *Bs*100S was related by a 180° rotational symmetry with the axis of rotation centered on the dimeric *Bs*HPF-CTD (Fig EV5D). As expected, we observed additional density for the HPF-NTD within the intersubunit space and for the HPF-CTD at the back of the 30S subunit (Fig EV5E and F). Comparison of the *Bs*100S with the previous cryo-EM and cryo-ET reconstructions of the *Ec*100S (Fig 6B) revealed a dramatically different monomer arrangement (Fig 6C). While *Ec*100S dimerization involves a "back-to-back" interaction of the 30S subunits of each 70S monomers, *Bs*100S dimerization involves a more "side-to-side" (platform-to-platform) interaction of the 30S subunits. In the *Ec*100S, dimerization is proposed to be stabilized by contacts between S2 on one 70S with the cavity formed by S3/S4/S5 on the other (Kato *et al*, 2010), which may be facilitated by a swivel movement of the head of the 30S subunit that was observed upon RMF binding (Polikanov *et al*, 2012). In contrast, the head position of the *Bs*100S is identical to that observed in the classic post-translocational state ribosome (Sohmen *et al*, 2015) and, unlike RMF, the *Bs*HPF-CTD directly comprises part of the dimerization interface. The spatial orientation of the 70S monomers in the *Bs*100S (Fig 6A) could be considered intermediate between that observed in the *Ec*100S (Fig 6B; Kato *et al*, 2010) and the orientation observed in the cryo-ET reconstructions of *E. coli* polysomes (Fig 6D; Brandt *et al*, 2009).

Discussion

The appearance of hibernating 100S ribosomes is a near universal response of bacteria to adapt to a variety of stress conditions, in particular nutrient limitation (Ueta *et al*, 2013; Yoshida & Wada, 2014). Under these circumstances, bacteria employ second messenger signaling molecules, such as (p)ppGpp and cyclic AMP (cAMP), to reprogram the cellular activity network, down-regulating genes associated with translation and up-regulating stress response and amino acid biogenesis pathways (Hauryliuk *et al*, 2015; Steinchen & Bange, 2016). In *E. coli*, transcription of *rmf*, the gene encoding RMF, is up-regulated by (p)ppGpp when amino acids become limiting (Izutsu *et al*, 2001) and by cAMP upon carbon starvation (Shimada *et al*, 2013). Transcription of *yvyD*, the gene encoding *Bs*LHPF, is under the control of the sigma factors σ^H and σ^B (Drzewiecki *et al*, 1998; Tam le *et al*, 2006; Akanuma *et al*, 2016), and up-regulated by the presence of the alarmone (p)ppGpp (Eymann *et al*, 2001; Tagami *et al*, 2012; Shimada *et al*, 2013; Fig 7A). Similarly, in the cyanobacterium *Synechococcus elongatus*, LHPF is also up-regulated by (p)ppGpp to enable dark adaptation (Hood *et al*, 2016).

The up-regulation of LHPF leads to increased 100S formation, indicating that LHPF competes effectively with translation factors, as evidenced by LHPF inhibition of *in vitro* translation systems (Ueta *et al*, 2013; Basu & Yap, 2016). Since we observed that *Bs*HPF is dimeric in solution, we favor a model whereby dimeric *Bs*HPF interacts independently with two 70S ribosomes (Fig 7B). In this model, we propose that *Bs*HPF utilizes the free NTDs and long linker to initially bring 70S ribosomes into close proximity, and then further stabilizes the 70S dimer using the *Bs*HPF-CTD ribosome interface (Fig 7B). However, we cannot exclude that at a fraction of *Bs*HPF resides as a monomer *in vivo*, and these *Bs*HPF monomers bind separately to the 70S ribosome, such that 100S formation could then occur concomitantly with *Bs*HPF-CTD homodimerization. Moreover, it remains unclear how hibernating 100S ribosomes exactly provide protection against stress. What is

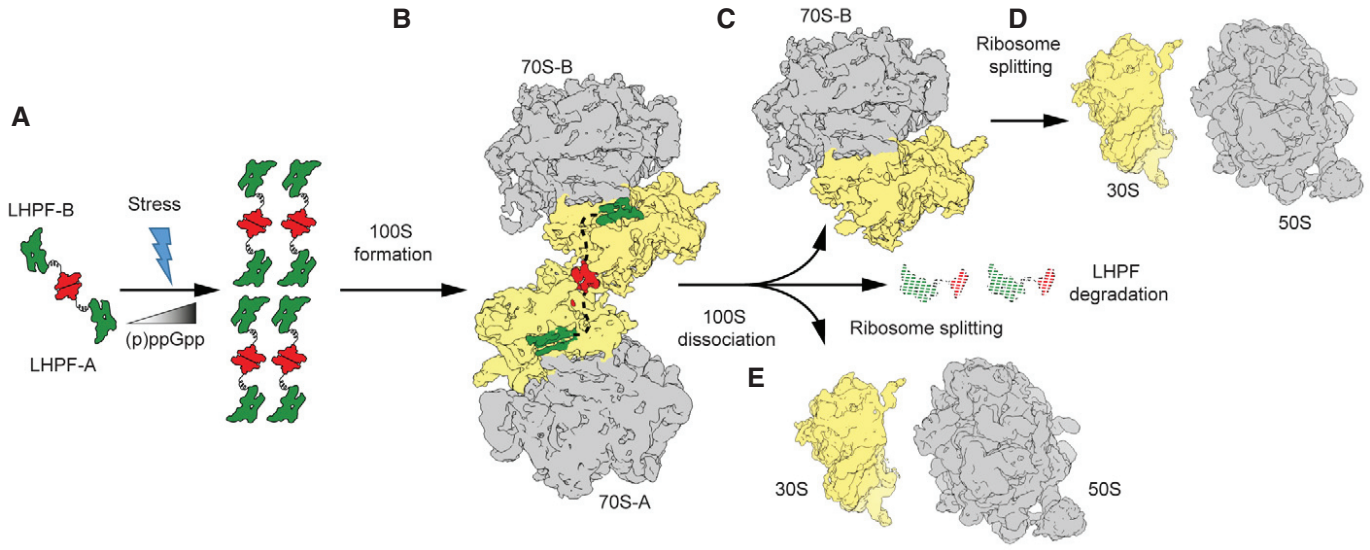

Figure 7. Model for *Bs*HPF-induced 100S formation.

A Stress conditions, such as nutrient deprivation, lead to elevated levels of (p)ppGpp, which up-regulates expression of the LHPF (NTD, green; CTD, red). The LHPF-CTD can interact to form homodimers in solution and therefore may also be present as dimers in the cell.

B The long linker of the dimeric LHPF enables the LHPF-NTD to interact with two independent 70S ribosomes and by bringing them in to close proximity stabilizes the 70S dimers, forming 100S.

C–E Following removal of the stress conditions, *Bs*HPF levels decline leading to (C) dissociation of 100S into 70S ribosomes and (D) eventually ribosome splitting into 30S and 50S subunits, or (E) alternatively directly in 30S and 50S subunits.

clear however is that in the absence of 100S, 70S ribosomes are slowly degraded leading to early cell death, suggesting that hibernating 100S are less susceptible to degradation by RNases (Fukuchi *et al*, 1995; Wada, 1998; Niven, 2004; Shcherbakova *et al*, 2015; Akanuma *et al*, 2016). Because 100S formation does not significantly alter the large rRNA surface exposed to RNases, we believe LHPF binding and 100S formation may interfere with a specific ribosome degradation pathway, rather than preventing non-specific RNase action on ribosomes. The identification of *Bs*HPF variant, such as the *Bs*HPF-LΔ10AA, which binds to the ribosome but does not promote 100S formation, may allow the contribution of these activities to ribosome protection to be dissected further.

In *E. coli*, disassembly of 100S is rapid and occurs within 1 min upon transfer to fresh medium, suggesting that an active mechanism exists to remove *Ec*HPF and RMF from the ribosome (Wada, 1998; Aiso *et al*, 2005). In contrast, *Bs*100S are more stable than *Ec*100S (Ueta *et al*, 2013) and upon transfer to fresh media significant dissociation of *Bs*100S was only observed after 120 min, where LHPF protein levels were also significantly decreased (Akanuma *et al*, 2016). Nevertheless, recycling factors, such as IF3, RRF, and EF-G, which have been reported to remove LHPF (PSRP-1) from Spinach chloroplast ribosomes (Sharma *et al*, 2010), might also be involved in *Bs*HPF release and 100S dissociation (Fig 7C–E).

In conclusion, the high conservation of the LHPF proteins suggests that most, if not all, LHPF proteins are present as dimers in the cell, with the implication that the majority of bacteria are likely to utilize an identical mechanism to induce 100S formation as we have described here for *B. subtilis* (Fig 7).

Materials and Methods

Cloning of *Bs*HPF and *Bs*HPF variants for protein purification

The *yvyD* gene encoding *Bs*HPF was amplified from *B. subtilis* PY79 genomic DNA by polymerase chain reaction using Phusion High-Fidelity DNA Polymerase (NEB) according to the manufacturer's manual. The *forward* primer encoded a hexa-histidine tag in-frame with the DNA sequence of *yvyD*. The fragment was cloned via *Nco*I/*Xho*I restriction sites into a modified pGAT2-vector incorporating a GST-tag N-terminal of His_6-*Bs*HPF. *Bs*HPF-CTD (amino acids 130–189 of *Bs*HPF), *Bs*HPF-NTD (amino acids 1–104 of *Bs*HPF), and *Bs*HPF(F160E) containing an N-terminal hexa-histidine tag were amplified by PCR as described above and cloned via *Nco*I/*Xho*I restriction sites into pET24d(+) vector (Novagen). Mutations within *Bs*HPF were introduced by overlapping PCR.

Protein production and purification for SEC and SLS

Escherichia coli BL21(DE3) cells (NEB) carrying the expression plasmid were grown in lysogeny broth (LB) medium supplemented with ampicillin (100 μg/ml) or kanamycin (50 μg/ml) and D(+)-lactose-monohydrate (12.5 g/l) for 16 h at 30°C under rigorous shaking (180 rpm). The cells were harvested (3,500 × *g*, 20 min, 4°C), resuspended in lysis buffer (20 mM HEPES-KOH, pH 8.0, 20 mM KCl, 20 mM $MgCl_2$, 500 mM NaCl, 40 mM imidazole) and lysed using a M-110L Microfluidizer (Microfluidics). After centrifugation (47,850 × *g*, 20 min, 4°C), the clear supernatant was loaded on a HisTrap HP 1 ml column (GE Healthcare) equilibrated with 15 column volumes (CV) of lysis buffer. After

washing with 15 CV of lysis buffer, the protein was eluted with 5 CV of elution buffer (lysis buffer containing 500 mM imidazole). The GST-tag was removed from *Bs*HPF variants by incubation with 100 U of bovine thrombin (Merck Millipore) for 2 h at 20°C. After dilution with 12 volume parts of lysis buffer without imidazole, *Bs*HPF variants were resubjected to Ni-NTA affinity chromatography as described above and the elution fraction containing *Bs*HPF were collected. *Bs*HPF and *Bs*HPF variants were then concentrated using an Amicon Ultracel-10K or 3K, respectively (Merck Millipore), and applied to size-exclusion chromatography (HiLoad 26/600 Superdex 75 pg, GE Healthcare) equilibrated in SEC buffer (20 mM HEPES-KOH, pH 8.0, 20 mM KCl, 20 mM $MgCl_2$, 500 mM NH_4Cl). Protein-containing fractions were pooled and concentrated to ~500 μM as determined by a spectrophotometer (NanoDrop Lite, Thermo Scientific).

Analysis of oligomerization states of *Bs*HPF variants by SEC and SLS

The apparent molecular weight was analyzed by size-exclusion chromatography using a HiLoad 26/600 Superdex 75 pg column (GE Healthcare) equilibrated in SEC buffer. A standard curve for molecular mass determination was obtained using BSA (66.5 kDa), ovalbumin (chicken, 44.3 kDa), myoglobin (horse, 17 kDa), and vitamin B12 (1.35 kDa). The absolute molecular weight was determined by static light scattering (SLS) with a DelsaMax CORE (Beckmann Coulter) according to the manufacturer's instructions.

Cloning of *Bs*HPF and *Bs*HPF variants for *in vivo* studies

Full-length *yvyD* was amplified from genomic DNA by PCR as described above with the forward primer encoding the strong ribosomal binding site of the *gsiB* gene (AGGAGGAATTCAAA) and cloned via *Sal*I/*Sph*I restriction sites into the pDR111 plasmid (Ben-Yehuda *et al*, 2003). The *Bs*HPF-LΔ10AA, *Bs*HPF-LΔ20AA, and *Bs*HPF-F160E mutation were introduced by overlap extension PCR and cloned via SalI/SphI restriction sites as described above. The resulting plasmids were linearized by digestion with *Sca*I and transformed into naturally competent *B. subtilis* cells. Proper integration into the *amyE* locus was checked by growing selected transformants on LB-Agar containing 1% starch overnight and staining the plates with a solution of 0.5% (w/v) iodine, 1% (w/v) potassium iodine. Strains and oligonucleotides used in this study are presented in Tables EV2 and EV3.

Western blotting of *Bs*HPF variants

Strains expressing HPF variants *in trans* were grown in LB medium supplemented with 1 mM IPTG with rigorous shaking to until the mid-exponential phase (OD_{600} of ~0.8), harvested by centrifugation at 11,000 × g, 4°C for 5 min, washed once in TE buffer (10 mM Tris–HCl, 1 mM EDTA, pH 8.0), and disrupted by sonication three times for 30 s on ice in TE buffer supplemented with 1 mM PMSF. The soluble protein was cleared from cell debris by centrifugation at 11,000 × g, 4°C for 5 min. 10 μg of the protein extract (as determined by the Bradford assay) was analyzed by SDS–PAGE and Western Blotting onto a nitrocellulose membrane. As controls, equally treated samples from a stationary phase overnight culture of *B. subtilis* wild-type or *Δhpf* cells were loaded. The *Bs*HPF protein was detected using a polyclonal antibody raised against *Bs*HPF (Pineda Antibody Service) and a polyclonal Goat anti-Rabbit IgG alkaline Phosphatase conjugated antibody (Antikörper Online). Western blotting using an antibody against the malate dehydrogenase (MDH) was used as a loading control. The ECF reagent (GE Healthcare) was used as a substrate according to the manufacturer's manual, and chemifluorescent signals were detected using a cooled CCD camera in a ChemiBIS 4.2 Bioimaging system (DNR).

Binding assay for *Bs*HPF variants with pelleted ribosomes

Bacillus subtilis cells were grown in 200-ml LB medium supplemented with 1 mM IPTG with rigorous shaking (200 rpm) to the mid-exponential phase (OD_{600} ~0.8) and harvested by centrifugation at 15,300 × *g*, 10 min, 4°C. Ribosomes were pelleted as described in (Schmalisch *et al*, 2002). Briefly, cells were washed once in buffer A (20 mM Tris–HCl, 100 mM NH_4Cl, 10 mM $MgCl_2$, 10 mM 2-mercaptoethanol, pH 7.5), resuspended in 3 ml of the same buffer with 1 mM PMSF and disrupted in a French Pressure Cell three times at 1,000 psi. The lysate was cleared from cell debris by centrifugation for 30 min at 29,953 × g, 4°C (SW55-Ti, Beckman Coulter), layered on top of a 8 ml 1.1 M sucrose cushion in buffer A, and centrifuged for 16 h at 119,307 × g, 4°C (SW40-Ti, Beckman Coulter). The cell pellet was washed three times in buffer A and resuspended in buffer B (20 mM Tris–HCl, 100 mM NH_4Cl, 6 mM $MgCl_2$, 2 mM DTT). The suspension was centrifuged at 10,000 × g, 10 min, 4°C, and the supernatant containing the ribosomes was collected. 10 μg of the total soluble protein ("CE", as determined by the Bradford assay) and an equal volume of the ribosome suspension ("R") was subjected to 15% SDS–PAGE and subsequent stained with Coomassie using standard procedures or Western blotting as described above.

Growth recovery from stationary phase

Precultures of *B. subtilis* cells were grown in 5-ml LB medium supplemented with 0.5 mM IPTG at 37°C for 18 h, to ensure the cells reached the stationary growth phase. The cultures were then diluted to an OD_{600} of 0.05 into 20-ml fresh LB medium and grown at 37°C with rigorous shaking. The cell growth was monitored by determining the optical density at 600 nm (OD_{600}) at regular intervals.

Sucrose density gradient centrifugation analysis

Analysis of 100S formation was performed as described previously for *B. subtilis* (Akanuma *et al*, 2016). Briefly, 50-ml LB medium was inoculated at a 1:100 dilution with an overnight culture. Expression was induced using 1 mM IPTG at an OD_{600} of 0.4. Cells were harvested at the stationary phase by centrifugation at 4,000 × *g* for 10 min at 4°C (Hettich Rotanta 46R) and the cell pellet re-suspended in buffer C (50 mM HEPES-KOH, pH7.4, 100 mM KOAc, 25 mM Mg $(OAc)_2$, 6 mM β-mercaptoethanol). Cells were lysed using the sonifier three times, with each cycle consisting of 30 s at 30% power followed by centrifugation at 16,000 × *g* for 15 min at 4°C to remove cellular debris. A total OD_{260} of 10 of the cleared lysate was loaded onto sucrose density gradients (10–60% sucrose in buffer C)

by centrifugation at 154,693 × *g* (SW-40 Ti, Beckman Coulter) for 3 h at 4°C and then analyzed using a Gradient Station (Biocomp) with an Econo UV Monitor (Bio-Rad) and a FC203B Fraction Collector (Gilson).

Preparation of *Bacillus subtilis* S12 extract

Bacillus subtilis S12 extract was prepared as described (Sohmen *et al*, 2015). Briefly, an "INFORCE HT minifors" bench top fermenter was used to grow *B. subtilis* strain 168 cells to an OD_{600} 4.5 in 2× YPTG medium (16 g/l peptone, 10 g/l yeast extract, 5 g/l NaCl, 22 mM NaH_2PO_4, 40 mM Na_2HPO_4, 19.8 g/l glucose (sterile filtered)), with extra glucose feeding at 37°C while maintaining a pH 7.0 and oxygen level (60%). After collecting cells at 5,000 × *g* at 4°C for 15 min, they were washed 3× in cold Buffer A (10 mM Tris–acetate (pH 8.2), 14 mM magnesium acetate, 60 mM potassium glutamate, 1 mM dithiothreitol, and 6 mM β-mercaptoethanol). Cells were then snap-frozen in liquid nitrogen and stored at −80°C. 15 g of cells was thawed on ice, resuspended in 10 ml of cold buffer B (buffer A missing β-mercaptoethanol), and lysed 3× at 15,000 psi in an "microfluidics model 110I lab homogenizer". The lysate was cleared at 12,000 × *g* and 4°C for 10 min and incubated in a water bath for 30 min at 37°C. The cell extract was aliquoted, snap-frozen, and stored at −80°C. Extracts were analyzed on sucrose density gradients (10–50% sucrose in buffer C), by centrifugation at 89,454 × *g* (SW-28, Beckman Coulter) for 4 h at 4°C. For 100S purification, 100S fractions were collected using a Gradient Station (Biocomp) with an Econo UV Monitor (Bio-Rad) and a FC203B Fraction Collector (Gilson). Purified 100S ribosomes were concentrated by centrifugation at 92,159 × *g* for 2.5 h at 4°C (TLA110 rotor, Beckman Coulter).

Negative stain electron microscopy

Ribosomal particles were diluted in buffer C to a final concentration of 0.2 OD_{260}/ml. A 3.5 μl sample was applied onto a carbon-coated grid. After 30 s, the grids were washed with distilled water and then stained with 2% aqueous uranyl acetate for 15 s. The remaining liquid was removed by touching the grid with filter paper. Micrographs were taken using a Morgagni transmission electron microscope (FEI).

Cryo-electron microscopy and single particle reconstruction

A total of 4 OD_{260}/ml *Bs*100S sample were applied to 2 nm precoated Quantifoil R3/3 holey carbon-supported grids and vitrified using Vitrobot Mark IV (FEI Company). Data collection was performed using EM-TOOLS (TVIPS GmbH) on a Titan Krios transmission electron microscope equipped with a Falcon II direct electron detector (FEI Company) at 300 kV at a pixel size of 1.084 Å and a defocus range of 0.7–2.2 μm. Ten frames (dose per frame of 2.5 e^-/Å) were aligned using Motion Correction Software (Li *et al*, 2013). Power-spectra, defocus values, and astigmatism were then determined using CTFFIND4 software (Rohou & Grigorieff, 2015). Micrographs showing Thon rings beyond 3.5 Å were manually inspected for a good areas and power-spectra quality. Automatic particle picking was then performed using SIGNATURE (Chen & Grigorieff, 2007), and single particles were windowed out in small box able to contain a 70S ribosome together with the majority of the small 30S subunit of the neighboring 70S ribosome. The particles were then further processed using FREALIGN (Grigorieff, 2007). The 253,905 particles were first subjected to an extensive 3D classification (Fig EV2A and B), and the selected 24,546 *Bs*100S particles of class 8 were then subjected to refinement using 30S-70S mask resulting in a final reconstruction of 3.8 Å (0.143 FSC) average resolution (Figs EV2C and EV3). Local resolution was finally calculated using ResMap (Kucukelbir *et al*, 2014). For the processing of the complete *Bs*100S, the coordinates of the selected 24,546 particles were carefully re-inspected in order to remove particles that were within close proximity of another particle, so as not to include particles twice in the final reconstruction; 5,511 particles were identified and removed from class 8, and the rest of particles were windowed out using a larger box size that encompassed two 70S ribosomes (Fig EV2D). The remaining 19,335 particles were then realigned and refined, resulting in a final reconstruction with an average resolution of 6.2 Å (0.143 FSC; Fig EV5A–C).

Molecular modeling, refinement, and validation

The molecular model for the ribosomal proteins and rRNA of the 70S ribosome of the *Bs*100S was based on the molecular model from the recent cryo-EM reconstruction of the *B. subtilis* 70S ribosome (PDB ID 3JW9; Sohmen *et al*, 2015). The molecular model was fitted as a rigid body into the cryo-EM density maps using UCSF Chimera (Pettersen *et al*, 2004). For *Bs*HPF-NTD domain, a homology model was generated using HHPred (Soding *et al*, 2005) based on the HPF protein template from *E. coli* (PDB ID 4V8H; Polikanov *et al*, 2012; Fig EV1C). Molecular models were fitted and adjusted by using COOT (Emsley & Cowtan, 2004) and refined in Phenix using *phenix.real_space_refine* (Adams *et al*, 2010). Model over-fitting was evaluated through its refinement against one cryo-EM half map as described previously (Brown *et al*, 2015). FSC curves were calculated between the resulting model and the half map used for refinement, as well as between the resulting model and the other half map for cross-validation (Fig EV3E). The final refinement statistics were determined using MolProbity (Chen *et al*, 2010) and are provided in Table EV1. For *Bs*HPF-CTD domain, a homology model was generated using HHPred based on the template from *C. acetobutylicum* (PDB ID 3KA5; Fig EV1D). The molecular model was rigid body fitted using UCSF Chimera (Pettersen *et al*, 2004).

Figure preparation

Figures showing map densities and atomic models were generated using UCSF Chimera (Pettersen *et al*, 2004).

Accession numbers

The cryo-EM map of the *Bs*70S-30S subcomplex and the complete *Bs*100S have been deposited in the EMDB with the accession codes EMD-3656 and EMD-3664, respectively. Atomic coordinates have been deposited in the Protein Data Bank with accession code PDB ID 5NJT.

Expanded View for this article is available online.

Acknowledgements
We thank Heidimarie Sieber, Charlotte Ungewickell, and Susanne Rieder for expert technical assistance; Uwe Linne (Marburg) for mass spectrometry support; and Beckmann-Coulter GmbH (Krefeld, Germany) for kindly providing the DelsaMax CORE. This research was supported by grants from the Deutsche Forschungsgemeinschaft (SPP-1879 to K.T., G.B., and D.N.W.).

Author contributions
DNW, GB, and KT designed and supervised the study. MA prepared the *Bs*100S sample for cryo-EM and performed all sucrose gradient analyses. OB collected the cryo-EM data. BB, MA, and SA processed the cryo-EM data. BB, MA, RB, and DNW interpreted the cryo-EM data. WS cloned and purified the *Bs*HPF protein variants and performed the SEC and SLS. HS generated all *Bs*HPF expression strains and performed Western blotting, growth curves, and ribosome pelleting assays. DNW, GB, and KT wrote the manuscript with comments from all authors.

Conflict of interest
The authors declare that they have no conflict of interest.

Note added in proof
The recent cryo-EM structure of the *Staphylococcus aureus* 100S determined by Khusainov *et al* (2017) reveals that the mechanism of 70S dimerization mediated by the *S. aureus* long-form HPF appears to be similar to that observed here for *Bacillus subtilis*.

References

Adams PD, Afonine PV, Bunkoczi G, Chen VB, Davis IW, Echols N, Headd JJ, Hung LW, Kapral GJ, Grosse-Kunstleve RW, McCoy AJ, Moriarty NW, Oeffner R, Read RJ, Richardson DC, Richardson JS, Terwilliger TC, Zwart PH (2010) PHENIX: a comprehensive python-based system for macromolecular structure solution. *Acta Crystallogr D Biol Crystallogr* 66(Pt 2): 213 – 221

Agafonov DE, Spirin AS (2004) The ribosome-associated inhibitor A reduces translation errors. *Biochem Biophys Res Commun* 320: 354 – 358

Aiso T, Yoshida H, Wada A, Ohki R (2005) Modulation of mRNA stability participates in stationary-phase-specific expression of ribosome modulation factor. *J Bacteriol* 187: 1951 – 1958

Akanuma G, Kazo Y, Tagami K, Hiraoka H, Yano K, Suzuki S, Hanai R, Nanamiya H, Kato-Yamada Y, Kawamura F (2016) Ribosome dimerization is essential for the efficient regrowth of *Bacillus subtilis*. *Microbiology* 162: 448 – 458

Basu A, Yap MN (2016) Ribosome hibernation factor promotes Staphylococcal survival and differentially represses translation. *Nucleic Acids Res* 44: 4881 – 4893

Ben-Yehuda S, Rudner DZ, Losick R (2003) RacA, a bacterial protein that anchors chromosomes to the cell poles. *Science* 299: 532 – 536

Bieri P, Leibundgut M, Saurer M, Boehringer D, Ban N (2017) The complete structure of the chloroplast 70S ribosome in complex with translation factor pY. *EMBO J* 36: 475 – 486

Brandt F, Etchells SA, Ortiz JO, Elcock AH, Hartl FU, Baumeister W (2009) The native 3D organization of bacterial polysomes. *Cell* 136: 261 – 271

Brown A, Long F, Nicholls RA, Toots J, Emsley P, Murshudov G (2015) Tools for macromolecular model building and refinement into electron cryo-microscopy reconstructions. *Acta Crystallogr D Biol Crystallogr* 71(Pt 1): 136 – 153

Chen JZ, Grigorieff N (2007) SIGNATURE: a single-particle selection system for molecular electron microscopy. *J Struct Biol* 157: 168 – 173

Chen VB, Arendall WB III, Headd JJ, Keedy DA, Immormino RM, Kapral GJ, Murray LW, Richardson JS, Richardson DC (2010) MolProbity: all-atom structure validation for macromolecular crystallography. *Acta Crystallogr D Biol Crystallogr* 66(Pt 1): 12 – 21

Drzewiecki K, Eymann C, Mittenhuber G, Hecker M (1998) The yvyD gene of *Bacillus subtilis* is under dual control of sigmaB and sigmaH. *J Bacteriol* 180: 6674 – 6680

El-Sharoud WM, Niven GW (2007) The influence of ribosome modulation factor on the survival of stationary-phase *Escherichia coli* during acid stress. *Microbiology* 153(Pt 1): 247 – 253

Emsley P, Cowtan K (2004) Coot: model-building tools for molecular graphics. *Acta Crystallogr D Biol Crystallogr* 60: 2126 – 2132

Eymann C, Mittenhuber G, Hecker M (2001) The stringent response, sigmaH-dependent gene expression and sporulation in *Bacillus subtilis*. *Mol Gen Genet* 264: 913 – 923

Fukuchi JI, Kashiwagi K, Yamagishi M, Ishihama A, Igarashi K (1995) Decrease in cell viability due to the accumulation of spermidine in spermidine acetyltransferase-deficient mutant of *Escherichia coli*. *J Biol Chem* 270: 18831 – 18835

Garay-Arroyo A, Colmenero-Flores JM, Garciarrubio A, Covarrubias AA (2000) Highly hydrophilic proteins in prokaryotes and eukaryotes are common during conditions of water deficit. *J Biol Chem* 275: 5668 – 5674

Graf M, Arenz S, Huter P, Donhofer A, Novacek J, Wilson DN (2016) Cryo-EM structure of the spinach chloroplast ribosome reveals the location of plastid-specific ribosomal proteins and extensions. *Nucleic Acids Res* 45: 2887 – 2896

Grigorieff N (2007) FREALIGN: high-resolution refinement of single particle structures. *J Struct Biol* 157: 117 – 125

Hauryliuk V, Atkinson GC, Murakami KS, Tenson T, Gerdes K (2015) Recent functional insights into the role of (p)ppGpp in bacterial physiology. *Nat Rev Microbiol* 13: 298 – 309

Hood RD, Higgins SA, Flamholz A, Nichols RJ, Savage DF (2016) The stringent response regulates adaptation to darkness in the cyanobacterium *Synechococcus elongatus*. *Proc Natl Acad Sci USA* 113: E4867 – E4876

Izutsu K, Wada A, Wada C (2001) Expression of ribosome modulation factor (RMF) in *Escherichia coli* requires ppGpp. *Genes Cells* 6: 665 – 676

Jenner L, Demeshkina N, Yusupova G, Yusupov M (2011) Structural rearrangements of the ribosome at the tRNA proofreading step. *Nat Struct Mol Biol* 17: 1072 – 1078

Kato T, Yoshida H, Miyata T, Maki Y, Wada A, Namba K (2010) Structure of the 100S ribosome in the hibernation stage revealed by electron cryomicroscopy. *Structure* 18: 719 – 724

Khusainov I, Vicens Q, Ayupov R, Usachev K, Myasnikov A, Simonetti A, Validov S, Kieffer B, Yusupova G, Yusupov M, Hashem Y (2017) Structures and dynamics of hibernating ribosomes from *Staphylococcus aureus* mediated by intermolecular interactions of HPF. *EMBO J* 36: 2073 – 2087

Kline BC, McKay SL, Tang WW, Portnoy DA (2015) The listeria monocytogenes hibernation-promoting factor is required for the formation of 100S ribosomes, optimal fitness, and pathogenesis. *J Bacteriol* 197: 581 – 591

Kucukelbir A, Sigworth FJ, Tagare HD (2014) Quantifying the local resolution of cryo-EM density maps. *Nat Methods* 11: 63 – 65

Li X, Mooney P, Zheng S, Booth CR, Braunfeld MB, Gubbens S, Agard DA, Cheng Y (2013) Electron counting and beam-induced motion correction

enable near-atomic-resolution single-particle cryo-EM. *Nat Methods* 10: 584 – 590

Maki Y, Yoshida H, Wada A (2000) Two proteins, YfiA and YhbH, associated with resting ribosomes in stationary phase *Escherichia coli*. *Genes Cells* 5: 965 – 974

McKay SL, Portnoy DA (2015) Ribosome hibernation facilitates tolerance of stationary-phase bacteria to aminoglycosides. *Antimicrob Agents Chemother* 59: 6992 – 6999

Niven GW (2004) Ribosome modulation factor protects *Escherichia coli* during heat stress, but this may not be dependent on ribosome dimerization. *Arch Microbiol* 182: 60 – 66

Ortiz JO, Brandt F, Matias VR, Sennels L, Rappsilber J, Scheres SH, Eibauer M, Hartl FU, Baumeister W (2010) Structure of hibernating ribosomes studied by cryoelectron tomography *in vitro* and *in situ*. *J Cell Biol* 190: 613 – 621

Pei J, Kim BH, Grishin NV (2008) PROMALS3D: a tool for multiple protein sequence and structure alignments. *Nucleic Acids Res* 36: 2295 – 2300

Pettersen EF, Goddard TD, Huang CC, Couch GS, Greenblatt DM, Meng EC, Ferrin TE (2004) UCSF chimera – a visualization system for exploratory research and analysis. *J Comput Chem* 25: 1605 – 1612

Polikanov YS, Blaha GM, Steitz TA (2012) How hibernation factors RMF, HPF, and YfiA turn off protein synthesis. *Science* 336: 915 – 918

Puri P, Eckhardt TH, Franken LE, Fusetti F, Stuart MC, Boekema EJ, Kuipers OP, Kok J, Poolman B (2014) *Lactococcus lactis* YfiA is necessary and sufficient for ribosome dimerization. *Mol Microbiol* 91: 394 – 407

Reiss S, Pane-Farre J, Fuchs S, Francois P, Liebeke M, Schrenzel J, Lindequist U, Lalk M, Wolz C, Hecker M, Engelmann S (2012) Global analysis of the *Staphylococcus aureus* response to mupirocin. *Antimicrob Agents Chemother* 56: 787 – 804

Rohou A, Grigorieff N (2015) CTFFIND4: fast and accurate defocus estimation from electron micrographs. *J Struct Biol* 192: 216 – 221

Schmalisch M, Langbein I, Stulke J (2002) The general stress protein Ctc of *Bacillus subtilis* is a ribosomal protein. *J Mol Microbiol Biotechnol* 4: 495 – 501

Sharma MR, Wilson DN, Datta PP, Barat C, Schluenzen F, Fucini P, Agrawal RK (2007) Cryo-EM study of the spinach chloroplast ribosome reveals the structural and functional roles of plastid-specific ribosomal proteins. *Proc Natl Acad Sci USA* 104: 19315 – 19320

Sharma MR, Donhofer A, Barat C, Marquez V, Datta PP, Fucini P, Wilson DN, Agrawal RK (2010) PSRP1 is not a ribosomal protein, but a ribosome-binding factor that is recycled by the ribosome-recycling factor (RRF) and elongation factor G (EF-G). *J Biol Chem* 285: 4006 – 4014

Shcherbakova K, Nakayama H, Shimamoto N (2015) Role of 100S ribosomes in bacterial decay period. *Genes Cells* 20: 789 – 801

Shimada T, Yoshida H, Ishihama A (2013) Involvement of cyclic AMP receptor protein in regulation of the rmf gene encoding the ribosome modulation factor in *Escherichia coli*. *J Bacteriol* 195: 2212 – 2219

Soding J, Biegert A, Lupas AN (2005) The HHpred interactive server for protein homology detection and structure prediction. *Nucleic Acids Res* 33(Web Server issue): W244 – W248

Sohmen D, Chiba S, Shimokawa-Chiba N, Innis CA, Berninghausen O, Beckmann R, Ito K, Wilson DN (2015) Structure of the *Bacillus subtilis* 70S ribosome reveals the basis for species-specific stalling. *Nat Commun* 6: 6941

Steinchen W, Bange G (2016) The magic dance of the alarmones (p)ppGpp. *Mol Microbiol* 101: 531 – 544

Tagami K, Nanamiya H, Kazo Y, Maehashi M, Suzuki S, Namba E, Hoshiya M, Hanai R, Tozawa Y, Morimoto T, Ogasawara N, Kageyama Y, Ara K, Ozaki K, Yoshida M, Kuroiwa H, Kuroiwa T, Ohashi Y, Kawamura F (2012) Expression of a small (p)ppGpp synthetase, YwaC, in the (p)ppGpp(0) mutant of *Bacillus subtilis* triggers YvyD-dependent dimerization of ribosome. *Microbiologyopen* 1: 115 – 134

Tam le T, Antelmann H, Eymann C, Albrecht D, Bernhardt J, Hecker M (2006) Proteome signatures for stress and starvation in *Bacillus subtilis* as revealed by a 2-D gel image color coding approach. *Proteomics* 6: 4565 – 4585

Ueta M, Yoshida A, Wada C, Baba T, Mori H, Wada A (2005) Ribosome binding proteins YhbH and YfiA have opposite functions during 100S formation in the stationary phase of *Escherichia coli*. *Genes Cells* 10: 1103 – 1112

Ueta M, Ohniwa RL, Yoshida H, Maki Y, Wada C, Wada A (2008) Role of HPF (hibernation promoting factor) in translational activity in *Escherichia coli*. *J Biochem* 143: 425 – 433

Ueta M, Wada C, Wada A (2010) Formation of 100S ribosomes in *Staphylococcus aureus* by the hibernation promoting factor homolog SaHPF. *Genes Cells* 15: 43 – 58

Ueta M, Wada C, Daifuku T, Sako Y, Bessho Y, Kitamura A, Ohniwa RL, Morikawa K, Yoshida H, Kato T, Miyata T, Namba K, Wada A (2013) Conservation of two distinct types of 100S ribosome in bacteria. *Genes Cells* 18: 554 – 574

Vila-Sanjurjo A, Schuwirth BS, Hau CW, Cate JHD (2004) Structural basis for the control of translational initiation during stress. *Nature Struct Mol Biol* 11: 1054 – 1059

Wada A, Yamazaki Y, Fujita N, Ishihama A (1990) Structure and probable genetic location of a ribosome modulation factor associated with 100S ribosomes in stationary-phase *Escherichia coli* cells. *Proc Natl Acad Sci USA* 87: 2657 – 2661

Wada A, Igarashi K, Yoshimura S, Aimoto S, Ishihama A (1995) Ribosome modulation factor: stationary growth phase-specific inhibitor of ribosome functions from *Escherichia coli*. *Biochem Biophys Res Commun* 214: 410 – 417

Wada A (1998) Growth phase coupled modulation of *Escherichia coli* ribosomes. *Genes Cells* 3: 203 – 208

Wada A, Mikkola R, Kurland CG, Ishihama A (2000) Growth-phase coupled changes of the ribosome profile in natural isolates and laboratory strains of *Escherichia coli*. *J Bacteriol* 182: 2893 – 2899

Yamagishi M, Matsushima H, Wada A, Sakagami M, Fujita N, Ishihama A (1993) Regulation of the *Escherichia coli* rmf gene encoding the ribosome modulation factor - growth phase-dependent and growth rate-dependent control. *EMBO J* 12: 625 – 630

Yoshida H, Maki Y, Kato H, Fujisawa H, Izutsu K, Wada C, Wada A (2002) The ribosome modulation factor (RMF) binding site on the 100S ribosome of *Escherichia coli*. *J Biochem* 132: 983 – 989

Yoshida H, Wada A (2014) The 100S ribosome: ribosomal hibernation induced by stress. *Wiley Interdiscip Rev RNA* 5: 723 – 732

Expanded View Figures

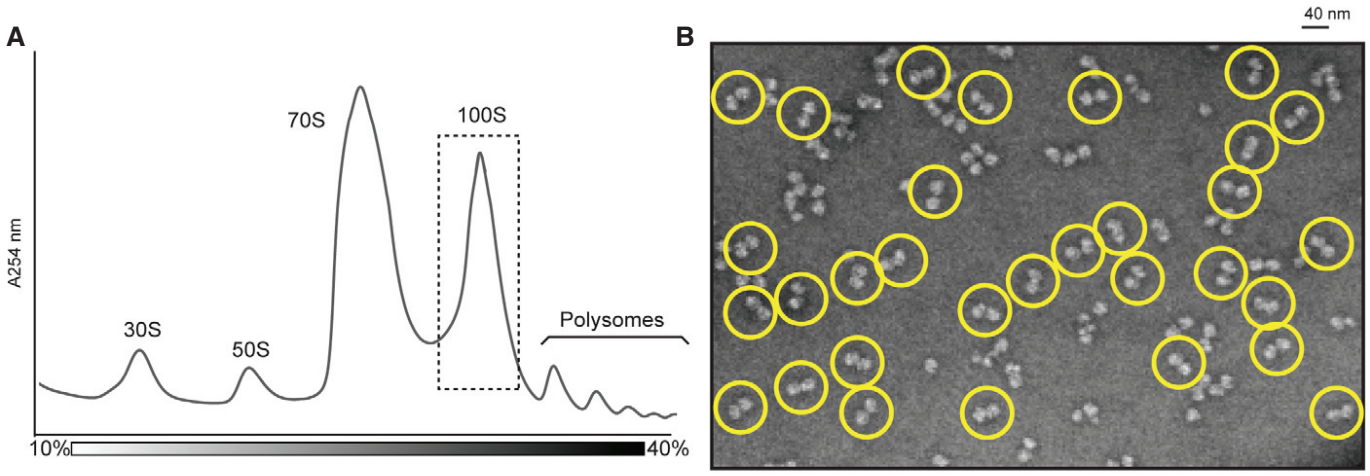

C

```
Conservation:    9  99 9 9 9 9 99   9  9  999 999      9                9
EcHPF          1  MQLNITGNNVEITEALREFVTAKFAKLEQYFDRINQVYVVLKVEKV---THTSDATLHVNGGEIHASAEG   67
4V8H.pdb       1  MQLNITGNNVEITEALREFVTAKFAKLEQYFDRINQVYVVLKVEKV---THTSDATLHVNGGEIHASAEG   67
BsNTD_HPF      1  MNYNIRGENIEVTPALKDHVERKIGKLERYFDHSVDADVNVNLKFYNDKESKVEVTIPMTDLALRSEVHN   70
Consensus_aa:     MphNIpGpNlElT.AL+-@Vp.KhtKLEpYFD+.sph.Vslplcbh...ppps-hTl.hss..l+tphcs
Consensus_ss:      eeeeeeeeee  hhhhhhhhhhhhhhhhh    eeeeeeeee       eeeeeeee    eeeeeee

Conservation:       999 999    99 99  999 9
EcHPF          68  QDMYAAIDGLIDKLARQLTKHKDKLKQH----------   95
4V8H.pdb       68  QDMYAAIDGLIDKLARQLTKHKDKLKQH----------   95
BsNTD_HPF      71  EDMYNAIDLATNKLERQIRKHKTKVNRKFREQGSPKYLL  109
Consensus_aa:     pDMYsAID.hhsKL.RQlpKHKsKlpp+..........
Consensus_ss:       hhhhhhhhhhhhhhhhhhhhhhhhhhh
```

D

```
Conservation:                  99  999  999  999 9 9  99999999 9   9  9999 9 99 999999
3KA5 chainA  1    ----------EIVKTKRFAIKPMSEEEAVLEMELLGHNFFVFQNGDSNEVNVVYKRKDGNYGLIEPE-   57
BsCTD        121  VQDDIEEEESLDIVRQKRFNLKPMDSEEAILQMNMLGHNFFVFTNAETNLTNVVYRRNDGKYGLIEPTE  189
Consensus_aa:     ..........-IV+pKRFslKPMspEEAlLpMphLGHNFFVFpNt-oNbhNVVY+RpDGpYGLIEPp.
Consensus_ss:                eeeeeeee     hhhhhhhh     eeeee      eeeeeee    eeeeee
```

Figure EV1. Isolation of *Bacillus subtilis* 100S and sequence alignments of *Bs*HPF with *Ec*HPF-NTD and *Ca*CTD.

A Sucrose density gradient profile of *B. subtilis* extract from late log phase cells, with 30S, 50S, 70S, 100S, and polysome peaks indicated.

B Negative stain electron microscopy images of purified *Bs*100S from (A), with selected 70S dimers circled in yellow.

C PROMALS3D (Pei *et al*, 2008) sequence alignment of *Bs*HPF-NTD with *Escherichia coli* HPF (PDB 4V8H)(Polikanov *et al*, 2012) that was used to generate the homology model for *Bs*HPF-NTD.

D PROMALS3D (Pei *et al*, 2008) sequence alignment of *Bs*HPF-CTD with *Clostridium acetobutylicum* HPF-CTD (*Ca*CTD; PDB ID 3KA5) that was used to generate the homology model for *Bs*HPF-CTD.

Data information: In (C) and (D), fully conserved residues are indicated with "9" and are bold in the Consensus_aa, whereas similar residues are indicated with a "+". Consensus_ss indicates β-sheet (e) and helical (h) regions.

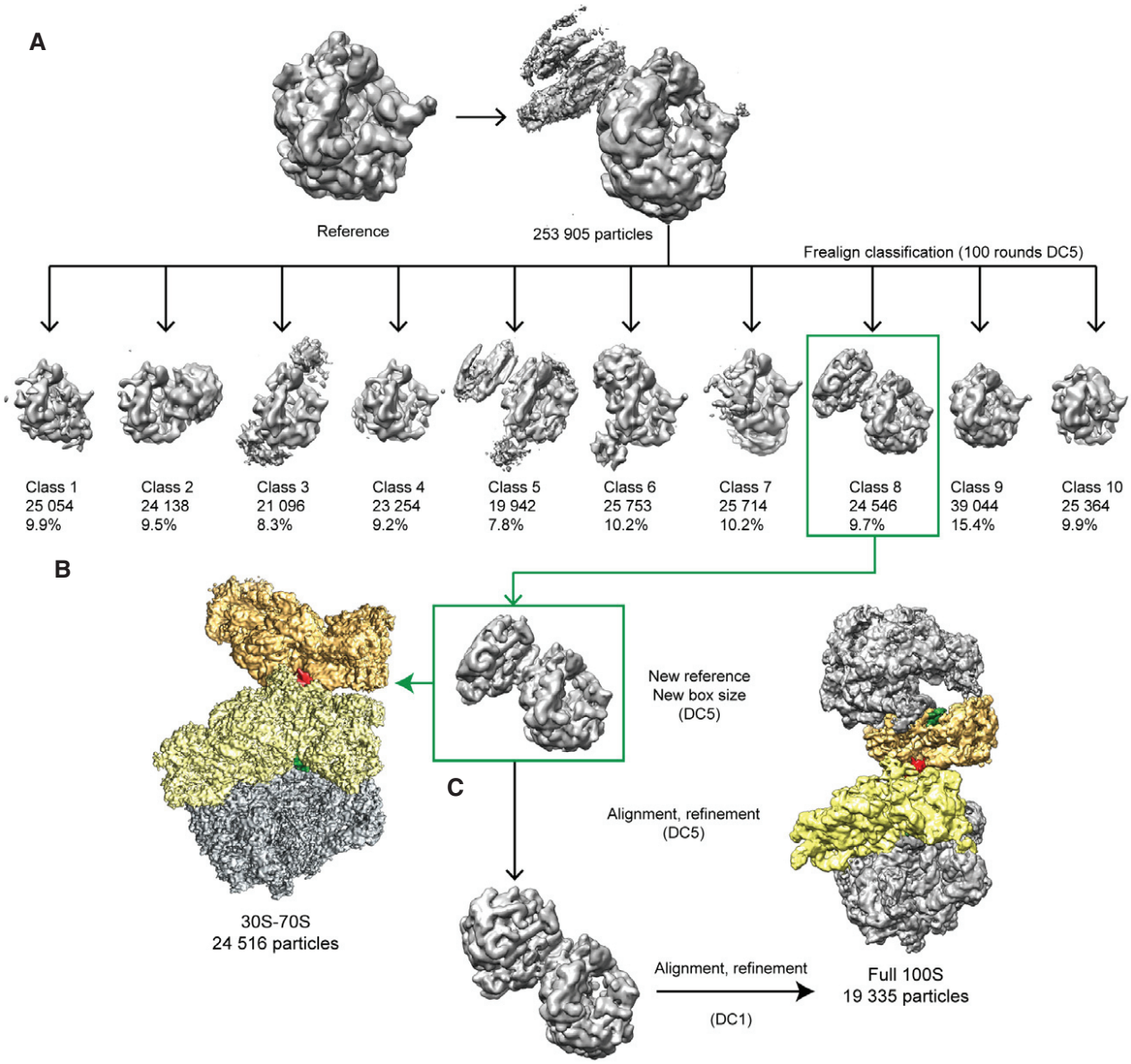

Figure EV2. ***In silico*** **sorting and refinement scheme for the *Bs*70S-30S subcomplex and complete *Bs*100S.**

A–C 253,905 particles were sorted into 10 classes. Class 8 had the most defined density for the 70S-B and was taken for further refinement using (B) a box size that includes the 70S-A ribosome and the 30S part of the 70S-B, and (C) a larger box size that encompasses both the 70S-A and 70S-B ribosomes.

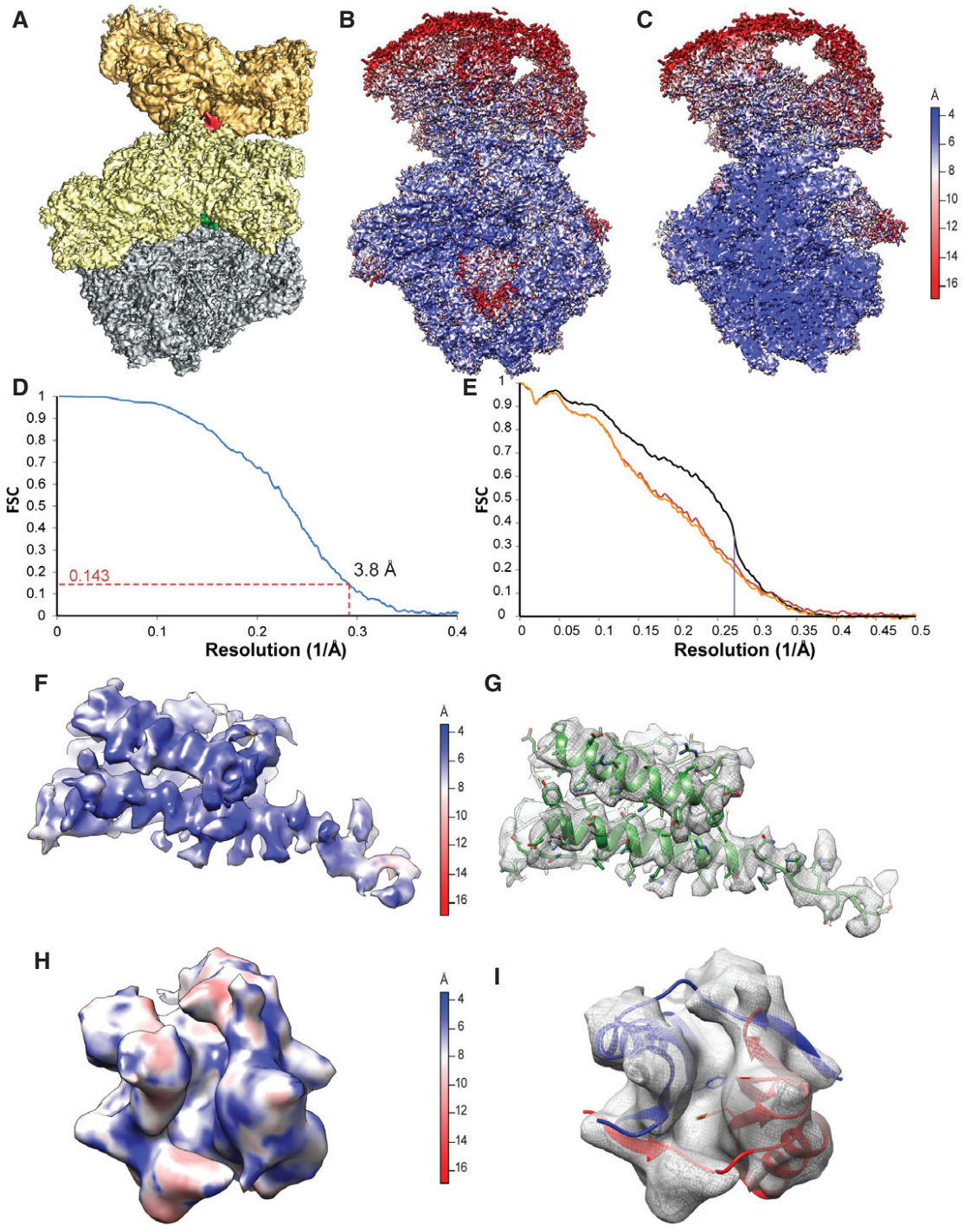

Figure EV3. Resolution of 70S-A in the *Bs*70S-30S subcomplex.

A Overview of the *Bs*70S-30S subcomplex with 30S-A (yellow), 50S-A (gray), and 30S-B (orange), as well as *Bs*HPF-NTD (green) and *Bs*HPF-CTD (red).

B, C Overview (B) and transverse section (C) of the *Bs*70S-30S subcomplex colored according to the local resolution, as calculated using ResMap (Kucukelbir *et al*, 2014).

D Fourier-shell correlation curve of the refined cryo-EM map, indicating the average resolution of 70S-A in the *Bs*70S-30S subcomplex is 3.8 Å.

E Fit of models to maps. FSC curves calculated between the refined model and the final map (black), with the self- and cross-validated correlations in orange and red, respectively. Information beyond 4 Å was not used during refinement and preserved for validation.

F–I Map density for the (F, G) *Bs*HPF-NTD and (H, I) *Bs*HPF-CTD, which are (F, H) colored according to the local resolution, as calculated using ResMap (see Materials and Methods), or (G, I) shown as a gray mesh with molecular models (G) for *Bs*HPF-NTD (green) or (I) *Bs*HPF-CTD for 70S-A (red) and 70S-B (blue), using the same respective view as in (F, H).

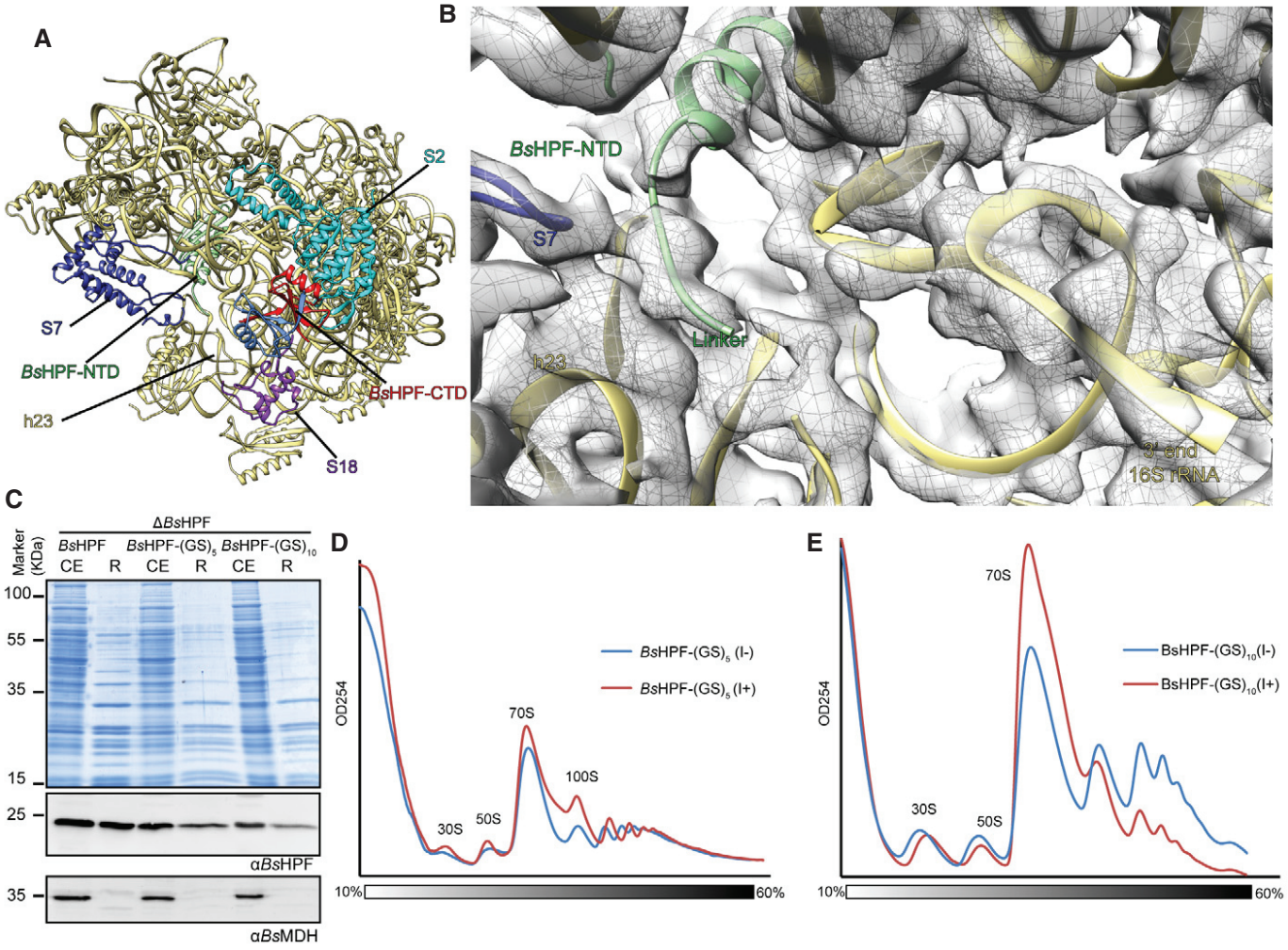

Figure EV4. *Bs*HPF linker region approaches the 30S platform cavity.

A Overview of the 30S cavity region showing *Bs*HPF-NTD (green) and *Bs*HPF-CTD (red) and 30S (yellow), except S2 (cyan), S7 (blue), and S18 (purple).

B Zoom of (A), showing map density (gray mesh) for the N-terminal part of the linker region of *Bs*HPF (green) as well as for the 3′ end of the 16S rRNA.

C Coomassie (upper panel) and Western blot of cell extracts (CE) and ribosome pelleted fractions (R) of the wild-type *Bs*168 (wt) strain or the Δ*Bs*HPF strains expressing either wild-type *Bs*HPF, *Bs*HPF-$(GS)_5$, or *Bs*HPF-$(GS)_{10}$.

D, E Sucrose gradient profiles of cell extracts from the (D) *Bs*168 Δ*Bs*HPF amyE::*Bs*HPF-$(GS)_5$ strain and (E) *Bs*168 Δ*Bs*HPF amyE::*Bs*HPF-$(GS)_{10}$ strain, in the absence (I−) or presence (I+) of IPTG.

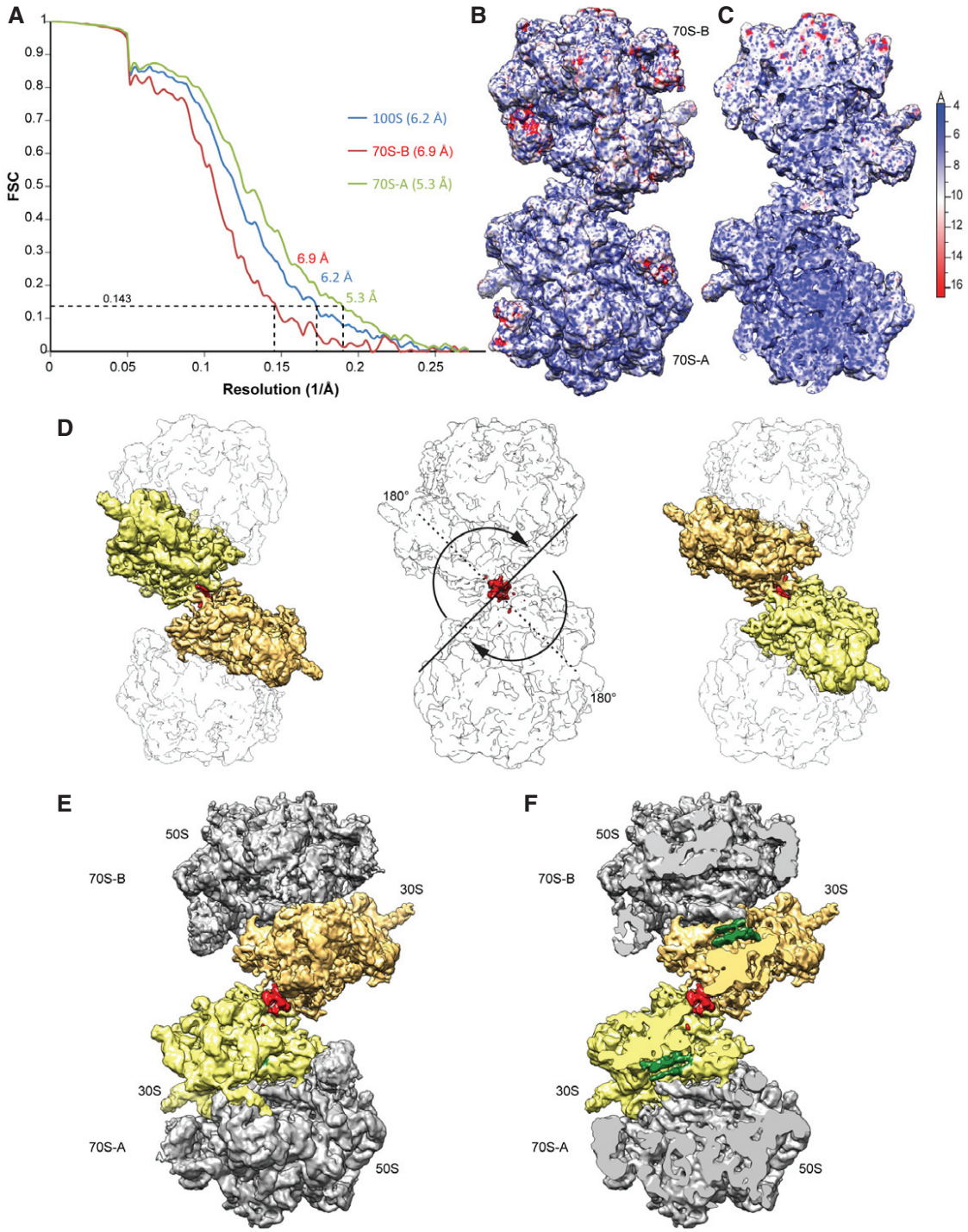

Figure EV5. Resolution of the complete dimeric *Bs*100S.

A Fourier-shell correlation curve of the refined cryo-EM map, indicating the average resolution of 70S-A, 70S-B, and the complete *Bs*100S is 5.3, 6.9 and 6.2 Å, respectively.

B, C Cryo-EM map of the dimeric *Bs*100S colored according to local resolution showing (B) overview and (C) transverse section of the complete 100S disome.

D The 70S-A and 70S-B monomers in the Bs100S are related by rotational symmetry of ~180°.

E, F Cryo-EM map of the (E) dimeric *Bs*100S with 30S-A (yellow), 30S-B (orange) and 50S (gray), and (F) transverse section of (E) highlighting the densities for the *Bs*HPF-NTD (green) and *Bs*HPF-CTD (red).

Table EV1 Cryo-EM data collection and model refinement statistics

Data Collection and Refinement	
Particles	25,516
Pixel size (Å)	1.084
Defocus range (μm)	0.7-2.2
Voltage (kV)	300
Electron dose ($e^-/Å^2$)	24
Model Composition	
Protein residues	6480
RNA bases	4642
Refinement	
Resolution (Å)	3.8
Map sharpening B factor ($Å^2$)	-95.95
Box size	450x450x450
Map CC (whole Unit Cell)	0.47
Map CC (around atoms)	0.75
Validation Proteins	
Poor rotamers (%)	1.42
Ramachandran outliers (%)	0.26
Ramachandran favored (%)	85.36
Bad backbone bonds (%)	0.04
Bad backbone angles (%)	0.15
Validation RNA	
Correct sugar puckers (%)	98.25
Good backbone conformations (%)	70.72
Bad bonds (%)	0.00
Bad angles (%)	0.04
Scores	
MolProbity score	2.22 (63^{th} percentile)
Clash score, all atoms	8.26 (81^{th} percentile)

Table EV2 Oligonucleotides

Name (relevant features)	**Sequence (5' to 3')**
P146_yvyD_for (*SalI*, RBS)	ACGC*GTCGAC*AGGAGGAATTCAAAATGAACTATAACATCAGAGGAG
P147_yvyD_rev (*SphI*)	ACA*GCATGC*TTATTCAGTCGGTTCAATTAAGC
P475_ LΔ10AA_for	GCTCTCCAAAATATTTATTGGCGGTTCAGGATGACATAGA
P476_ LΔ10AA_rev	TCTATGTCATCCTGAACCGC CAATAAATATTTTGGAGAGC
P477_ LΔ20AA_for	AATTCCGTGAGCAGGGCTCT ATAGAAGAGGAGGAGAGCTTG
P478_ LΔ20AA_rev	CAAGCTCTCCTCCTCTTCTATAGAGCCCTGCTCACGGAATT
P480_F160E_for	ATGCTCGGCCATAAT GAA TTTGTTTTCACAAATGCGGAAAC
P481_F160E_rev	ATTTGTGAAAACAAA TTC ATTATGGCCGAGCATATTCATTTG

Table EV3 Strains used in this work

Strain	Relevant characteristics	Source
168	trpC2	[1-]BGSC: 1A1
BKD1	trpC2 lys-3 ΔHPF::kan	(Drzewiecki et al, 1998)
BHS008	ΔHPF::kan	this work
BHS399	amyE::Phyperspank-HPF spec ΔHPF::kan	this work
BHS607	amyE::Phyperspank-HPFΔ20AA(Δ105-124) spec HPF::kan	this work
BHS613	amyE::Phyperspank-HPFΔ10AA(110-194) spec ΔHPF::kan	this work
BHS617	amyE::Phyperspank-HPF (F160E) spec ΔHPF::kan	this work

[1-]BGSC: Bacillus Genetic Stock Center, Columbus, Ohio, USA.

Published online 25 May 2016

Nucleic Acids Research, 2016, Vol. 44, No. 13 ***6471–6481***
doi: 10.1093/nar/gkw470

The stringent factor RelA adopts an open conformation on the ribosome to stimulate ppGpp synthesis

Stefan Arenz[1,†], Maha Abdelshahid[1,†], Daniel Sohmen[1,†], Roshani Payoe[2], Agata L. Starosta[1], Otto Berninghausen[1], Vasili Hauryliuk[2,3], Roland Beckmann[1,4] and Daniel N. Wilson[1,4,*]

[1]Gene Center and Department for Biochemistry, University of Munich, Munich 81377, Germany, [2]University of Tartu, Institute of Technology, Nooruse 1, 50411 Tartu, Estonia, [3]Laboratory for Molecular Infection Medicine Sweden (MIMS), Umeå University, Building 6K and 6L, University Hospital Area, SE-901 87 Umeå, Sweden and [4]Center for integrated Protein Science Munich (CiPSM), University of Munich, Munich 81377, Germany

Received April 06, 2016; Revised April 29, 2016; Accepted May 12, 2016

ABSTRACT

Under stress conditions, such as nutrient starvation, deacylated tRNAs bound within the ribosomal A-site are recognized by the stringent factor RelA, which converts ATP and GTP/GDP to (p)ppGpp. The signaling molecules (p)ppGpp globally rewire the cellular transcriptional program and general metabolism, leading to stress adaptation. Despite the additional importance of the stringent response for regulation of bacterial virulence, antibiotic resistance and persistence, structural insight into how the ribosome and deacylated-tRNA stimulate RelA-mediated (p)ppGpp has been lacking. Here, we present a cryo-EM structure of RelA in complex with the *Escherichia coli* 70S ribosome with an average resolution of 3.7 Å and local resolution of 4 to >10 Å for RelA. The structure reveals that RelA adopts a unique 'open' conformation, where the C-terminal domain (CTD) is intertwined around an A/T-like tRNA within the intersubunit cavity of the ribosome and the N-terminal domain (NTD) extends into the solvent. We propose that the open conformation of RelA on the ribosome relieves the autoinhibitory effect of the CTD on the NTD, thus leading to stimulation of (p)ppGpp synthesis by RelA.

INTRODUCTION

The stringent response (SR) is a central bacterial adaptation mechanism. In response to various environmental stimuli, the RelA/SpoT Homologue (RSH) proteins modulate the intracellular concentration of the alarmone nucleotides guanosine tetraphosphate (ppGpp) and guanosine pentaphosphate (pppGpp), commonly referred to as (p)ppGpp (1–3). Production of (p)ppGpp mediates global rewiring of the cellular transcriptional program and general metabolism, leading to stress adaptation. The SR has been shown to play an important role in regulation of bacterial virulence (4), survival during host invasion (5), as well as antibiotic resistance (6) and persistence (7). Together with the absence of a cytoplasmic (p)ppGpp-mediated SR system in eukaryotes, this makes the RSH enzymes involved in (p)ppGpp metabolism promising new targets for drug development (3,8,9).

Historically, investigations of the SR were focused on the γ-proteobacterium *Escherichia coli*. In *E. coli*, the SR is orchestrated by two multi-domain long form RSH enzymes: RelA (10) and SpoT (11). The activity of the two proteins is regulated by different sets of stress signals. SpoT has a strong (p)ppGpp hydrolytic activity and a weak (p)ppGpp synthesis activity (12–14). By contrast, RelA has no hydrolytic activity, but possesses a strong ribosome-dependent (p)ppGpp synthetic activity that is activated by amino acid starvation via sensing of deacylated tRNA in the ribosomal A-site (15–17). It has also been shown that there is another activator of RelA, namely its product ppGpp (18). There are conflicting models for the mechanism of action of RelA. Biochemical studies suggested that (p)ppGpp synthesis causes RelA to 'hop' between ribosomes to sample the translational status of the cell (16). Subsequent live cell single molecule tracking experiments suggested that while activation of RelA by starved ribosomes induces RelA dissoci-

*To whom correspondence should be addressed. Tel: +49 89 2180 76903; Fax: +49 89 2180 76945; Email: wilson@lmb.uni-muenchen.de
†These authors contributed equally to the paper as first authors.
Present address: Agata L. Starosta, Centre for Bacterial Cell Biology, Institute for Cell and Molecular Biosciences, University of Newcastle, Newcastle upon Tyne, UK.

ation, RelA can perform multiple rounds of catalysis off the ribosome (19). This is hard to reconcile with recent live cell single molecule tracking experiments suggesting that under starvation conditions RelA remains bound to the ribosome and synthesis multiple rounds of (p)ppGpp synthesis (20).

Sequence analysis (2) and biochemical studies (21–23) suggest that RelA has a two domain architecture: An N-terminal domain (NTD) bearing hydrolase (HD) and synthetase (SYNTH) subdomains, the structure of which is available from the Gram-positive bacterium *Streptococcus dysgalactiae* subsp. *equisimilis* Rel protein (24). To date, there is no atomic structure of the RelA C-terminal domain (CTD), however, sequence homology suggests the presence of a TGS (Thr-RS, GTPase and SpoT) motif followed by a helical linker region connected to the C-terminal conserved cysteine (CC) and Aspartokinase, Chorismate mutase and TyrA (ACT) subdomains (2). Although the precise function of these subdomains is unclear, the CTD is critical for ribosome binding (25) as well as autoinhibition of the synthetase activity of RelA in the absence of the ribosome (21–23,26). Structural insights into the RSH interaction with the ribosome come from a cryo-electron microscopy (EM) structure of *E. coli* RelA bound to the *Thermus thermophilus* 70S ribosome programmed with $tRNA_f^{Met}$ in the P-site and $tRNA^{Phe}$ in the A-site (25). The structure reveals that on the ribosome RelA interacts with a distorted A/T-tRNA (25), similar but distinct from the A/T-tRNA observed on the ribosome in the presence of EF-Tu (27–29). The limited resolution (~11 Å) and conformation flexibility of the bound RelA, however, precluded assignment of the NTD and CTD (25).

Here, we present a cryo-EM structure of *E. coli* RelA in complex with a translating ribosome stalled with a deacylated-tRNA in the A-site, with an average resolution of 3.7 Å and local resolution of 4 to >10 Å for RelA. The structure reveals that the HD and SYNTH domains within the NTD of RelA are highly flexible and protrude into the solvent where no contact with the ribosome is apparent. In contrast, the CTD of RelA adopts an open conformation on the ribosome that stabilizes an A/T-like conformation of the deacylated tRNA in the A-site, which we term the A/R-tRNA state. The TGS domain of RelA interacts with the CCA-end, suggesting its involvement in discriminating deacylated- from aminoacylated-tRNAs. A long helical linker region extends from the TGS domain, wraps around the A/R-tRNA and positions the CC and ACT domains deeper within the intersubunit cavity, where they interact with H38 of the 23S rRNA. Overall, the structure enables a model to be proposed for how the open conformation of the CTD of RelA on the ribosome leads to stimulation of the (p)ppGpp activity of the NTD.

MATERIALS AND METHODS

Generation and purification of ErmCL_S10K-SRC

The RelA-stalled ribosomal complex (SRC) was generated based on the disome approach (Figure 1A-D), aspreviously described (30). The *2XermCL* construct was modified by mutation of codon 10 AGC (Ser) to AAG (Lys) and synthesized (Eurofins, Martinsried, Germany) such that it contained a T7 promoter followed by a strong ribosome binding site (RBS) spaced by 7 nucleotides (nts) to the ATG start codon of the first *ermCL_S10K* cistron. A linker of 22 nts separated the stop codon of the first *ermCL_S10K* cistron and the start codon of the second *ermCL_S10K* cistron. The linker also comprised the strong RBS 7 nts upstream of the ATG start codon of the second *ermCL_S10K* cistron, enabling initiation of translation independent from the first *ermCL_S10K* cistron. With the exception of the S10K mutation, each *ermCL_S10K* cistron encoded amino acids 1–19 corresponding to the ErmCL leader peptide (Genbank accession number V01278) present on the macrolide resistance plasmid pE194 (31,32). The complete sequence of *2XermCL_S10K* construct is: 5'-*TAATACGACTCACTATAGGG*AGTTTTATA**AG GAGG**AAAAAATATGGGCATTTTTAGTATTTTTGT A**ATC**AAGACAGTTCATTATCAACCAAACAAAA AATAAAGTTTTATA**AGGAGG**AAAAAATATGGG CATTTTTAGTATTTTTGTA**ATC**AAGACAGTTCAT TATCAACCAAACAAAAAATAA-3' (T7 promoter, italics; RBS, bold; ErmCL ORF, underlined with ATC codon in P-site of stalled ribosome shown in bold; Annealing site for complementary DNA oligonucleotide, underlined). *In vitro* translation of the *ermCL_S10K* construct was performed using the Rapid Translation System RTS 100 *E. coli* HY Kit (5PRIME). Translation reactions were analyzed on sucrose density gradients (10%-55% sucrose in buffer A, containing 50 mM HEPES-KOH, pH 7.4, 100 mM KOAc, 25 mM $Mg(OAc)_2$, 6 mM β-mercaptoethanol, 10 μM erythromycin and 1x Complete EDTA-free Protease Inhibitor cocktail (Roche)) by centrifugation at 154 693 × *g* (SW-40 Ti, Beckman Coulter) for 3 h at 4°C. For ErmCL_S10K-SRC purification, disome fractions were collected using a Gradient Station (Biocomp) with an Econo UV Monitor (Biorad) and a FC203B Fraction Collector (Gilson). Purified ErmCL_S10K-SRC disomes were concentrated by centrifugation at 88 760 × *g* for 4 h at 4°C (TLA120.2 rotor, Beckman Coulter). To obtain monosomes of the ErmCL_S10K-SRC, a short DNA oligonucleotide (5′-ttcctccttataaaact-3′, Metabion) was annealed to the linker between the *ermCL_S10K* cistrons, generating a DNA–RNA hybrid that could be cleaved by RNase H (NEB) treatment in buffer A at 25°C for 1 h. After cleavage of the disomes, ErmCL_S10K-SRC monosomes were again purified and concentrated by centrifugation at 88 760 × *g* for 4 h at 4°C (TLA120.2 rotor, Beckman Coulter).

Expression and purification of RelA

RelA (Gene ID: 947244) was cloned into pET46LIC vector with an N-terminal hexahistidine tag (His_6) for purification and detection purposes. An enterokinase cleavage site (bold) connects the His_6 tag (underlined) to the RelA (MAHHHHHH**VDDDDK**M). The RelA plasmid was chemically transformed into *E. coli* BL21 (DE3) competent cells. A volume of 4L LB medium was inoculated at a 1:100 dilution with an overnight culture. RelA expression was induced by addition of 1 mM Isopropyl β-D-1-thiogalactopyranoside (IPTG) at OD_{600} = 0.5 for 1 h at 30°C. Cells were harvested by centrifugation at 5000 × *g* for 10 min at 4°C (Sorvall, SLC 6000 rotor) and the cell

pellet was re-suspended using lysis buffer (300 mM NaCl, 50 mM NaH_2PO_4, 5 mM imidazole and 1 mM PMSF, pH 8.0). Cells were lysed using the microfluidizer (Microfluidics), followed by centrifugation at 38 724 × *g* for 30 min at 4°C to remove cellular debris (Sorvall, SS-34 rotor). The cleared lysate was then incubated at 4°C for 20 min with 1.6 ml of Ni-NTA slurry pre-equilibrated with lysis buffer. The lysate–Ni-NTA mixture was centrifuged at 500 × *g* for 1 min after which the beads were washed four times with 10 ml of washing buffer (300 mM NaCl, 50 mM NaH_2PO_4 and 10 mM imidazole, pH8.0). Elution of RelA was carried out using 1 ml of elution buffer (300 mM NaCl, 50 mM NaH_2PO_4, 250 mM imidazole and 1 mM PMSF, pH 8.0). Eluted RelA was further purified by gel-filtration (Superdex 200 10/300 GL; pre-equilibrated in buffer B (50 mM HEPES, 100 mM KCl, 200 mM NaCl, 10 mM $MgCl_2$, 5 mM β-mercaptoethanol, 2% glycerol and 1 mM PMSF, pH 7.8). Subsequently, purified RelA protein was concentrated via centrifugation through Amicon Ultra-0.5 ml centrifugal filters (30K, Merck Millipore). The activity of the RelA protein was confirmed using the ribosome-dependent ppGpp synthesis assay (Supplementary Figure S1) pasting.

ppGpp synthesis assay

The assays were performed as described in (18) with minor modifications. Ribosomal complexes were formed using heat activated vacant *E. coli* 70S ribosomes (0.5 μM) programmed with synthetic MF-mRNA 5′-GGCAAGGAGGUAAAAAUGUUCAAA-3′ (Sigma Aldrich) (1 μM), 0.3 mM ^{3}H-GDP, 1 mM ATP, deacylated $tRNA_f^{Met}$ and $tRNA^{Phe}$ (Chemical Block Ltd.) (1.5 μM each) (25 mM HEPES-KOH pH 7.5, 15 mM $Mg(OAc)_2$, 95 mM KCl, 5 mM NH_4Cl, 0.5 mM $CaCl_2$, 8 mM putrescine and 1 mM spermidine) (33). ^{3}H-ppGpp was separated from ^{3}H-GDP on TLC (PEI cellulose, Macherey-Nagel) in 0.5 M KH_2PO_4 pH 3.5. UV shadowing of TLC with non-radioactive nucleotides was used to identify the ^{3}H-GDP and ^{3}H-ppGpp spots, the TLC plate was cut and ^{3}H-GDP and ^{3}H-ppGpp fragments of the plate were subjected to scintillation counting individually (Supplementary Figure S1).

Generation of the RelA-SRC using the ErmCL_S10K-SRC

The RelA-SRC complex was assembled using a final concentration of 0.125 μM ErmCL_S10K-SRC, 0.625 μM RelA, 0.625 μM $tRNA^{Lys}$ (Sigma-Aldrich), 500 μM α, β-methylene-ATP (Sigma-Aldrich), 500 μM GDP and 10 μM erythromycin. All components were pre-dissolved in buffer A (as mentioned before but excluding Ery and 1x Complete EDTA-free Protease Inhibitor cocktail). The binding reaction (RelA-SRC sample) was incubated at 37°C for 20 min.

Negative-stain electron microscopy

Ribosomal particles were diluted in buffer A to a final concentration of 0.5 A260/ml. One drop of each sample was deposited on a carbon-coated grid. After 30 s, grids were washed with distilled water and then stained with 2% aqueous uranyl acetate for 15 s. The remaining liquid was removed by touching the grid with filter paper. Micrographs were taken using a Morgagni transmission electron microscope (FEI), 80 kV, wide angle 1K CCD at direct magnifications of 72K.

Cryo-electron microscopy and single particle reconstruction

A total of 4 A_{260}/ml monosomes of the RelA-SRC sample were applied to 2 nm pre-coated Quantifoil R3/3 holey carbon supported grids and vitrified using a Vitrobot Mark IV (FEI Company). Data collection was performed using EM-TOOLS (TVIPS GmbH) on a Titan Krios transmission electron microscope equipped with a Falcon II direct electron detector (FEI Company) at 300 kV at a pixel size of 1.084 Å and a defocus range of 0.7–2.2 μm. Ten frames (dose per frame of 2.5 $e^-/Å^2$) were aligned using Motion Correction software (34) and then processed using a frequency-limited refinement protocol that helps prevent overfitting (35), specifically by truncation of high frequencies (in this case, at 8 Å). As reported and expected (35), we find that using this processing regime the 0.143 FSC value provides a good indicator for the true average resolution of the map. Additionally, the local resolution of the map was calculated using ResMap (36). Power-spectra, defocus values, astigmatism and estimation of micrograph resolution were determined using the CTFFIND4 software (37). Micrographs showing Thon rings beyond 3.5 Å resolution were further manually inspected for good areas and power-spectra quality. Data were processed using the SPIDER software package (38), in combination with an automated workflow as described previously (39). After initial, automated particle selection based on the program SIGNATURE (40), initial alignment was performed with 197 090 particles using *E. coli* 70S ribosome as a reference structure (41). The data set could be sorted into four homogeneous subpopulations using an incremental K-means-like method of unsupervised 3D sorting (42) (Supplementary Figure S2): The ligand-bound subpopulation (24 749 particles; 13%) was defined by the presence of stoichiometric densities for P-tRNA, A/R-tRNA and RelA and could be refined to an average resolution of 3.7 Å (0.143 FSC) and a local resolution extending to 3.5 Å for the core of the 30S and 50S subunit as computed using ResMap (36) (Supplementary Figure S3). The final map of the RelA-SRC was Butterworth-filtered to 4 Å resolution.

Molecular modeling and map-docking procedures

The molecular model of the RelA-SRC was based on the ErmCL-TetM-SRC structure (PDB3J9Y, (43)), which was in turn based on an *E. coli* ribosome model from (29). The L11 stalk, 30S head domain, H38 and the L1 stalk were fitted as individual rigid bodies into the RelA-SRC map and subsequently manually adjusted and refined in Coot (44). Homology models of the RelA domains TGS (PDB2EKI) and ACT (PDB2KO1) were generated using HHPred (45) and Modeller (46) and could be unambiguously rigid body-fitted into the RelA-SRC cryo-EM density (Supplementary Figure S3). The homology model for the RelA HD-SYNTH domain was based on PDB1VJ7 (24) and fitted into the 12 Å filtered density. In order to yield the best fit, the HD was rotated slightly with respect to the SYNTH.

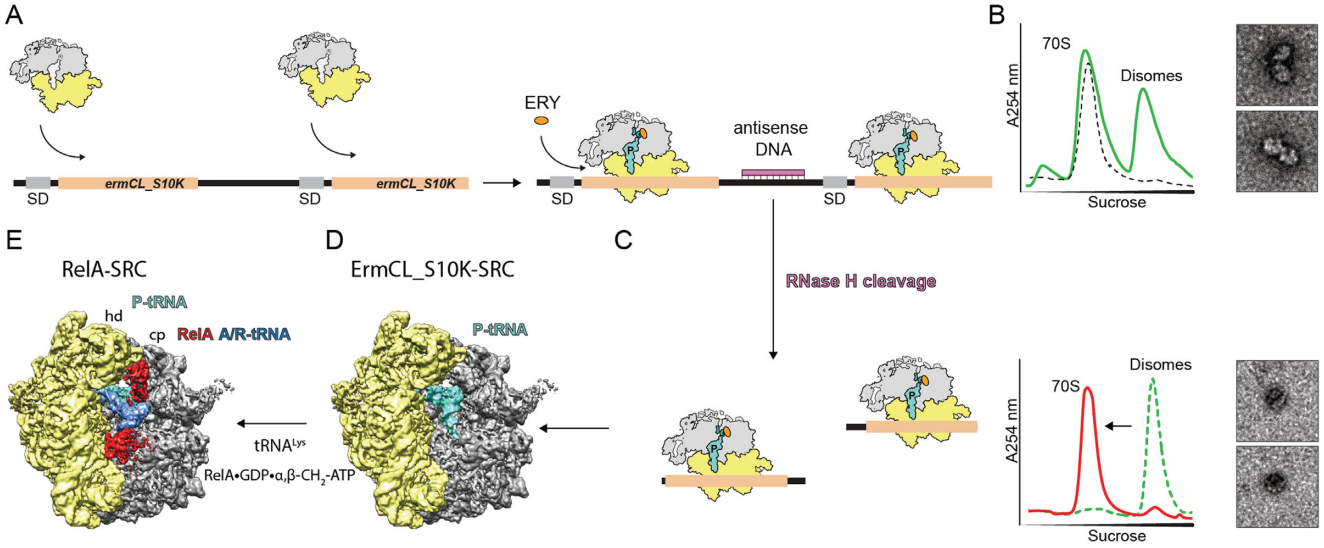

Figure 1. Generation of a RelA-stalled ribosome complex. (**A**) The bicistronic 2XermCL_S10K mRNA was translated in the presence of 10 μM erythromycin (ERY) in order to generate (**B**) ErmCL-S10K_SRC disomes. (**C**) ErmCL_S10K-SRC disomes were converted to monosomes by antisense DNA-mediated RNase H cleavage, as shown by sucrose density gradient centrifugation and negative stain electron microscopy (EM). (**D**) A-tRNA deficient ErmCL_S10K-SRCs were used as substrate for (**E**) RelA binding in the presence of deacylated $tRNA^{Lys}$, GDP and α, β-methylene-ATP.

The molecular model for the A/R-tRNA was based on the A/T tRNA of a crystal structure of EF-Tu-bound ribosomes (PDB2WRN, (27)), which was rigid body-fitted into the density. The CCA-end of the A/R-tRNA was tentatively adjusted in Coot (44) to illustrate its rough positioning within the TGS domain of RelA. Alignment of the EF-Tu structure (PDB5AFI) was performed in Chimera on the basis of the 23S rRNA, and has an rmsd of 0.64 with the 23S rRNA of the RelA structure.

Figure preparation

All figures showing electron densities and atomic models were generated using UCSF Chimera (47).

RESULTS

Generation of a RelA-stalled ribosome complex

The RelA-ribosome complex was generated *in vitro* by addition of purified RelA protein to SRCs. As in our previous studies (30,41,43), the SRCs were obtained using a dicistronic *2Xerm*-mRNA encoding two identical Erm-stalling leader peptides (Figure 1A). *In vitro* translation of the *2Xerm* mRNA in the presence of the macrolide antibiotic erythromycin generates disomes, where two ribosomes are stalled on the same mRNA (Figure 1B). The disomes were then separated from non-translating 70S ribosomes using sucrose gradients (Figure 1B). For structural analysis, the disomes were converted back to monosomes by annealing of an antisense DNA oligonucleotide to the linker region between the two *erm* cistrons (Figure 1C). We first used this disome approach to determine cryo-EM structures of ErmBL-SRCs, revealing that the sample contained a large population of ribosomes bearing A- and P-tRNAs (30) and was thus unsuitable for binding of ligands to the A-site. In contrast, our more recent structure of the ErmCL-SRC contained a single homogenous population of ribosomes with the ErmCL-peptidyl-tRNA (with codon 9 of the mRNA) in the P-site and a free A-site (41) (Figure 1D), which is thus suitable for determination of ErmCL-SRC structures with A-site bound ligands, as exemplified by the ribosome protection protein TetM (43). In the case of the RelA-SRC, we used a variant form of the ErmCL-SRC, termed ErmCL_S10K, where the A-site codon was mutated from AGC (Ser) to AAG (Lys) (Figure 1A). In agreement with previous studies (48,49), mutation of the Ser10 codon, which would be in the A-site of an erythromycin-stalled ErmCL-SRC (41,49), did not noticeably affect the stalling efficiency, and resulted in disome formation in the presence of erythromycin (Figure 1B). The reason for using the ErmCL_S10K construct rather than the wild type ErmCL was simply that, unlike deacylated $tRNA^{Ser}$, deacylated $tRNA^{Lys}$ is commercially available. RelA-SRCs were therefore formed by incubating the ErmCL_S10K-SRC with deacylated $tRNA^{Lys}$ and purified recombinant *E. coli* RelA protein (that was shown to be active in ppGpp synthesis, Supplementary Figure S1). Synthesis of ppGpp by RelA has been proposed to lead to dissociation of RelA from the ribosome (16), thus we generated the RelA-SRCs in the presence of GDP and the non-hydrolysable ATP analogue α, β-methylene-ATP (Figure 1E).

Cryo-EM structure of the RelA-SRC

Cryo-EM data were collected on a Titan Krios transmission electron microscope with a Falcon II direct electron detector. From a total of 197 090 ribosomal particles, *in silico* sorting revealed a large mixture of ribosome populations containing either P-tRNA only (11%), A- and P-tRNAs without an E-tRNA (18%), or fully accommodated A-, P- and E-tRNAs (58%). Despite this heterogeneity, we were able to sort for a small population (24 749 particles,

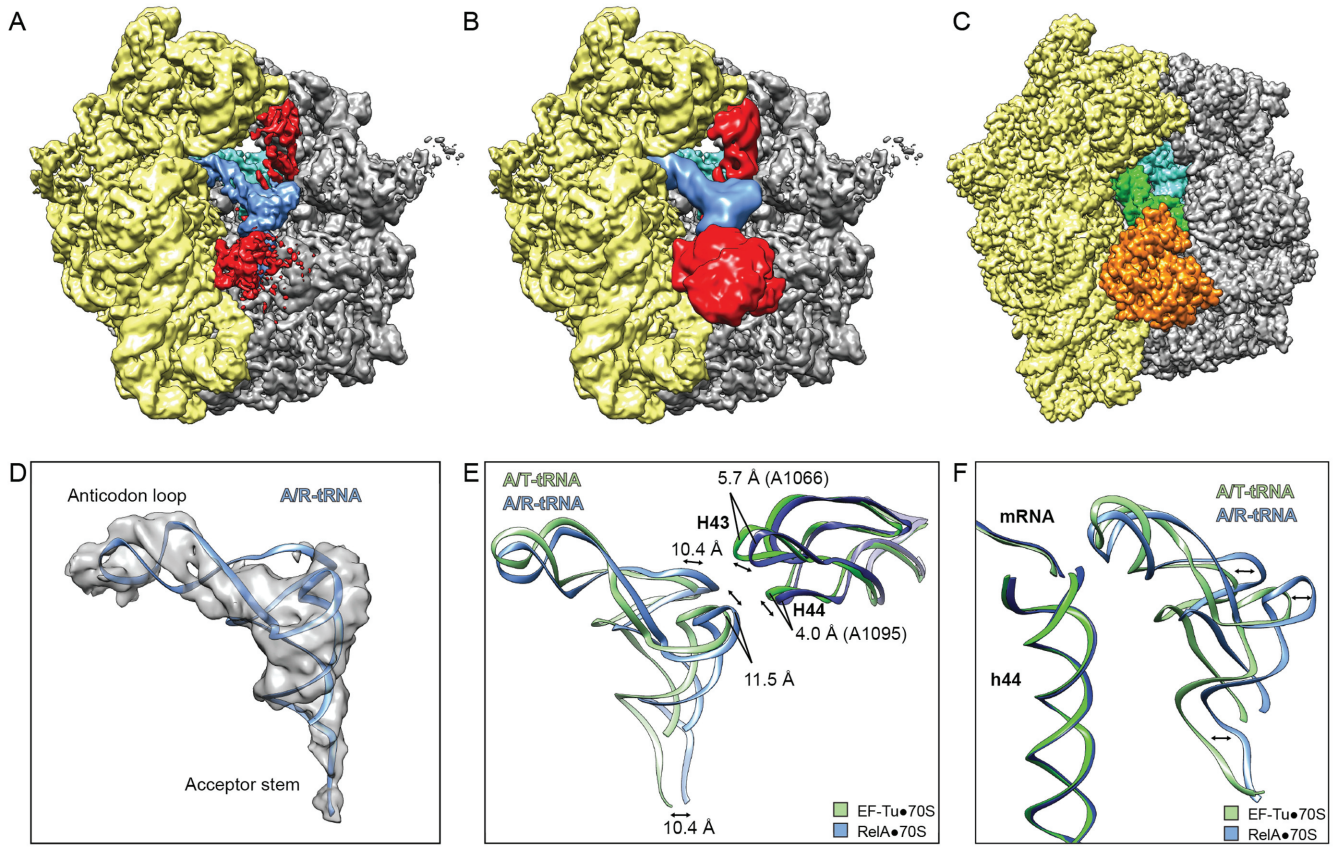

Figure 2. Novel binding site for RelA on the ribosome. (**A** and **B**) Overview of the cryo-EM reconstruction of the RelA-SRC filtered to (**A**) 4 Å and (**B**) 12 Å resolution showing 30S subunit (yellow), 50S subunit (grey), P-tRNA (cyan), A/R-tRNA (blue) and RelA (red). (**C**) Overview of EF-Tu-bound *E. coli* 70S ribosomes with P-tRNA (cyan), A/T-tRNA (green) and EF-Tu (orange) (29). (**D**) Isolated cryo-electron density with fitted model for the A/R-tRNA (blue). (**E** and **F**) Comparison of (**E**) H43 and H44 of the 23S rRNA and (**F**) A/R-tRNA of RelA-SRC (blue) and A/T-tRNA of EF-Tu-70S (green) (29).

13%) that contained a P-tRNA, but also the presence of A/R-tRNA and RelA bound within the ribosomal A-site (Supplementary Figure S2). The large heterogeneity of the data set was similar to that observed previously for the complex of *E. coli* RelA with the *T. thermophilus* 70S ribosome, where the RelA-containing ribosomes represented 15% of the total population (25). The RelA-containing ribosomes, which we term the RelA-SRC (Figure 1E), could be further refined to final average resolution of 3.7 Å (Fourier shell correlation (FSC) cut-off of 0.143, Supplementary Figure S3A). Although the average and local resolution calculations indicate that the majority of the core of the ribosome is 4.0 Å or better, the resolution of the A/R-tRNA and RelA ranged from 4 Å to >10 Å (Supplementary Figure S3B and C), indicating high flexibility of the A/R-tRNA and RelA within the ribosomal binding site, as observed previously (25).

Novel binding site for RelA on the ribosome

In the RelA-SRC, RelA is bound in the A-site of the ribosome and interacts with a tRNA that has adopted an A/T-tRNA-like conformation (Figure 2A and B), similar but distinct to that observed during decoding when the EF-Tu delivers the aminoacyl-tRNA to the A-site of the ribosome (27–29) (Figure 2C). Since we observed no subpopulations of ribosomes bearing A/T-like tRNA conformations in the absence of RelA but rather only fully accommodated A-tRNAs (Supplementary Figure S2), we reason that this state requires RelA for stabilization and therefore we refer to this binding state of the deacylated tRNA as the A/R-tRNA conformation. Within the limits of the resolution, the anticodon stem loop of the A/R-tRNA in the RelA-SRC appears to be similar to that observed during decoding with EF-Tu (29) (Figure 2D–F). Interaction of the anticodon stem-loop of the A/R-tRNA with the codon of the mRNA is not unexpected in the RelA-SRC, since the stimulation of ribosome-dependent RelA-mediated (p)ppGpp synthesis requires the deacylated tRNA to be cognate to the codon in the A-site (15). In contrast, the most prominent differences between the A/R-tRNA and A/T-tRNA states are in the placement of the elbow and acceptor arm of the tRNA, including the CCA-end, which are shifted by ∼10 Å with respect to one another (Figure 2E and F). Accordingly, the stalk base (H43/H44 of the 23S rRNA) is also shifted by ∼4-6 Å between the RelA and EF-Tu structures (Figure 2E).

Stabilization of an A/R-tRNA state by RelA was also observed in the previous cryo-EM reconstruction of the RelA-70S complex (25). In this reconstruction, density assigned to RelA was observed to interact with A/R-tRNA using the external surface of the acceptor arm, whereas no den-

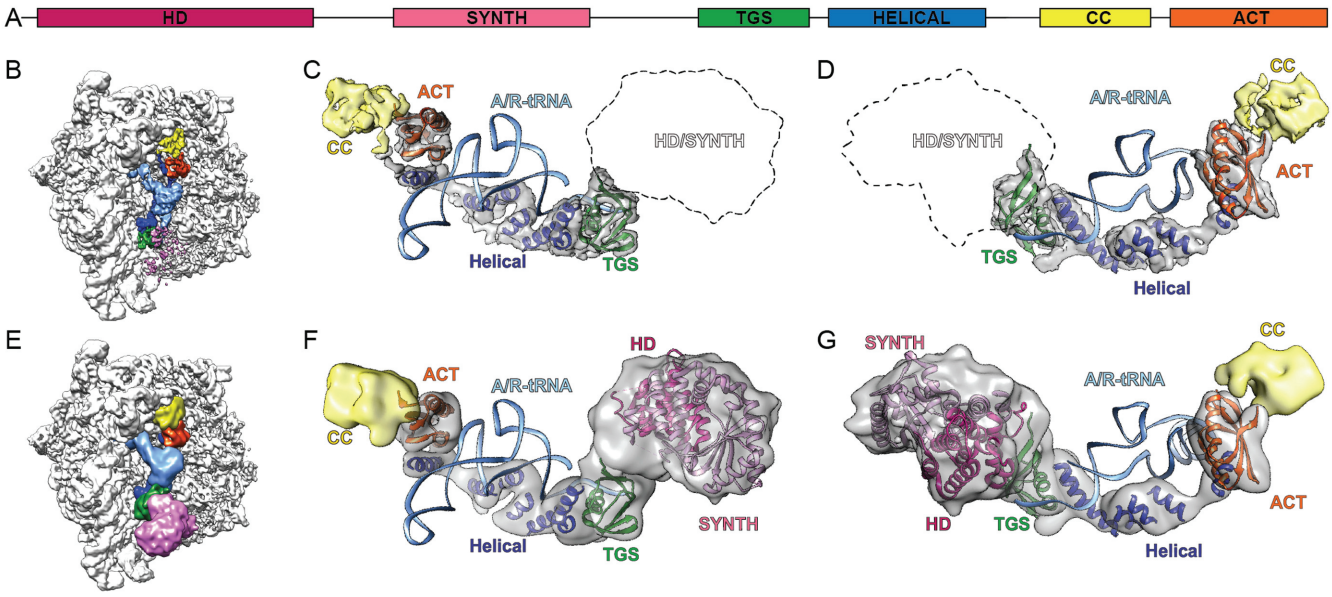

Figure 3. RelA adopts an extended conformation on the ribosome. (**A**) Schematic showing the domain organization of *E. coli* RelA with HD (magenta), SYNTH (pink), TGS (green), HELICAL (blue), CC (yellow) and ACT (orange) subdomains. (**B**) Overview of RelA-SRC with subdomains colored according to (A) and A/R-tRNA (light blue). (**C** and **D**) Complementary views showing isolated electron density of RelA with fitted homology models for TGS (green, PDB2EKI) and ACT (orange, PDB2KO1) subdomains, as well as model poly-Alanine helices fitted to the helical linker region (blue) and density for CC colored in yellow. (**E**–**G**) As (**B**–**D**) with 12 Å filtered maps and additional fitted homology models for HD (magenta) and SYNTH (pink) based on PDB1VJ7 (24).

sity was reported to extend into the intersubunit region of the ribosome (25). In contrast, at higher resolution additional density is observed in the RelA-SRC for RelA that extends from the CCA-end of the A/R-tRNA into the intersubunit region, namely, passing between the small subunit and acceptor arm of the tRNA toward the large ribosomal subunit and occupying the space between the elbow of the A/R-tRNA and the intersubunit bridge contact between the head (hd) of the small subunit and central protuberance (cp) of the large subunit (Figure 2A). When the cryo-EM map for the RelA-SRC was filtered to 12 Å, additionally density for RelA was also observed extending out of the A-site of the ribosome into the solvent (Figure 2B), indicating the extreme flexibility of this region of RelA. To our knowledge, the extended binding site for RelA observed within the A-site intersubunit crevice of the RelA-SRC is distinct from any other translation factor binding sites so far visualized on the ribosome.

RelA adopts an extended conformation on the ribosome

Although *de novo* model building for RelA was not possible, and despite the absence of a crystal structure for the CTD of RelA, the resolution and density features of the RelA-SRC map enabled homology models for distinct parts of the *E. coli* RelA to be fitted unambiguously (Figure 3A–D). In particular, homology models were generated and fitted for the TGS and ACT domains located in the CTD of RelA based on nuclear magnetic resonance (NMR) spectroscopy structures of *Homo sapiens* GTP-binding protein1 TGS domain (PDB2EKI) and of the ACT domain from the *Chlorobium tepidum* GTP pyrophosphokinase (PDB2KO1), respectively (Figure 3B–D and Supplementary Figure S3D–G). Additionally, we could identify five tubular densities that we assigned to the five predicted α-helices (Supplementary Figure S4) present in the helical linker region that connects the TGS with the CC/ACT subdomains (Figure 3B–D). The poor density for the connections between the helices does not allow us to unambiguously assign the order of the helices, nor the directionality, and therefore polyalanine helices were fitted as placeholders. Moreover, it was not possible to generate a suitable homology model for the CC domain and therefore this domain was left unmodelled (Figure 3B–D). Our model for the CTD of RelA reveals that the TGS domain interacts with the CCA-end of the A/R-tRNA, whereas the helical linker wraps around the acceptor arm, positioning the ACT domain to interact with the elbow region of the A/R-tRNA (Figure 3B–D).

Additionally, a homology model could be generated for the HD and SYNTH domains comprising the NTD of RelA based on the X-ray structure of the *S. dysgalactiae* Rel protein (24). Despite the low resolution of the NTD in the RelA-SRC, the distinct features of the density allowed an good fit (cross-correlation coefficient of 0.82) of the helical bundle of HD domain and the long extended helices within the SYNTH domain (Figure 3E–G). Moreover, only this orientation allows the C-terminal end of the SYNTH domain to be oriented toward the TGS domain of the CTD of RelA. Overall, our model for RelA suggests that the NTD of RelA does not form any stable interactions with the ribosome, with the SYNTH domain extending toward but not contacting the spur (helix 6 of the 16S rRNA) of the small subunit (Figure 3E), whereas in contrast the CTD of RelA snakes through the intersubunit space establishing, in ad-

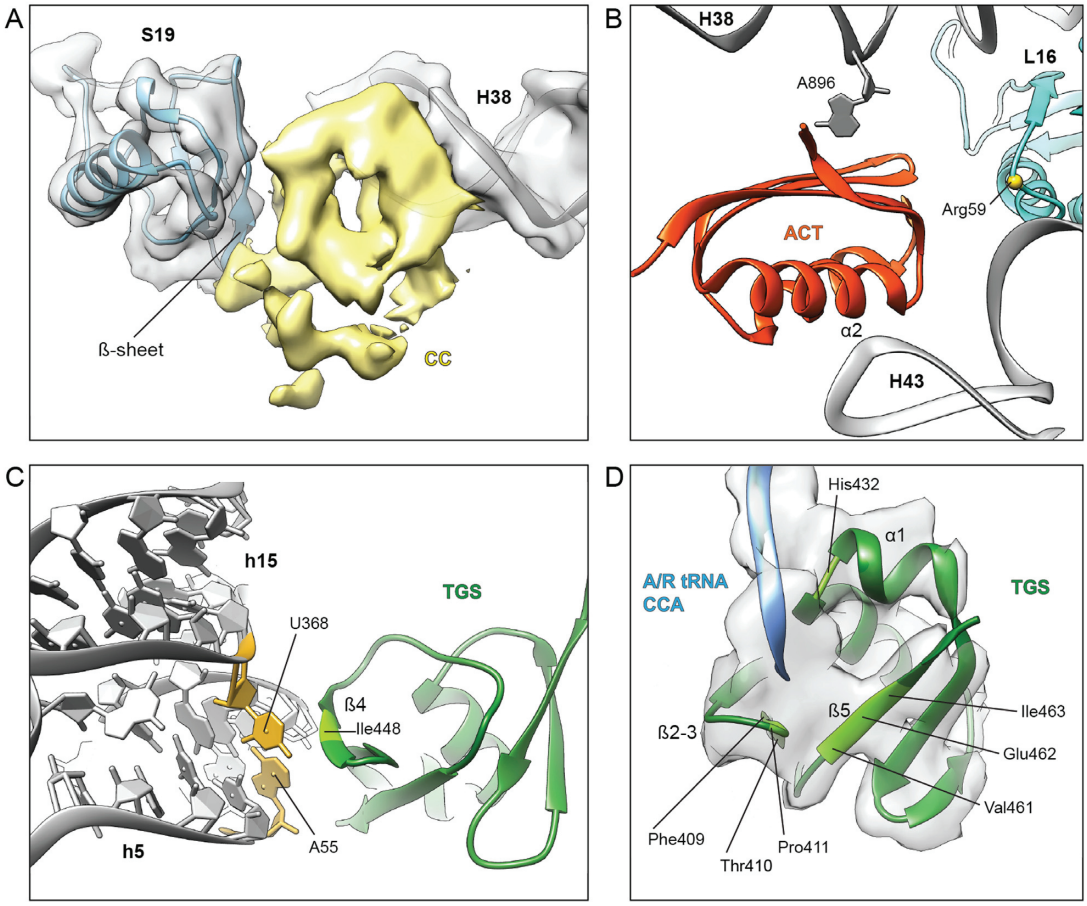

Figure 4. Interactions of RelA with the ribosome and A/R-tRNA. (**A**) Cryo-electron density of the CC subdomain of RelA (yellow) suggests interaction with the β-sheet of r-protein S19 (blue) and the minor groove of H38 in the 23S rRNA (grey). (**B**) Interaction of the C-terminal RelA ACT domain with Arg59 of r-protein L16 (blue) as well as 23S rRNA residues A896 of H38 and the tip of H43. (**C**) The β4-strand of the TGS domain of RelA (green) approaches the minor groove of h5 of the 16S rRNA, where residues in the vicinity of Ile448 (light green) appear to interact with the base-pair formed by nucleotides A55 and U368 (yellow), which are flipped-out of helices h5 and h15, respectively. (**D**) Tentative placement of the A/R-tRNA CCA-end (blue) shows vicinity of C74 of the A/R-tRNA with His432 located at the kink in α-helix α1, whereas C75 and A76 enter into a pocket formed by the β1–β2 hairpin and β5-strand of TGS (green).

dition to the A/R-tRNA, interactions with both the small and large ribosomal subunits (Figure 3B).

Interactions of the RelA CTD with the ribosome and A/R-tRNA

The most extensive interactions between RelA and the ribosome are between the ACT and CC subdomains (Figure 4A and B). The electron density for the CC domain indicates that it contacts components of both the small and large ribosomal subunit, namely, via interaction with the minor groove near the tip of H38 and by contacting the β-sheet of ribosomal protein S19 (Figure 4A). In contrast, the ACT domain contacts only components of the large subunit; specifically, the proximal end of α-helix α2 contacts the tip of H43 of the 23S rRNA, whereas the β-sheet of the ACT domain clearly interacts with A896, which is flipped out of H38 (Figure 4B), as it is in the unbound and vacant 70S structures. Interaction is also observed between the vicinity of Arg59 of ribosomal protein L16 and the terminal end of the β-sheet of the ACT domain (Figure 4B). In addition, α-helix α1 of the ACT domain contacts the elbow region of the A/R-tRNA and α-helix H5 of the helical linker of RelA.

The TGS domain of RelA contains one α-helix α1 and four β-strands β1–β4 (Supplementary Figure S4). The β4-strand of the TGS domain of RelA approaches the minor groove of helix 5 (h5 of the 16S rRNA) of the small subunit, where residues in the vicinity of Ile448 appear to interact with the base-pair formed by nucleotides A55 and U368, which are flipped-out of helices h5 and h15, respectively (Figure 4C), as they are in the unbound and vacant 70S structures. The other contacts of the TGS domain are with the CCA-end of the A/R-tRNA (Figure 4D), which adopts a distinct conformation from the A/T-tRNA (Figure 2E and F). Unfortunately, the density does not allow the nucleotides to be unambiguously modelled and therefore only a general description of the interactions can be provided: C74 of the A/R-tRNA is in the vicinity of His432 located at the kink in α-helix α1, whereas C75 and A76 enter into a pocket formed by the β1–β2 hairpin and β5-strand (Figure 4D). This interaction area of the CCA-end encompasses one of the most highly conserved regions of RelA, including

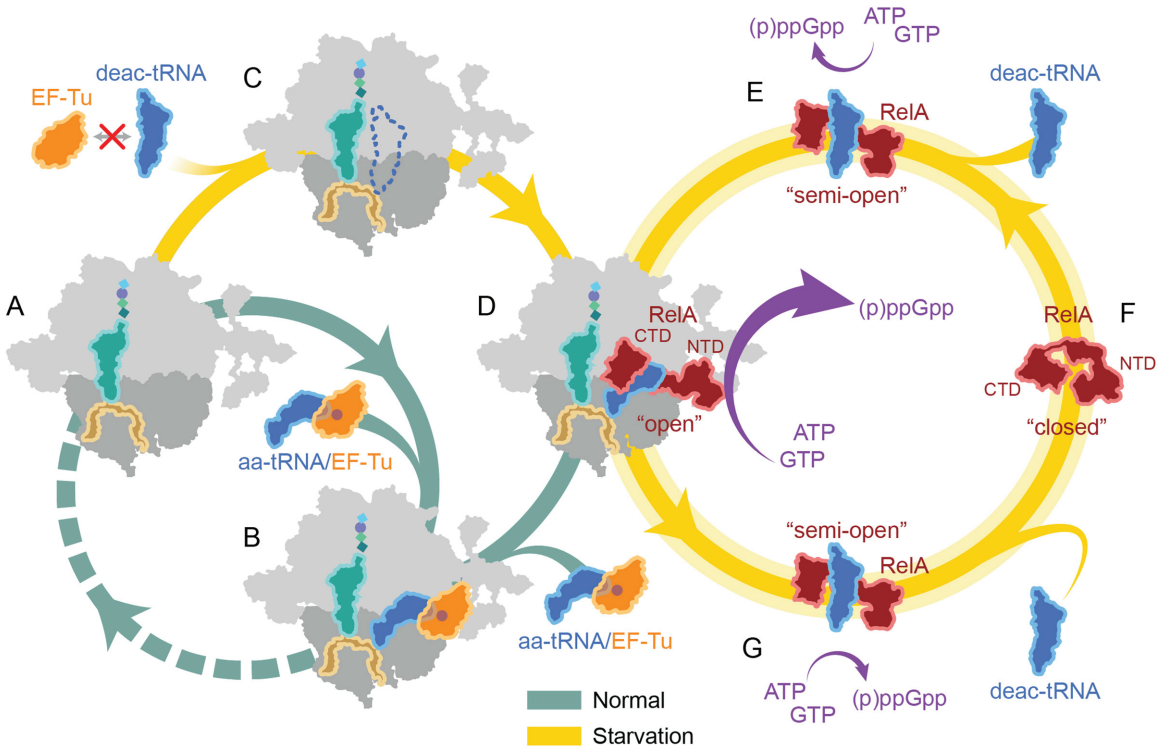

Figure 5. Model for RelA action during the stringent response. (**A** and **B**) Under optimal conditions, aminoacyl-tRNAs (aa-tRNAs) are delivered by EF-Tu (orange) to the A-site of the ribosome (green pathway). (**C**–**G**) Under starvation conditions (yellow pathway), the interaction of RelA (red) with deacylated A/R-tRNA at the A-site of the ribosome leads to the conversion of RelA from a 'closed' to an 'open' conformation and thereby stimulating high levels of (p)ppGpp synthesis. For more details, please refer to the text.

His432 in α-helix α1, Phe409-Pro411 in the β1–β2 hairpin and Val461-Ile463 in the β5-strand (Supplementary Figure S5). Although higher resolution will be required to ascertain exactly how these highly conserved amino acids discriminate between deacylated and aminoacylated tRNAs, our structure provides evidence indicating that the TGS domain of RelA is directly involved in this monitoring activity.

DISCUSSION

Based on our structural results, together with the available biochemical results from the literature, we present a model for the ribosome-dependent stimulation of RelA-mediated (p)ppGpp synthesis (Figure 5A–G): Under optimal growth conditions, aminoacylated tRNAs are delivered to the ribosome in a ternary complex with EF-Tu and GTP (Figure 5A and B). In contrast, under environmental conditions that evoke the stringent response, such as amino acid starvation, the levels of aminoacylated-tRNAs decrease leading to a concomitant accumulation of deacylated or uncharged tRNAs (50). The absence of aminoacylated tRNAs for the codon displayed in the A-site leads to ribosome stalling during translation elongation (Figure 5C). Although the deacylated tRNAs are not bound by EF-Tu or delivered by EF-Tu to the ribosome, it is possible for deacylated tRNAs to bind non-enzymatically to the A-site of the ribosome (Figure 5C). RelA has been proposed to recognize the deacylated tRNA bound in the A-site and catalyze (p)ppGpp synthesis (15–17). However, given the complex intertwined nature of the interaction between RelA and A/R-tRNA observed in our RelA-SRC structure, as well as the apparent lack of the A/R-tRNA conformation of the deacylated tRNA in the absence of RelA, we favor an alternative hypothesis whereby RelA and deacylated tRNA bind to the ribosome as a preformed complex (Figure 5D and E). Indeed, RelA has been shown to interact with deacylated tRNA (but not aminoacylated tRNA) in the absence of the ribosome (26,51,52) (Figure 5E).

Biochemical and genetic evidence suggests that in the absence of the ribosome and deacylated tRNA, RelA exists in an autoinhibited state that produces only low levels of (p)ppGpp (1,3). Specifically, it has been shown that the CTD of RelA is responsible for the observed autoinhibition (21–23,26), leading to the hypothesis that the autoinhibition results from direct interaction between the CTD and NTD of RelA (23), which we term here the 'closed' conformation (Figure 5F). While interaction of deacylated tRNA with the CTD of RelA in the absence of the ribosome promotes a slight increase in (p)ppGpp synthesis activity (26,51,52) (Figure 5E), full activity requires the additional presence of the ribosome (15–17,53,54) (Figure 5D).

The structure of RelA-SRC provides a rationale for this increased activity, namely, that the ribosome and A/R-tRNA stabilize an 'open' conformation of RelA, which relieves the inhibitory interaction that the CTD imparts on the NTD, and thereby allows the uninhibited NTD to efficiently catalyze the synthesis of (p)ppGpp from GTP/GDP and ATP (Figure 5D). This model is consistent with the

observation that deletion of the CTD of RelA prevents interaction of RelA with the ribosome (25) and allows the NTD to synthesize (p)ppGpp in a ribosome-independent manner (21,26,55). Moreover, the RelA-SRC structure indicates that the TGS domain of RelA directly contacts the 3′-end of the deacylated tRNA (Figure 4D), explaining how RelA can monitor and distinguish the aminoacylation state of the A-tRNA (56). It should be noted that ppGpp itself dramatically stimulates the ribosome-dependent RelA-mediated synthesis of itself (18), presumably by acting allosterically through a second, as yet undetermined, binding site on the factor, similar to the allosteric regulation of pppGpp observed recently for the small alarmone synthetase 1 (SAS1) RelQ from *Bacillus subtilis* (57) and *Enterococcus faecalis* (58).

While it is easy in our model to envisage how multiple rounds of (p)ppGpp synthesis by RelA could occur on the ribosome, as reported recently (20), we cannot exclude alternative models where (p)ppGpp synthesis leads to dissociation of RelA from the ribosome (16,19). Moreover, it remains unclear as to the order and timing of release of RelA and deacylated-tRNA from the ribosome following synthesis of (p)ppGpp (59), with one report suggested (p)ppGpp synthesis leads to release of deacylated-tRNA but not RelA, whereas another observed release of RelA, but not deacylated tRNA upon (p)ppGpp synthesis (16). From a structural viewpoint, it is hard to envisage how the intertwined CTD of RelA could dissociate from the ribosome without prior or concomitant dissociation of the deacylated A/R-tRNA. As mentioned, RelA has been shown to interact with deacylated tRNA in the absence of the ribosome and that this interaction occurs with the CTD and promotes a slight increase in (p)ppGpp synthesis activity (26,51,52). Consistently, fluorescence resonance energy transfer experiments indicate that the distance between the NTD and CTD of RelA increases upon binding of deacylated tRNA (60). This suggests to us that following dissociation from the ribosome, but still in the presence of deacylated tRNA, RelA can adopt a 'semi-open' conformation that can retain (p)ppGpp synthesis activity for an extended period of time (Figure 5G), consistent with the interpretation of single molecule experiments examining RelA action in living cells (19). Nevertheless, RelA has low affinity for deacylated tRNA in the absence of the ribosome (51), suggesting that either the RelA-tRNA complex becomes stabilized by rebinding to the ribosome and stimulating higher levels of (p)ppGpp synthesis, or the RelA-tRNA complex disassembles, allowing RelA to adopt the less active closed conformation (Figure 5F). It seems probable that the former pathway of rebinding would be favoured under conditions of starvation where a high ratio of deacylated tRNAs over aminoacylated tRNAs exists in the cell. In contrast, the latter pathway of disassembly would be favored as the nutrient deprivation is alleviated and the ratio is reversed, such that the increased intracellular levels of charged aminoacyl-tRNA promote A-site binding and thereby allows translation to resume (Figure 5B).

ACCESSION NUMBERS

The coordinates and cryo-EM map for the RelA-SRC have been deposited in the Protein Data Bank and EM Data-Bank under accession codes 5L3P and EMD-4001, respectively.

NOTE ADDED IN PROOF

During production of our work, a cryo-EMreconstruction of a *E. coli* RelA-70S complex was published by Ramakrishnan and coworkers (61). Our findings are in perfect agreement with their results and lead to the same conclusion: The ribosome and A/R-tRNA stabilize an 'open' conformation of RelA, which relieves the inhibitory interaction that the CTD imparts on the NTD, and thereby allows the uninhibited NTD to efficiently catalyze the synthesis of (p)ppGpp from GTP/GDP and ATP.

SUPPLEMENTARY DATA

Supplementary Data are available at NAR Online.

ACKNOWLEDGEMENT

The authors would like to thank Gemma Atkinson for help with the Weblogo and Heidimarie Sieber and Charlotte Ungewickell for expert technical assistance.

FUNDING

Deutsche Forschungsgemeinschaft [FOR-1805 and GRK1721 to D.N.W. and R.B., SPP-1879 to D.N.W, SFB-646 to R.B.]; Swedish Research council Vetenskapsrådet [2013-4680 to V.H.]. Funding for open access charge: DFG [FOR-1805 and SPP-1879 to D.N.W].
Conflict of interest statement. None declared.

REFERENCES

1. Potrykus,K. and Cashel,M. (2008) (p)ppGpp: still magical? *Annu. Rev. Microbiol.*, **62**, 35–51.
2. Atkinson,G.C., Tenson,T. and Hauryliuk,V. (2011) The RelA/SpoT homolog (RSH) superfamily: distribution and functional evolution of ppGpp synthetases and hydrolases across the tree of life. *PLoS One*, **6**, e23479.
3. Hauryliuk,V., Atkinson,G.C., Murakami,K.S., Tenson,T. and Gerdes,K. (2015) Recent functional insights into the role of (p)ppGpp in bacterial physiology. *Nat. Rev. Microbiol.*, **13**, 298–309.
4. Dalebroux,Z.D., Svensson,S.L., Gaynor,E.C. and Swanson,M.S. (2010) ppGpp conjures bacterial virulence. *Microbiol. Mol. Biol. Rev.*, **74**, 171–199.
5. Geiger,T., Francois,P., Liebeke,M., Fraunholz,M., Goerke,C., Krismer,B., Schrenzel,J., Lalk,M. and Wolz,C. (2012) The stringent response of Staphylococcus aureus and its impact on survival after phagocytosis through the induction of intracellular PSMs expression. *PLoS Pathog.*, **8**, e1003016.
6. Poole,K. (2012) Bacterial stress responses as determinants of antimicrobial resistance. *J. Antimicrob. Chemother.*, **67**, 2069–2089.
7. Maisonneuve,E. and Gerdes,K. (2014) Molecular mechanisms underlying bacterial persisters. *Cell*, **157**, 539–548.
8. Wexselblatt,E., Kaspy,I., Glaser,G., Katzhendler,J. and Yavin,E. (2013) Design, synthesis and structure-activity relationship of novel Relacin analogs as inhibitors of Rel proteins. *Eur. J. Med. Chem.*, **70**, 497–504.

9. Wexselblatt,E., Oppenheimer-Shaanan,Y., Kaspy,I., London,N., Schueler-Furman,O., Yavin,E., Glaser,G., Katzhendler,J. and Ben-Yehuda,S. (2012) Relacin, a novel antibacterial agent targeting the Stringent Response. *PLoS Pathog.*, **8**, e1002925.
10. Cashel,M. and Gallant,J. (1969) Two compounds implicated in the function of the RC gene of Escherichia coli. *Nature*, **221**, 838–841.
11. Laffler,T. and Gallant,J. (1974) spo T, a new genetic locus involved in the stringent response in E. coli. *Cell*, **1**, 27–30.
12. Xiao,H., Kalman,M., Ikehara,K., Zemel,S., Glaser,G. and Cashel,M. (1991) Residual guanosine 3′,5′-bispyrophosphate synthetic activity of relA null mutants can be eliminated by spoT null mutations. *J. Biol. Chem.*, **266**, 5980–5990.
13. Seyfzadeh,M., Keener,J. and Nomura,M. (1993) spoT-dependent accumulation of guanosine tetraphosphate in response to fatty acid starvation in Escherichia coli. *Proc. Natl. Acad. Sci. U.S.A.*, **90**, 11004–11008.
14. Vinella,D., Albrecht,C., Cashel,M. and D'Ari,R. (2005) Iron limitation induces SpoT-dependent accumulation of ppGpp in Escherichia coli. *Mol. Microbiol.*, **56**, 958–970.
15. Haseltine,W.A. and Block,R. (1973) Synthesis of guanosine tetra- and pentaphosphate requires the presence of a codon-specific, uncharged transfer ribonucleic acid in the acceptor site of ribosomes. *Proc. Natl. Acad. Sci. U.S.A.*, **70**, 1564–1568.
16. Wendrich,T.M., Blaha,G., Wilson,D.N., Marahiel,M.A. and Nierhaus,K.H. (2002) Dissection of the mechanism for the stringent factor RelA. *Mol. Cell*, **10**, 779–788.
17. Jenvert,R.-M. and Schiavone,L. (2005) Characterization of the tRNA and ribosome-dependent pppGpp-synthesis by recombinant stringent factor from *Escherichia coli*. *FEBS J.*, **272**, 685–695.
18. Shyp,V., Tankov,S., Ermakov,A., Kudrin,P., English,B.P., Ehrenberg,M., Tenson,T., Elf,J. and Hauryliuk,V. (2012) Positive allosteric feedback regulation of the stringent response enzyme RelA by its product. *EMBO Rep.*, **13**, 835–839.
19. English,B.P., Hauryliuk,V., Sanamrad,A., Tankov,S., Dekker,N.H. and Elf,J. (2011) Single-molecule investigations of the stringent response machinery in living bacterial cells. *Proc. Natl. Acad. Sci. U.S.A.*, **108**, E365–E373.
20. Li,W., Bouveret,E., Zhang,Y., Liu,K., Wang,J.D. and Weisshaar,J.C. (2016) Effects of amino acid starvation on RelA diffusive behavior in live Escherichia coli. *Mol. Microbiol.*, **99**, 571–585.
21. Schreiber,G., Metzger,S., Aizenman,E., Roza,S., Cashel,M. and Glaser,G. (1991) Overexpression of the relA gene in Escherichia coli. *J. Biol. Chem.*, **266**, 3760–3767.
22. Gropp,M., Strausz,Y., Gross,M. and Glaser,G. (2001) Regulation of *Escherichia coli* RelA requires oligomerization of the C- terminal domain. *J. Bacteriol.*, **183**, 570–579.
23. Mechold,U., Murphy,H., Brown,L. and Cashel,M. (2002) Intramolecular regulation of the opposing (p)ppGpp catalytic activities of Rel(Seq), the Rel/Spo enzyme from Streptococcus equisimilis. *J. Bacteriol.*, **184**, 2878–2888.
24. Hogg,T., Mechold,U., Malke,H., Cashel,M. and Hilgenfeld,R. (2004) Conformational antagonism between opposing active sites in a bifunctional RelA/SpoT homolog modulates (p)ppGpp metabolism during the stringent response. *Cell*, **117**, 57–68.
25. Agirrezabala,X., Fernandez,I.S., Kelley,A.C., Carton,D.G., Ramakrishnan,V. and Valle,M. (2013) The ribosome triggers the stringent response by RelA via a highly distorted tRNA. *EMBO Rep.*, **14**, 811–816.
26. Jain,V., Saleem-Batcha,R., China,A. and Chatterji,D. (2006) Molecular dissection of the mycobacterial stringent response protein Rel. *Protein Sci.*, **15**, 1449–1464.
27. Schmeing,T.M., Voorhees,R.M., Kelley,A.C., Gao,Y.G., Murphy,F.V.t., Weir,J.R. and Ramakrishnan,V. (2009) The crystal structure of the ribosome bound to EF-Tu and aminoacyl-tRNA. *Science*, **326**, 688–694.
28. Schuette,J.C., Murphy,F.V. IV, Kelley,A.C., Weir,J.R., Giesebrecht,J., Connell,S.R., Loerke,J., Mielke,T., Zhang,W., Penczek,P.A. *et al.* (2009) GTPase activation of elongation factor EF-Tu by the ribosome during decoding. *EMBO J.*, **28**, 755–765.
29. Fischer,N., Neumann,P., Konevega,A.L., Bock,L.V., Ficner,R., Rodnina,M.V. and Stark,H. (2015) Structure of the E. coli ribosome-EF-Tu complex at <3 A resolution by C-corrected cryo-EM. *Nature*,**520**, 567–570.
30. Arenz,S., Ramu,H., Gupta,P., Berninghausen,O., Beckmann,R., Vazquez-Laslop,N., Mankin,A.S. and Wilson,D.N. (2014) Molecular basis for erythromycin-dependent ribosome stalling during translation of the ErmBL leader peptide. *Nat. Commun.*, **5**, 3501.
31. Iordanescu,S. (1976) Three distinct plasmids originating in the same Staphylococcus aureus strain. *Arch. Roum. Pathol. Exp. Microbiol.*, **35**, 111–118.
32. Narayanan,C.S. and Dubnau,D. (1985) Evidence for the translational attenuation model: ribosome-binding studies and structural analysis with an in vitro run-off transcript of ermC. *Nucleic Acids Res.*, **13**, 7307–7326.
33. Antoun,A., Pavlov,M.Y., Tenson,T. and Ehrenberg,M.M. (2004) Ribosome formation from subunits studied by stopped-flow and Rayleigh light scattering. *Biol. Proced. Online*, **6**, 35–54.
34. Li,X., Mooney,P., Zheng,S., Booth,C.R., Braunfeld,M.B., Gubbens,S., Agard,D.A. and Cheng,Y. (2013) Electron counting and beam-induced motion correction enable near-atomic-resolution single-particle cryo-EM. *Nat. Methods*, **10**, 584–590.
35. Scheres,S.H. (2012) RELION: implementation of a Bayesian approach to cryo-EM structure determination. *J. Struct. Biol.*, **180**, 519–530.
36. Kucukelbir,A., Sigworth,F.J. and Tagare,H.D. (2014) Quantifying the local resolution of cryo-EM density maps. *Nat. Methods*, **11**, 63–65.
37. Rohou,A. and Grigorieff,N. (2015) CTFFIND4: Fast and accurate defocus estimation from electron micrographs. *J. Struct. Biol.*, **192**, 216–221.
38. Frank,J., Radermacher,M., Penczek,P., Zhu,J., Li,Y., Ladjadj,M. and Leith,A. (1996) SPIDER and WEB: processing and visualization of images in 3D electron microscopy and related fields. *J. Struct. Biol.*, **116**, 190–199.
39. Becker,T., Franckenberg,S., Wickles,S., Shoemaker,C.J., Anger,A.M., Armache,J.P., Sieber,H., Ungewickell,C., Berninghausen,O., Daberkow,I. *et al.* (2012) Structural basis of highly conserved ribosome recycling in eukaryotes and archaea. *Nature*, **482**, 501–506.
40. Chen,J.Z. and Grigorieff,N. (2007) SIGNATURE: a single-particle selection system for molecular electron microscopy. *J. Struct. Biol.*, **157**, 168–173.
41. Arenz,S., Meydan,S., Starosta,A.L., Berninghausen,O., Beckmann,R., Vazquez-Laslop,N. and Wilson,D.N. (2014) Drug sensing by the ribosome induces translational arrest via active site perturbation. *Mol. Cell*, **56**, 446–452.
42. Loerke,J., Giesebrecht,J. and Spahn,C.M. (2010) Multiparticle cryo-EM of ribosomes. *Methods Enzymol.*, **483**, 161–177.
43. Arenz,S., Nguyen,F., Beckmann,R. and Wilson,D.N. (2015) Cryo-EM structure of the tetracycline resistance protein TetM in complex with a translating ribosome at 3.9-A resolution. *Proc. Natl. Acad. Sci. U.S.A.*, **112**, 5401–5406.
44. Emsley,P. and Cowtan,K. (2004) Coot: Model-building tools for molecular graphics. *Acta Crystallogr. D Biol. Crystallogr.*, **60**, 2126–2132.
45. Soding,J., Biegert,A. and Lupas,A.N. (2005) The HHpred interactive server for protein homology detection and structure prediction. *Nucleic Acids Res.*, **33**, W244–W248.
46. Eswar,N., Eramian,D., Webb,B., Shen,M.Y. and Sali,A. (2008) Protein structure modeling with MODELLER. *Methods Mol. Biol.*, **426**, 145–159.
47. Pettersen,E.F., Goddard,T.D., Huang,C.C., Couch,G.S., Greenblatt,D.M., Meng,E.C. and Ferrin,T.E. (2004) UCSF Chimera - A Visualization System for Exploratory Research and Analysis. *J. Comput. Chem.*, **25**, 1605–1612.
48. Mayford,M. and Weisblum,B. (1989) ermC leader peptide. Amino acid sequence critical for induction by translational attenuation. *J. Mol. Biol.*, **206**, 69–79.
49. Vazquez-Laslop,N., Thum,C. and Mankin,A.S. (2008) Molecular mechanism of drug-dependent ribosome stalling. *Mol. Cell*, **30**, 190–202.
50. Yegian,C.D., Stent,G.S. and Martin,E.M. (1966) Intracellular condition of *Escherichia coli* transfer RNA. *Proc. Natl. Acad. Sci. U.S.A.*, **55**, 839–846.
51. Avarbock,D., Avarbock,A. and Rubin,H. (2000) Differential regulation of opposing RelMtb activities by the aminoacylation state

of a tRNA.ribosome.mRNA.RelMtb complex. *Biochemistry*, **39**, 11640–11648.
52. Avarbock,A., Avarbock,D., Teh,J.S., Buckstein,M., Wang,Z.M. and Rubin,H. (2005) Functional regulation of the opposing (p)ppGpp synthetase/hydrolase activities of RelMtb from Mycobacterium tuberculosis. *Biochemistry*, **44**, 9913–9923.
53. Rojiani,M.V., Jakubowski,H. and Goldman,E. (1989) Effect of variation of charged and uncharged tRNA(Trp) levels on ppGpp synthesis in *Escherichia coli*. *J. Bacteriol.*, **171**, 6493–6502.
54. Payoe,R. and Fahlman,R.P. (2011) Dependence of RelA-mediated (p)ppGpp formation on tRNA identity. *Biochemistry*, **50**, 3075–3083.
55. Svitil,A.L., Cashel,M. and Zyskind,J.W. (1993) Guanosine tetraphosphate inhibits protein synthesis in vivo - a possible protective mechanism for starvation stress in Escherichia-coli. *J. Biol. Chem.*, **268**, 2307–2311.
56. Sprinzl,M. and Richter,D. (1976) Free 3′-OH group of the terminal adenosine of the tRNA molecule is essential for the synthesis in vitro of guanosine tetraphosphate and pentaphosphate in a ribosomal system from Escherichia coli. *Eur. J. Biochem.*, **71**, 171–176.
57. Steinchen,W., Schuhmacher,J.S., Altegoer,F., Fage,C.D., Srinivasan,V., Linne,U., Marahiel,M.A. and Bange,G. (2015) Catalytic mechanism and allosteric regulation of an oligomeric (p)ppGpp synthetase by an alarmone. *Proc. Natl. Acad. Sci. U.S.A.*, **112**, 13348–13353.
58. Gaca,A.O., Kudrin,P., Colomer-Winter,C., Beljantseva,J., Liu,K., Anderson,B., Wang,J.D., Rejman,D., Potrykus,K., Cashel,M. *et al.* (2015) From (p)ppGpp to (pp)pGpp: Characterization of Regulatory Effects of pGpp Synthesized by the Small Alarmone Synthetase of Enterococcus faecalis. *J. Bacteriol.*, **197**, 2908–2919.
59. Richter,D. (1976) Stringent factor from *Escherichiacoli* directs ribosomal binding and release of uncharged tRNA. *Proc. Natl. Acad. Sci. U.S.A.*, **73**, 707–711.
60. Jain,V., Saleem-Batcha,R. and Chatterji,D. (2007) Synthesis and hydrolysis of pppGpp in mycobacteria: a ligand mediated conformational switch in Rel. *Biophys. Chem.*, **127**, 41–50.
61. Brown,A., Fernández,I.S., Gordiyenko,Y. and Ramakrishnan,V. (2016) Ribosome-dependent activation of stringent control. *Nature*, doi:10.1038/nature17675.

SUPPLEMENTARY ONLINE MATERIALS

for

Stefan Arenz[1,†], Maha Abdelshahid[1,†], Daniel Sohmen[1,†], Roshani Payoe[2], Agata L. Starosta[1,§], Otto Berninghausen[1], Vasili Hauryliuk[2,3], Roland Beckmann[1,4], Daniel N. Wilson[1,4,*]

[1] Gene Center and Department for Biochemistry, University of Munich, Munich, 81377, Germany

[2] University of Tartu, Institute of Technology, Nooruse 1, 50411 Tartu, Estonia

[3] Laboratory for Molecular Infection Medicine Sweden (MIMS), Umeå University, Building 6K and 6L, University Hospital Area, SE-901 87 Umeå, Sweden

[4] Center for integrated Protein Science Munich (CiPSM), University of Munich, Munich, 81377, Germany

* To whom correspondence should be addressed. Tel: +49 89 2180 76903; Fax: +49 89 2180 76945; Email: wilson@lmb.uni-muenchen.de.

§ Present Address: Centre for Bacterial Cell Biology, Institute for Cell and Molecular Biosciences, University of Newcastle, Newcastle upon Tyne, United Kingdom.

† These authors contributed equally to the paper as first authors.

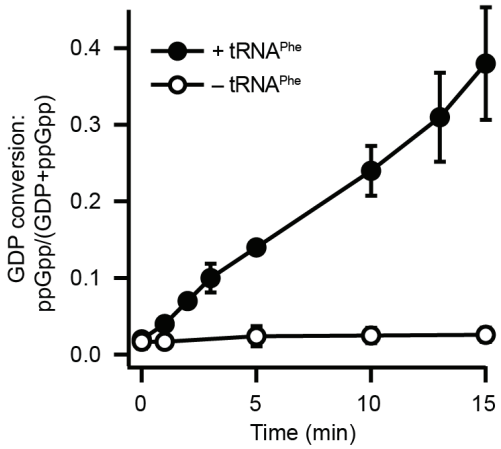

Figure S1 Activity of *E. coli* RelA to synthesize ppGpp. Cognate deacylated tRNA strongly activates ppGpp synthesis by RelA. Time courses of ^{3}H-ppGpp synthesis by RelA in the presence (filled circles) or absence (empty circles) of 1.5 μM deacylated tRNA^{Phe}. In both cases the reaction mixture contained 0.5 μM 70S programmed with 1 μM MF-mRNA and 1.5 μM tRNA$_f^{Met}$, 100 nM RelA, 100 μM ppGpp, 0.3 mM ^{3}H-GDP and 1 mM ATP. Results are shown as mean values of 3 replicates and error bars indicate standard error of the mean.

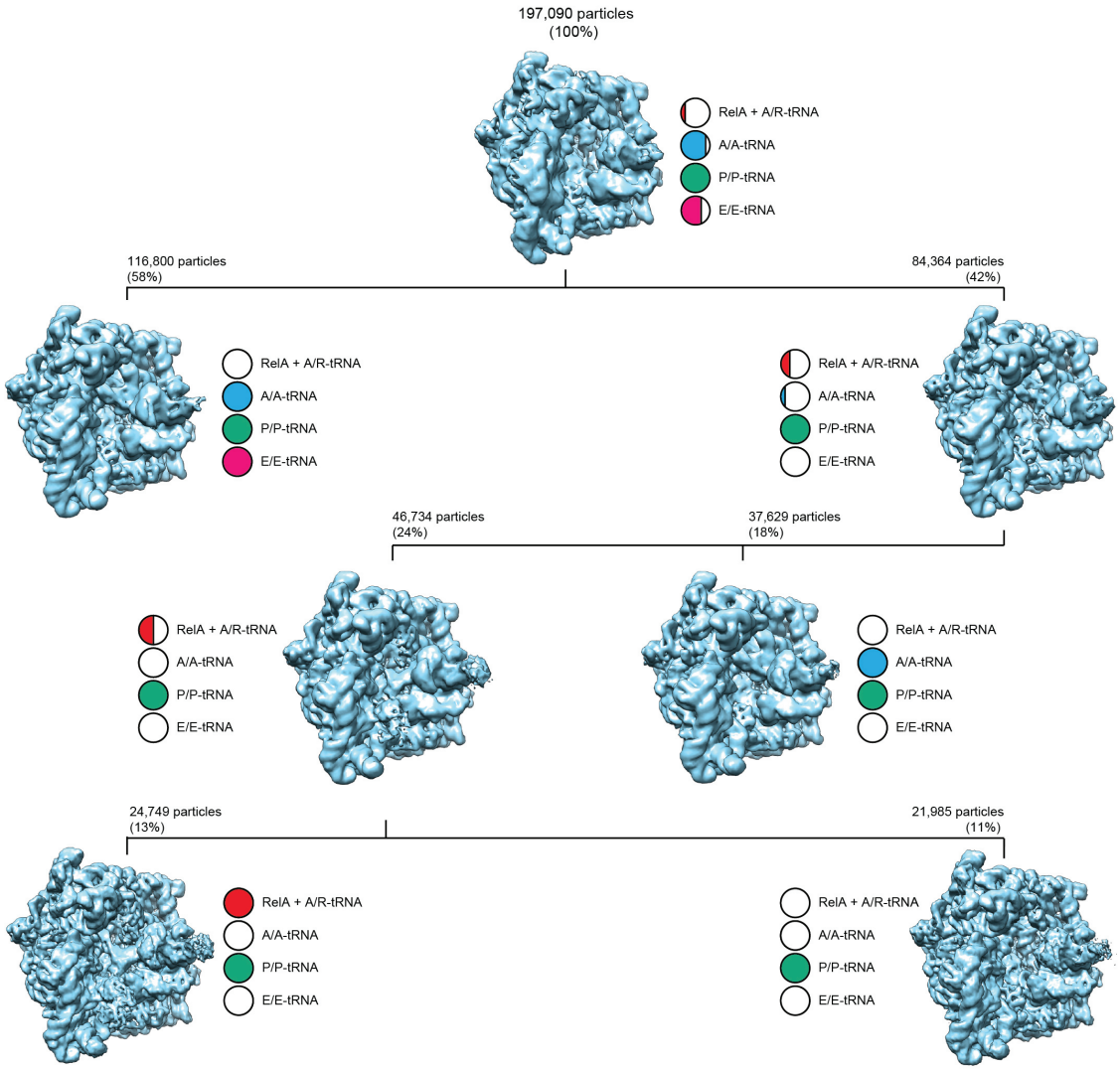

Figure S2: *In silico* sorting scheme of the RelA-SRC cryo-EM dataset. After removal of non-aligning and edge particles, sorting of the dataset yielded four homogenous sub-datasets. The first (58%; 116,800 particles) contained stoichiometric density for A-, P- and E-tRNAs, the second (18%; 37,629 particles) contained stoichiometric density for A- and P-tRNAs, the third (11%; 21,985 particles) contained stoichiometric density for P-tRNA and the fourth sub-dataset (13%; 24,749 particles) contained stoichiometric density for RelA, A/R-tRNA and P-tRNA (RelA-SRC).

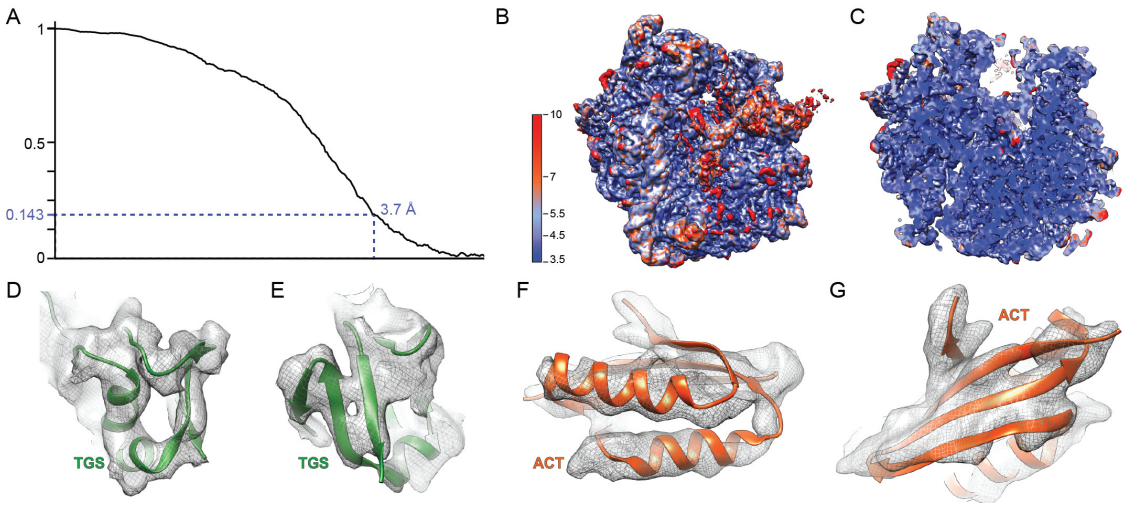

Figure S3: Resolution of the cryo-EM reconstruction of the RelA-SRC. (A) Fourier-shell correlation curve of the refined final map, indicating the average resolution of the RelA-SRC is 3.7 Å. (B,C) (B) Overview and (C) slice through of the RelA-SRC colored according to the local resolution as calculated using ResMap (1). (D,E) Different views showing the rigid body-fitted homology model of the TGS subdomain of RelA (green, PDB2EKI) into the cryo-EM density (grey mesh). (F,G) Different views showing the rigid body-fitted homology model of the ACT subdomain of RelA (orange, PDB2KO1) into the cryo-EM density (grey mesh).

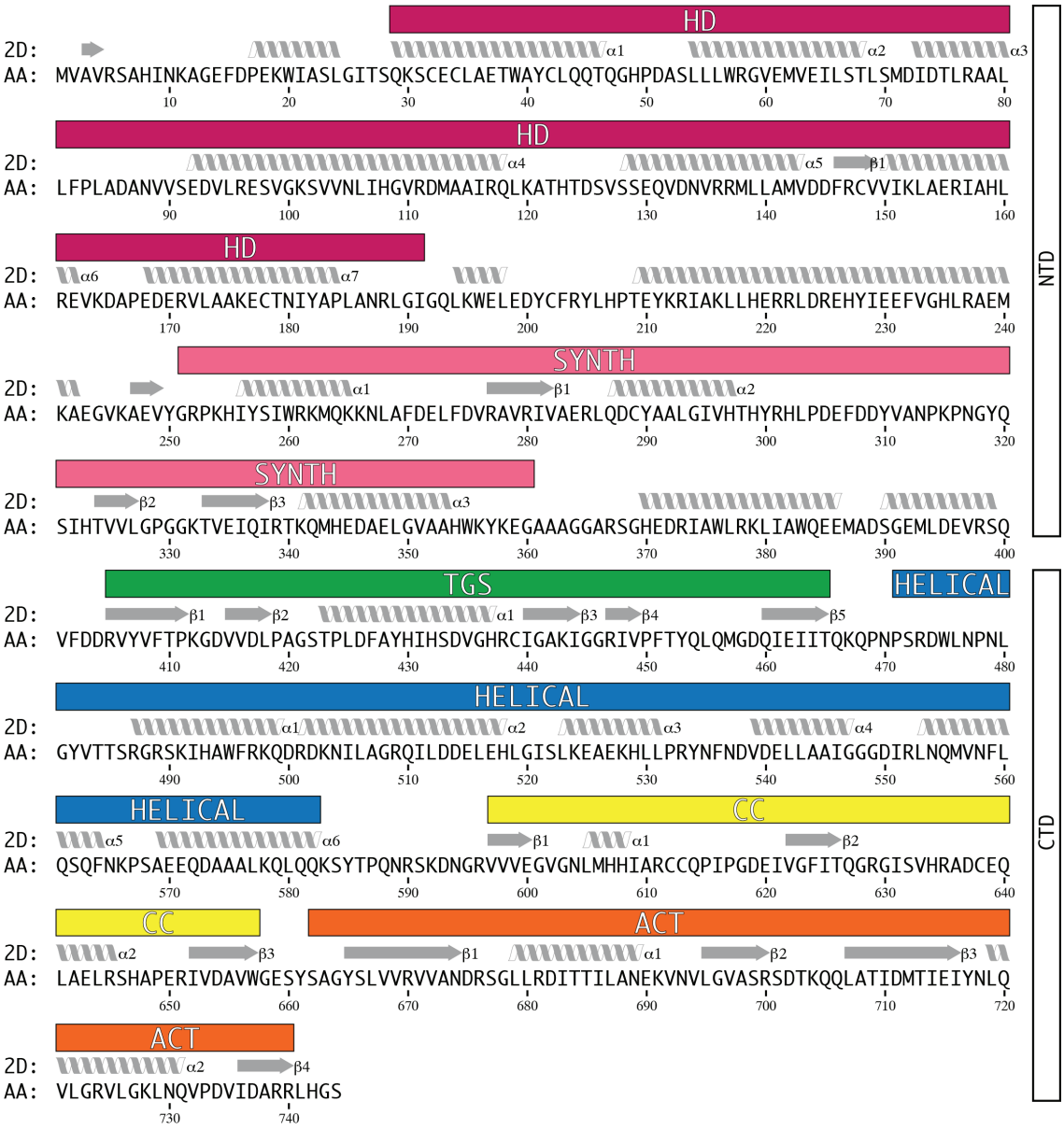

Figure S4: Secondary structure prediction for subdomains of *E. coli* RelA. The amino acid (AA) sequence of *E. coli* RelA with the HD (magenta), SYNTH (pink), TGS (green), HELICAL (blue), CC (gold) and ACT (orange) subdomains is shown together with secondary structure predictions for α-helices and β-strands (2D) based on PSIPRED (2). The secondary structures predictions for TGS and ACT domains were adjusted based on homology models generated from HHPred (3) and Modeller (4).

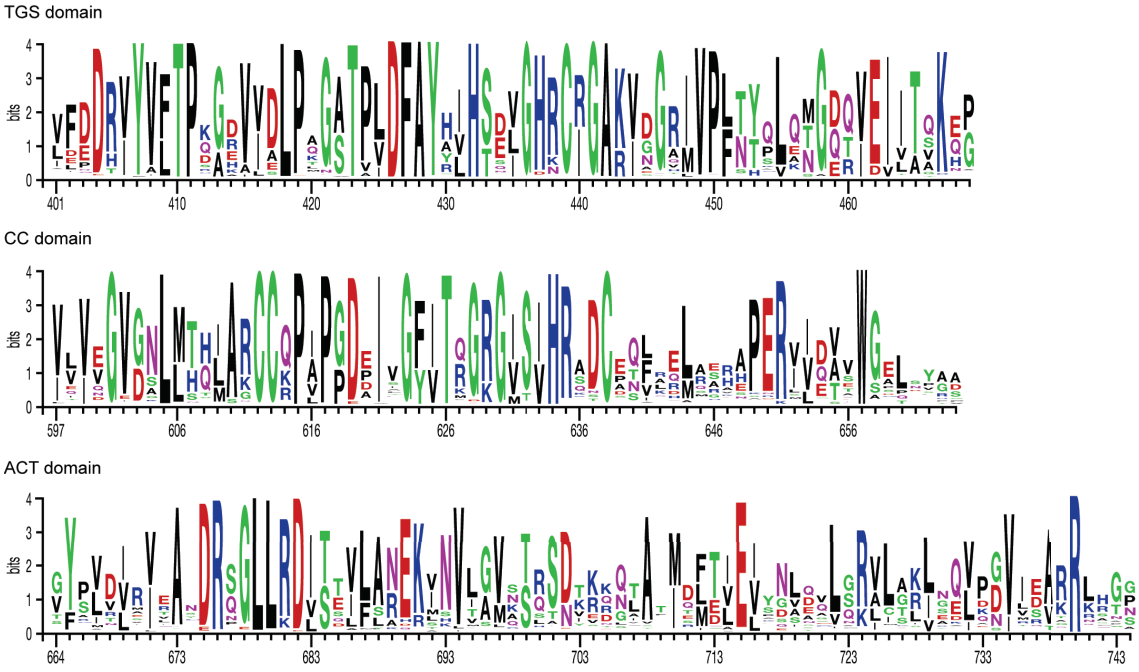

Figure S5: Weblogo plots showing conservation for TGS, CC and ACT subdomains of *E. coli* RelA. The amino acid number for *E. coli* RelA subdomains is shown on the x-axis and the figure was generated using the Weblogo server (5).

SUPPLEMENTARY REFERENCES

1. Kucukelbir, A., Sigworth, F.J. and Tagare, H.D. (2014) Quantifying the local resolution of cryo-EM density maps. *Nat Methods*, **11**, 63-65.
2. Buchan, D., Minneci, F., Nugent, T., Bryson, K. and Jones, D. (2013) Scalable web services for the PSIPRED Protein Analysis Workbench. *Nucleic Acids Research*, **41** W340-W348.
3. Soding, J., Biegert, A. and Lupas, A.N. (2005) The HHpred interactive server for protein homology detection and structure prediction. *Nucleic Acids Res*, **33**, W244-248.
4. Eswar, N., Eramian, D., Webb, B., Shen, M.Y. and Sali, A. (2008) Protein structure modeling with MODELLER. *Methods Mol Biol*, **426**, 145-159.
5. Crooks, G.E., Hon, G., Chandonia, J.M. and Brenner, S.E. (2004) WebLogo: a sequence logo generator. *Genome Res.*, **14**, 1188-1190.